

**Final Report on CFD and Thermal-Mechanical Stress
Analysis of PWR Surge Line under Transient
Condition Thermal Stratification and an Evolutionary
Cyclic Plasticity Based Transformative Fatigue
Evaluation Approach without Using S~N Curve: Rev.1**

Nuclear Engineering Division

About Argonne National Laboratory

Argonne is a U.S. Department of Energy laboratory managed by UChicago Argonne, LLC under contract DE-AC02-06CH11357. The Laboratory's main facility is outside Chicago, at 9700 South Cass Avenue, Argonne, Illinois 60439. For information about Argonne and its pioneering science and technology programs, see www.anl.gov.

DOCUMENT AVAILABILITY

Online Access: U.S. Department of Energy (DOE) reports produced after 1991 and a growing number of pre-1991 documents are available free via DOE's SciTech Connect (<http://www.osti.gov/scitech/>)

Reports not in digital format may be purchased by the public from the National Technical Information Service (NTIS):

U.S. Department of Commerce
National Technical Information Service
5301 Shawnee Rd
Alexandria, VA 22312
www.ntis.gov
Phone: (800) 553-NTIS (6847) or (703) 605-6000
Fax: (703) 605-6900
Email: **orders@ntis.gov**

Reports not in digital format are available to DOE and DOE contractors from the Office of Scientific and Technical Information (OSTI):

U.S. Department of Energy
Office of Scientific and Technical Information
P.O. Box 62
Oak Ridge, TN 37831-0062
www.osti.gov
Phone: (865) 576-8401
Fax: (865) 576-5728
Email: **reports@osti.gov**

Disclaimer

This report was prepared as an account of work sponsored by an agency of the United States Government. Neither the United States Government nor any agency thereof, nor UChicago Argonne, LLC, nor any of their employees or officers, makes any warranty, express or implied, or assumes any legal liability or responsibility for the accuracy, completeness, or usefulness of any information, apparatus, product, or process disclosed, or represents that its use would not infringe privately owned rights. Reference herein to any specific commercial product, process, or service by trade name, trademark, manufacturer, or otherwise, does not necessarily constitute or imply its endorsement, recommendation, or favoring by the United States Government or any agency thereof. The views and opinions of document authors expressed herein do not necessarily state or reflect those of the United States Government or any agency thereof, Argonne National Laboratory, or UChicago Argonne, LLC.

**Final Report on CFD and Thermal-Mechanical Stress Analysis of
PWR Surge Line under Transient Condition Thermal Stratification
and an Evolutionary Cyclic Plasticity Based Transformative
Fatigue Evaluation Approach without Using S~N Curve: Rev.1**

**Subhasish Mohanty, Bipul Barua, Joseph Listwan, Saurin Majumdar, and
Ken Natesan**

Nuclear Engineering Division, Argonne National Laboratory

August 2018

This page intentionally left blank

ABSTRACT

This report presents an evolutionary cyclic plasticity based transformative approach for fatigue evaluation of safety critical components. This approach is generic which can be used not only for the present generation light water reactor components (which is our focus) but also for advanced reactor components. The approach is based on the fundamental concept of time-evolution of progressive fatigue damage rather than the end-of-life data based conventional S~N curve approaches. Series of fatigue tests on 316 stainless steel uniaxial specimens were conducted under strain-controlled and stress-controlled cyclic loading in two different environment such as in-air at 300 °C and PWR coolant water condition at 300 °C. Material models are developed to capture the uniaxial test data and are subsequently programmed into commercially available ABAQUS code to transform the uniaxial material behavior to multiaxial loading domain. The developed evolutionary cyclic-plasticity approach is verified by both analytical and 3D-FE modeling of uniaxial fatigue test specimens. Results show that the developed material models can capture the time-dependence of material hardening and softening with great accuracy. In addition, results show that the material models not only can capture the material behavior under constant amplitude loading but also can capture the load-sequence effect under variable and random amplitude loading. The ANL developed approach is one of its kind, which shows first in the fatigue research community that fatigue evaluation of a component (in our case verified for laboratory scale fatigue test specimens with great accuracy) can be performed for its entire fatigue life, including the hardening and softening behavior, without using a conventional S~N curve based approach.

Additionally results are presented related to fatigue evaluation of real reactor components such as of a pressurized water reactor (PWR) surge line (SL), under upset transient conditions. SLs of PWR experience complex thermal stratification due to the mixing of differential temperature flow from hot leg and pressurizer. A detailed parametric study of thermal stratification in SL is performed through both standalone computational fluid dynamics (CFD) analysis and fluid-structure-interaction based coupled CFD and heat transfer analysis. Results show that the mass flow rate in SL substantially affects the extent of its thermal stratification. The resulting thermal boundaries conditioned are used as inputs for thermal-mechanical stress analysis and component level fatigue evaluation. Fatigue evaluation of SL pipe under example loading conditions was performed using the above-mentioned evolutionary-plasticity based approach and ASME code (for in-air life) and NUREG-6909 (for PWR environment life) based approaches. Results show that the evolutionary plasticity based approach estimate substantially different life compared to the conventional ASME based approach.

To show the entirety of the proposed evolutionary fatigue-modeling framework, this report includes the results presented in semi-annual March report (ANL/LWRS-17/01). Sections 2-5 of March report are directly included as Sections 2-5 in this report, without any significant changes. However, Sections 6-9 of this report present the work performed during March-September of 2017. Whereas, Sections 1 and 10 present the organization of this report and the summary and future work, respectively.

This report (ANL/LWRS-17/03 Rev. 1) is a slightly revised version of the earlier published report (ANL/LWRS-17/03). In this revised version, some of the results and associated discussion have been corrected/updated.

This page intentionally left blank

TABLE OF CONTENTS

Final Report on CFD and Thermal-Mechanical Stress Analysis of PWR Surge Line under Transient Condition Thermal Stratification and an Evolutionary Cyclic Plasticity Based Transformative Fatigue Evaluation Approach without Using S~N Curve	i
ABSTRACT	i
Table of Contents	iii
List of Figures	vi
List of TABLES	xv
Abbreviations	xvi
Acknowledgments	xvii
1 Organization of This Report	1
2 Theoretical Background on Evolutionary Cyclic Plasticity: APSE-Based 1D-Analytical and 3D-FE Modeling	2
2.1 Constitutive Relations for Evolutionary Cyclic Plasticity Model.....	3
2.2 Time-Based Estimation of Time-Dependent Material Parameters	5
2.3 Modeling Fatigue Behavior using Evolutionary Cyclic Plasticity Model	7
2.3.1 Time-Based Modeling	7
2.3.2 APSE-Based Modeling	7
2.4 FE Implementation of Evolutionary Cyclic Plasticity Model.....	9
3 Results from Strain-controlled Tensile/Fatigue Test and Material Parameter Estimation Models of 316 SS	10
3.1 Tensile Test and Associated Time/Cycle Independent Elastic-Plastic Material Model Results	10
3.2 Constant-Amplitude Fatigue Test and Associated Cyclic Elastic-Plastic Material Model Results	11
3.3 Variable-Amplitude Fatigue Test and Associated Cyclic Elastic-Plastic Material Model Results	17
3.4 Random-Amplitude Fatigue Test Results	24
4 Results from Analytical Modeling of Constant, Variable, and Random Load Strain-controlled Fatigue Tests	28
4.1 Results from Time-Based Analytical Models.....	28
4.1.1 Constant-Amplitude Fatigue Test	28
4.1.2 Variable-Amplitude Fatigue Test	32
4.2 Results from Accumulated Plastic Strain Energy (APSE)-Based Analytical Models.....	35
4.2.1 Constant-Amplitude Fatigue Test	35

4.2.2	Variable-Amplitude Fatigue Test	37
4.2.3	Random-Amplitude Fatigue Test	37
4.3	Summary of Analytical Modeling Results.....	40
5	Results from FE Modeling of Strain-controlled Fatigue Tests	43
5.1	Results from Time-Based 3D-FE Models.....	45
5.1.1	Constant-Amplitude Fatigue Test	45
5.1.2	Variable-Amplitude Fatigue Test	49
5.2	Results from APSE-Based 3D-FE Models	52
5.2.1	Constant-Amplitude Fatigue Test	52
5.2.2	Variable-Amplitude Fatigue Test	54
5.2.3	Random-Amplitude Fatigue Test	55
5.3	Summary of FE Modeling Results and Comparison with Analytical Modeling Results.....	58
6	Stress-Controlled Tensile/Fatigue Tests of 316 SS	61
6.1	Tensile Test.....	62
6.2	Fatigue Test.....	63
6.2.1	Test Procedures	63
6.2.2	Experimental Observations	66
6.2.2.1	In-air Tests	66
6.2.2.2	PWR Tests	73
6.2.3	Prediction of Strain from Actuator Position Data of PWR Tests	76
6.2.4	Effect of Stress Rate on Material Behavior	81
6.2.5	Effect of PWR Environment on Material Behavior	84
7	Results from Analytical Modeling of Stress-Controlled Fatigue Tests of 316 SS	87
7.1	Analytical Modeling of In-air Test Cases	87
7.2	PWR Test.....	91
8	CFD and Thermal-Mechanical Stress Analysis under Transient Conditions	93
8.1	CFD and CFD-HT Theoretical Background.....	93
8.2	Finite Element Model Information	97
8.2.1	Finite element model	97
8.2.2	Thermal-mechanical boundary conditions	99
8.2.3	Material properties	102
8.3	Stand-alone CFD Results.....	108
8.3.1	Effect of different type of CFD solver	108
8.3.2	Effect of finite element type	110
8.3.3	Effect of finite element size	112
8.3.4	Effect of buoyancy and variable density	113

8.3.5 Effect of SL mass flow rate	115
8.3.6 Effect of HL mass flow rate	118
8.4 CFD-HT Fluid Structure Interaction Model Results	120
8.4.1 CFD-HT fluid structure interaction model results for out-surge case	120
8.4.2 CFD-HT fluid structure interaction model results for in-surge case	123
8.5 Stress Analysis Results	126
8.5.1 Structural analysis model results for out-surge case	126
8.5.2 Structural analysis model results for in-surge case	134
9 Fatigue Life Estimation of SL Pipe based on ANL Developed Fully Mechanistic Approach and ASME and NUREG-6909 Mandated S~N Curve based Approaches	137
9.1 Fatigue Life Estimation of SL Pipe under Imaginary Strain-Controlled Loading Conditions	137
9.1.1 Strain-controlled case elastic-plastic analysis and fully mechanics based life estimation	137
9.1.2 Strain-controlled case ASME code and NUREG based life estimation	147
9.2 Fatigue Life Estimation of SL Pipe under Actual Stress-Controlled or Thermal-Mechanical Loading Conditions	155
9.2.1 In-air and environmental fatigue lives estimation of SL pipe under out-surge flow condition discussed in Section 8.4.1.	156
9.2.2 In-air and environmental fatigue lives estimation of SL pipe under in-surge flow condition discussed in Section 8.4.2.	158
10 Summary and Future Study	161
10.1 Summary	161
10.2 Future Work	162
References	163
Appendices	167
Appendix-3A: Supplementary Results for ET-T04 Tensile Test	167
Appendix-3B: Supplementary Results for ET-F06 Fatigue Test.....	188
Appendix-3C: Supplementary Results for ET-F41 Fatigue Test.....	200
Appendix-3D: Supplementary Results for ET-F38 Fatigue Test	214
Appendix-3E: Supplementary Results for ET-F40 Fatigue Test.....	227

LIST OF FIGURES

Figure 2. 1 Interpretation of plastic strain energy for a fatigue cycle.....	8
Figure 3. 1 Engineering stress-strain curve estimated from ET-T04 tensile test (in air, 300 °C) data for 316 SS base metal. Data point shows the elastic limit stress and strain.	11
Figure 3. 2 Observed stress during the entire ET-F06 fatigue test. Data points show stress after 1 st quarter cycle and the maximum hardening stress and corresponding cycle.	12
Figure 3. 3 Observed stress during the entire ET-F41 fatigue test. Data points show stress after 1 st quarter cycle and the maximum hardening stress and corresponding cycle.	13
Figure 3. 4 Equivalent monotonic stress-strain curves over 50 cycles estimated from ET-F06 fatigue test data and comparison with ET-T04 tensile test data.	14
Figure 3. 5 Equivalent monotonic stress-strain curves over 50 cycles estimated from ET-F41 fatigue test data and comparison with ET-T04 tensile test data.	14
Figure 3. 6 Time/cycle-dependent elastic modulus estimated from constant-amplitude fatigue tests.	15
Figure 3. 7 Time/cycle-dependent elastic limit stress estimated from constant-amplitude fatigue tests.	15
Figure 3. 8 Time/cycle-dependent nonlinear kinematic hardening parameter, C1 estimated from constant-amplitude fatigue tests.....	16
Figure 3. 9 Time/cycle-dependent nonlinear kinematic hardening parameter, γ_1 estimated from constant-amplitude fatigue tests.....	16
Figure 3. 10 Block loading during variable-amplitude strain-controlled fatigue test (ET-F38). Data points show minimum and maximum amplitudes.	18
Figure 3. 11 Observed stress during the entire ET-F38 fatigue test.	19
Figure 3. 12 Observed stress-strain hysteresis behavior during the 1 st block (each block comprising 12 cycles) of ET-F38.	19
Figure 3. 13 Example comparison of experimental true back stress (as a function of true plastic strain) and predicted back stress (using kinematic hardening equation and estimated parameters: C1 and γ_1 pertaining to that block). Black solid line: prediction; Circles: experimental data from 12 fatigue cycles of that block.	20
Figure 3. 14 Time/block-dependent elastic modulus estimated from variable-amplitude fatigue test (ET-F38).	20
Figure 3. 15 Time/block-dependent elastic limit stress estimated from variable-amplitude fatigue test (ET-F38).	21
Figure 3. 16 Time/block-dependent nonlinear kinematic hardening parameter, C1 estimated from variable-amplitude fatigue test (ET-F38).....	21
Figure 3. 17 Time/block-dependent nonlinear kinematic hardening parameter, γ_1 estimated from variable-amplitude fatigue test (ET-F38).....	22
Figure 3. 18 APSE-dependent elastic modulus estimated from variable-amplitude fatigue test (ET-F38). The y-data corresponding to x=0 is ignored in the semi-logx plot.	22
Figure 3. 19 APSE -dependent elastic limit stress estimated from variable-amplitude fatigue test (ET-F38). The y-data corresponding to x=0 is ignored in the semi-logx plot.....	23
Figure 3. 20 APSE -dependent nonlinear kinematic hardening parameter, C1 estimated from variable-amplitude fatigue test (ET-F38). The y-data corresponding to x=0 is ignored in the semi-logx plot.	23

Figure 3. 21 APSE-dependent nonlinear kinematic hardening parameter, γ_1 estimated from variable-amplitude fatigue test (ET-F38). The y-data corresponding to $x=0$ is ignored in the semilogx plot.....	24
Figure 3. 22 Block loading during random-amplitude strain-controlled fatigue test (ET-F40). ..	25
Figure 3. 23 Observed stress during the entire ET-F40 fatigue test.	25
Figure 3. 24 Magnified plot of applied strain during ET-F40.	26
Figure 3. 25 Magnified plot of observed stress (corresponding to strain shown in Figure 3.24) during ET-F40.....	26
Figure 3. 26 Example hysteresis plot of stress (shown in Figure 3.25) and strain (shown in Figure 3.24) during ET-F40.	27
Figure 4. 1 Simulated (analytical) vs experimental axial stress history of ET-F41. Predictions are from simulation using time/cycle-dependent parameters (ET-F41) and two sets of time-independent parameters (tensile test ET-T04 and half-life cycle of ET-F41).	29
Figure 4. 2 Magnified version of Figure 4.1 showing the ability of evolutionary cyclic plasticity model (time/cycle-dependent prediction) to predict initial hardening behavior of 316 SS under constant-amplitude loading.	30
Figure 4. 3 Magnified version of Figure 4.1 showing the ability of evolutionary cyclic plasticity model (time/cycle-dependent prediction) to predict softening behavior of 316 SS under constant-amplitude loading.	30
Figure 4. 4 Magnified version of Figure 4.1 showing the ability of evolutionary cyclic plasticity model (time/cycle-dependent prediction) to predict the fast stress drop toward the end of the fatigue life of specimen, representing unstable or rapid crack propagation, under constant-amplitude loading.....	31
Figure 4. 5 Simulated (analytical) vs experimental axial stress history of ET-F06. Predictions are from simulation using time/cycle-dependent parameters from ET-F06 test and two sets of time-independent parameters (tensile test ET-T04 and half-life cycle of ET-F06).....	31
Figure 4. 6 Simulated (analytical) vs experimental axial stress history of ET-F38. Predictions are from simulation using time/block-dependent parameters (ET-F38) and two sets of time-independent parameters (tensile test ET-T04 and half-life block of ET-F38).	32
Figure 4. 7 Magnified version of Figure 4.6 showing the ability of evolutionary cyclic plasticity model (time/block-dependent prediction) to predict initial hardening behavior of 316 SS under variable-amplitude loading.	33
Figure 4. 8 Magnified version of Figure 4.6 showing the ability of evolutionary cyclic plasticity model (time/ block -dependent prediction) to predict softening behavior of 316 SS under variable-amplitude loading.	33
Figure 4. 9 Magnified version of Figure 4.6 showing the ability of evolutionary cyclic plasticity model (time/ block -dependent prediction) to predict the fast stress drop toward the end of the fatigue life of specimen, representing unstable or rapid crack propagation, under variable-amplitude loading.....	34
Figure 4. 10 Simulated (analytical) vs experimental hysteresis curves of 1 st block (with 12 variable-amplitude cycles) of ET-F38. Predictions are from simulation using time/block-dependent parameters and two sets of time-independent parameters (tensile test ET-T04 and half-life block of ET-F38).	34

Figure 4. 11 Simulated (analytical) vs experimental axial stress history of ET-F41. Prediction is from simulation using APSE-dependent material parameters estimated from variable-amplitude test (ET-F38).	36
Figure 4. 12 Simulated (analytical) vs. experimental axial stress history of ET-F06. Prediction is from simulation using APSE-dependent material parameters estimated from variable-amplitude test (ET-F38).	36
Figure 4.13 Simulated (analytical) vs. experimental axial stress history of ET-F38. Prediction is from simulation using APSE-dependent material parameters estimated from variable-amplitude test (ET-F38).	37
Figure 4.14 Simulated (analytical) vs. experimental axial stress history of ET-F40. Predictions are from simulation using APSE-dependent material parameters estimated from variable-amplitude test (ET-F38) and fixed parameters estimated from tensile test (ET-T04).	38
Figure 4.15 Magnified version of Figure 4.14. Experimental and predicted stress corresponds to applied strain shown in Figure 3.24.	39
Figure 4.16 Simulated (analytical) vs. experimental hysteresis plot of stress shown in Figure 4.15 and strain shown in Figure 3.24.	39
Figure 5. 1 Geometry of fatigue test specimen.	44
Figure 5.2 Three-dimensional 8-node brick element used for FE simulation of fatigue experiment in ABAQUS.	44
Figure 5.3 An example simulated stress profile at a given instant during fatigue test simulation.	45
Figure 5.4 3D-FE simulated (evolutionary cycle plasticity model) vs. experimental axial stress of ET-F41 specimen for first 100 cycles. Predictions are from simulation using time/cycle-dependent parameters (ET-F41) and two sets of time-independent parameters (tensile test ET-T04 and half-life cycle of ET-F41).	46
Figure 5.5 Magnified version of Figure 5.4.	47
Figure 5.6 3D-FE simulated (evolutionary cycle plasticity model) vs. experimental axial stress of ET-F41 specimen for whole fatigue life.	47
Figure 5.7 Magnified version of Figure 5.6 showing that the 3D-FE results can predict material behavior during initial stress hardening, softening, and stabilized cycles under constant-amplitude loading.	48
Figure 5.8 Magnified version of Figure 5.6 showing that the 3D-FE results can predict material behavior during rapid crack propagation and failure under constant-amplitude loading.	48
Figure 5.9 3D-FE simulated (evolutionary cycle plasticity model) vs. experimental axial stress of ET-F06 specimen for whole fatigue life.	49
Figure 5.10 3D-FE simulated (evolutionary cycle plasticity model) vs. experimental axial stress of ET-F38 specimen for first 50 blocks. Predictions are from simulation using time/block-dependent parameters (ET-F38) and two sets of time-independent parameters (tensile test ET-T04 and half-life block of ET-F38).	50
Figure 5.11 3D-FE simulated (evolutionary cycle plasticity model) vs. experimental axial stress history of ET-F38 specimen for whole fatigue life.	51
Figure 5.12 Magnified version of Figure 5.11 showing that the 3D-FE results can predict material behavior during initial stress hardening, softening, and stabilized cycles under variable-amplitude loading.	51

Figure 5.13 Magnified version of Figure 5.11 showing that the 3D-FE results can predict material behavior during rapid crack propagation and failure under variable-amplitude loading.....	52
Figure 5.14 3D-FE simulated (evolutionary cycle plasticity model) vs. experimental axial stress history of ET-F41 specimen for whole fatigue life. Prediction is from simulation using APSE-dependent material parameters estimated from variable-amplitude test (ET-F38).	53
Figure 5.15 3D-FE simulated (evolutionary cycle plasticity model) vs. experimental axial stress history of ET-F06 specimen for whole fatigue life. Prediction is from simulation using APSE-dependent material parameters estimated from variable-amplitude test (ET-F38).	54
Figure 5.16 3D-FE simulated (evolutionary cycle plasticity model) vs. experimental axial stress history of ET-F38 specimen for whole fatigue life. Prediction is from simulation using APSE-dependent material parameters estimated from variable-amplitude test (ET-F38).	55
Figure 5.17 3D-FE simulated (evolutionary cycle plasticity model) vs. experimental axial stress of ET-F40 specimen during 1 st block (block period = 4251 s) loading. Predictions are from simulation using APSE-dependent material parameters estimated from variable-amplitude test (ET-F38) and fixed parameters estimated from tensile test (ET-T04).	56
Figure 5.18 Magnified version of Figure 5.17. Experimental and predicted stress correspond to applied strain shown in Figure 3.24.	57
Figure 5.19 3D-FE simulated (evolutionary cycle plasticity model) vs. experimental hysteresis plot of stress shown in Figure 5.18 and strain shown in Figure 3.24.	57
Figure 5.20 3D-FE simulated (evolutionary cycle plasticity model) vs. experimental axial stress history of ET-F40 specimen for whole fatigue life. Prediction is from simulation using APSE-dependent material parameters estimated from variable-amplitude test (ET-F38).	58
Figure 6. 1 Engineering stress-strain curve estimated from ET-T04 [37] and ET-T11 data.	63
Figure 6. 2 Stress input during ET-F43 and EN-F44.	64
Figure 6. 3 Repeating constant-amplitude stress input at high rate (after low-rate variable-amplitude stress input in first block) during ET-F43 and EN-F44.	64
Figure 6. 4 Observed stress during the ET-F41. Data point shows stress amplitude during stabilized cycle.	65
Figure 6. 5 Stress input during ET-F45 and EN-F46.	66
Figure 6. 6 Observed strain during ET-F43.	67
Figure 6. 7 Mean true stress during variable-amplitude loading of ET-F43.	68
Figure 6. 8 Mean true stress during constant-amplitude loading of ET-F43.	68
Figure 6. 9 Observed actuator position during ET-F43.	69
Figure 6. 10 Observed strain during ET-F45 fatigue test.	70
Figure 6. 11 Observed actuator position during ET-F45 fatigue test.	70
Figure 6. 12 Comparison of ratcheting strain during variable-amplitude block loading of ET-F43 (top) and ET-F45 (bottom).	72
Figure 6. 13 Comparison of ratcheting strain during variable-amplitude loading of ET-F43 and ET-F45.	73
Figure 6. 14 Observed actuator position during PWR water test EN-F44.	74
Figure 6. 15 Observed actuator position during PWR water test EN-F46.	75
Figure 6. 16 Comparison of observed actuator position during variable-amplitude block loading of ET-F43 and ET-F45.	76

Figure 6. 17 A comparison between actual strain and regenerated strain from stroke measurements of a stroke-controlled in-air test [42].	77
Figure 6. 18 Ratcheting strain as function of actuator position measurements at the end of each cycle from ET-F43 and ET-F45.	78
Figure 6. 19 Actual strain measured by strain gauge vs. predicted strain regenerated from position data of ET-F43 during variable-amplitude loading.	79
Figure 6. 20 Actual strain measured by strain gauge vs. predicted strain regenerated from position data of ET-F43 during constant-amplitude loading.	79
Figure 6. 21 Predicted engineering strain from actuator position data during EN-F44.	80
Figure 6. 22 Predicted engineering strain from actuator position data during EN-F46.	81
Figure 6. 23 Engineering strain vs. fatigue cycles during constant-amplitude loading of ET-F43 and ET-F45.	82
Figure 6. 24 Normalized engineering strain vs. fatigue cycles during constant-amplitude loading of ET-F43 and ET-F45.	82
Figure 6. 25 Normalized engineering strain vs. fatigue cycles during constant-amplitude loading of EN-F44 and EN-F46.	83
Figure 6. 26 Normalized ratcheting strain vs. fatigue cycles during constant-amplitude loading of ET-F43 and ET-F45.	83
Figure 6. 27 Normalized ratcheting strain vs. fatigue cycles during constant-amplitude loading of EN-F44 and EN-F46.	84
Figure 6. 28 Comparison of ratcheting strain during variable-amplitude loading of in-air tests (ET-F43 and ET-F45) and PWR tests (EN-F44 and EN-F46).	85
Figure 6. 29 Comparison of normalized ratcheting strain during constant-amplitude loading of ET-F43 and EN-F44.	86
Figure 6. 30 Comparison of normalized ratcheting strain during constant-amplitude loading of ET-F45 and EN-F46.	86
Figure 7. 1 Experimental vs. predicted true strain during initial variable-amplitude loading of ET-F43. Prediction is based on tensile-test-based constant parameters and the Chaboche model.	88
Figure 7. 2 Experimental vs. predicted true strain during initial variable-amplitude loading of ET-F43. Prediction is based on cycle-dependent parameters and the evolutionary cyclic plasticity model.	88
Figure 7. 3 Experimental vs. predicted true strain during constant-amplitude loading of ET-F43. Prediction is based on cycle-dependent parameters and ANL-developed evolutionary cyclic plasticity model.	89
Figure 7. 4 Experimental vs. predicted true strain during initial variable-amplitude loading of ET-F45. Prediction is based on cycle-dependent parameters and the evolutionary cyclic plasticity model.	90
Figure 7. 5 Experimental vs. predicted true strain during constant-amplitude loading of ET-F45. Prediction is based on cycle-dependent parameters and the evolutionary cyclic plasticity model.	90
Figure 7. 6 Experimental vs. predicted true strain during initial variable-amplitude loading of EN-F44. Prediction is based on cycle-dependent parameters and the evolutionary cyclic plasticity model.	91

Figure 7. 7 Experimental vs. predicted true strain during constant-amplitude loading (first 50 cycles) of ET-F46. Prediction is based on cycle-dependent parameters and the evolutionary cyclic plasticity model.	92
Figure 8. 1 ABAQUS model of surge line that connects the hot leg and pressurizer.	98
Figure 8. 2 Example hexahedral mesh of (a) SL inside fluid with highlighted observation nodes for which the related results are presented (b) SL outside pipe.	99
Figure 8. 3 Pressurizer and HL temperature during plant heat-up, cool-down, and normal operation. Mode-5 to Mode-4 transition regime (which is considered in the discussed results) is also highlighted.	101
Figure 8. 4 Example pressure history of the primary loop during plant heat-up, cool-down, and normal operation. Mode-5 to Mode-4 transition regime (which is considered in the discussed results) is also highlighted.	101
Figure 8. 5 Temperature-dependent density (ρ) of water.	103
Figure 8. 6 Temperature-dependent volume expansion coefficient (β) of water. Estimated using Boussinesq approximation (Eq. 8.14) and temperature-dependent density.....	103
Figure 8. 7 Temperature-dependent dynamic viscosity (μ) of water.	104
Figure 8. 8 Temperature-dependent heat capacity (C_p) of water.	104
Figure 8. 9 Temperature-dependent thermal conductivity (k) of water.	105
Figure 8. 10 Temperature-dependent Prandtl number.	105
Figure 8. 11 Temperature-dependent water saturation pressure.	106
Figure 8. 12 Temperature-dependent thermal conductivity (κ_s) of 316 SS.	106
Figure 8. 13 Temperature-dependent specific heat capacity (C_{ps}) of 316 SS	107
Figure 8. 14 Temperature-dependent coefficient of thermal expansion (α_s) of 316 SS	107
Figure 8. 15 CFD simulation results of SL for out-surge case. Sub figure pairs (a1 and a2), (b1 and b2), and (c1 and c2) show temperature contours (left inset figures show temperature iso-surfaces near HL end of SL) at end of 500 s and temperature-time history at different nodes (along the length of SL as shown in Figure 8.2a) for $k - \epsilon$, Spalart-Allmaras, and ILES models.	109
Figure 8. 16 Comparison of temperature history at PRZ-end node, mid node, and HL-end node of SL, which are simulated by using $k - \epsilon$, Spalart-Allmaras, and ILES stand-alone CFD models.	110
Figure 8. 17 CFD simulation results of SL with tetrahedral mesh: (a1) temperature contour (left inset figures show temperature iso-surfaces near HL end of SL) at end of 500 s, (a2) temperature-time history at different nodes (along the length of SL as shown in Figure 8.2a)	111
Figure 8. 18 Comparison of temperature history at PRZ-end node, mid node, and HL-end node of SL, which are simulated using hexahedral and tetrahedral meshes.	111
Figure 8. 19 CFD simulation results of SL with finer hexahedral mesh: (a1) temperature contour (left inset figures show temperature iso-surfaces near HL end of SL) at end of 500 s and (a2) temperature-time history at different nodes (along the length of SL as shown in Figure 8.2a).	112
Figure 8. 20 Comparison of temperature history at PRZ-end node,, mid node, and HL-end node of SL, which are simulated by using coarser and finer hexahedral meshes.	113

Figure 8. 21 CFD simulation results of SL for out-surge case. Figure pairs (a1 and a2), (b1 and b2), and (c1 and c2) show temperature contours (left inset figures show temperature iso-surfaces near HL end of SL) at end of 500 s and temperature-time-history at different nodes (along the length of SL, as shown in Figure 8.2a) for $\beta = \text{constant}$ and $\beta = 0$ models..	114
Figure 8. 22 Comparison of temperature history at PRZ-end node, mid node, and HL-end node of SL, which are simulated by using model with $\beta = f(\theta)$, $\beta = \text{constant}$, and $\beta = 0$	115
Figure 8. 23 SL temperature at end of 500 s for out-surge case with SL mass flow rate (a1) 10 gpm, (a2) 50 gpm, (a3) 100 gpm, and (a4) 200 gpm.	116
Figure 8. 24 SL temperature history for out-surge case with SL mass flow rate (a1) 10 gpm, (a2) 50 gpm, (a3) 100 gpm, and (a4) 200 gpm.....	117
Figure 8. 25 Comparison of temperature history at a mid-node (refer to Figure 8.2a) of SL, which is simulated with 10 gpm, 50 gpm, 100 gpm, and 200 gpm of SL mass flow rate.....	117
Figure 8. 26 SL temperature at end of 500 s for out-surge case with HL mass flow rate (a1) 0 gpm, (a2) 3451 gpm, (a3) 34,510 gpm, and (a4) 69,020 gpm.	118
Figure 8. 27 SL temperature history for out-surge case with HL mass flow rate (a1) 0 gpm, (a2) 3451 gpm, (a3) 34,510 gpm, and (a4) 69,020 gpm.....	119
Figure 8. 28 Comparison of temperature history at a mid-node (refer to Figure 8.2a) of SL, which are simulated with 0 gpm, 3451 gpm, 34,510 gpm, and 69,020 gpm of HL mass flow rate.	119
Figure 8. 29 Comparison of temperature contour (at different times) of OD surface of SL fluid for stand-alone CFD and CFD-HT models (both under out-surge condition).	121
Figure 8. 30 Temperature history at selected nodes (refer to Figure 8.2a) under out-surge case for SL determined with (a1) standalone CFD model and (a2) CFD-HT model.....	122
Figure 8. 31 Comparison of temperature history at PRZ-end node, mid node, and HL-end node of SL, simulated using stand-alone CFD and CFD-HT models (both under out-surge condition).	122
Figure 8. 32 OD surface temperature contour (at different times) of SL metallic pipe under out-surge condition determined with CFD-HT model.	123
Figure 8. 33 OD surface temperature contours (at different times) of SL fluid under in-surge condition determined with the CFD-HT model.	124
Figure 8. 34 OD surface temperature contours (at different times) of SL metallic pipe under in-surge condition determined with the CFD-HT model.	125
Figure 8. 35 SL temperature history at selected nodes (refer to Figure 8.2a) under in-surge case determined with the CFD-HT model.	126
Figure 8. 36 Stress analysis (with elastic limit as yield limit) results for SL pipe under out-surge conditions: contour plots at end of 2000 s for (a1) von Mises stress, (a2) maximum principal total strain, (a3) maximum principal thermal strain, and (a4) maximum principal plastic strain.	128
Figure 8. 37 Stress analysis (with elastic limit as yield limit) results for SL pipe under out-surge conditions: PRZ-end versus HL-end node time-dependent results for (a1) von Mises stress, (a2) maximum principal total strain, (a3) maximum principal thermal strain, and (a4) plastic strain magnitude.....	129
Figure 8. 38 Time variation of out-surge condition for maximum von Mises stress obtained using elastic (EL) and different elastic-plastic (EL-PL) yield conditions.	130
Figure 8. 39 Time variation of out-surge condition for maximum principal total strain obtained using elastic (EL) and different elastic-plastic (EL-PL) yield conditions.	130

Figure 8. 40 Time variation of out-surge condition for maximum principal thermal strain obtained using elastic (EL) and different elastic-plastic (EL-PL) yield conditions.	131
Figure 8. 41 Time variation of out-surge condition for plastic strain magnitude obtained using elastic (EL) and different elastic-plastic (EL-PL) yield conditions.	131
Figure 8. 42 Relative displacement of SL pipe at different times for out-surge case (magnification factor =10).....	132
Figure 8. 43 Out-surge condition maximum principal strain versus von Mises stress at two typical integration points (of elements near PRZ and HL end of SL pipe) and their comparison with respect to 22 °C and 300 °C tensile test curves. Associated elastic-plastic properties were used for discussed structural analysis models.....	133
Figure 8. 44 Nodal temperature at the two elements near PRZ and HL end of SL pipe, where strain versus stress results are presented in Figure 8.43.	133
Figure 8. 45 Stress analysis (with elastic limit as yield limit) results for SL pipe under in-surge conditions: contour plots at end of 2000 s for (a1) von Mises stress, (a2) maximum principal total strain, (a3) maximum principal thermal strain, and (a4) maximum principal plastic strain.	134
Figure 8. 46 Stress analysis (with elastic limit as yield limit) results for SL pipe under in-surge conditions: PRZ-end versus HL-end node time-dependent results for (a1) von Mises stress, (a2) maximum principal total strain, (a3) maximum principal thermal strain, and a4) maximum principal plastic strain.....	135
Figure 8. 47 Relative displacement of SL pipe at different time for in-surge condition (magnification factor =10).	136
Figure 9. 1 Flowchart showing the steps in the ANL mechanics-based modeling.....	139
Figure 9. 2 (a) FE mesh of the PWR surge line. Blue arrows at two ends show the fixed boundary condition and yellow arrows indicate the location and direction of applied cyclic displacement. (c) Profile of the applied cyclic displacement.	140
Figure 9. 3 Contour plot of the von Misses stress at an instant during the strain control fatigue loading shown in Figure 9.1. The highlighted element in the magnified inset is the element of interest.....	141
Figure 9. 4 Simulated (elastic-plastic analysis) ϵ_z as function of fatigue cycles.	142
Figure 9. 5 Simulated (elastic-plastic analysis) vs experimental maximum principal stress as function of fatigue cycles. Experimental results are shown for first 100 cycles. Simulation was performed for only 100 cycles.	142
Figure 9. 6 Simulated (elastic-plastic analysis) vs experimental mid principal stress as function of fatigue cycles. Experimental results are shown for first 100 cycles. Simulation was performed for only 100 cycles.....	143
Figure 9. 7 Simulated (elastic-plastic analysis) vs experimental minimum principal stress as function of fatigue cycles. Experimental results are shown for first 100 cycles. Simulation was performed for only 100 cycles.	143
Figure 9. 8 Simulated (elastic-plastic analysis) vs experimental von Mises stress amplitudes as function of fatigue cycles.....	144
Figure 9. 9 Simulated (elastic-plastic analysis) vs experimental von Mises stress amplitudes (with negative sign during compression cycle) as function of fatigue cycles.....	145

Figure 9. 10 Simulated (elastic-plastic analysis) Tresca stress amplitudes as function of fatigue cycles.....	145
Figure 9. 11 Simulated (elastic-plastic analysis) vs experimental APSE as function of fatigue cycles.....	146
Figure 9. 12 Contour plot (from elastic analysis) of the maximum principal stress at an instant during the strain control fatigue loading shown in Figure 9.1. The highlighted element shown in the magnified inset is the element of interest.	148
Figure 9. 13 Simulated (elastic analysis) maximum (σ_1), mid (σ_2), and minimum (σ_3) principal stresses.	149
Figure 9. 14 Stress amplitude history according to Eq. 9.1.	151
Figure 9. 15 ASME code fatigue design curve for austenitic steel [1].	151
Figure 9. 16 Strain amplitude history estimated using Eq. 9.11.	153
Figure 9. 17 Simulated (elastic analysis) maximum (σ_1), mid (σ_2), and minimum (σ_3) principal stresses at pressurizer-end of SL pipe under out-surge flow condition discussed in section 8.4.1.....	156
Figure 9. 18 Stress amplitude history according to Eq. 9.1 and at pressurizer-end of SL pipe under out-surge flow condition discussed in section 8.4.1.	157
Figure 9. 19 Strain amplitude history according to Eq. 9.9 and at pressurizer-end of SL pipe under out-surge flow condition discussed in section 8.4.1.	157
Figure 9. 20 Simulated (elastic analysis) maximum (σ_1), mid (σ_2), and minimum (σ_3) principal stresses at pressurizer-end of SL pipe under in-surge flow condition discussed in section 8.4.2.	158
Figure 9. 21 Stress amplitude history according to Eq. 9.1 and at pressurizer-end of SL pipe under in-surge flow condition discussed in section 8.4.2.	159
Figure 9. 22 Strain amplitude history according to Eq. 9.9 and at pressurizer-end of SL pipe under in-surge flow condition discussed in section 8.4.2.	159

LIST OF TABLES

Table 3. 1 Test conditions for 316 SS base metal tensile and fatigue tests.	10
Table 3. 2 Time-independent material parameters estimated from tensile test ET-T04.....	11
Table 4. 1 Experimentally observed and predicted (analytical modeling) maximum hardening stress.....	40
Table 4. 2 Determination of failure criteria for simulation results.	41
Table 4. 3 Experimental and predicted (analytical modeling) fatigue lives.	42
Table 5. 1 Experimentally observed and predicted (3D-FE modeling) maximum hardening stress.	59
Table 5. 2 Comparison between experimental and predicted (3D-FE modeling) fatigue lives....	60
Table 5. 3 Comparison of APSE-based predicted fatigue lives between analytical modeling and 3D-FE modeling results.	60
Table 6. 1 Test conditions for 316 SS base metal tensile and fatigue tests.	62
Table 8. 1 Elastic-plastic material properties for 316SS estimated from ANL tensile test data.	102
Table 9. 1 Estimated in-air and PWR environment fatigue lives at 300 °C (using $Ke=1.32$ in Eq. 9.3)	154
Table 9. 2 Estimated in-air and PWR environment fatigue lives at 300 °C (using $Ke=1$ in Eq. 9.3)	155
Table 9. 3 Fatigue lives of SL pipe, estimated under out-surge flow condition discussed in section 8.4.1.....	158
Table 9. 4 Fatigue lives of SL pipe, estimated under in-surge flow condition discussed in Section 8.4.2.....	160

ABBREVIATIONS

1D	One Dimensional
3D	Three Dimensional
ANL	Argonne National Laboratory
ASME	American Society of Mechanical Engineers
APSE	Accumulated Plastic Strain Energy
CFD	Computational Fluid Dynamics
CL	Cold Leg
FE	Finite Element
HL	Hot Leg
LAS	Low Alloy Steel
LWRS	Light Water Reactor Sustainability
PWR	Pressurized Water Reactor
SL	Surge Line
SS	Stainless Steel

ACKNOWLEDGMENTS

This research was supported through the U.S. Department of Energy's Light Water Reactor Sustainability program under the work package of environmental fatigue study, program manager Dr. Keith Leonard.

This page intentionally left blank

1 Organization of This Report

This report is organized in to following sections:

Section 1: Organization of this report

Section 2: Theoretical Background on Evolutionary Cyclic Plasticity: APSE-Based 1D-Analytical and 3D-FE Modeling

Section 3: Results from Strain-controlled Tensile/Fatigue Test and Material Parameter Estimation Models of 316 SS

Section 4: Results from Analytical Modeling of Constant, Variable, and Random Load Strain-controlled Fatigue Tests

Section 5: Results from FE Modeling of Strain-controlled Fatigue Tests

Section 6: Stress-Controlled Tensile/Fatigue Tests of 316 SS

Section 7: Results from Analytical Modeling of Stress-Controlled Fatigue Tests of 316 SS

Section 8: CFD and Thermal-Mechanical Stress Analysis under Transient Conditions

Section 9: Fatigue Life Estimation of SL Pipe based on ANL Developed Fully Mechanistic Approach and ASME and NUREG-6909 Mandated S~N Curve based Approaches

Section 10: Summary and Future Study

2 Theoretical Background on Evolutionary Cyclic Plasticity: APSE-Based 1D-Analytical and 3D-FE Modeling

The current procedures for fatigue life assessment of nuclear reactor components exposed to thermal-mechanical loading cycles and reactor environment are usually based on stress/strain versus life (S-N) curves and/or similar empirical approaches [1-7]. Although these empirical approaches allow engineers to quickly assess the component's design lives, they are not directly based on time-dependent damage evolution and damage accumulation, which can lead to the fatigue failure of metallic components. Furthermore, there remains considerable debate on how to incorporate the effect of the reactor environment while evaluating the fatigue life of reactor components by empirical approaches [8]. Also, as many different codes and standards use different approaches (e.g., based on stress [3-5] or strain range methods [6, 7]), it is sometimes difficult to decide which method to use. Recently, organizations like the World Nuclear Association's working group Cooperation in Reactor Design Evaluation and Licensing (CORDEL) and the Standards Development Organizations (SDOs) Code Convergence Board have been set up to homogenize the international codes and standards for nuclear power components [9].

By adopting more mechanistic-based approaches for fatigue evaluation, the issues associated with fatigue life evaluation can be greatly reduced. Moreover, with the current availability of advanced computation tools, such as the finite element (FE) method, along with high performance computing, it may be possible to model a component or an overall system more mechanistically than the traditional approach of over dependence on test-based methods. The resulting mechanistic approach will provide engineers with more accurate prediction of fatigue lives of the reactor components as compared with current approaches, which have large uncertainties due to the use of empirical relations.

Nuclear power plant components are subjected to complex stress/strain cycle loading during day-to-day operations. In some situations, cyclic loading may induce large-amplitude stress reversals, which may exceed the elastic limit due to presence of welds, notches, etc. Under these conditions, the behavior of materials such as 316 stainless steel (SS) [which is primarily used in U.S. reactor primary pipes, such as Pressurized Water Reactor (PWR) surge line (SL), hot leg, and cold leg] may become inelastic and may exhibit related phenomena such as the Bauschinger effect, cyclic hardening/softening, and mean stress relaxation or ratcheting [10]. Thus, the development of advanced models that can address the above-mentioned phenomena and the successful incorporation of those models into a generalized finite element code such as ABAQUS or ANSYS are necessary to ensure more accurate evaluation of the mechanistic-based structural integrity of reactor and other safety-critical components.

Several material models [11-18] have been developed in last few decades to better describe the cyclic plasticity behavior of materials under different loading conditions. Among them, the Chaboche-type [13-15] models are found widely used in engineering calculations and included in several commercial FE software, such as ABAQUS and ANSYS. The basis of Chaboche type models is the Armstrong-Frederick non-linear kinematic hardening model [12]. Although various successful simulations were carried out numerically for both rate-independent and rate-dependent plasticity, it was found that the Armstrong-Frederick model over-predicts the cyclic stress relaxation and ratcheting behavior by up to a factor of

about ten [17]. Chaboche and Rousselier [15] improved the prediction of ratcheting by superposition of multiple Armstrong- Frederick formulas. Although the Chaboche-type model in its original form can accurately describe plasticity under monotonic loading as well as the saturated (or stabilized) cyclic hardening behavior of reactor materials, it may not be accurate for modeling the non-saturation feature of cyclic hardening and/or softening [18]. Even though much improvement of the Chaboche model has been made by other researchers [18-20], none of the existing models in the literature is versatile and robust enough to simulate the cyclic plasticity behavior accurately [21]. Improved understanding of the cyclic plasticity of metal, therefore, is required before a robust plasticity model can be developed for practical applications, such as evaluating the stress-strain state and fatigue life of a reactor component.

In previous work [22-26], we proposed an evolutionary cyclic plasticity model for mechanistic fatigue modeling of key reactor materials. In the present work, we further improved the evolutionary cyclic plasticity model by focusing on model development for 316 SS, which is used in U.S. PWRs as primary pipe.

An evolutionary cyclic plasticity model was developed based on Chaboche [13] or Armstrong-Frederick [12] type analytical expressions for nonlinear kinematic hardening. The details of the material model development are discussed in our previous work [22, 24]. However, for the completeness of this report the evolutionary cyclic plasticity model and related constitutive relations are presented here briefly. Note that the constitutive relations are in more generalized form. Previously [22, 24], we presented a cycle-by-cycle technique to estimate time/cycle-dependent parameters from experimental data from a constant-amplitude uniaxial fatigue test. In later work [26], we presented a more generalized estimation scheme (refer to “method-2” in the reference), which can be used for estimating time/cycle-dependent or time/block-dependent material parameters from constant- or variable-amplitude test data, respectively. We briefly present the generalized estimation technique here. In addition, since material behavior under random-amplitude fatigue loading cannot be modeled by using earlier developed time-dependent material parameters, we discuss the possibility of using an APSE-dependent material model. To accommodate the APSE-based approach in a more generalized framework (than the earlier presented [22, 24, 26] time/cycle based model), the constitutive relations are symbolically expressed with respect to a generalized field variable v , which can be a function of time or fatigue cycle/block or any other physical state (e.g., APSE). The details of the constitutive relations and other analytical expressions are given in the following subsections. Furthermore, at the end of this section, the implementation of our evolutionary cyclic plasticity model into a commercial FE software, ABAQUS, is also discussed.

2.1 Constitutive Relations for Evolutionary Cyclic Plasticity Model

We consider a rate-independent elastic-plastic material. We assume the strain is small and can be additively decomposed into an elastic part obeying Hooke’s law and a plastic part governed by the associated flow rule based on Von-Mises yield criteria ($f=0$). At any instant, the yield function f_v , corresponding to the evolutionary cyclic plasticity model, can be expressed as,

$$f_v(\boldsymbol{\sigma}, \boldsymbol{\alpha}) = \sqrt{\frac{3}{2}(\boldsymbol{S} - \boldsymbol{\alpha}) : (\boldsymbol{S} - \boldsymbol{\alpha})} - \sigma_v^y = 0 \quad (2.1)$$

where $\boldsymbol{\sigma}$ is the stress vector at that instant, $\boldsymbol{\alpha}$ is the corresponding back stress vector, and σ_v^y is the yield stress. Note that the subscript v is used to demonstrate that the yield stress is not constant as it is in the case of conventional cyclic plasticity model, rather it is a variable that can be a function of time or fatigue cycle/block or any other physical state (e.g., APSE). In addition, \boldsymbol{S} represents the deviatoric stress portion of $\boldsymbol{\sigma}$. The associated flow rule can be expressed as:

$$d\boldsymbol{\varepsilon}^{pl} = dP \frac{\partial f_v}{\partial \boldsymbol{\sigma}} \quad (2.2)$$

where dP is the effective plastic strain increment. According to the additive rule the total strain can be expressed as:

$$\boldsymbol{\varepsilon} = \boldsymbol{\varepsilon}^{el} + \boldsymbol{\varepsilon}^{pl} \quad (2.3)$$

with Hooke's law for elastic strain,

$$\boldsymbol{\sigma} = \boldsymbol{C}_v \boldsymbol{\varepsilon}^{el} = \boldsymbol{C}_v(\boldsymbol{\varepsilon} - \boldsymbol{\varepsilon}^{pl}) \quad (2.4)$$

where $\boldsymbol{\varepsilon}^{el}$ and $\boldsymbol{\varepsilon}^{pl}$ are the elastic and plastic portion of the strain ($\boldsymbol{\varepsilon}$) at that instant and \boldsymbol{C}_v is the variable elastic stiffness matrix.

The evolutionary cyclic plasticity model based on Chaboche-type nonlinear kinematic hardening can be expressed as,

$$d\boldsymbol{\alpha} = \frac{2}{3} C1_v d\boldsymbol{\varepsilon}^{pl} - \gamma 1_v \boldsymbol{\alpha} dP \quad (2.5)$$

where $C1_v$ and $\gamma 1_v$ are material parameters. The parameter $C1_v$ is a proportional constant that gives a linear relation between the increment in the back stress, $d\boldsymbol{\alpha}$, and the increment in the plastic strain, $d\boldsymbol{\varepsilon}^{pl}$, while $\gamma 1_v$ describes the rate at which the back stress decreases with the increase in accumulated effective plastic strain, dP .

For incremental plasticity, the plastic strain increment, $d\boldsymbol{\varepsilon}^{pl}$, associated with the nonlinear kinematic hardening rule, given in Eq. (2.5), can be expressed as

$$d\boldsymbol{\varepsilon}^{pl} = \left(\frac{\frac{\partial f_v}{\partial \boldsymbol{\sigma}} \cdot \boldsymbol{C}_v d\boldsymbol{\varepsilon}}{\left(\frac{\partial f_v}{\partial \boldsymbol{\sigma}} \right) \cdot \boldsymbol{C}_v \left(\frac{\partial f_v}{\partial \boldsymbol{\sigma}} \right) + \gamma 1_v \left(\frac{\partial f_v}{\partial \boldsymbol{\sigma}} \right) \cdot \boldsymbol{\alpha} - \frac{2}{3} C1_v \left(\frac{\partial f_v}{\partial \boldsymbol{\sigma}} \right) \cdot \left(\frac{\partial f_v}{\partial \boldsymbol{\alpha}} \right)} \right) \frac{\partial f_v}{\partial \boldsymbol{\sigma}} \quad (2.6)$$

The above expression for the incremental plastic strain can be used for developing a cyclic-plasticity finite element or analytical model. The associated parameters include the variable elastic modulus (E_v , used for estimating the stiffness matrix \boldsymbol{C}_v), kinematic hardening parameters ($C1_v$ and $\gamma 1_v$), and yield stress (σ_v^y , used for estimating the yield function f_v).

2.2 Time-Based Estimation of Time-Dependent Material Parameters

Time-dependent material parameters are estimated from either a constant- or a variable-amplitude fatigue test. Stress-strain data from all the cycles within a block are used together to estimate time/block-dependent (i.e., block-by-block) material parameters from variable-amplitude tests. In addition, stress-strain data from each cycle are used to estimate time/cycle-dependent material parameters from constant-amplitude test. Here we briefly present our block-by-block parameter estimation technique, which can also be used to estimate cycle-by-cycle parameter estimation. To estimate block-dependent material parameters, all the cyclic stress-strain curves in a block are first converted into equivalent monotonic stress-strain curves. Based on an assumed elastic limit strain, the material parameters are then determined for all the blocks by using the Gauss-Newton optimization scheme. The steps for estimating the material parameters for block i are as follows:

Step 1: Estimate the kinematic hardening stress or back stress ($\alpha_{i,j,k}$) and corresponding accumulated intra-cycle plastic strain ($\bar{p}_{i,j,k}$) for k instances ($k = 1, 2, \dots, m_j$) using the expressions:

$$\alpha_{i,j,k} = \sigma_{i,j,k} - \sigma_i^y \quad (2.7)$$

$$\bar{p}_{i,j,k} = \varepsilon_{i,j,k} - \frac{\sigma_i^y}{E_i} \quad (2.8)$$

where subscript j represents the j^{th} ($i=1, 2, \dots, 2n$) up/down cycle of the i^{th} block, superscript k represents the k^{th} data point in the shifted and scaled j^{th} ($i=1, 2, \dots, 2n$) up/down cycle of the i^{th} block, and σ_i^y and E_i are the average yield stress and average elastic modulus in the i^{th} block, respectively. Note that there are n fatigue cycles in each block, i.e., n upward cycles and n downward cycles, which make the total number of monotonic cycles in each block $2n$.

Step 2: Assume initial values of nonlinear kinematic hardening parameters: $\mathbf{L} = [C1_i \ \gamma1_i]^T$

Step 3: Estimate the residual function vector

$$\mathbf{r} = [r_{i,j=1,k=1} \dots r_{i,j=1,k=m_1} \ r_{i,j=2,k=1} \dots r_{i,j=2,k=m_2} \dots r_{i,j=2n,k=1} \dots r_{i,j=2n,k=m_{2n}}]^T \quad (2.9)$$

with the k^{th} instance residual in the j^{th} cycle of the i^{th} block as

$$r_{i,j,k} = \frac{C1_i}{\gamma1_i} \left[1 - \exp \left((-\gamma1_i(p) \bar{p}_{i,j,k}) \right) \right] - \alpha_{i,j,k} \quad (2.10)$$

Step 4: Estimate the Jacobian matrix \mathbf{J} as follows:

$$J = \begin{bmatrix} \frac{\partial r_{i,j=1,k=1}}{\partial C1_i} & \frac{\partial r_{i,j=1,k=1}}{\partial \gamma1_i} \\ \vdots & \vdots \\ \frac{\partial r_{i,j=1,k=m_1}}{\partial C1_i} & \frac{\partial r_{i,j=1,k=m_1}}{\partial \gamma1_i} \\ \frac{\partial r_{i,j=2,k=1}}{\partial C1_i} & \frac{\partial r_{i,j=2,k=1}}{\partial \gamma1_i} \\ \vdots & \vdots \\ \frac{\partial r_{i,j=2,k=m_2}}{\partial C1_i} & \frac{\partial r_{i,j=2,k=m_2}}{\partial \gamma1_i} \\ \vdots & \vdots \\ \frac{\partial r_{i,j=2n,k=1}}{\partial C1_i} & \frac{\partial r_{i,j=2n,k=1}}{\partial \gamma1_i} \\ \vdots & \vdots \\ \frac{\partial r_{i,j=2n,k=m_{2n}}}{\partial C1_i} & \frac{\partial r_{i,j=2n,k=m_{2n}}}{\partial \gamma1_i} \end{bmatrix} \quad (2.11)$$

In Eq. 2.11, the k^{th} instance expression for the partial derivatives is given below:

$$\frac{\partial r_{i,j,k}}{\partial C1_i} = \frac{1}{\gamma1_i} \left[1 - \exp \left((-\gamma1_i \bar{p}_{i,j,k}) \right) \right] \quad (2.12)$$

and

$$\frac{\partial r_{i,j,k}}{\partial \gamma1_i} = \frac{-C1_i}{(\gamma1_i)^2} \left[1 - \exp(-\gamma1_i \bar{p}_{i,j,k}) \right] + \frac{C1_i \bar{p}_{i,j,k}}{(\gamma1_i)} \exp(-\gamma1_i \bar{p}_{i,j,k}) \quad (2.13)$$

Step 5: Estimate the incremental change in parameters:

$$\Delta L = [\Delta C1_i \ \Delta \gamma1_i]^T = -[J^T J]^{-1} J^T r \quad (2.14)$$

Step 6: Update parameters as:

$$L = [C1_i \ \gamma1_i]^T = L + \Delta L \quad (2.15)$$

Step 7: Repeat step 3 to step 6 unless the L_2 norm of the incremental parameters ΔL is less than a tolerance value, i.e.,

$$||\Delta L||_2 \leq t_{tol} \quad (2.16)$$

In Eqs. 2.7 to 2.16, the subscripts i , j , and k respectively represent block number, cycle number in block i , and data number in cycle j . This is the convention used for estimating time/block-dependent material parameters from variable-amplitude fatigue tests, while for estimating time/cycle-dependent material parameters from constant-amplitude fatigue tests, i and j are considered to be the same.

2.3 Modeling Fatigue Behavior using Evolutionary Cyclic Plasticity Model

The major aim of our research is to develop an FE modeling framework based on the proposed evolutionary cyclic plasticity model for estimating the lives of nuclear reactor components subjected to random cyclic loading. The cyclic plasticity model must be validated for laboratory experimental data through analytical modeling and 3D-FE modeling of the specimen before it can be implemented on component-level 3D-FE modeling. In this work, we modeled various fatigue experiment cases using the evolutionary cyclic plasticity model. The two modeling schemes used are discussed in the following subsections.

2.3.1 Time-Based Modeling

Material behavior under constant- or variable-amplitude fatigue loading can be predicted from the constitutive relations (Eqs. 2.1 to 2.6) for the evolutionary cyclic plasticity model and the time-dependent material parameters estimated via the technique described in Section 2.2. For a constant-amplitude fatigue loading, time/cycle-dependent (i.e., cycle-by-cycle) parameters are used while time/block-dependent (i.e., block-by-block) parameters are used to model material behavior under variable-amplitude block loading. For analytical modeling of the evolutionary cyclic plasticity model, we adopted the radial return method proposed by Wilkins [27]. Using this method, the stress increment for a given strain increment is computed. Results from time-based analytical modeling of the fatigue tests are presented in Section 4.

2.3.2 APSE-Based Modeling

As discussed in Section 2.3.1, time-dependent material parameters are used to model material fatigue behavior under constant- or variable-amplitude loading. However, time-dependent material parameters cannot be used when the test material is subjected to random-amplitude loading. In this case, material parameters must be expressed as functions of a non-time physical/field variable that changes as fatigue progresses. Here, we consider APSE as the physical variable that changes as material fatigue progresses.

As the fatigue process involves a dissipation of strain energy in each cycle of loading due to the irreversibility of the micro-plastic deformation, fatigue life can be related to the strain energy [28]. According to Lin et al. [29], the total dissipated energy (W_f) during a fatigue cycle can be divided into

$$W_f = W_p + Q + E_o + E_k \quad (2.17)$$

where W_p is the plastic energy; Q is the thermal energy, E_k is the kinematic energy, and E_o is other kind of energy. The kinetic energy and the other kinds of energy tend to zero [30]. Moreover, if the tests are done at constant temperature, without the carrying away of heat but with low cycle fatigue loading, the thermal energy Q is zero [30]. Thus, the total energy dissipation is

$$W_f = W_p \quad (2.18)$$

The plastic strain energy of a fatigue cycle is defined by the area bounded by the hysteresis loop in the cyclic stress-strain curve [31], as illustrated in Figure 2.1. The plastic strain energy can be calculated by simply integrating the stress-strain plot. We used the trapezoidal rule of numerical integration to calculate the area. Plastic strain energy of the stabilized cycle or plastic strain energy density (i.e., APSE divided by number of fatigue cycles) has been used by many researchers [28-35] for damage evaluation of material under low cycle fatigue loading. By considering similar maximum strain amplitude applied during all the fatigue tests, where all the tests were done at same strain rate, we assume the APSE value at the failure of a specimen to be close for all the test cases. Therefore, the APSE was used as a physical variable for fatigue modeling in the random-amplitude test. The material parameters estimated from the variable-amplitude test are used as function of APSE for APSE-based fatigue modeling

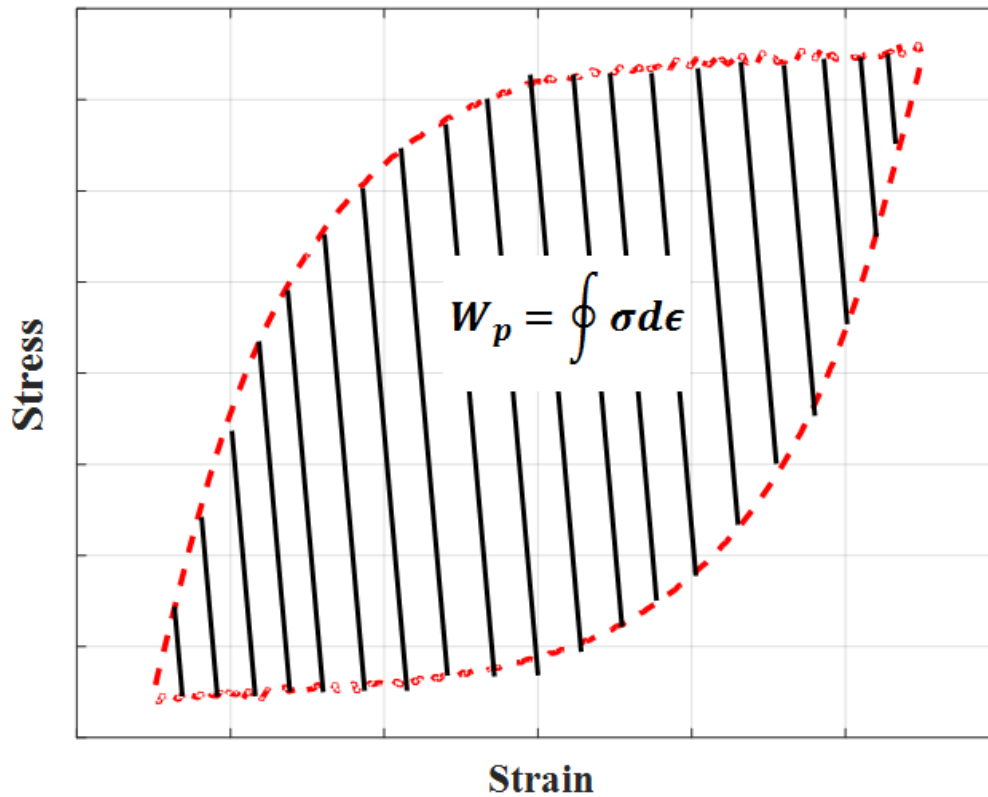


Figure 2. 1 Interpretation of plastic strain energy for a fatigue cycle.

2.4 FE Implementation of Evolutionary Cyclic Plasticity Model

The cyclic plasticity model was incorporated into the developed FE code for Chaboche-type models in the ABAQUS/Standard environment. As ABAQUS uses the backward Euler method [36], it provides unconditional stability for integration of rate equations. However, ABAQUS does not allow the use of time/cycle-dependent material properties. A user subroutine, called USDFLD (written in Fortran), was developed to enable the use of time- or APSE-dependent material properties in the implementation of the evolutionary cyclic plasticity model into ABAQUS. The time- and APSE-dependent material properties such as elastic modulus, yield stress, and kinematic hardening parameters are provided in the ABAQUS input file in tabular form, where the cycle/block numbers or APSE values (calculated at the end of each block from variable-amplitude fatigue test results) are assigned under a user-defined field variable. At the start of each integration, the USDFLD accesses the current time, from which it calculates current cycle/block number in the case of time-based modeling. In the case of APSE-based simulation, it accesses a user-defined state variable, where the APSE from the previous time step has been stored. The USDFLD then accesses the corresponding material properties from the table provided in the input file. If properties are not provided for a value of the user-defined field variable, ABAQUS uses interpolation to calculate the material properties.

3 Results from Strain-controlled Tensile/Fatigue Test and Material Parameter Estimation Models of 316 SS

Strain-controlled uniaxial tensile/fatigue experiments were conducted on 316 SS base metal using small hourglass specimens. The experimental data were used to estimate material parameters and to validate the evolutionary cyclic plasticity model through analytical and 3D-FE modeling of the fatigue experiments. Constant, variable, and random strain amplitudes were employed during the fatigue experiments. All the tests were performed in air at 300 °C using a hydraulic-controlled MTS test frame. The details of the test setup can be found in a previous Argonne report [24]. Experimental data from a previously [37] conducted strain controlled tensile test (ET-T04) in air at 300 °C were also used in this work. A constant strain rate of 0.1%/s was used during both the tensile and fatigue experiments. The test conditions along with the test IDs are presented in Table 3.1. It should be noted here that the experimental results from the constant-amplitude fatigue test ET-F06 were published in our earlier report [22] but are presented here since the resulting test data are used for analytical FE model validation, which are discussed in the later part of this report.

Table 3. 1 Test conditions for 316 SS base metal tensile and fatigue tests.

Test ID	Test Condition
ET-T04	In air, 300 °C, strain control, tensile test [37]
ET-F06	In air, 300 °C, strain control, constant amplitude = 0.5%, fatigue test [22]
ET-F38	In air, 300 °C, strain control, variable amplitude = 0.05% to 0.55%, fatigue test
ET-F40	In air, 300 °C, strain control, maximum strain = 0.55%, minimum strain = -0.55%, fatigue test
EN-F41	In air, 300 °C, strain control, constant amplitude = 0.5%, fatigue test

3.1 Tensile Test and Associated Time/Cycle Independent Elastic-Plastic Material Model Results

Figure 3.1 depicts the engineering stress-strain plot (up to 2% strain) estimated from tensile test ET-T04. The tensile test data were further analyzed to evaluate fixed material parameters such as tensile modulus, elastic stress limit, and the non-linear kinematic hardening parameters ($C1$ and $\gamma1$). These fixed material parameters were then used to model all the fatigue test cases discussed in this report. The predicted (using analytical and 3D-FE models) stress profiles using tensile test based fixed parameters were then compared with the experimental data. The predicted stress profiles were also compared with those predicted using time/cycle-dependent material properties. The fixed material parameters estimated from ET-T04 test are provided in Table 3.2.

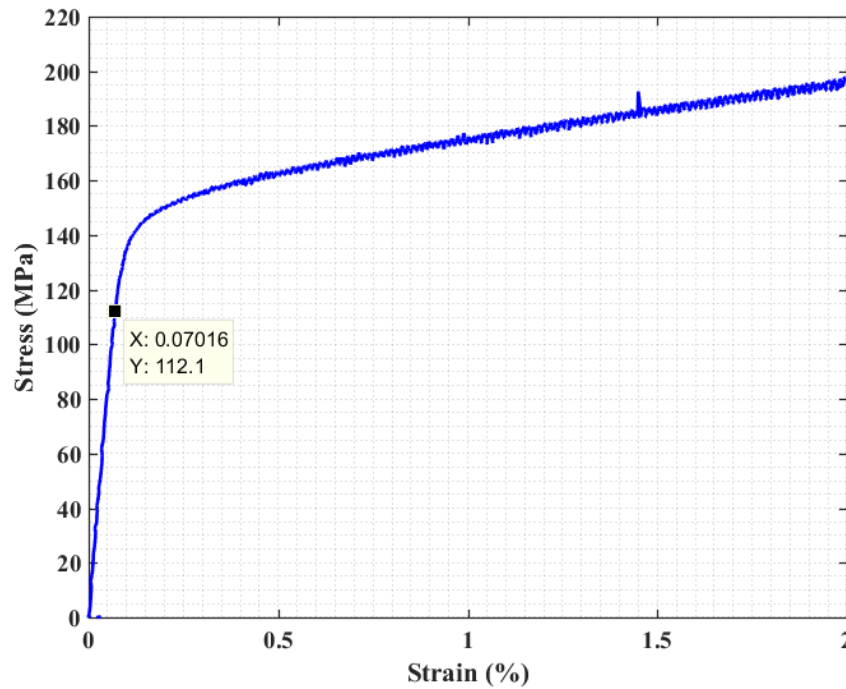


Figure 3. 1 Engineering stress-strain curve estimated from ET-T04 tensile test (in air, 300 °C) data for 316 SS base metal. Data point shows the elastic limit stress and strain.

Table 3. 2 Time-independent material parameters estimated from tensile test ET-T04

Elastic modulus (GPa)	Elastic limit stress used in models as yield stress (MPa)	Nonlinear kinematic hardening parameters	
		C1 (MPa)	γ_1
167	112	21488	279

3.2 Constant-Amplitude Fatigue Test and Associated Cyclic Elastic-Plastic Material Model Results

Two constant-amplitude fatigue tests (ET-F06 and ET-F41) were performed under the same conditions. As mentioned in Table 3.1, the applied strain amplitude was 0.5% during the constant-amplitude fatigue tests. The time histories of the observed stress from fatigue experiments ET-F06 and ET-F41 are shown in Figures 3.2 and 3.3, respectively. The curves show that the material exhibits initial cyclic hardening followed by cyclic softening. The maximum hardening stress was 249.8 MPa for ET-F06 and 244.5 MPa for ET-F41. The difference (5.3 MPa) in the maximum hardening stresses can be explained by considering the difference in the stresses after the 1st quarter cycle (162.6 MPa for ET-F06 and 158.7 MPa for ET-F41; difference: 3.9 MPa), which represents the initial (i.e., tensile) behavior of

the specimen before application of any fatigue/cycle loading. In both cases, the maximum hardening stress was observed at the 53rd cycle. However, there is a big difference in the fatigue lives for the two specimens. The fatigue life was 4202 cycles for the ET-F06 specimen and 6918 cycles for the ET-F41 specimen. The criteria for fatigue life estimation are discussed in Section 7. Considering the intrinsic nature of fatigue failure in metallic materials, this difference in fatigue lives under the same loading condition is not unexpected. It is due to the usual scatter in material microstructure. Thus, many repeat tests are needed to estimate average material properties along with their statistical variations, which need to be included in evaluating the lives of the components.

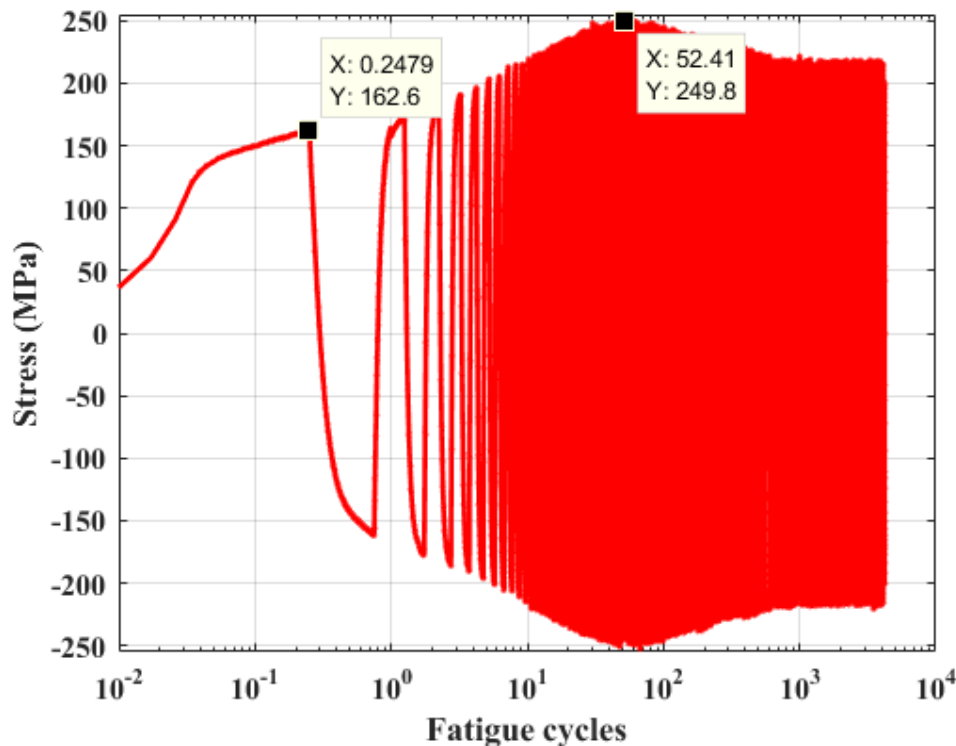


Figure 3. 2 Observed stress during the entire ET-F06 fatigue test. Data points show stress after 1st quarter cycle and the maximum hardening stress and corresponding cycle.

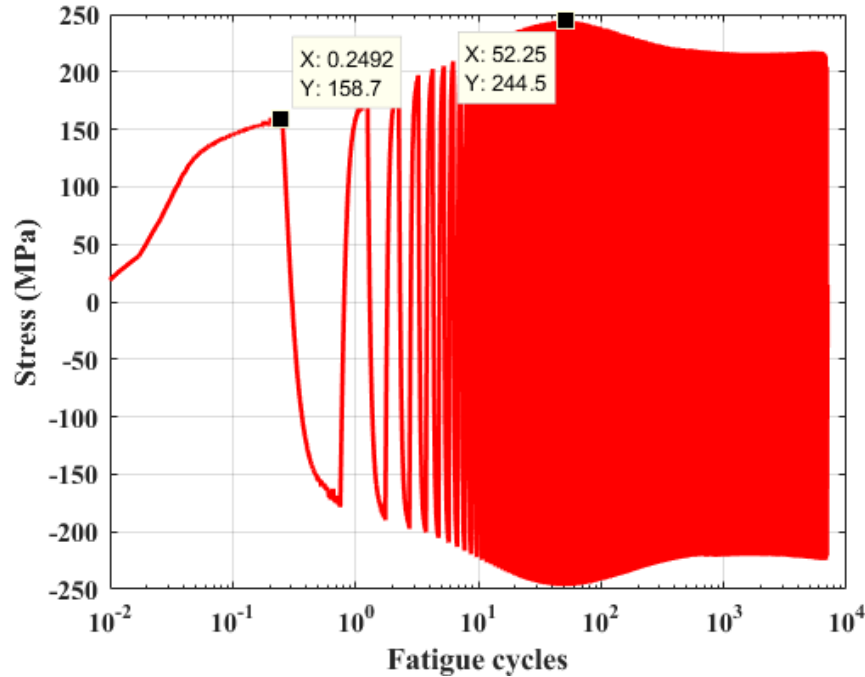


Figure 3.3 Observed stress during the entire ET-F41 fatigue test. Data points show stress after 1st quarter cycle and the maximum hardening stress and corresponding cycle.

Time/cycle-dependent material properties were estimated from the two constant-amplitude fatigue tests (ET-F06 and ET-F41). To evaluate the material properties, equivalent monotonic curves estimated from the cyclic stress-strain data (acquired from the ET-F06, ET-F41 fatigue tests) were used (for details refer to our earlier work [24]). Figures 3.4 and 3.5 depict the equivalent-monotonic curves estimated from the first 50 fatigue cycles of ET-F06 and ET-F41 test, respectively. The stress-strain curve from tensile test T-04 is also shown in the figures. It can be seen from the figure that the stress at 0.5% strain increases from ~160 MPa to 250 MPa, which again verifies a significant amount of stress hardening/softening during the fatigue experiment and hence the importance of the evolutionary cyclic plasticity model for more accurate fatigue evaluation of 316 SS. The equivalent-monotonic stress-strain curves were further analyzed to estimate the time/cycle-dependent material parameters, such as elastic modulus, elastic limit stress (or yield stress), and kinematic hardening parameters ($C1$ and $\gamma1$). Section 2 summarizes the time/cycle-dependent parameter estimation technique, which was first reported by our research group in an earlier report [24].

The estimated parameters are shown in Figures 3.6 to 3.9. Figures 3.6 and 3.7 show the time/cycle variation of elastic modulus and elastic limit stress, respectively, whereas Figures 3.8 and 3.9 show the nonlinear kinematic hardening parameters $C1$ and $\gamma1$, respectively. As seen in the figures, the material parameters vary significantly (particularly the nonlinear kinematic hardening parameters in this case) over the fatigue cycles, in contrast to the tensile-test-based fixed parameters (refer to Table 3.2). The variations of the cycle-by-cycle material parameters are similar for both test cases (ET-F06 and ET-F41), where the differences that do exist are due to the variations in stress between the two tests, as discussed before.

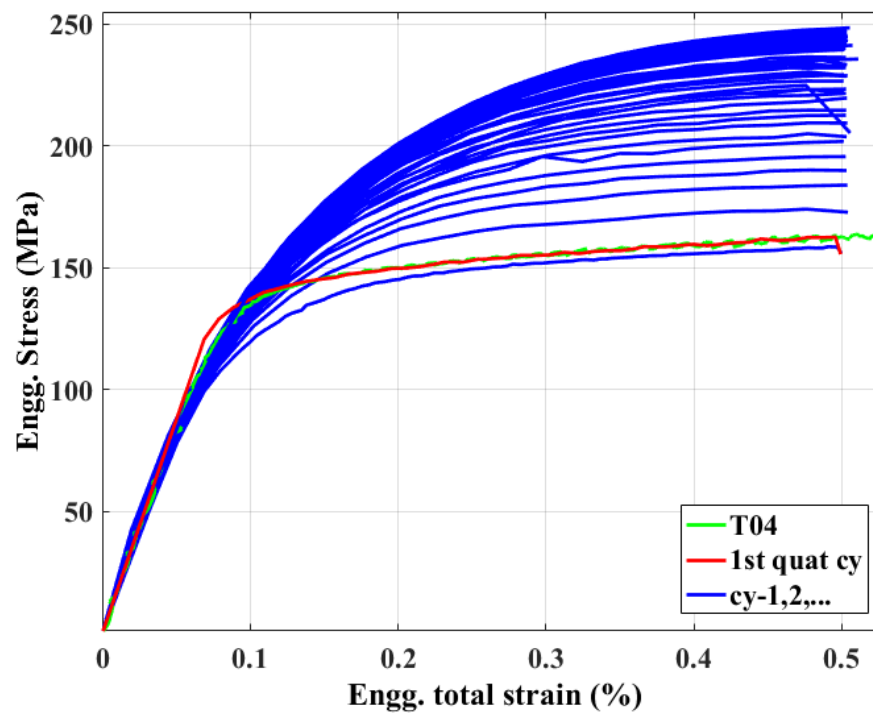


Figure 3. 4 Equivalent monotonic stress-strain curves over 50 cycles estimated from ET-F06 fatigue test data and comparison with ET-T04 tensile test data.

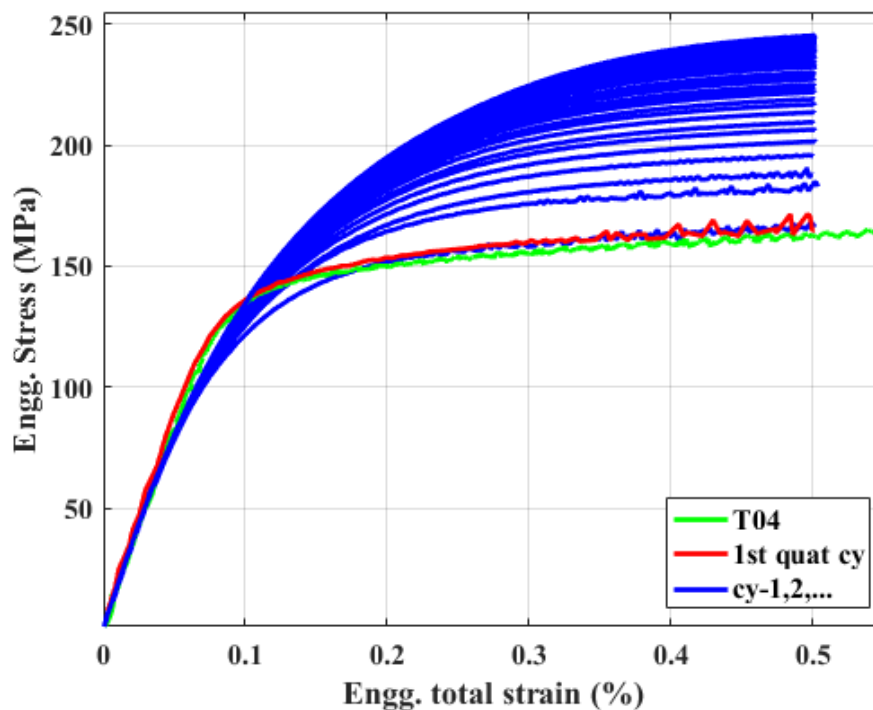


Figure 3. 5 Equivalent monotonic stress-strain curves over 50 cycles estimated from ET-F41 fatigue test data and comparison with ET-T04 tensile test data.

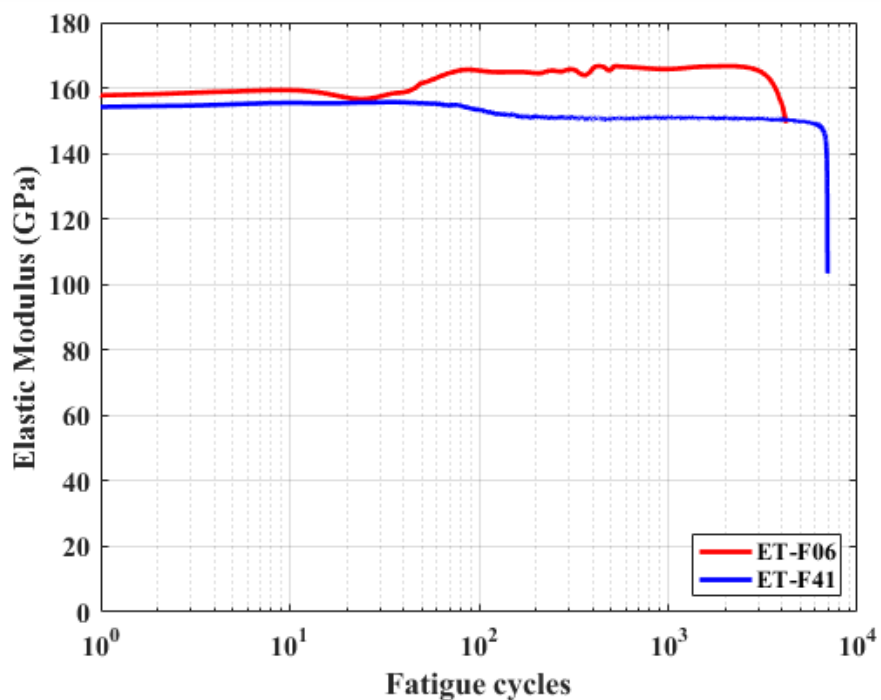


Figure 3. 6 Time/cycle-dependent elastic modulus estimated from constant-amplitude fatigue tests.

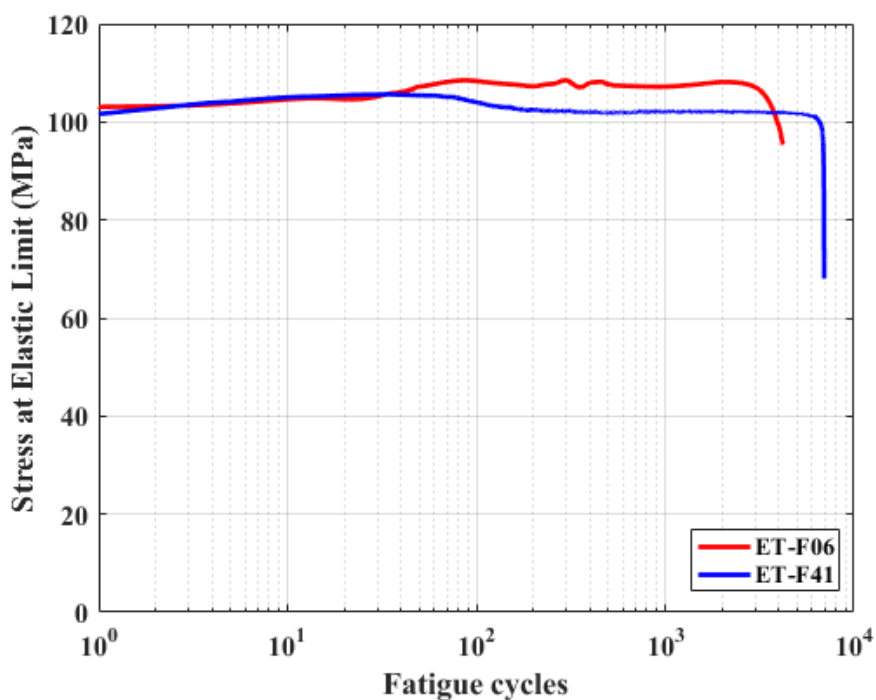


Figure 3. 7 Time/cycle-dependent elastic limit stress estimated from constant-amplitude fatigue tests.

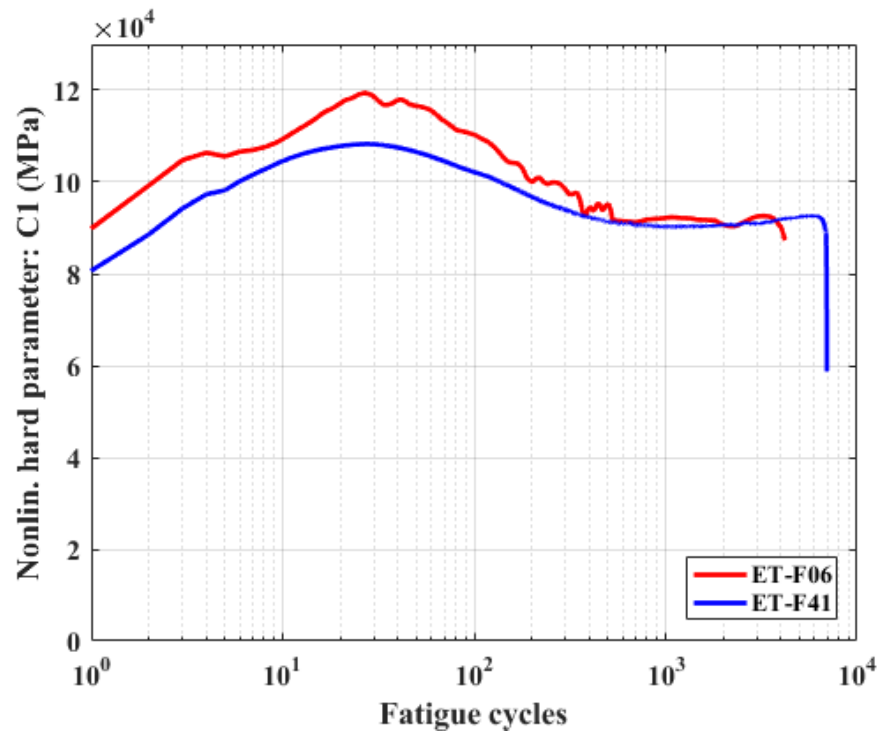


Figure 3. 8 Time/cycle-dependent nonlinear kinematic hardening parameter, C1 estimated from constant-amplitude fatigue tests.

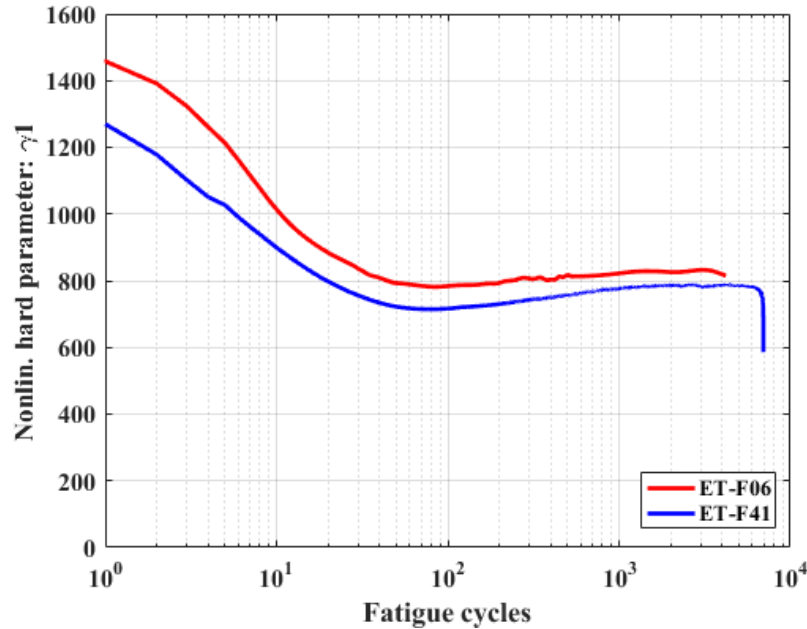


Figure 3. 9 Time/cycle-dependent nonlinear kinematic hardening parameter, γ_1 estimated from constant-amplitude fatigue tests.

3.3 Variable-Amplitude Fatigue Test and Associated Cyclic Elastic-Plastic Material Model Results

In our earlier work [22] we found that, although the constant-amplitude fatigue test can be used for time-dependent material properties, the estimated properties are sensitive to loading amplitude. To avoid the issues of amplitude dependency of material parameters, in our earlier work [26], we estimated material parameters for 508 low alloy steel (LAS) based on variable-amplitude fatigue test. In this report, we present fatigue test and associated material model results from variable-amplitude fatigue testing of a 316 SS specimen. The ultimate aim is to develop mechanistic models of real plant components subjected to random fatigue loading with different loading amplitudes.

Since it is not possible to perform constant-amplitude fatigue tests for each loading amplitude in a loading spectrum and then estimate the material properties for those loading amplitudes as separate constant-amplitude cases (as discussed in Section 3.2), we propose to estimate average material parameters based on a generic variable-amplitude fatigue test. Those average parameters then can be used for estimating the stress-strain state of a specimen/component subjected to any loading amplitude (constant or random) bounded within the loading spectrum and environmental conditions of the proposed variable-amplitude fatigue test. For the purpose, we conducted the ET-F38 variable-amplitude fatigue test at 300 °C and in air using a 316 SS specimen. During ET-F38, a repetitive block consists of 12 cycles with different amplitudes being applied during the variable-amplitude fatigue experiment. The strain amplitude was varied by gradually increasing from a minimum value of 0.05% (selected to fall within the elastic limit, see Figure 3.1) to a maximum value of 0.55% and then gradually decreasing to the minimum again. Figure 3.10 depicts the applied cyclic strain input within a block during ET-F38. The corresponding time history of the measured stress data from ET-F38 is shown in Figure 3.11. As seen in the case of the constant-amplitude fatigue test, significant initial stress hardening followed by stress softening was observed during ET-F38. The stress-strain hysteresis plot for the 1st block is shown in Figure 3.12. As seen in the figure, there are 12 cyclic stress-strain curves within a block. As there are several stress-strain cycles with different amplitudes within a block, the estimated time/block-dependent material parameters should capture the amplitude dependency of the parameters.

The Section 2 presents the block-dependent material parameter estimation technique. The method used for estimating the block-dependent parameters of 508 LAS is reported in [26]. Note that the cycle-dependent parameters discussed in Section 3.2 are different from the block-dependent parameters discussed in this section. The cycle-dependent parameters are estimated to capture the stress-strain state of a specimen subjected to single-loading amplitude, whereas the purpose of block-dependent parameters is to capture the stress-strain state of a material subjected to multiple loading amplitudes through a single test of average parameters at a given time.

An example comparison between experimental and predicted true back stress (using the estimated average parameters and analytical Chaboche equation) as a function of true plastic strain for a particular block (comprising all 12 cycles within that block) is shown in Figure 3.13. The estimated block-dependent elastic-plastic material parameters using ET-F38 test data are plotted in Figures 3.14 to 3.17. Figures 3.14 and 3.15 show the block variation of the estimated elastic modulus and elastic limit stress, respectively, while Figures 3.16 and 3.17 show the block variation of the estimated nonlinear kinematic hardening parameters $C1$ and $\gamma1$, respectively.

In addition to estimating appropriate elastic-plastic parameters, those parameters need to be described as a function of an appropriate field variable, which needs to be estimated by time/cycle/block-dependent mechanistic modeling. Among the possible choices for the field variable (that affects the fatigue damage process), the time/cycle/block is an obvious choice because of its easy tracking. However, direct tracking of the time/cycle/block can only be useful for modeling a test case using the parameters estimated from the same test case. As discussed earlier in Section 2, describing material behavior with respect to time/cycle/block may not allow selection of an appropriate set of parameters for a modeling test case, if the parameters are estimated from a different fatigue test. Hence, the estimated parameters must be described with respect to a physical/field variable different from the time/cycle/block.

In this report, we propose a parameter mapping approach based on APSE. The APSE-based modeling approach is discussed in detail in Section 2. In this approach, the calculated APSE at the end of a time step is used to select the material parameters for predicting the stress-strain in the next step. The material parameters estimated from variable-amplitude test ET-F38 were used for APSE-based modeling. Figures 3.18 to 3.21 show the material parameters estimated from ET-F38 as functions of APSE. These functions were used to map the material parameters between the variable-amplitude test and the test being modeled.

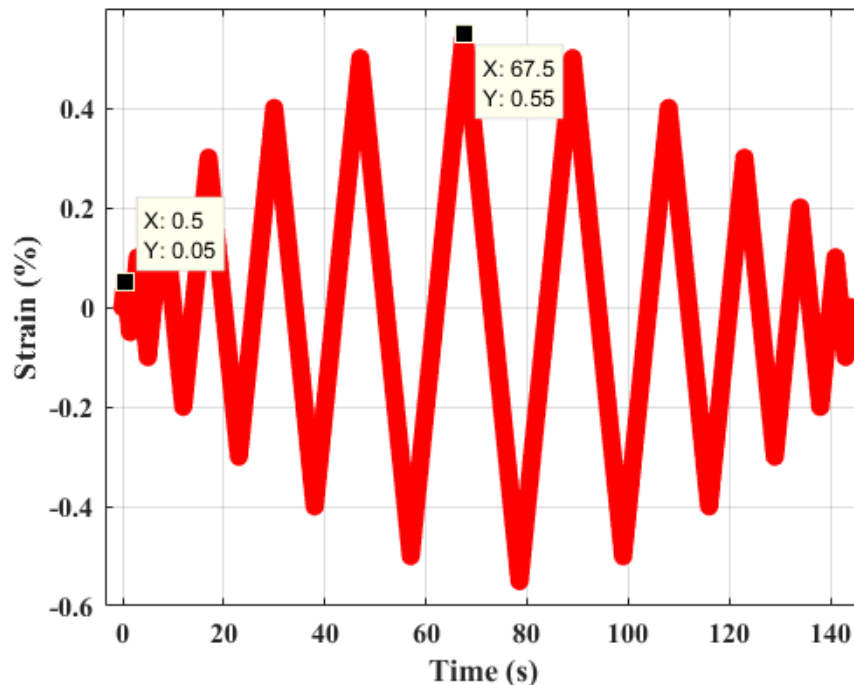


Figure 3. 10 Block loading during variable-amplitude strain-controlled fatigue test (ET-F38). Data points show minimum and maximum amplitudes.

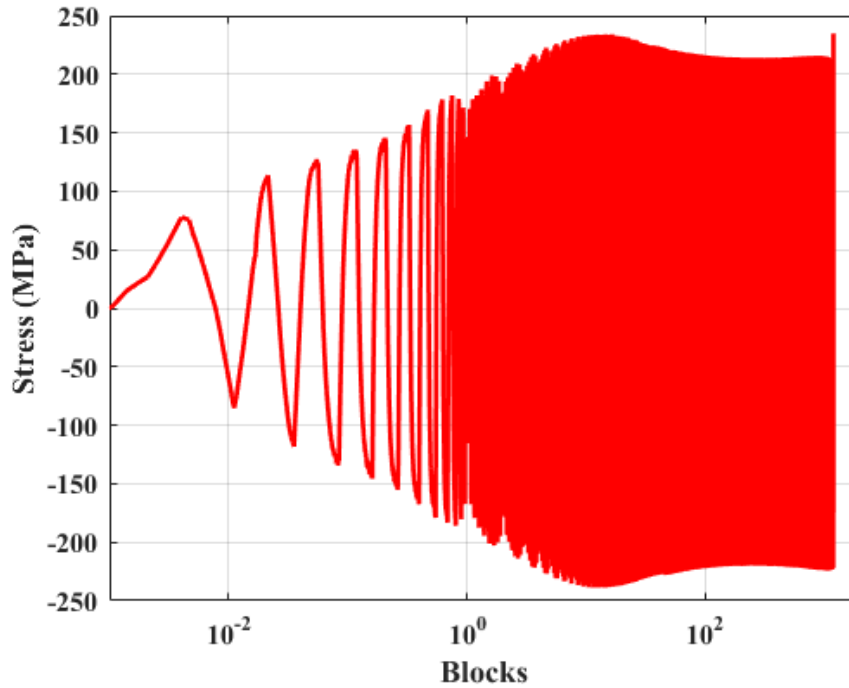


Figure 3. 11 Observed stress during the entire ET-F38 fatigue test.

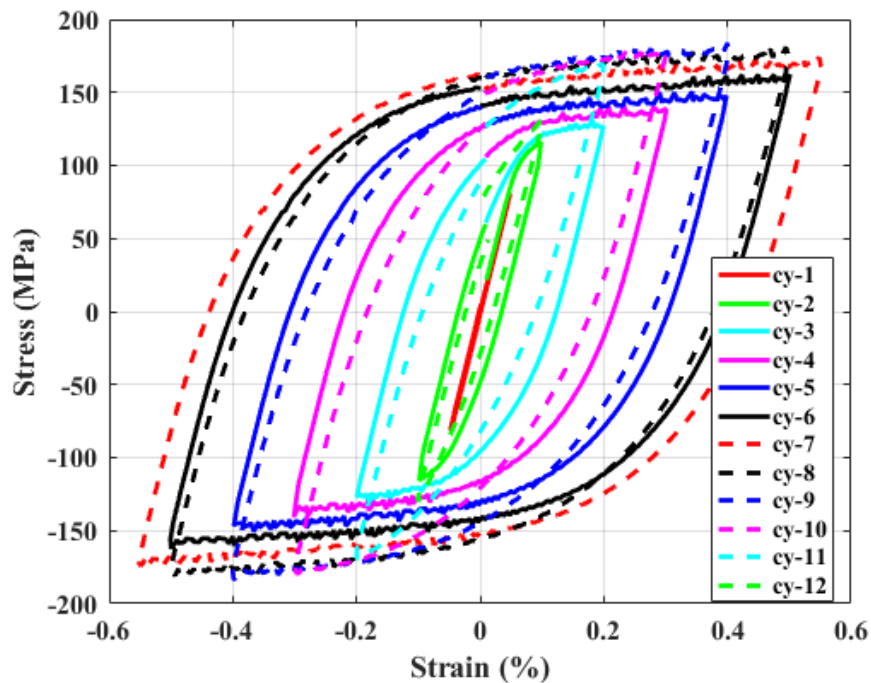


Figure 3. 12 Observed stress-strain hysteresis behavior during the 1st block (each block comprising 12 cycles) of ET-F38.

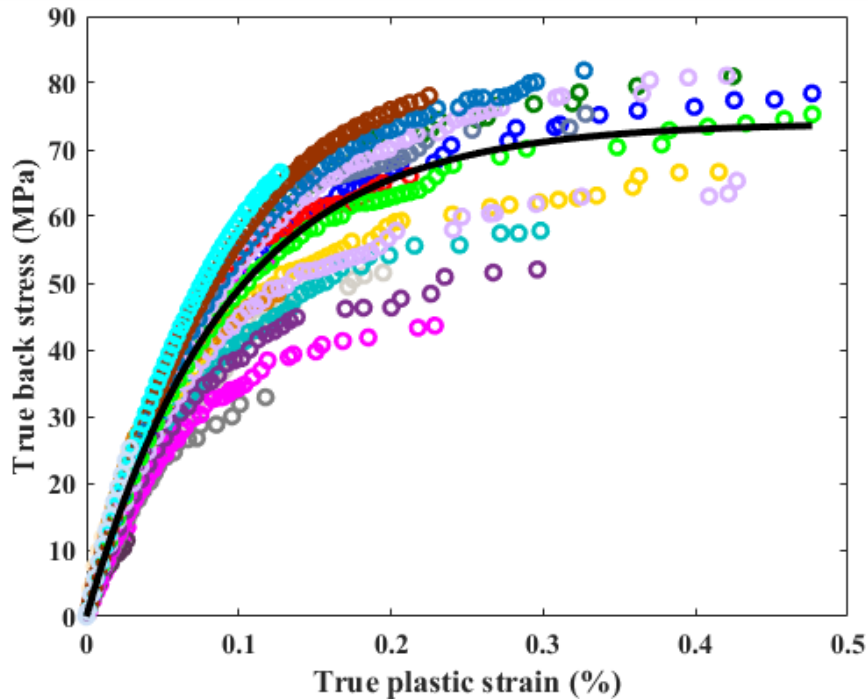


Figure 3. 13 Example comparison of experimental true back stress (as a function of true plastic strain) and predicted back stress (using kinematic hardening equation and estimated parameters: $C1$ and $\gamma1$ pertaining to that block). Black solid line: prediction; Circles: experimental data from 12 fatigue cycles of that block.

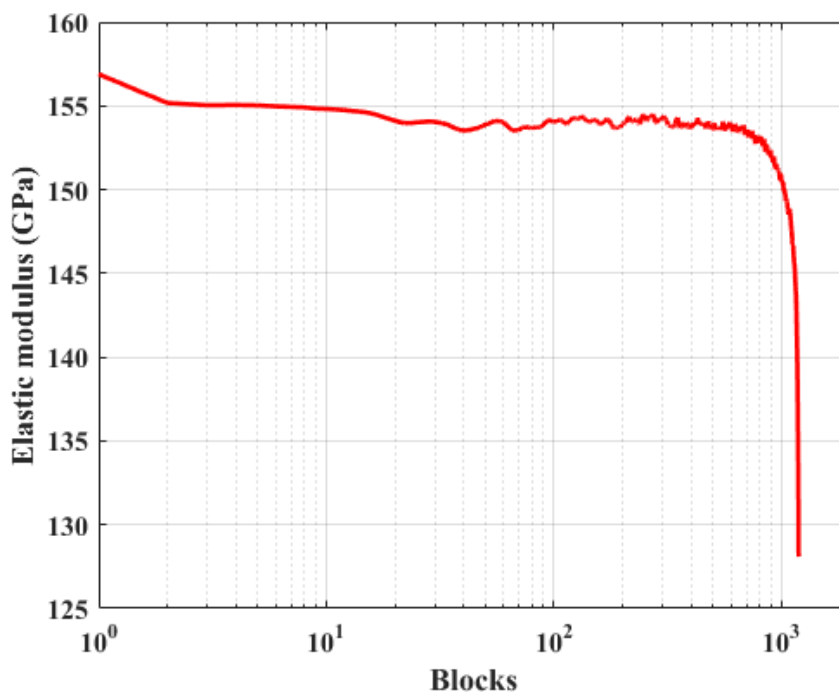


Figure 3. 14 Time/block-dependent elastic modulus estimated from variable-amplitude fatigue test (ET-F38).

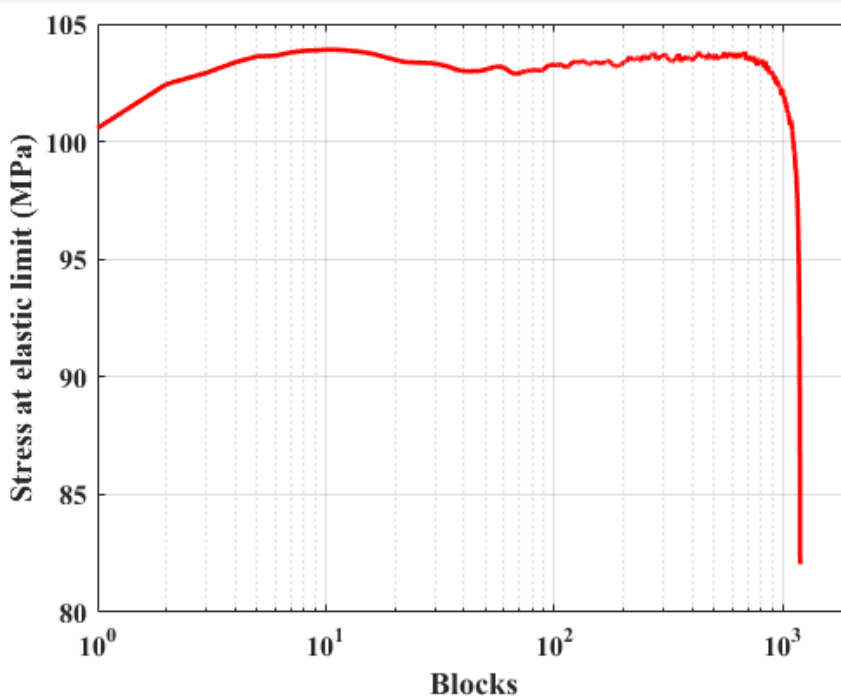


Figure 3. 15 Time/block-dependent elastic limit stress estimated from variable-amplitude fatigue test (ET-F38).

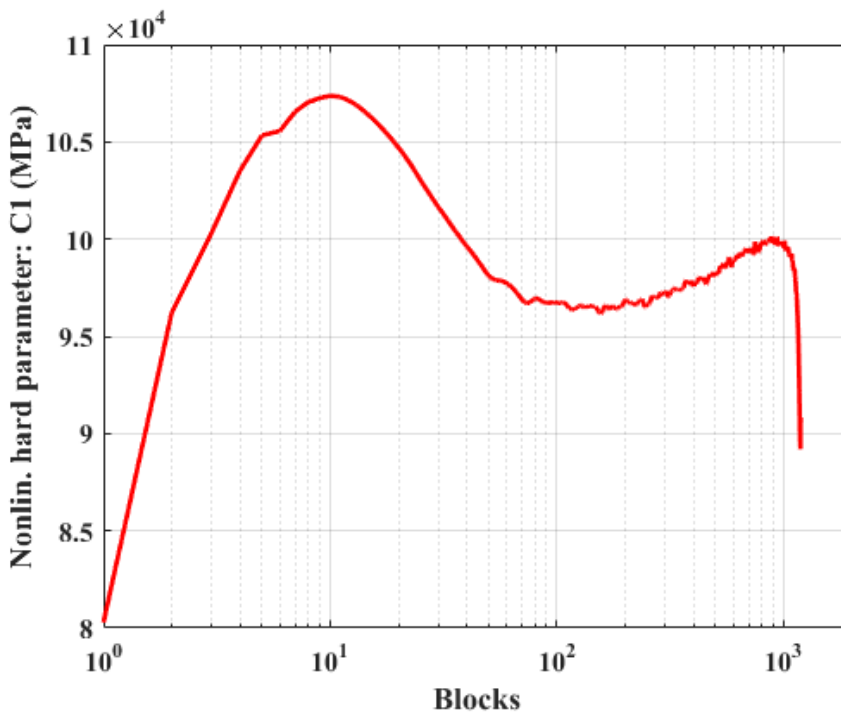


Figure 3. 16 Time/block-dependent nonlinear kinematic hardening parameter, C1 estimated from variable-amplitude fatigue test (ET-F38).

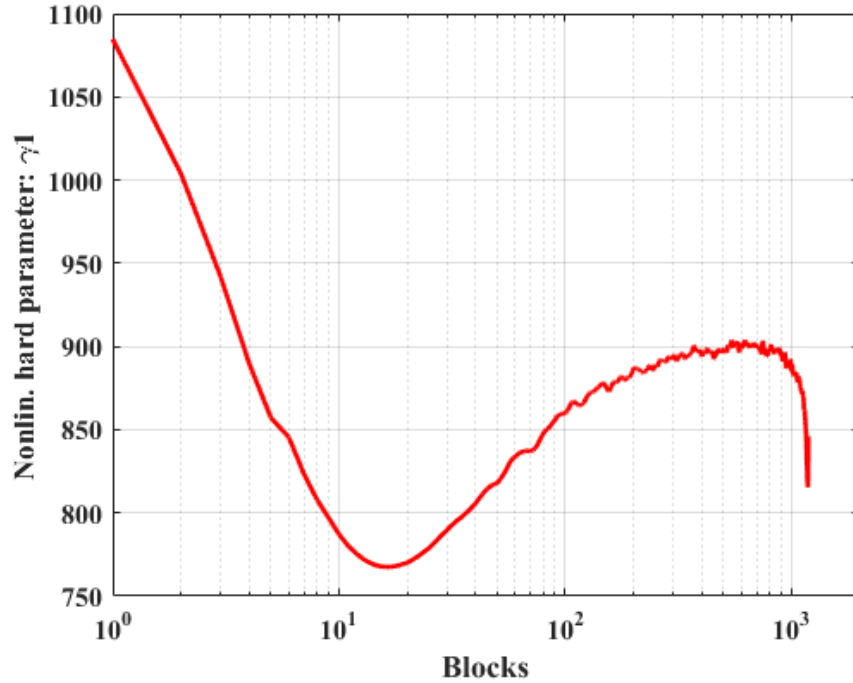


Figure 3. 17 Time/block-dependent nonlinear kinematic hardening parameter, γ_1 estimated from variable-amplitude fatigue test (ET-F38).

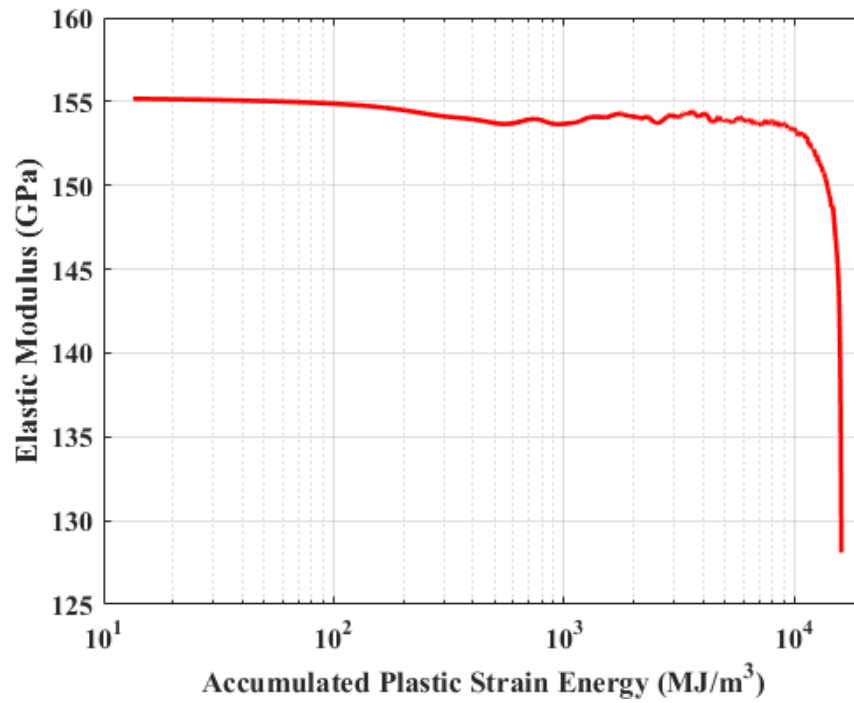


Figure 3. 18 APSE-dependent elastic modulus estimated from variable-amplitude fatigue test (ET-F38).
The y-data corresponding to $x=0$ is ignored in the semi-logx plot.

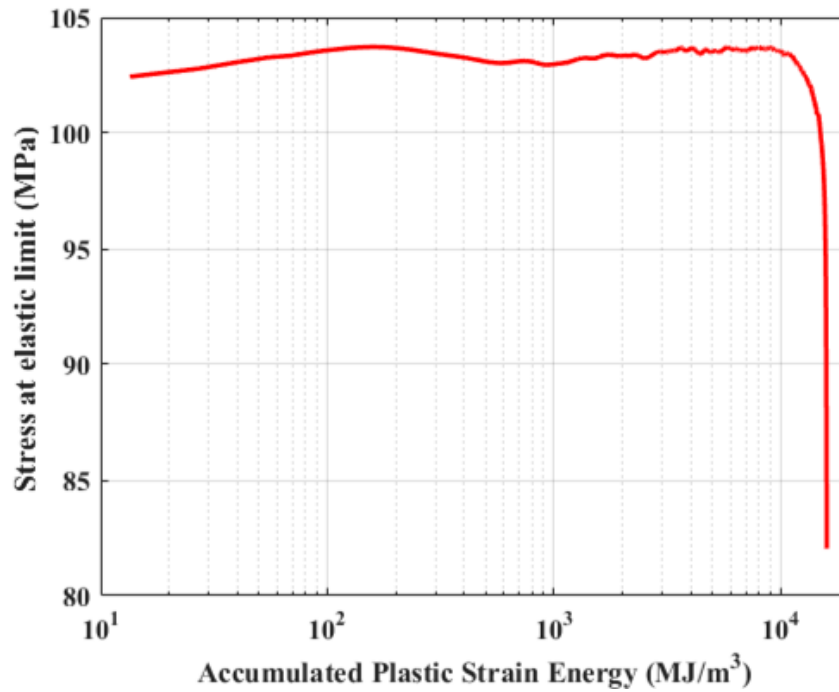


Figure 3. 19 APSE -dependent elastic limit stress estimated from variable-amplitude fatigue test (ET-F38). The y-data corresponding to $x=0$ is ignored in the semi-logx plot.

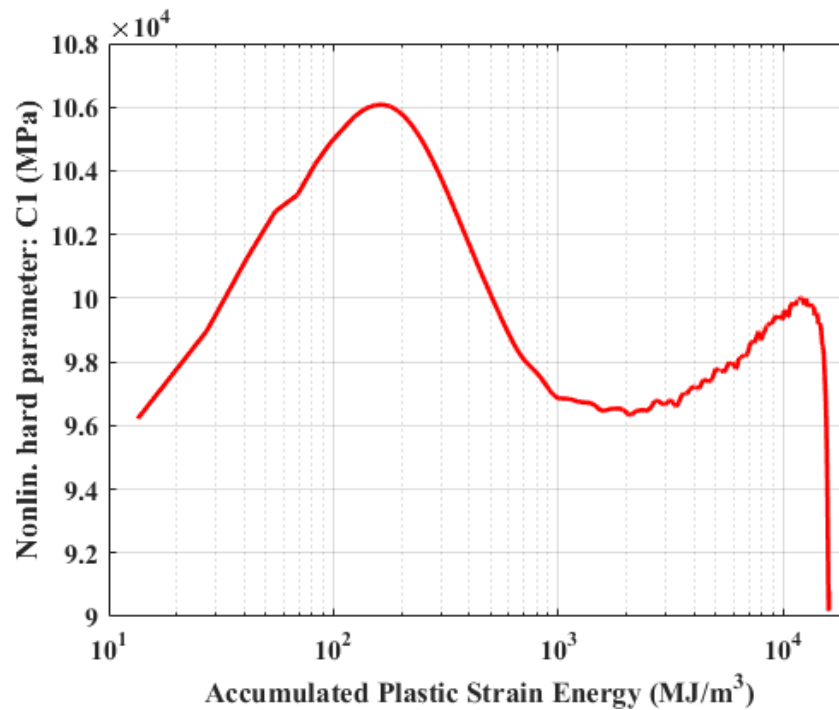


Figure 3. 20 APSE -dependent nonlinear kinematic hardening parameter, C1 estimated from variable-amplitude fatigue test (ET-F38). The y-data corresponding to $x=0$ is ignored in the semi-logx plot.

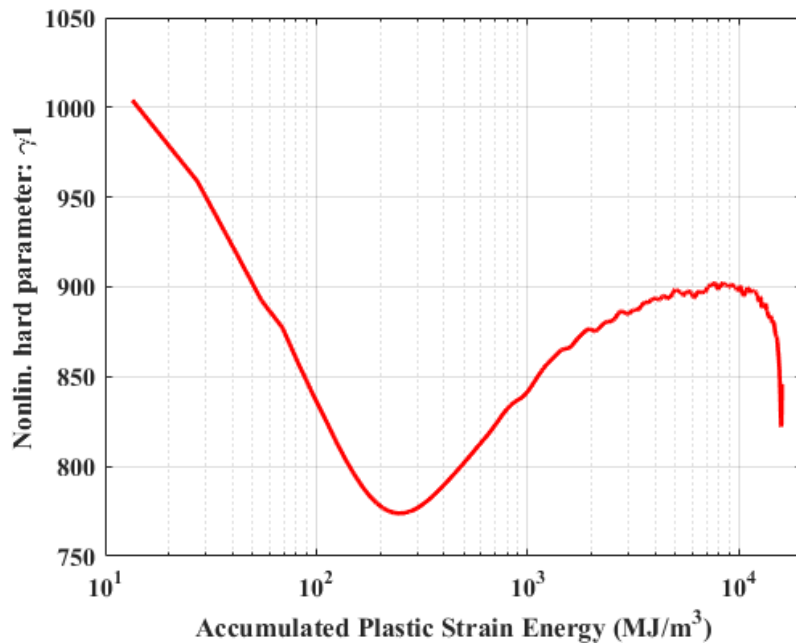


Figure 3. 21 APSE-dependent nonlinear kinematic hardening parameter, γ_1 estimated from variable-amplitude fatigue test (ET-F38). The y-data corresponding to $x=0$ is ignored in the semilogx plot.

3.4 Random-Amplitude Fatigue Test Results

Nuclear reactor structures encounter random complex loading during their service life due to random temperature and pressure transients. Thus, developing a fatigue model that can capture material behavior under random loading is essential for accurate life prediction of nuclear reactor components. With this in mind, we conducted a strain-controlled random-amplitude test fatigue test (ET-F40). The aim of the test was to develop a validated model to predict the material stress-strain state under random loading. The random test was conducted for validation purposes only. For modeling the random load case, we used the parameters estimated based on the variable loading test ET-F38. The respective analytical and 3D-FE modeling results will be discussed in Sections 4 and 5. Here we discuss a few results directly related to the fatigue test.

During the random-amplitude fatigue test (ET-F40), a repetitive block of random strain inputs was applied to the specimen. The applied random strain input within a block is shown in Figure 3.22. As seen from the figure, the strain inputs were bounded with a maximum/minimum strain amplitude of $\pm 0.55\%$, the same as the bounded strain inputs for the variable-amplitude test (ET-F38). The in-between strain inputs were selected based on a MATLAB-based random number generator. The observed stress history for the entire test ET-F40 is shown in Figure 3.23. As seen in the figure, there was substantial initial stress hardening followed by stress softening for the 316 SS under the random-amplitude strain-controlled test. Similar behavior was observed for the constant-amplitude (ET-F06 and ET-F41) and variable-amplitude (ET-F38) strain-controlled tests. To better check the randomness of the applied strain, Figure 3.24 presents a magnified (in time axis) plot of strain vs. time. The corresponding observed stress and hysteresis plots

are shown in Figures 3.25 and 3.26, respectively. As seen in Figure 3.26, there are many small hysteresis loops inside the big hysteresis loop. However, these loops are not symmetric about the x- and y-axes, as observed for the variable-amplitude test case (see Figure 3.12). Thus, modeling fatigue behavior under random-amplitude loading is a complex problem.

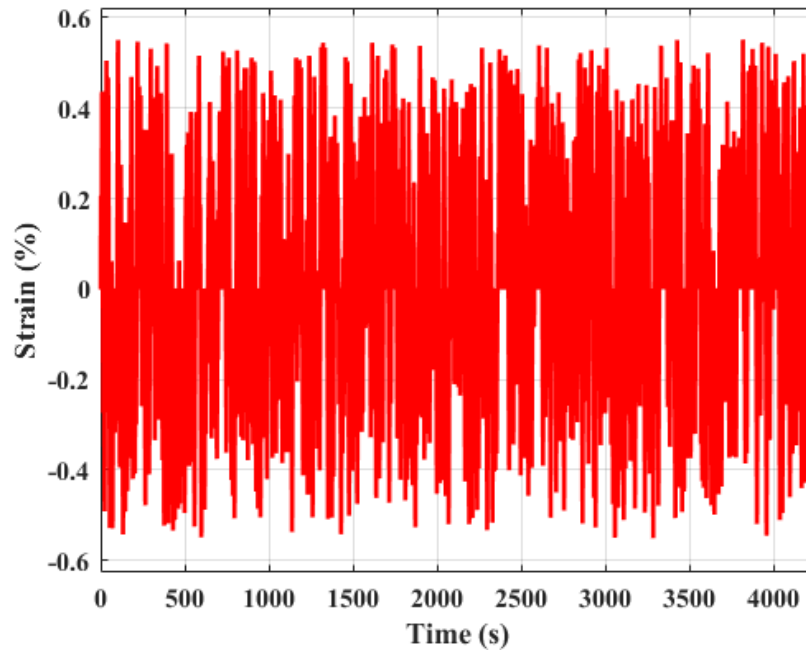


Figure 3. 22 Block loading during random-amplitude strain-controlled fatigue test (ET-F40).

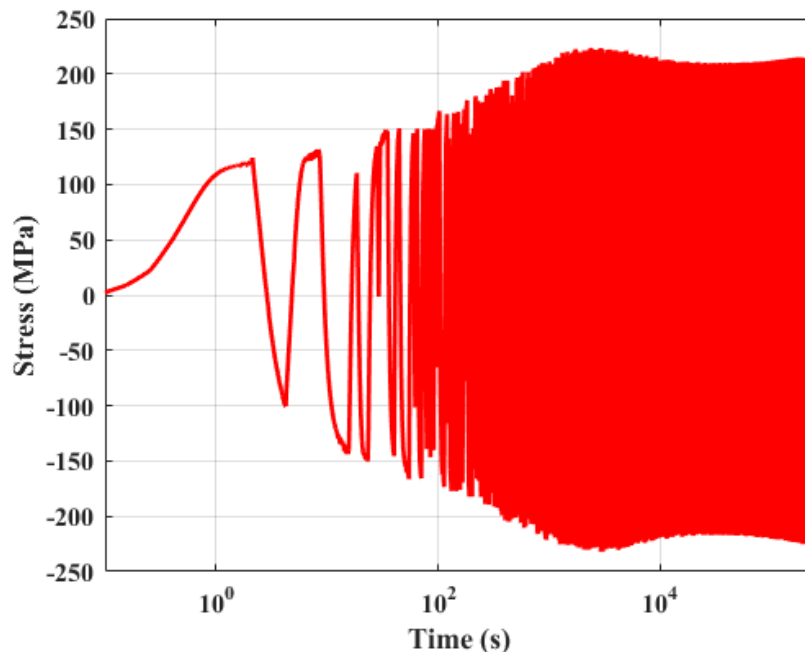


Figure 3. 23 Observed stress during the entire ET-F40 fatigue test.

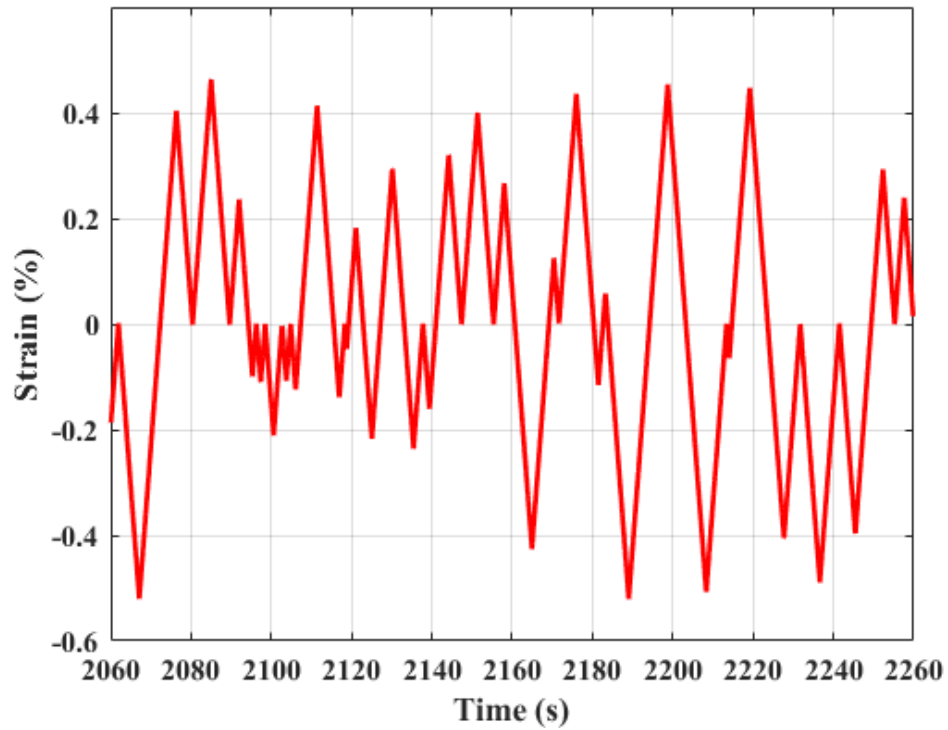


Figure 3. 24 Magnified plot of applied strain during ET-F40.

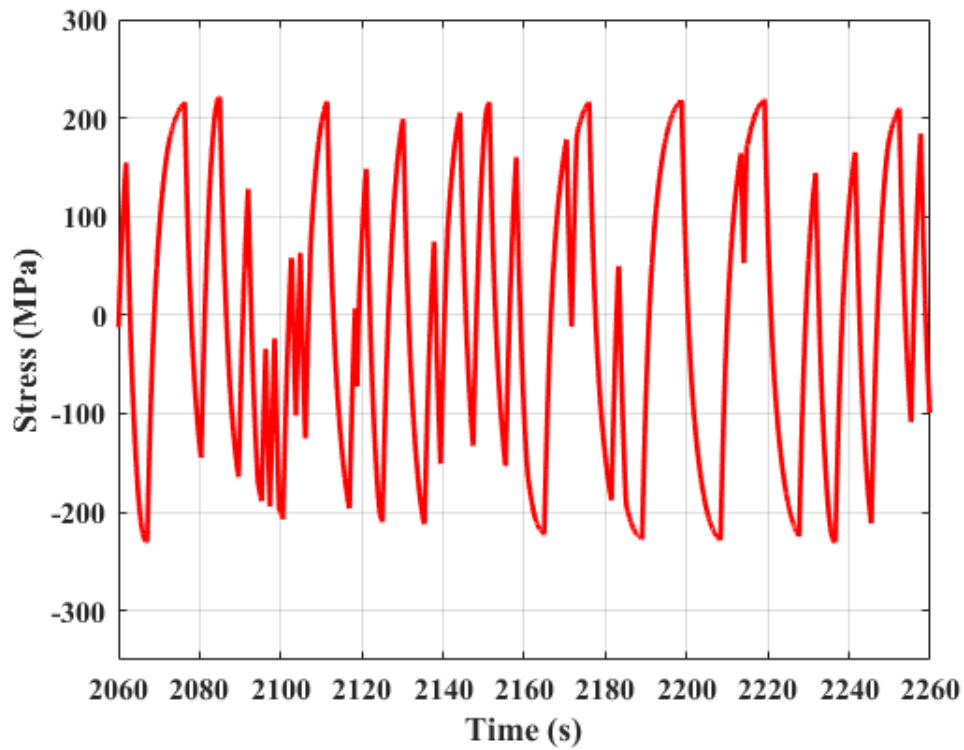


Figure 3. 25 Magnified plot of observed stress (corresponding to strain shown in Figure 3.24) during ET-F40.

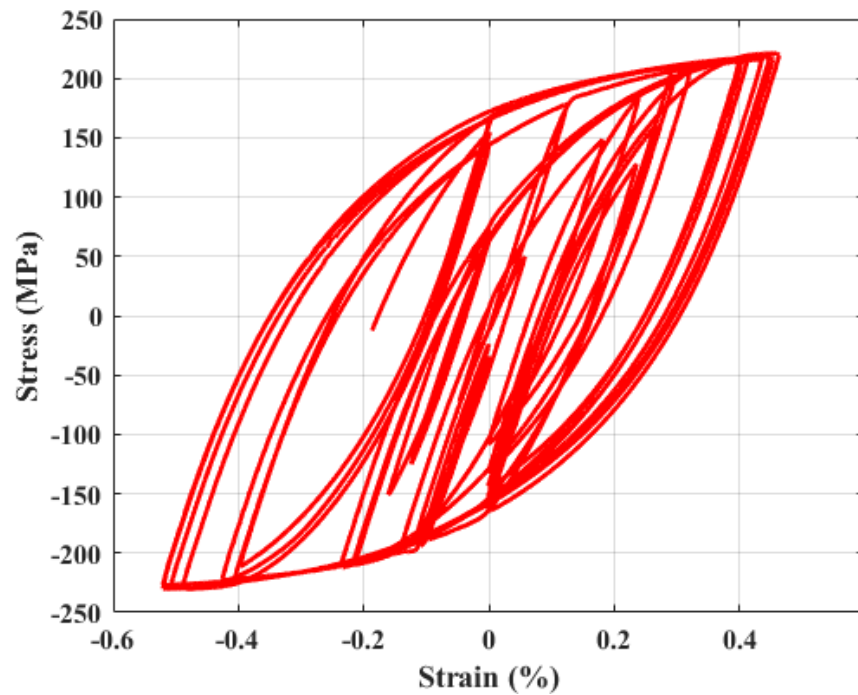


Figure 3. 26 Example hysteresis plot of stress (shown in Figure 3.25) and strain (shown in Figure 3.24) during ET-F40.

4 Results from Analytical Modeling of Constant, Variable, and Random Load Strain-controlled Fatigue Tests

Our evolutionary cyclic plasticity model along with related material parameter estimation technique is described in Section 2. Section 2 also describes a time- and APSE-based material parameter mapping approach during modeling of the fatigue tests. A time-based approach can be used when a constant- or variable-amplitude loading is applied but cannot be used to model fatigue behavior under random loading. To solve this issue, a more versatile approach based on APSE is proposed. The APSE-based modeling can be used to model fatigue behavior under any loading condition (constant, variable, or random). In this section, results from time-based analytical modeling of constant-amplitude (ET-F06 and ET-F41) and variable-amplitude (ET-F38) tests are presented. Results from APSE-based analytical modeling of constant, variable, and random (ET-F40) amplitudes are also presented. Note that, for the APSE-based modeling, the material parameters estimated from the variable-amplitude test (ET-F38) were used for predicting the different test cases. All the tests were also modeled by using fixed material parameters estimated from the tensile test (ET-T04) and parameters at the half-life of the fatigue test specimen. All the fixed, time-dependent, and APSE-dependent material parameters are presented in Section 3.

4.1 Results from Time-Based Analytical Models

4.1.1 Constant-Amplitude Fatigue Test

Figure 4.1 presents experimentally observed and analytically modeled stress results for the constant-amplitude fatigue test ET-F41. The figure shows predicted stress using time/cycle-dependent material parameters estimated from ET-F41 and two sets of time-independent or fixed parameters estimated from the tensile test ET-T04 and the half-life cycle of ET-F41. Three magnified versions of Figure 4.1 are shown in Figures 4.2 to 4.4, representing various important stages of material behavior during the specimen's fatigue life.

Figure 4.2 represents the initial hardening behavior of the material. The data indicate that the evolutionary cyclic plasticity model based on time/cycle-dependent material properties predicted the material hardening behavior with excellent accuracy, but that the model based on time-independent material properties estimated from tensile test ET-T04 and half-life cycle of ET-F41 test did not predict the material hardening behavior. Note that the tensile-test-based material parameter predicts this behavior well only up to the 1st quarter cycle, as expected. The experimental condition up to the 1st quarter cycle is similar to a tensile test, and after that a reverse loading is applied, and material behavior is more influenced by cyclic-loading-related reversals.

Figure 4.3 represents the softening behavior (after initial hardening) followed by stabilized cycles. As seen in the curves, the evolutionary cyclic plasticity model predicts both softening and stabilized cycle behavior of the material well. The prediction of stabilized cycles is found to be good when half-life material

properties are used. This finding is expected as the half-life cycle falls in the stabilized region, and material behavior does not change significantly in this region.

Figure 4.4 represents the most important stage of a specimen in the context of fatigue life and final failure of a specimen. In this stage, stress drops at a high rate, and eventually, the specimen breaks in a way characteristic of unstable or rapid crack propagation. An accurate prediction of this stage is essential to determine the life of the specimen and, therefore, the life times of the components. Figure 4.4 also shows that the evolutionary cyclic plasticity model can accurately predict the last and most important stage of material behavior under constant-amplitude fatigue loading.

Similarly, another constant-amplitude fatigue test (ET-F06) was analytically modeled with the time/cycle-dependent material parameters estimated from ET-F06 and two sets of time-independent or fixed parameters estimated from the tensile test ET-T04 and the half-life cycle of ET-F06. The experimental and simulated stress is compared in Figure 4.5. As was the case for modeling the ET-F41 test, the evolutionary cycle plasticity model based on time/cycle-dependent material parameters can accurately predict all the stages of material behavior during the fatigue life of the specimen.

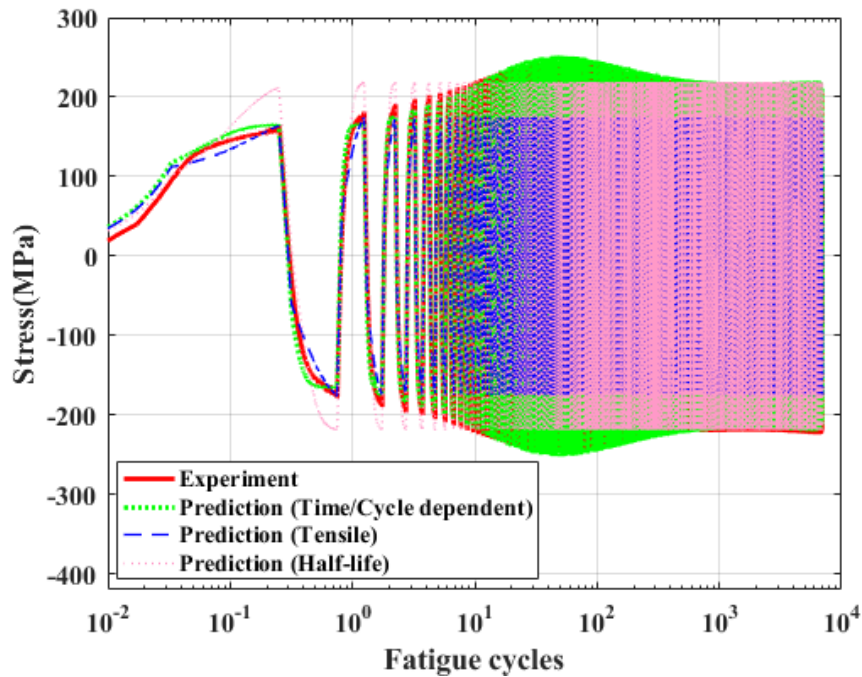


Figure 4. 1 Simulated (analytical) vs experimental axial stress history of ET-F41. Predictions are from simulation using time/cycle-dependent parameters (ET-F41) and two sets of time-independent parameters (tensile test ET-T04 and half-life cycle of ET-F41).

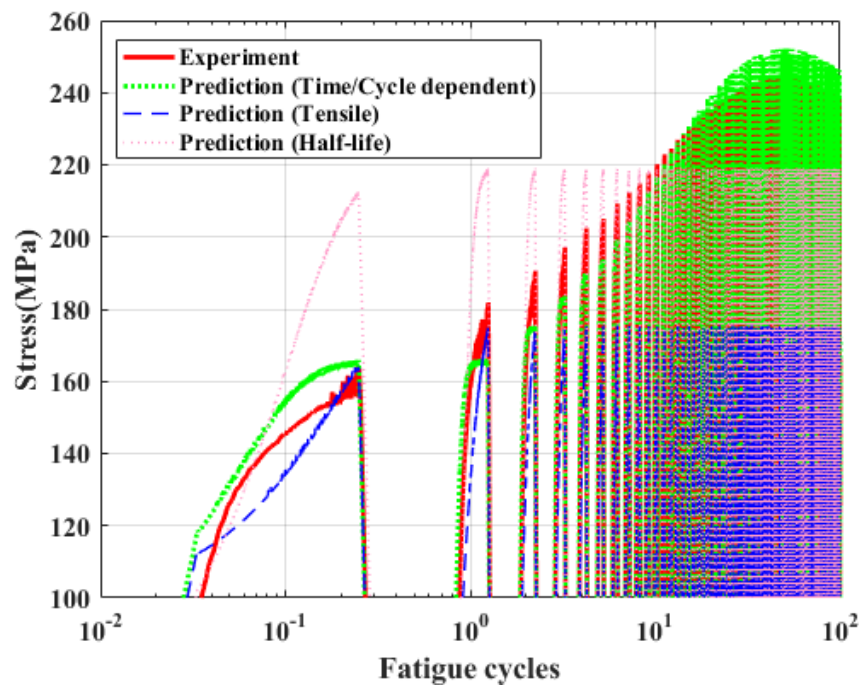


Figure 4. 2 Magnified version of Figure 4.1 showing the ability of evolutionary cyclic plasticity model (time/cycle-dependent prediction) to predict initial hardening behavior of 316 SS under constant-amplitude loading.

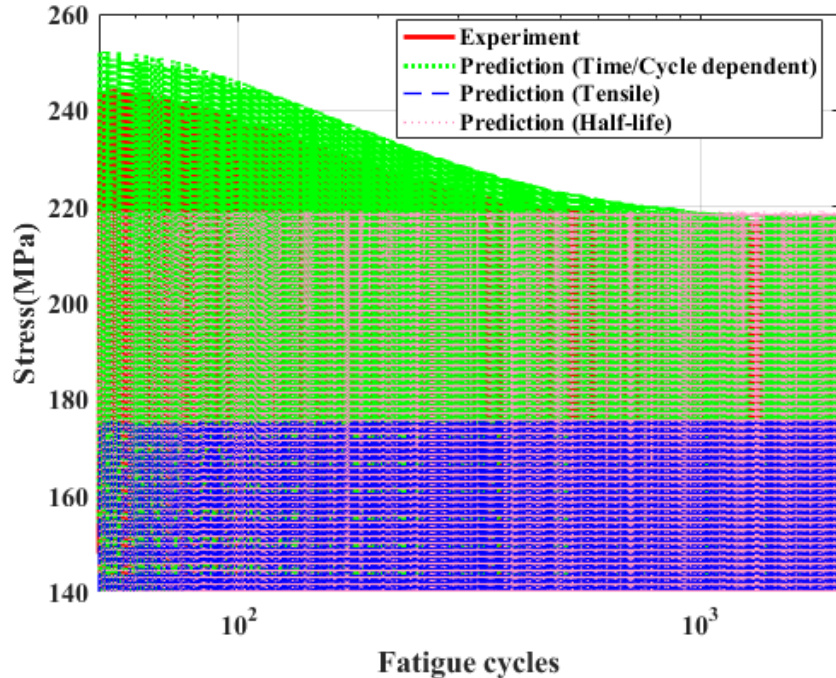


Figure 4. 3 Magnified version of Figure 4.1 showing the ability of evolutionary cyclic plasticity model (time/cycle-dependent prediction) to predict softening behavior of 316 SS under constant-amplitude loading.

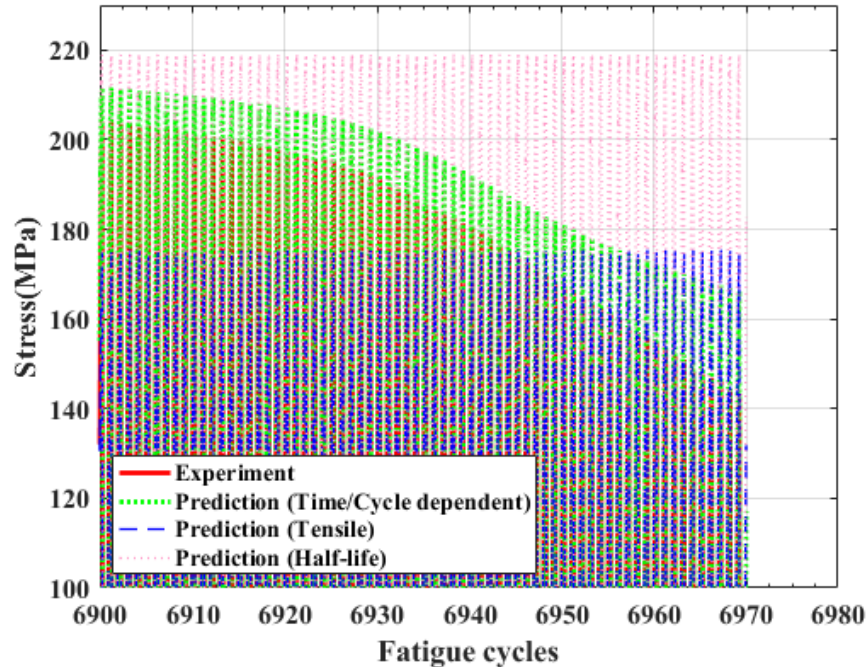


Figure 4. 4 Magnified version of Figure 4.1 showing the ability of evolutionary cyclic plasticity model (time/cycle-dependent prediction) to predict the fast stress drop toward the end of the fatigue life of specimen, representing unstable or rapid crack propagation, under constant-amplitude loading.

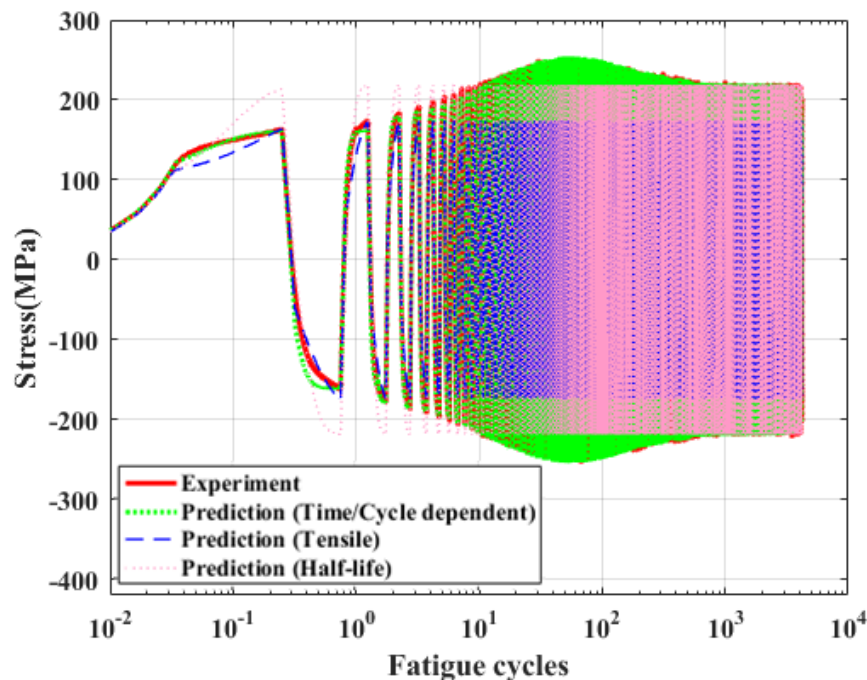


Figure 4. 5 Simulated (analytical) vs experimental axial stress history of ET-F06. Predictions are from simulation using time/cycle-dependent parameters from ET-F06 test and two sets of time-independent parameters (tensile test ET-T04 and half-life cycle of ET-F06).

4.1.2 Variable-Amplitude Fatigue Test

Time-based analytical modeling of the variable-amplitude fatigue test (ET-F38) was done with time/block-dependent material properties estimated from this test. The ET-F38 test was also analytically modeled using two sets of time-independent or fixed parameters estimated from the tensile test ET-T04 and the half-life block of ET-F38. The experimental and simulated stress is compared in Figure 4.6. Magnified versions of Figure 4.6 are shown in Figures 4.7 to 4.9. These magnified figures represent various stages of material behavior, such as initial hardening, softening and stabilized cycles, and rapid crack propagation and failure, respectively, during the specimen's fatigue life. As seen in the case of constant-amplitude tests (discussed in Section 4.1.1), the evolutionary cycle plasticity model based on time/cycle-dependent material parameters can accurately predict all the stages of material fatigue behavior under variable-amplitude fatigue loading. The experimental and simulated hysteresis stress-strain plots of 12 cycles within the 1st block are shown in Figure 4.10 to demonstrate the importance of the time/block-dependent material parameters. As discussed earlier, the time/block-dependent parameters are amplitude independent and will be used as generic/baseline parameters for predicting the stress-strain state of material subjected to an arbitrary loading profile such as random loading; example results will be discussed in the later part of Section 4.

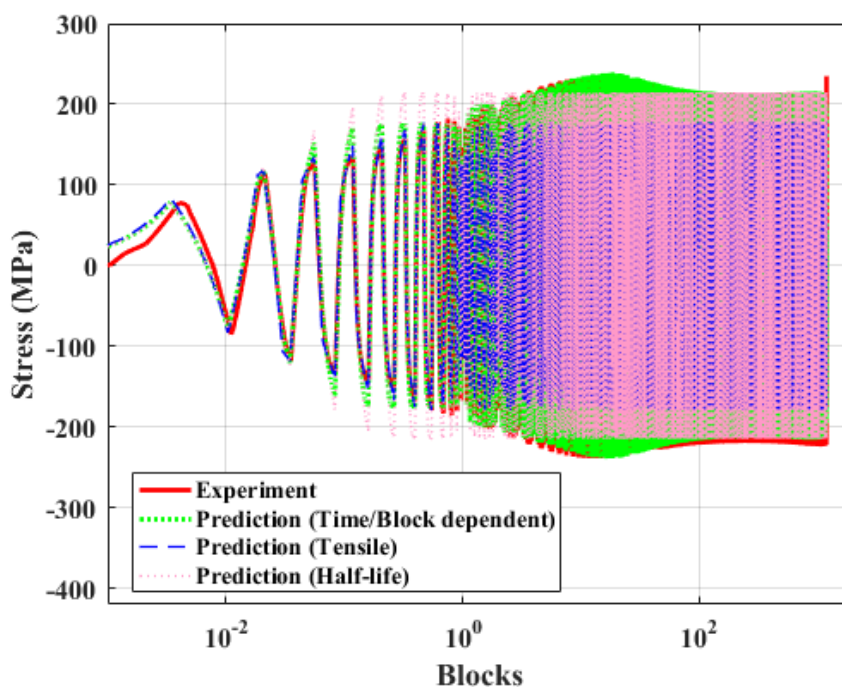


Figure 4. 6 Simulated (analytical) vs experimental axial stress history of ET-F38. Predictions are from simulation using time/block-dependent parameters (ET-F38) and two sets of time-independent parameters (tensile test ET-T04 and half-life block of ET-F38).

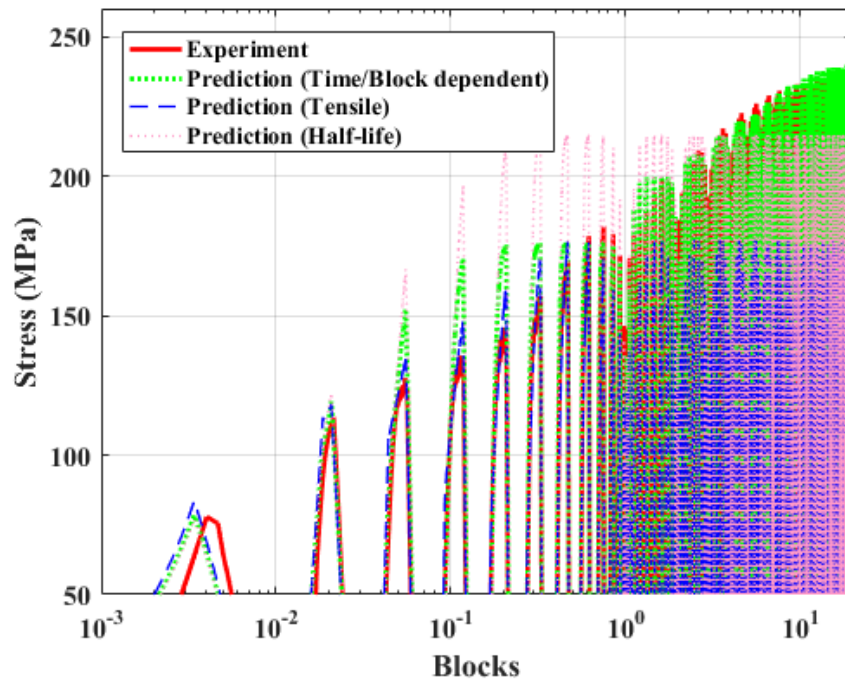


Figure 4.7 Magnified version of Figure 4.6 showing the ability of evolutionary cyclic plasticity model (time/block-dependent prediction) to predict initial hardening behavior of 316 SS under variable-amplitude loading.

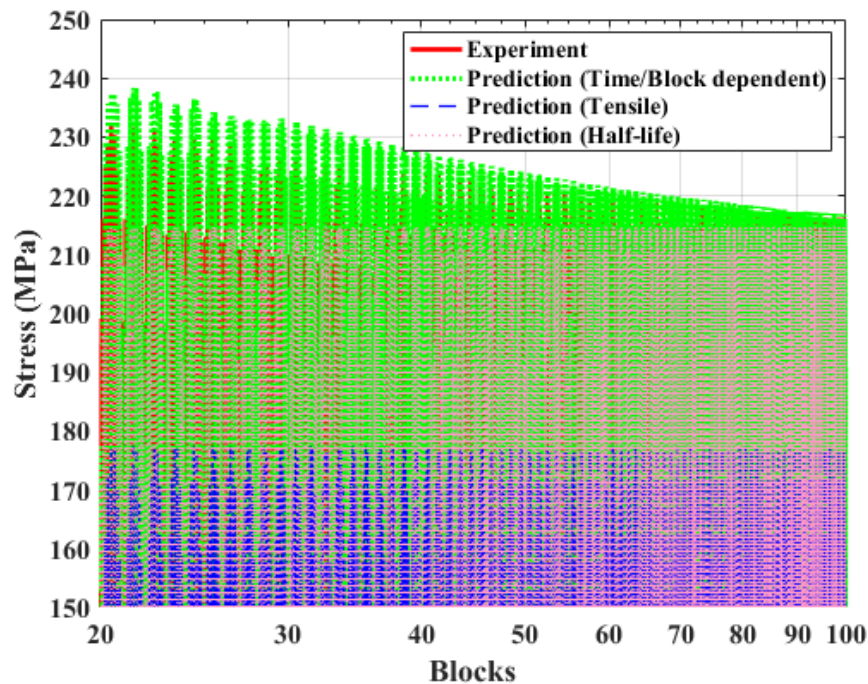


Figure 4.8 Magnified version of Figure 4.6 showing the ability of evolutionary cyclic plasticity model (time/ block -dependent prediction) to predict softening behavior of 316 SS under variable-amplitude loading.

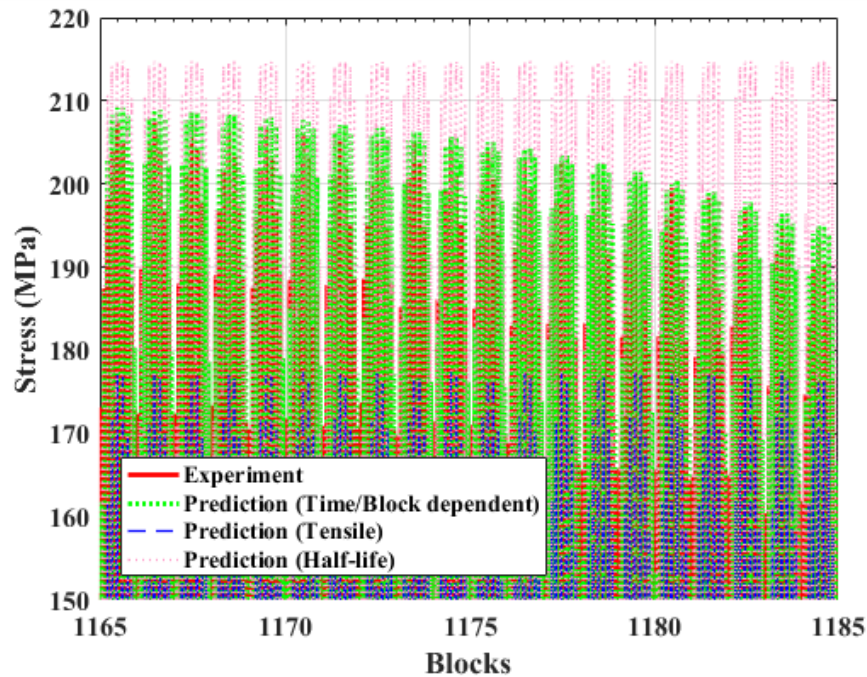


Figure 4. 9 Magnified version of Figure 4.6 showing the ability of evolutionary cyclic plasticity model (time/ block -dependent prediction) to predict the fast stress drop toward the end of the fatigue life of specimen, representing unstable or rapid crack propagation, under variable-amplitude loading.

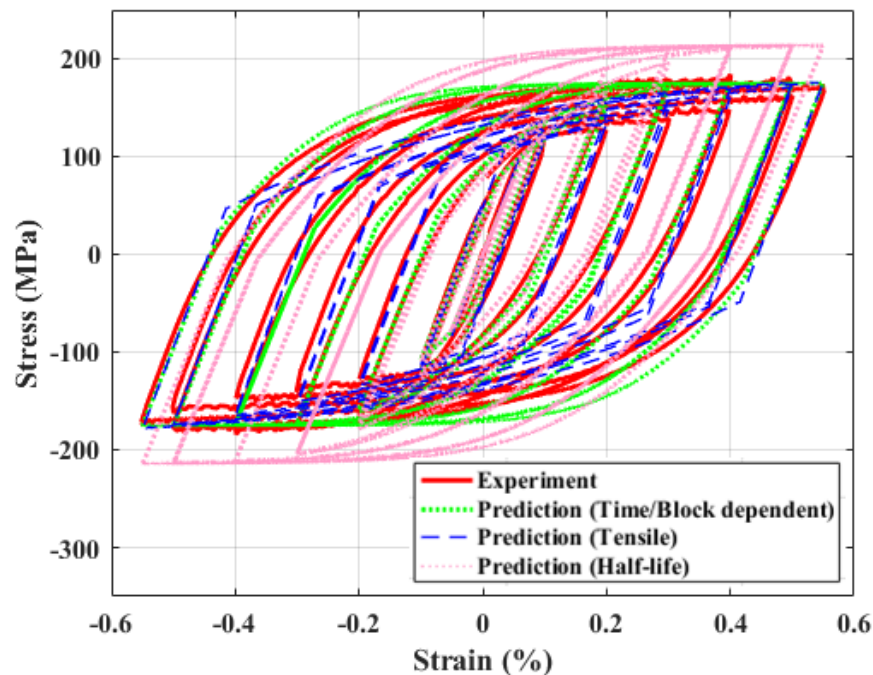


Figure 4. 10 Simulated (analytical) vs experimental hysteresis curves of 1st block (with 12 variable-amplitude cycles) of ET-F38. Predictions are from simulation using time/block-dependent parameters and two sets of time-independent parameters (tensile test ET-T04 and half-life block of ET-F38).

4.2 Results from Accumulated Plastic Strain Energy (APSE)-Based Analytical Models

4.2.1 Constant-Amplitude Fatigue Test

Constant-amplitude fatigue tests (ET-F41 and ET-F06) were analytically modeled with the evolutionary cyclic plasticity model and APSE-dependent material parameters. The predicted stress profile from the simulation was compared with the experimentally observed stress profiles from both ET-F41 and ET-F06. The comparison plots are shown in Figures 4.11 and 4.12 for ET-F41 and ET-F06, respectively. Note that the amplitude condition was the same for both tests, and thus, the predicted (not the experimental/observed) stress profiles in Figures 4.11 and 4.12 are the same. As seen in the figures, the simulated stress profile exhibits all the characteristic behavior (initial hardening followed by softening and stabilized cycles and rapid crack propagation toward the end of fatigue life) of 316 SS under fatigue load. However, the APSE-based prediction is not as close to the experimental data as the time-based prediction. For example, the maximum hardening stress occurs at the 53rd cycle for ET-F06 and ET-F41, while it occurs at the 75th cycle in the simulated results. However, the predicted fatigue life from the simulation was found to be 5860 cycles, which is between experimentally observed fatigue lives for the two experiments (6914 cycles for ET-F41 and 4202 cycles for ET-F06). Section 4.3 provides a comparison between the time- and APSE-based analytical modeling predictions.

For the time-based modeling, the material parameters were estimated from the same test, and therefore, the prediction was very close to the experimental data. By contrast, the material parameters used for APSE-based modeling were estimated from a different test (variable-amplitude test ET-F38), and thus, prediction was not as accurate as for the time-based model. However, considering the variation in experimentally observed fatigue lives between the two constant-amplitude tests with the same conditions, the APSE-based prediction is not bad at all. Moreover, APSE-based modeling provides the robustness of predicting material behavior under any type of amplitude loading, including random. As mentioned earlier, there is a limitation and difficulties in selecting time/cycle/block-dependent parameters for a test case from the parameters estimated from a different fatigue test with different time scale.

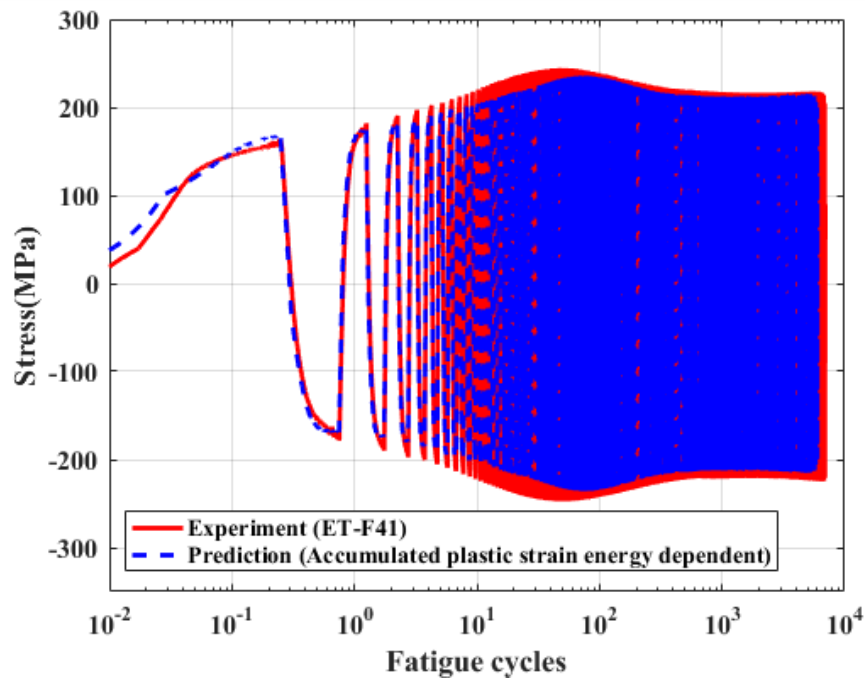


Figure 4. 11 Simulated (analytical) vs experimental axial stress history of ET-F41. Prediction is from simulation using APSE-dependent material parameters estimated from variable-amplitude test (ET-F38).

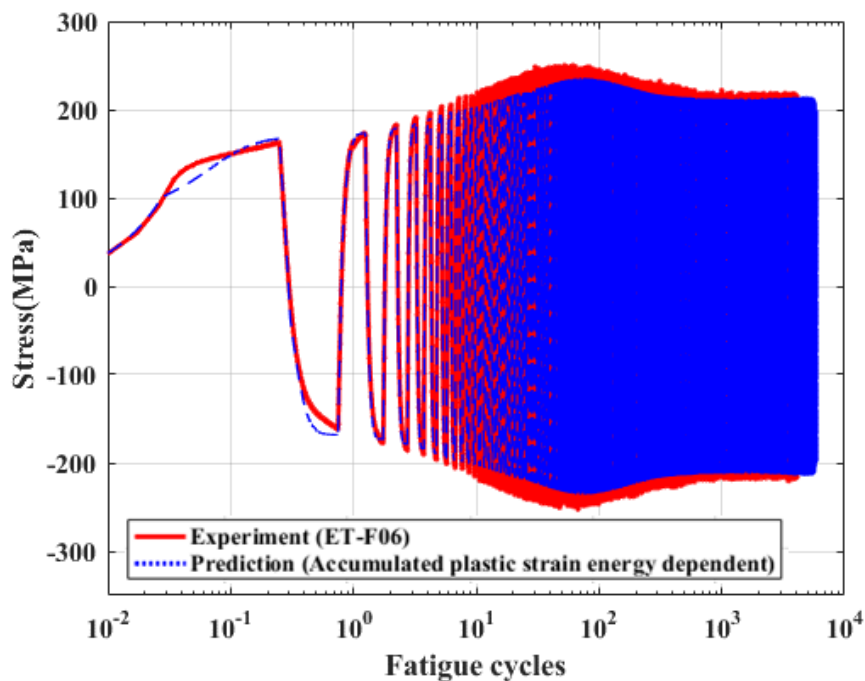


Figure 4. 12 Simulated (analytical) vs. experimental axial stress history of ET-F06. Prediction is from simulation using APSE-dependent material parameters estimated from variable-amplitude test (ET-F38).

4.2.2 Variable-Amplitude Fatigue Test

Figure 4.13 compares the experimental stress history observed from the variable-amplitude test ET-F38 and the analytically simulated stress using the evolutionary cyclic plasticity model and the APSE-dependent material parameters. As seen from the figure, APSE-based analytical modeling can predict the behavior of 316 SS under variable-amplitude loading with good accuracy. The comparison between experimentally observed and predicted life is discussed in Section 4.3.

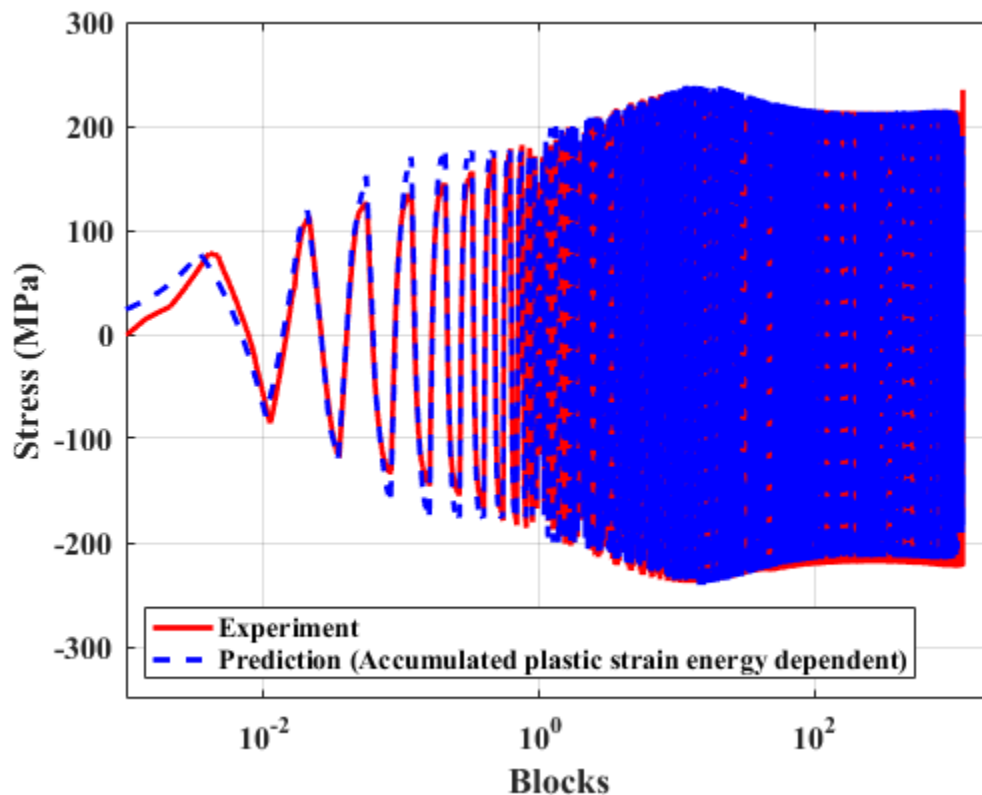


Figure 4.13 Simulated (analytical) vs. experimental axial stress history of ET-F38. Prediction is from simulation using APSE-dependent material parameters estimated from variable-amplitude test (ET-F38).

4.2.3 Random-Amplitude Fatigue Test

The random-amplitude fatigue test ET-F40 was analytically modeled using the evolutionary cyclic plasticity model and the APSE-dependent material properties estimated from variable-amplitude fatigue test ET-F38. The predicted and experimentally observed stress history is compared in Figure 4.14. Also plotted are results from analytical modeling using fixed material parameters estimated from tensile test ET-T04. The figure shows that the APSE-based evolutionary cyclic plasticity model can accurately predict

the stress profile of the material under random-amplitude loading, but that the Chaboche model based on fixed material properties cannot predict the overall hardening and softening behavior. A magnified version of Figure 4.14 is shown in Figure 4.15. The experimental and predicted stresses shown in this figure correspond to the strain input shown in Figure 3.24 (see Section 3.4). The corresponding stress-strain hysteresis plots are shown in Figure 4.16. Figures 4.15 and 4.16 depict the complexity in the stress-strain variation during random loading and the great accuracy of the APSE-based modeling in predicting material behavior under this loading. The comparison between the experimentally observed and predicted life is discussed in Section 4.3.

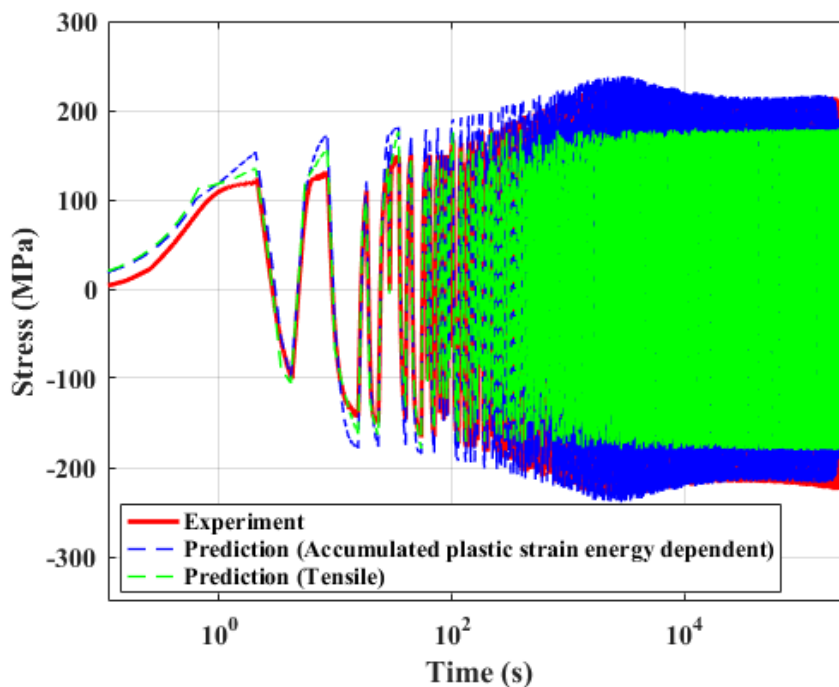


Figure 4.14 Simulated (analytical) vs. experimental axial stress history of ET-F40. Predictions are from simulation using APSE-dependent material parameters estimated from variable-amplitude test (ET-F38) and fixed parameters estimated from tensile test (ET-T04).

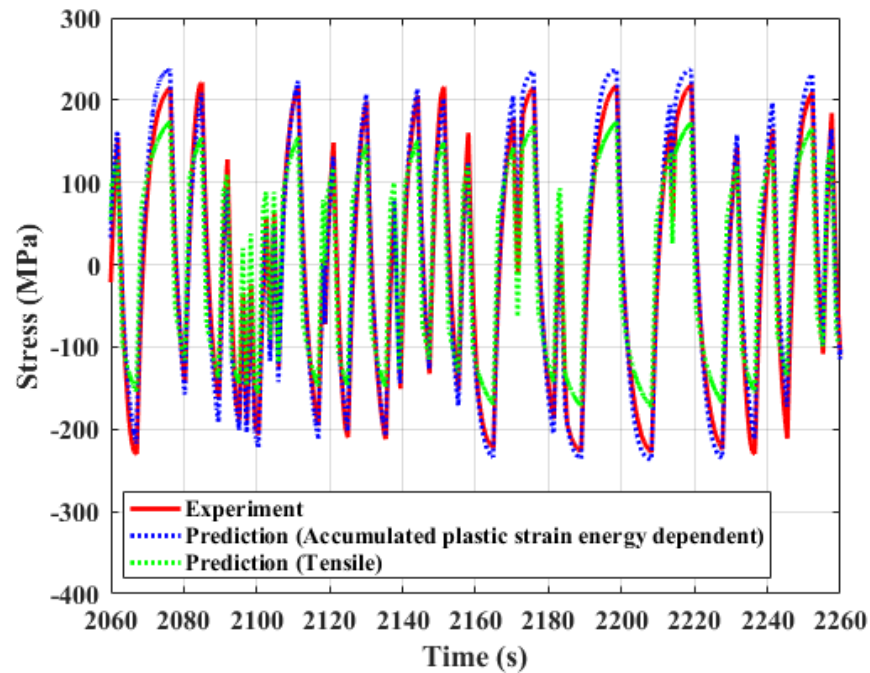


Figure 4.15 Magnified version of Figure 4.14. Experimental and predicted stress corresponds to applied strain shown in Figure 3.24.

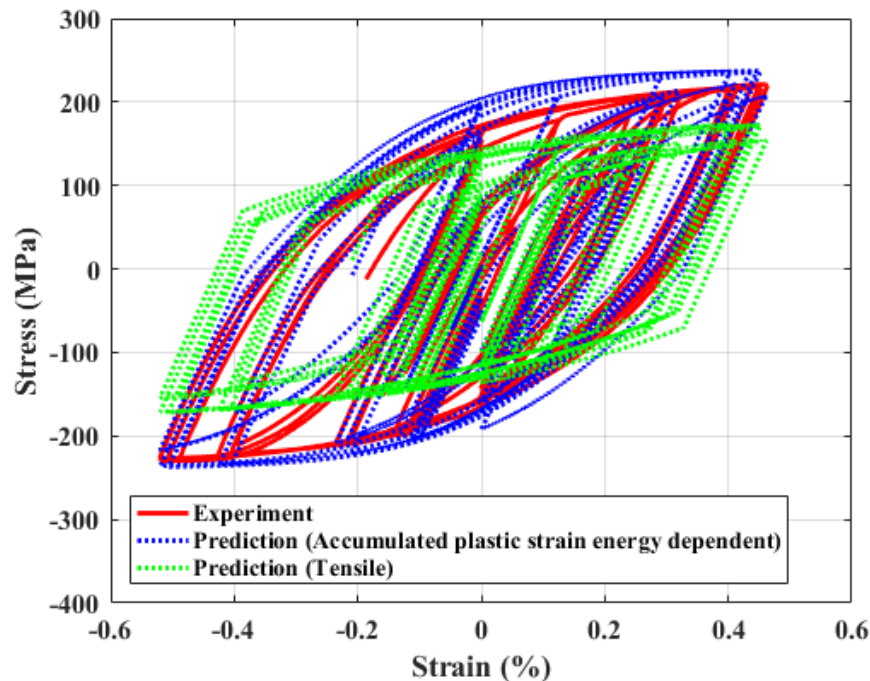


Figure 4.16 Simulated (analytical) vs. experimental hysteresis plot of stress shown in Figure 4.15 and strain shown in Figure 3.24.

4.3 Summary of Analytical Modeling Results

Results from the analytical modeling are summarized here to provide an overall picture of the predicted results and to compare with the experimental results. Table 4.1 compares the experimentally observed maximum hardening stresses during all the fatigue tests with those predicted through time- and APSE-based analytical modeling. As seen from the table, predicted maximum hardening stress is more than 90% accurate for all the fatigue test cases. However, the time-based prediction is more accurate in general, as the material parameters used for modeling were estimated from the same test.

Table 4. 1 Experimentally observed and predicted (analytical modeling) maximum hardening stress.

Test ID	Amplitude type	Experimental observation	Analytical Modeling			
			Time-based prediction		APSE-based prediction	
		Stress (MPa)	Stress (MPa)	Accuracy (%)	Stress (MPa)	Accuracy (%)
F06	Constant	250.0	254.5	98.2	235.8	95.2 [#]
F41	Constant	245.5	252.2	97.3		
F38	Variable	234.9	238.9	98.3	240.4	97.7
F40	Random	223.5	N/A [*]	N/A [*]	238.3	93.4

[#] An average experimental maximum hardening stress (247.8 MPa) based on observation from ET-F06 and ET-F41 tests is used to calculate the accuracy in predicted maximum hardening stress.

^{*} Time-based modeling is not possible for random-amplitude loading.

To determine the fatigue lives of the specimen, a failure criterion is required. As all the tests were performed uniaxially and under strain control, a drop in uniaxial stress in the direction of applied strain was used for determining a failure criterion for the fatigue tests. Conventionally, a 25% load-drop from the maximum load is used as a failure criterion of fatigue specimens. The experimentally observed maximum stress and failure stress values according to the 25% load drop criterion are given in Table 4.2. The table also provides experimental observations during fatigue testing. As mentioned in Table 4.2, the ET-F06 and ET-F38 specimens broke into two pieces before the stress dropped to 25% load-drop stress. Furthermore, the ET-F06 specimen broke as early as the stress dropped to 199.5 MPa. Thus, a stress drop to 200 MPa was used as failure criterion for all the strain-controlled fatigue tests.

Table 4. 2 Determination of failure criteria for simulation results.

Test ID	Amplitude type	Experimental maximum stress (MPa)	Failure stress (MPa) according to 25% load-drop criteria	Experimental observation	Stress value used as failure criteria
F06	Constant	250	187.5	Stress at breaking point: 199.5 MPa (specimen broke into 2 pieces)	200 MPa
F41	Constant	245.5	184.1	Stress continued to drop below 184.1 MPa without breaking into 2 pieces	
F38	Variable	234.9	176.2	Stress at breaking point: 175.2 MPa (specimen broke into 2 pieces)	
F40	Random	223.5	167.6	Stress continued to drop below 167.6 MPa without breaking into 2 pieces	

The experimental and predicted fatigue lives for all the fatigue tests and analytical modeling cases are provided in Table 4.3. As seen from the table, the Chaboche model based on time-independent or fixed material parameters predicts infinite fatigue life for all cases. The evolutionary cyclic plasticity model predicts the fatigue life of the specimen with an accuracy of more than 90%. The accuracy in predicted life based on time-dependent material parameters is almost 100% for both constant- and variable-amplitude fatigue tests as the material parameters were estimated from same test. Because the time-based approach cannot be used for predicting material behavior under random-amplitude loading, the APSE-based approach was used. The predicted fatigue life for the random-amplitude fatigue test was surprisingly accurate (94.7%).

Table 4. 3 Experimental and predicted (analytical modeling) fatigue lives.

Test ID	Amplitude type	Fatigue life unit	Experiment	Analytical Modeling				
				Fixed properties (tensile/half-life)	Time-based		APSE-based	
			Observed life	Predicted life	Predicted Life	Accuracy (%)	Predicted life	Accuracy (%)
ET-F06	Constant	Cycles	4202	∞	4200	100.0	5860	94.6 [#]
ET-F41	Constant	Cycles	6914	∞	6932	99.7		
ET-F38	Variable	Blocks	1179	∞	1180	99.9	1090	92.5
ET-F40	Random	Time (s)	215900	∞	N/A*	N/A*	204400	94.7

An average experimental life (5558 cycles) based on observation from ET-F06 and ET-F41 tests is used to calculate the accuracy in predicted life.

* Time-based modeling is not possible for random amplitude loading

5 Results from FE Modeling of Strain-controlled Fatigue Tests

One of our major tasks in mechanics-based fatigue modeling is to develop an FE model framework based on the previously discussed evolutionary cyclic plasticity model. The FE model framework can then be used for extrapolating material behavior based on uni-axial tests to a multi-axial domain for stress analysis and fatigue evaluation of realistic reactor components, which are ideally subjected to multi-axial loading. Compared to the conventional FE model, the evolutionary cyclic plasticity FE model would be able to predict the cyclic hardening and softening behavior of a component. It is assumed that, similar to the conventional tensile-test-based FE model, which is extensively used by industry for stress analysis of metallic components subjected to monotonic loading transients, the new FE model would be able to simulate a component subjected to cyclic loading. Also similar to the tensile-test-based FE model, it is assumed that the translation from a uni-axial to multi-axial fatigue-test-based model is isotropic and based on the assumption that the metallic components are homogeneous, with material behavior being similar in all directions. However, before the new FE model can be used for component-level stress analysis, the FE framework must be validated with experimental test cases.

We used a commercially available FE software, ABAQUS, for FE implementation of the proposed evolutionary cyclic plasticity model. The FE implementation technique is discussed in Section 2, and results from time- and APSE-based FE simulations are presented here. A single 3D 8-node brick element representing the gauge section (0.5 in.) was used for FE simulation of the fatigue experiments. A single element was used to reduce the computational time for simulating thousands of fatigue cycles. However, we assume that if the basic modeling technology is available, it would not be difficult to model a real-life component in an age of exascale supercomputing. Nevertheless, the first priority in this work is to validate the proposed evolutionary plasticity FE model by the 3D-FE modeling of the earlier discussed fatigue test specimens. In the new FE model, the cross-section of the 3D brick element (hexahedral: 8-node linear brick element: C3D8) was considered equal to the nominal cross-section of the specimen.

The geometry of the fatigue specimen and the 3D ABAQUS model are shown in Figures 5.1 and 5.2, respectively. Simulations representing strain-controlled fatigue tests with constant, variable, and random amplitudes were performed by applying corresponding deformation in the z-direction, as shown by the arrows in Figure 5.2. An example simulated axial-stress profile at a given instant for a general fatigue test simulation is shown Figure 5.3.

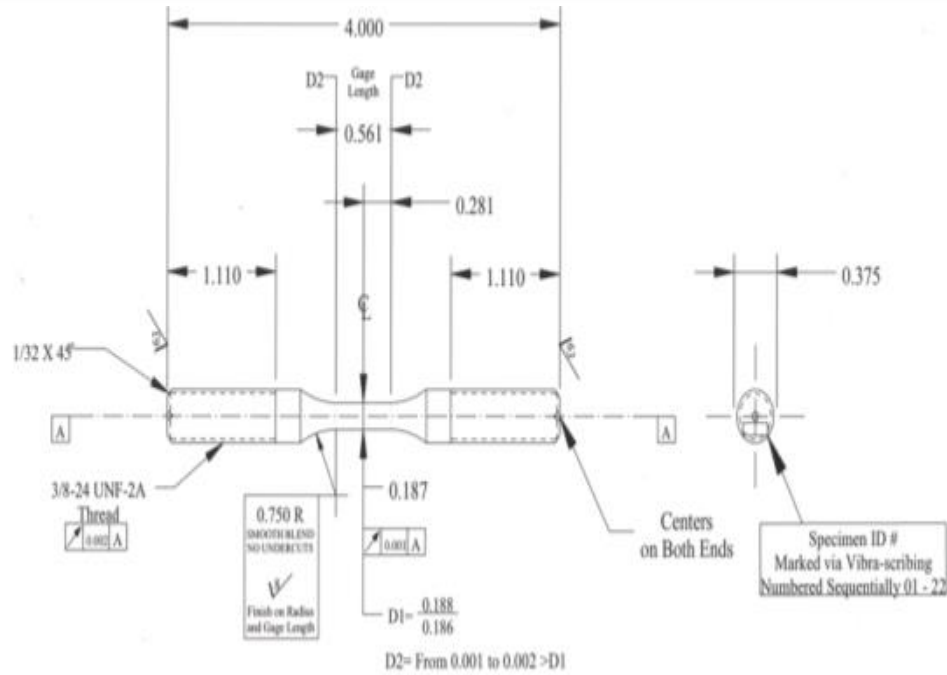


Figure 5. 1 Geometry of fatigue test specimen.

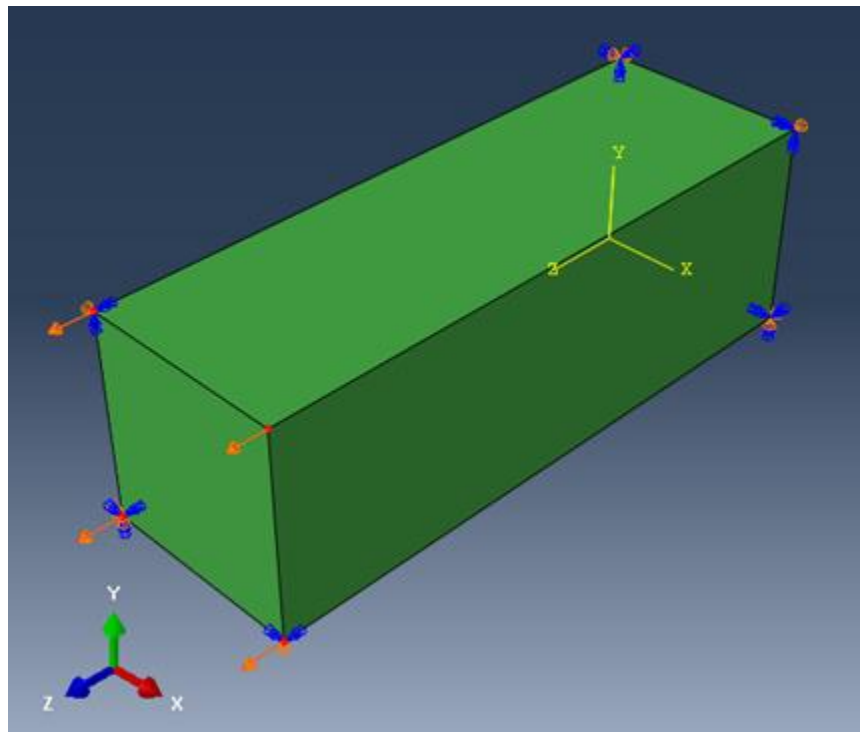


Figure 5.2 Three-dimensional 8-node brick element used for FE simulation of fatigue experiment in ABAQUS.

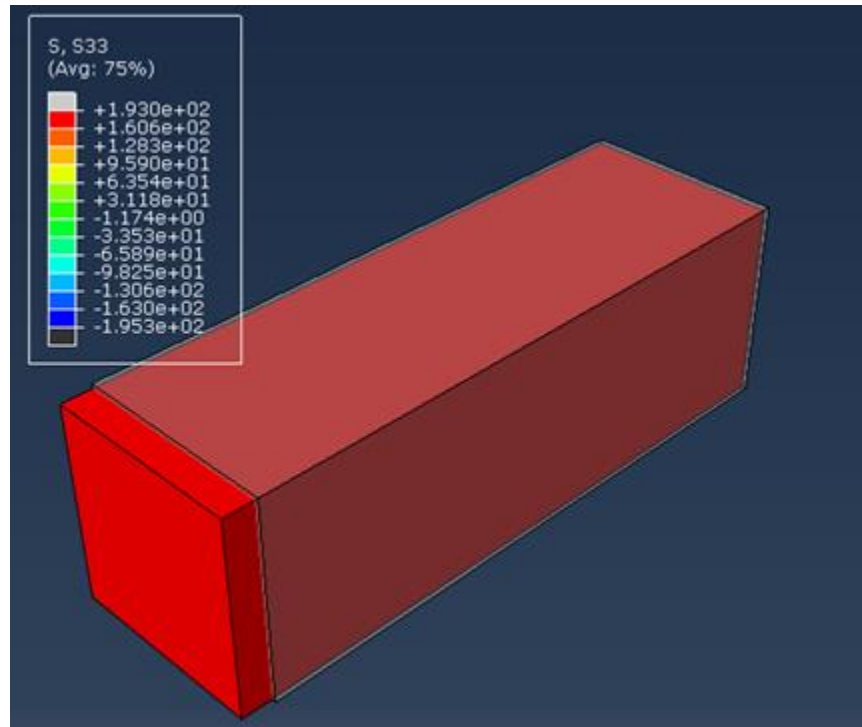


Figure 5.3 An example simulated stress profile at a given instant during fatigue test simulation.

5.1 Results from Time-Based 3D-FE Models

5.1.1 Constant-Amplitude Fatigue Test

We performed three 3D-FE simulations representing the ET-F41 fatigue experiment using time/cycle-dependent and time-independent material properties. Figure 5.4 compares the experimentally observed and simulated stress for the first 100 cycles. The figure shows predicted stress using time/cycle-dependent material parameters estimated from ET-F41 and two sets of time-independent or fixed parameters estimated from tensile test ET-T04 and the half-life cycle of ET-F41. A magnified version of Figure 5.4 is shown in Figure 5.5. It can be seen from the figures that the evolutionary cyclic plasticity model based on time/cycle-dependent material properties can accurately predict the material hardening behavior, while the model based on time-independent material properties estimated from ET-T04 and half-life cycle of ET-F41 could not predict the material hardening behavior. The ABAQUS model was then simulated for the entire life of the fatigue specimen in the FE model framework. The 3D-FE simulated axial stress along with the experimentally observed stress for the entire life of the specimen is shown in Figure 5.6. A magnified version of Figure 5.6, demonstrating initial stress hardening and then softening followed by stabilized cycles, is shown in Figure 5.7. These figures demonstrate that the evolutionary cyclic plasticity model predicts not only the stress hardening but also the stress softening with significant accuracy. The model also predicts the stabilized cycles, which represent a quasi-stable state during fatigue. Most

importantly, as shown in Figure 5.8, it accurately predicts the fast stress drop toward the end of the fatigue life of the specimen, which represents unstable or rapid crack propagation.

Results from the 3D-FE simulation of the constant-amplitude fatigue test ET-F06 are shown in Figure 5.9. As seen in the case of ET-F41, the evolutionary cyclic plasticity FE model using time/cycle-dependent material properties can accurately predict the material behavior during ET-F06.

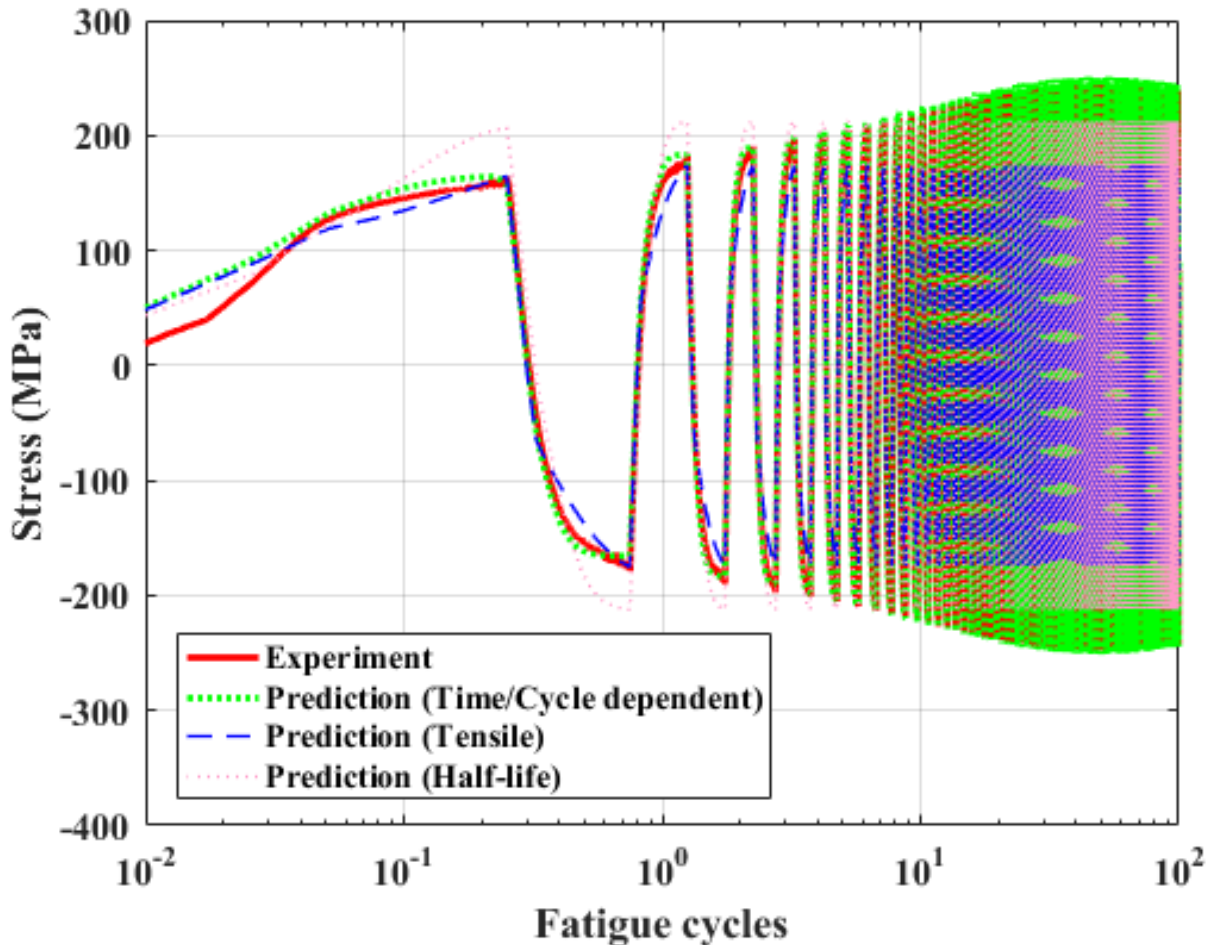


Figure 5.4 3D-FE simulated (evolutionary cycle plasticity model) vs. experimental axial stress of ET-F41 specimen for first 100 cycles. Predictions are from simulation using time/cycle-dependent parameters (ET-F41) and two sets of time-independent parameters (tensile test ET-T04 and half-life cycle of ET-F41).

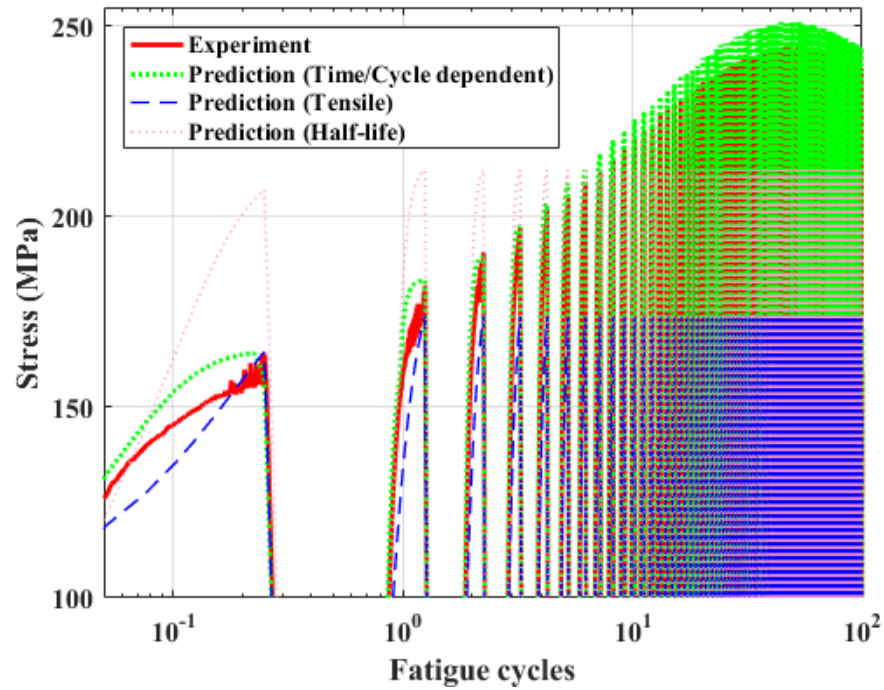


Figure 5.5 Magnified version of Figure 5.4.

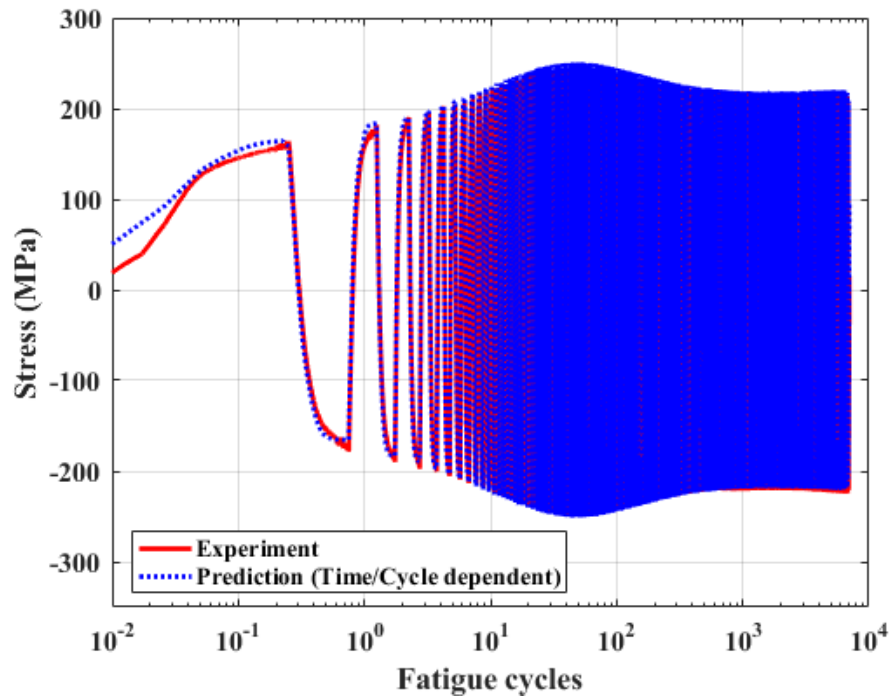


Figure 5.6 3D-FE simulated (evolutionary cycle plasticity model) vs. experimental axial stress of ET-F41 specimen for whole fatigue life.

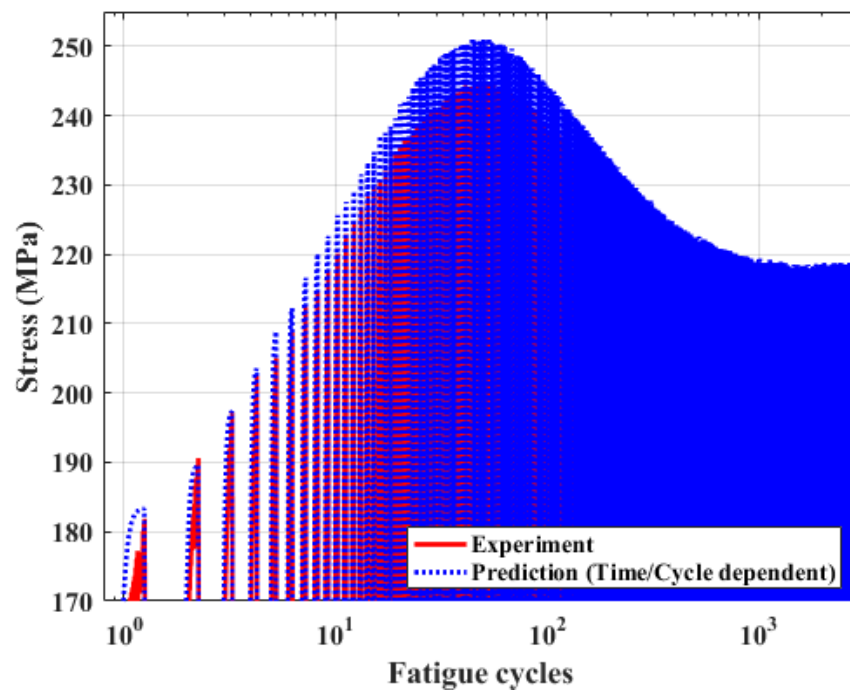


Figure 5.7 Magnified version of Figure 5.6 showing that the 3D-FE results can predict material behavior during initial stress hardening, softening, and stabilized cycles under constant-amplitude loading.

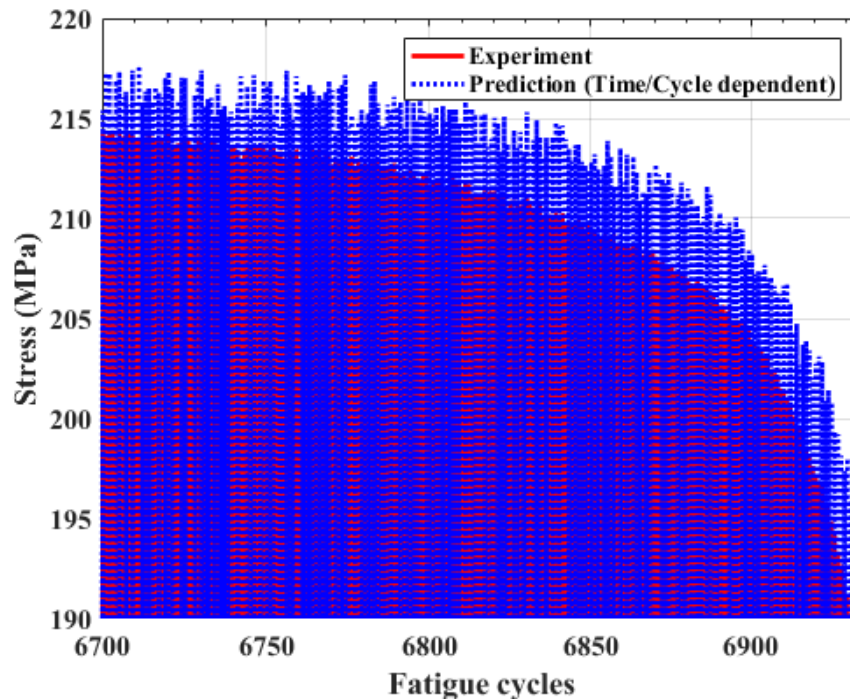


Figure 5.8 Magnified version of Figure 5.6 showing that the 3D-FE results can predict material behavior during rapid crack propagation and failure under constant-amplitude loading.

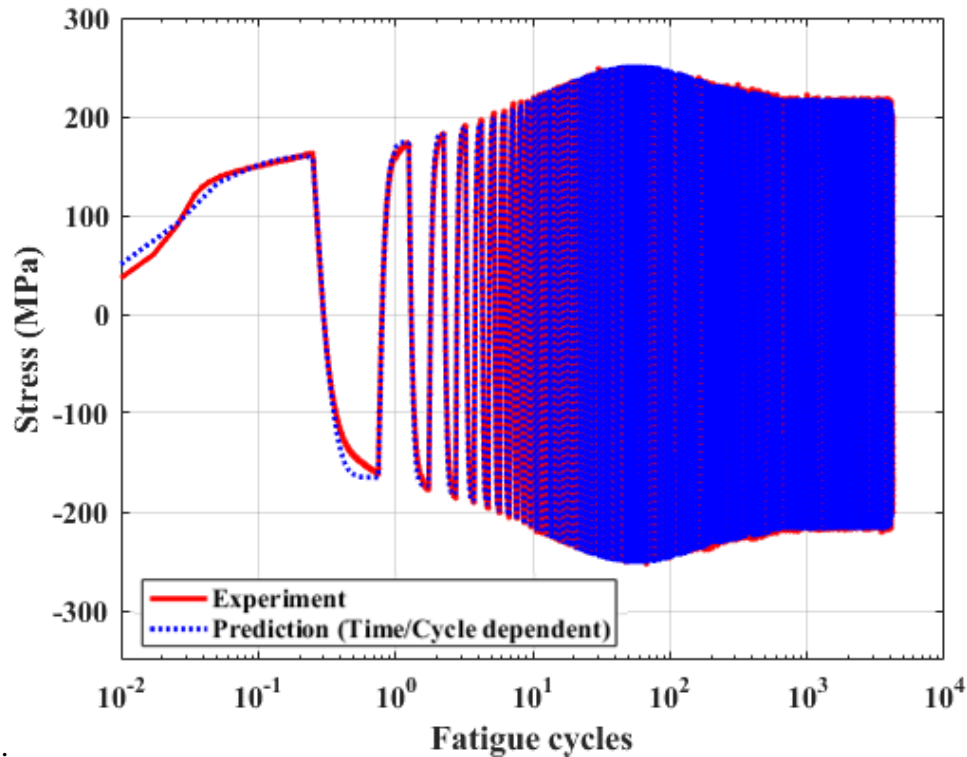


Figure 5.9 3D-FE simulated (evolutionary cycle plasticity model) vs. experimental axial stress of ET-F06 specimen for whole fatigue life.

5.1.2 Variable-Amplitude Fatigue Test

We performed 3D-FE simulations of variable-amplitude fatigue test ET-F38 using time/block-dependent material properties and time-independent material properties. The simulated stress profiles (first 50 blocks) are compared with the experimentally observed stresses in Figure 5.10. As seen in the case of constant-amplitude fatigue tests, the evolutionary cyclic plasticity model can accurately predict the material behavior under variable-amplitude loading using the block-dependent material properties. By contrast, the FE model using time-independent fixed parameters does not predict the material behavior well. The entire fatigue life of the ET-F38 specimen was simulated using the block-dependent material properties. The 3D-FE simulated axial stress along with experimentally observed stress for the entire fatigue life of ET-F38 specimen is shown in Figure 5.11. Different magnified versions of Figure 5.11 are also shown in Figures 5.12 and 5.13.

As seen from Figures 5.12 and 5.13, the 3D-FE simulated stress profile exhibits all the characteristic fatigue life stages (initial hardening, softening, stabilized cycles, and rapid crack propagation followed by failure) and is close to the experimentally observed stresses. The experimental and FE simulated maximum hardening stresses and fatigue lives are compared in Section 5.3.

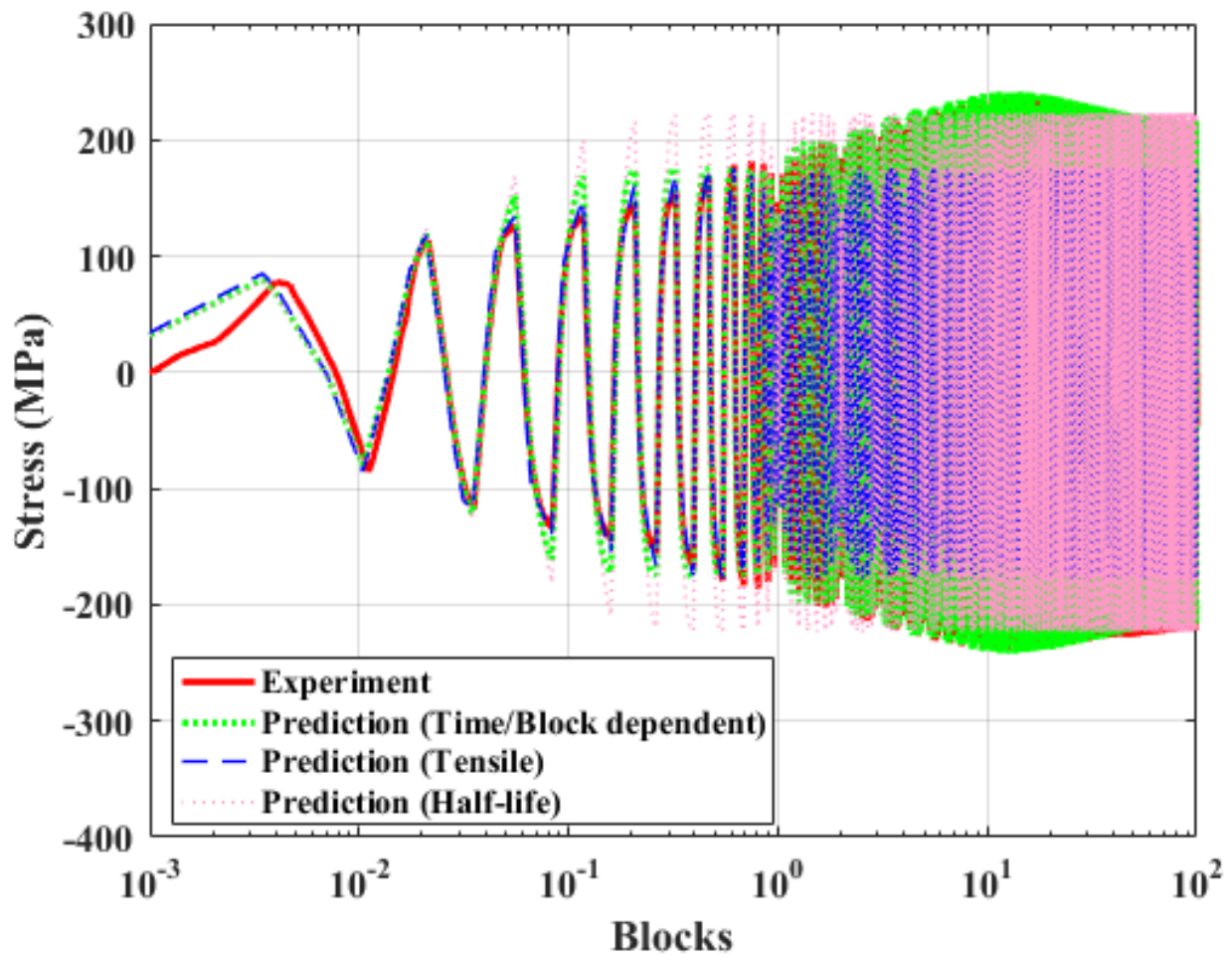


Figure 5.10 3D-FE simulated (evolutionary cycle plasticity model) vs. experimental axial stress of ET-F38 specimen for first 50 blocks. Predictions are from simulation using time/block-dependent parameters (ET-F38) and two sets of time-independent parameters (tensile test ET-T04 and half-life block of ET-F38).

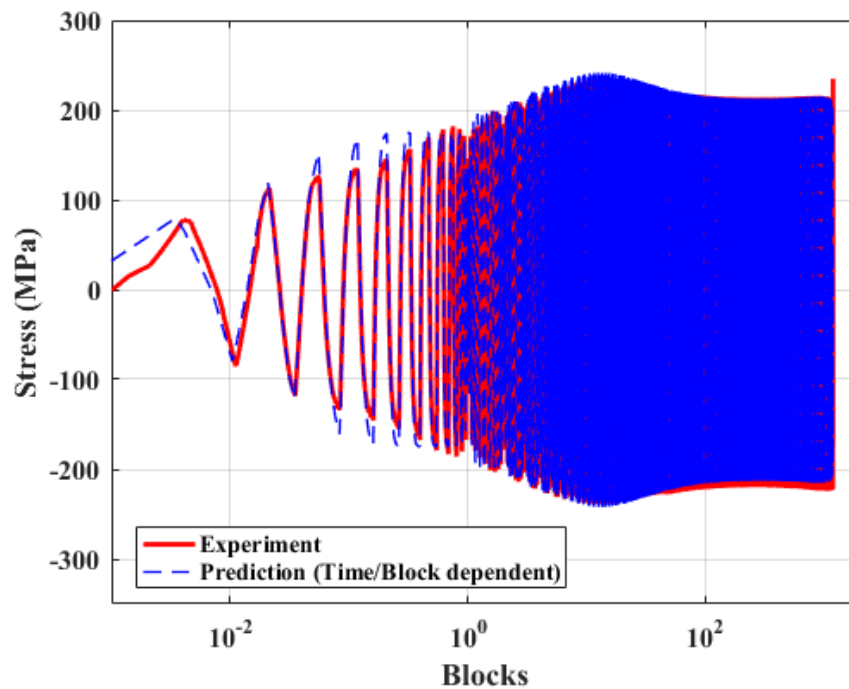


Figure 5.11 3D-FE simulated (evolutionary cycle plasticity model) vs. experimental axial stress history of ET-F38 specimen for whole fatigue life.

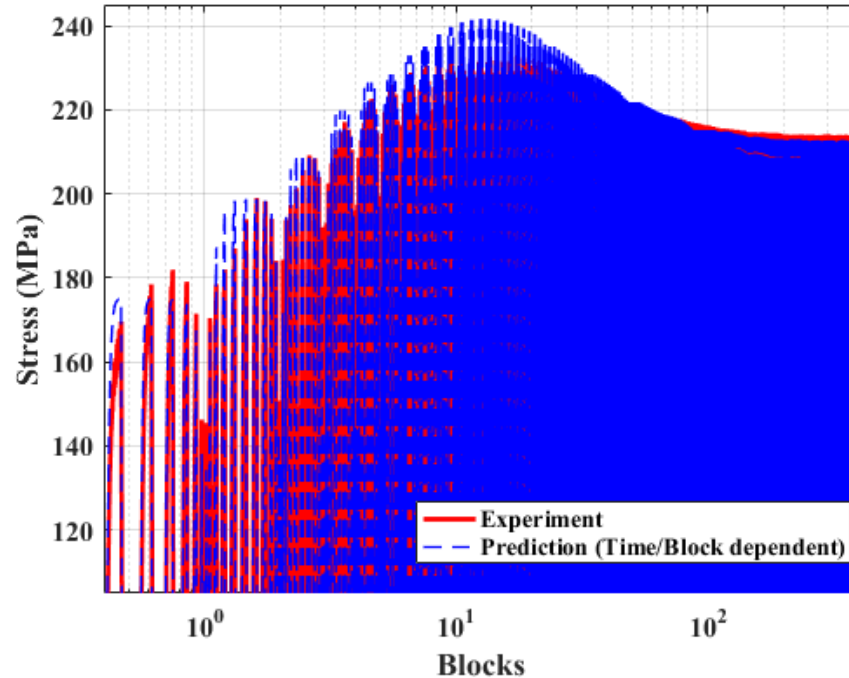


Figure 5.12 Magnified version of Figure 5.11 showing that the 3D-FE results can predict material behavior during initial stress hardening, softening, and stabilized cycles under variable-amplitude loading.

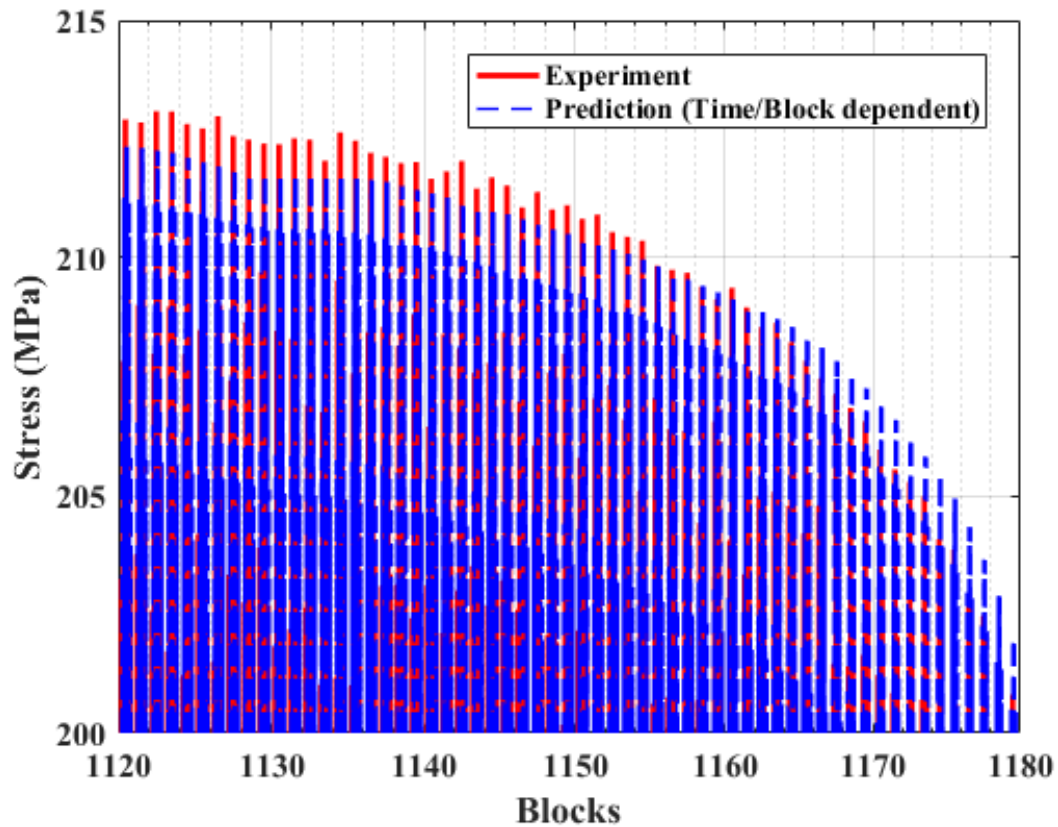


Figure 5.13 Magnified version of Figure 5.11 showing that the 3D-FE results can predict material behavior during rapid crack propagation and failure under variable-amplitude loading.

5.2 Results from APSE-Based 3D-FE Models

5.2.1 Constant-Amplitude Fatigue Test

The constant-amplitude fatigue tests ET-F41 and ET-F06 were 3D-FE modeled by using the ET-F38 material parameters as a function of APSE. The predicted axial stress profile from the 3D-FE simulation was compared with the experimentally observed stress profiles from ET-F41 and ET-F06. Comparison plots are shown in Figures 5.14 and 5.15 for ET-F41 and ET-F06, respectively. Note that the amplitude condition was the same for both tests, and thus the predicted stress profiles shown in Figures 5.14 and 5.15 are the same, but the experimental stress profiles are different. As seen from the figures, the simulated stress profile exhibits all the characteristic behavior (initial hardening followed by softening and stabilized cycles and rapid crack propagation toward the end of fatigue life) of 316 SS under constant-amplitude fatigue load. However, the APSE-based prediction is not as close to the experimental data as the time-based prediction. For example, the maximum hardening stress occurs at the 53rd cycle during experiments (ET-F06 and ET-F41) but at the 69th cycle in the 3D-FE results. In addition, the predicted fatigue life from the simulation was found to be 6151 cycles, which is between the experimentally observed fatigue lives

from the two experiments (6914 cycles for ET-F41 and 4202 cycles for ET-F06). See Section 5.3 for a complete comparison between the time-based and APSE-based 3D-FE predictions.

For the time-based modeling, the material parameters were estimated from the same test, and therefore, the prediction was very close to experimental data. By contrast, the material parameters used for APSE-based modeling were estimated from a different test (variable-amplitude test ET-F38), and thus, the prediction was not as accurate as for time-based modeling. However, considering the variation in experimentally observed fatigue lives between two constant-amplitude tests with the same condition, the APSE-based prediction was not bad at all. Moreover, APSE-based modeling provides the robustness of predicting material behavior under any type of amplitude loading, including random. The APSE-based 3D-FE modeling of random-amplitude test ET-F40 is discussed in Section 5.2.3.

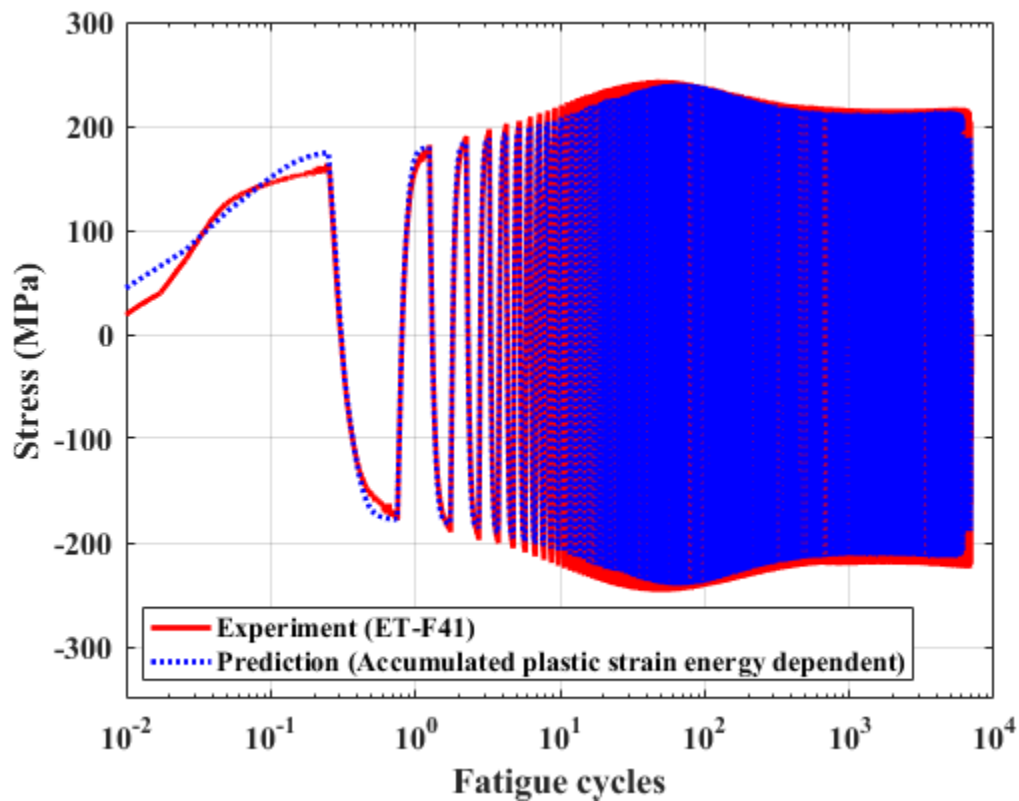


Figure 5.14 3D-FE simulated (evolutionary cycle plasticity model) vs. experimental axial stress history of ET-F41 specimen for whole fatigue life. Prediction is from simulation using APSE-dependent material parameters estimated from variable-amplitude test (ET-F38).

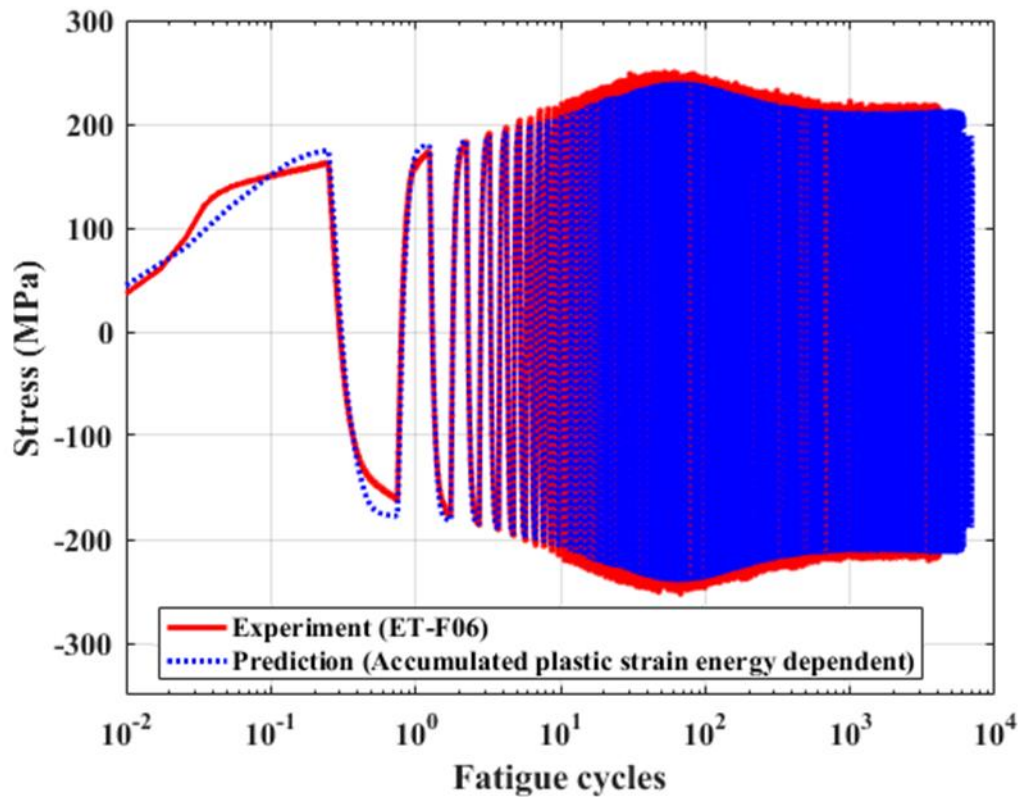


Figure 5.15 3D-FE simulated (evolutionary cycle plasticity model) vs. experimental axial stress history of ET-F06 specimen for whole fatigue life. Prediction is from simulation using APSE-dependent material parameters estimated from variable-amplitude test (ET-F38).

5.2.2 Variable-Amplitude Fatigue Test

Figure 5.16 compares the experimental stress history observed from the variable-amplitude test ET-F38 and the 3D-FE simulated stress using the evolutionary cyclic plasticity model and the APSE-dependent material parameters. As seen from the figure, the simulated stress profile exhibits all the characteristic behavior (initial hardening followed by softening and stabilized cycles and rapid crack propagation toward the end of fatigue life) of 316 SS under variable-amplitude fatigue load. The accuracy of the prediction in terms of maximum hardening stress and fatigue life will be discussed Section 5.3.

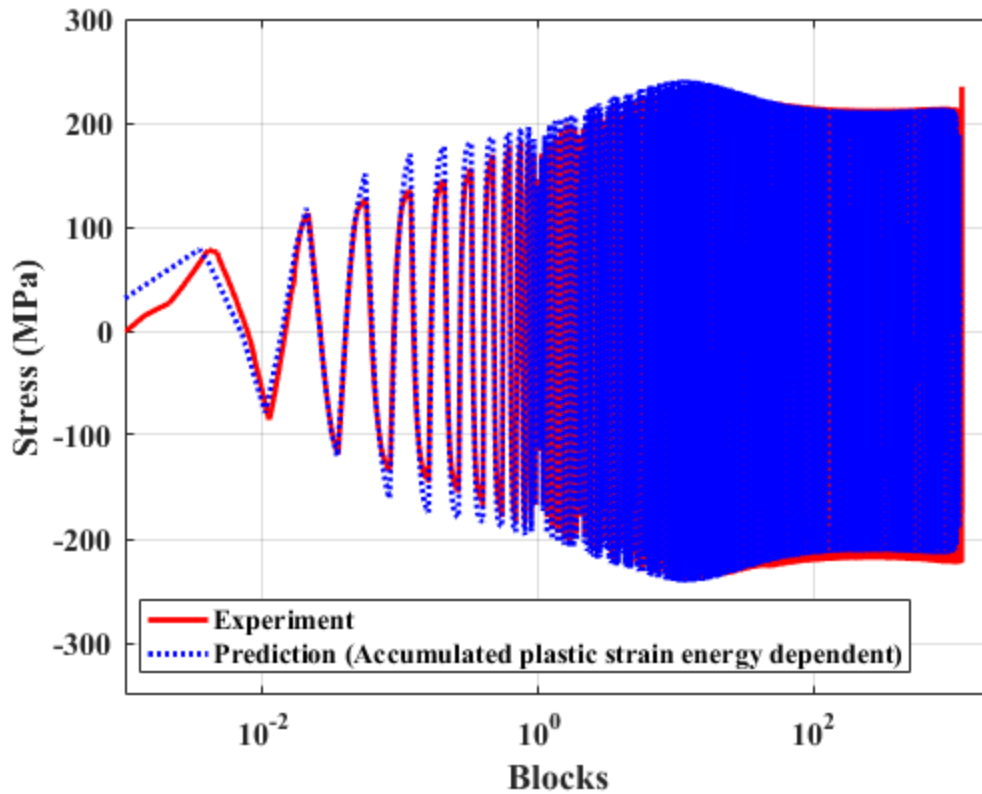


Figure 5.16 3D-FE simulated (evolutionary cycle plasticity model) vs. experimental axial stress history of ET-F38 specimen for whole fatigue life. Prediction is from simulation using APSE-dependent material parameters estimated from variable-amplitude test (ET-F38).

5.2.3 Random-Amplitude Fatigue Test

The random-amplitude fatigue test ET-F40 was 3D-FE modeled with the evolutionary cyclic plasticity model and the APSE-dependent material parameters estimated from variable-amplitude fatigue test ET-F38. The ET-F40 test was also 3D-FE modeled with fixed material parameters estimated from tensile test ET-T04. The 3D-FE simulated axial stress profiles for the 1st block (see Figure 3.22 for block strain input) along with the experimentally observed stress history is shown in Figure 5.17. The figure shows that the APSE-based evolutionary cyclic plasticity model can accurately predict material behavior during initial stress hardening and following stress softening, whereas the model based on fixed material properties cannot. A magnified version of Figure 5.17 is shown in Figure 5.18. The experimental and predicted stresses shown in this figure correspond to the strain input in Figure 3.24 (see Section 3.4). The corresponding stress-strain hysteresis plots are shown in Figure 5.18. Figures 5.18 and 5.19 depict the intricacy in the stress-strain variation during random loading. Despite this variation, the FE model prediction of stress response is reasonably good. For this test case, the FE simulation of the entire test was performed with APSE-dependent material properties only. The 3D-FE simulated axial stress along with

experimentally observed stress for the entire fatigue life of the ET-F40 specimen is shown in Figure 5.20. As seen from this figure, APSE-based 3D-FE modeling can predict the behavior of 316 SS under random-amplitude loading with good accuracy. The experimentally observed and predicted life from 3D-FE simulation is discussed in Section 5.3.

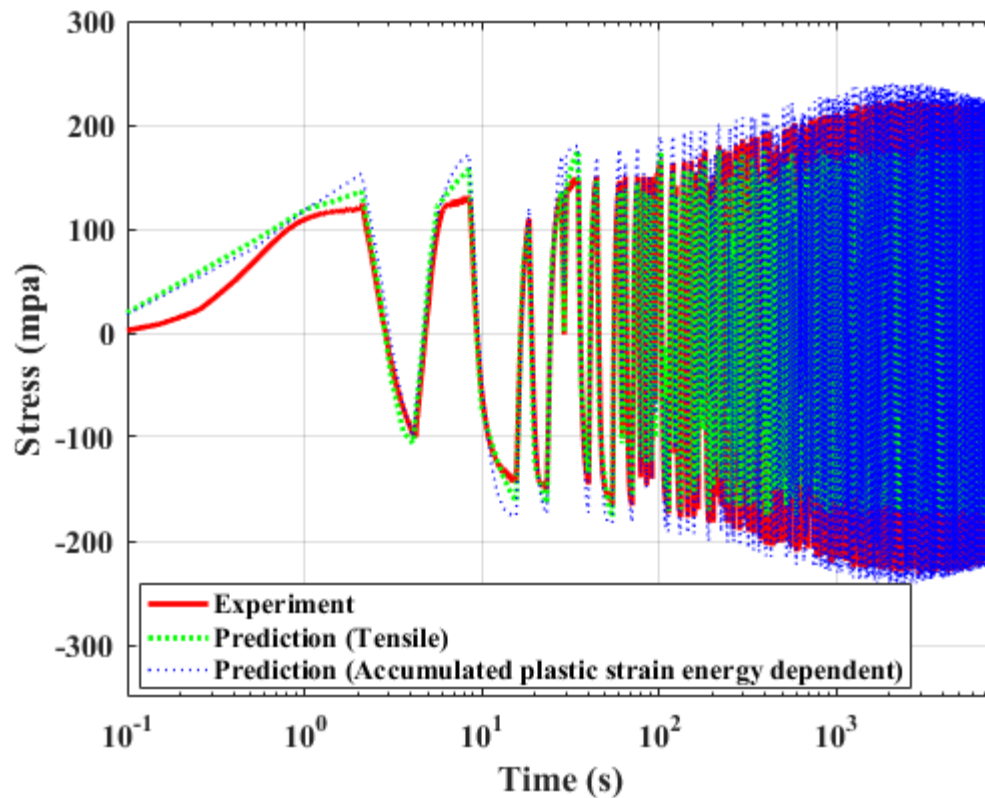


Figure 5.17 3D-FE simulated (evolutionary cycle plasticity model) vs. experimental axial stress of ET-F40 specimen during 1st block (block period = 4251 s) loading. Predictions are from simulation using APSE-dependent material parameters estimated from variable-amplitude test (ET-F38) and fixed parameters estimated from tensile test (ET-T04).

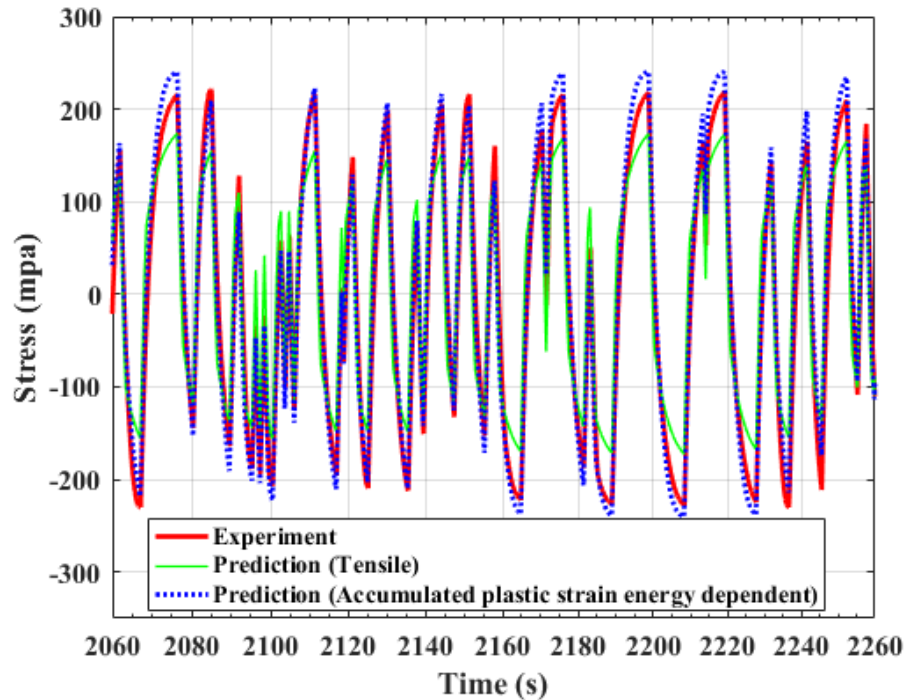


Figure 5.18 Magnified version of Figure 5.17. Experimental and predicted stress correspond to applied strain shown in Figure 3.24.

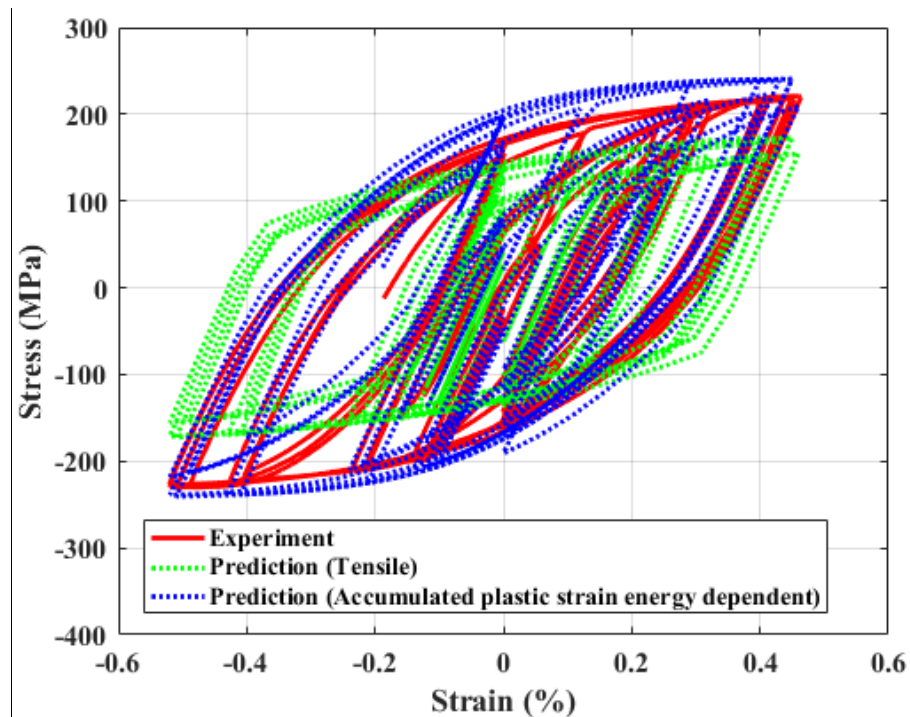


Figure 5.19 3D-FE simulated (evolutionary cycle plasticity model) vs. experimental hysteresis plot of stress shown in Figure 5.18 and strain shown in Figure 3.24.

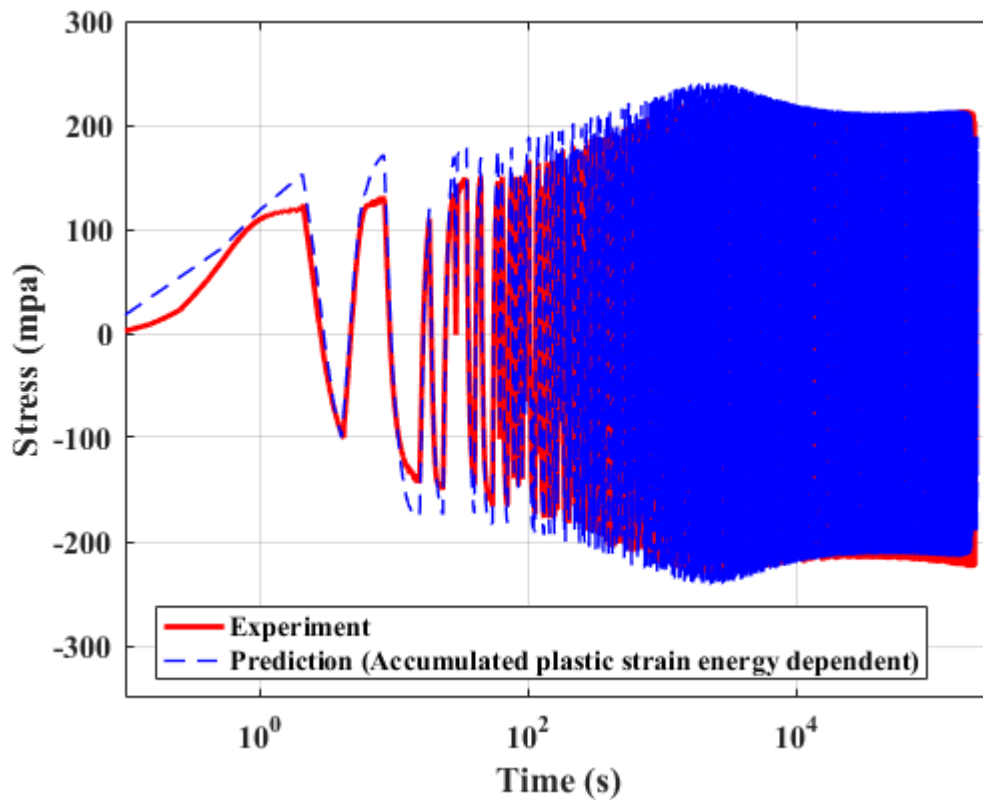


Figure 5.20 3D-FE simulated (evolutionary cycle plasticity model) vs. experimental axial stress history of ET-F40 specimen for whole fatigue life. Prediction is from simulation using APSE-dependent material parameters estimated from variable-amplitude test (ET-F38).

5.3 Summary of FE Modeling Results and Comparison with Analytical Modeling Results

Results from the 3D-FE modeling are summarized here to provide an overall picture of the predicted results and to compare them with the experimental results and analytical modeling results. Table 5.1 compares the experimentally observed maximum hardening stresses during all the fatigue tests with those predicted through time-based and APSE-based 3D-FE modeling. As seen from the table, the maximum hardening stress predicted through 3D-FE simulation is more than 90% accurate for all the fatigue test cases. However, the time-based prediction is more accurate, in general, as the material parameters used for modeling were estimated from the same test. Similar results were also found from analytical modeling of the fatigue tests (see Table 4.1 in Section 4.3)

Table 5. 1 Experimentally observed and predicted (3D-FE modeling) maximum hardening stress.

Test ID	Amplitude type	Experimental observation	FE Modeling			
			Time-based prediction		APSE-based prediction	
		Stress (MPa)	Stress (MPa)	Accuracy (%)	Stress (MPa)	Accuracy (%)
ET-F06	Constant	250.0	252.6	99.0	240.8	96.3
ET-F41	Constant	245.5	251.2	97.7		
ET-F38	Variable	234.9	241.6	97.1	241.5	97.1
ET-F40	Random	223.5	N/A*	N/A*	240.7	92.3

An average experimental maximum hardening stress (247.8 MPa) based on ET-F06 and ET-F41 tests is used to calculate the accuracy in predicted maximum hardening stress.

* Time-based modeling is not possible for random amplitude loading.

In this work, stress drop to 200 MPa was used as the failure criterion for determining the fatigue lives of the specimens. See Section 4.3 for a discussion of the failure criterion. The experimental and predicted lives for all fatigue tests and the 3D-FE modeling cases are given in Table 5.2. As seen from the table, the 3D-FE simulation based on evolutionary cyclic plasticity model predicts the fatigue life of the specimen with an accuracy more than 89%. By contrast, the 3D-FE model based on time-independent or fixed material parameters predicts infinite fatigue life for all cases. The accuracy in predicted life from time-based 3D-FE simulation (i.e., using time-dependent material properties) is almost 100% for both constant- and variable-amplitude fatigue tests as the material parameters were estimated from the same test. Similar results were also found from time-based analytical modeling results (see Table 4.3 in Section 4.3). Table 5.3 compares the fatigue lives predicted through APSE-based analytical and 3D-FE modeling for all the different-amplitude fatigue cases. Fatigue lives determined from experimental data are also provided in the table. As seen from the table, the FE modeling results are very close to the analytical modeling results. Note that the analytical models are mathematical models that have a closed-form solution, while the FE method uses a numerical technique to obtain an approximate solution through discretization. However, despite the approximate solution method the FE modeling predicts fatigue lives of the specimen with excellent accuracy. Moreover, FE modeling is required to perform component- or system-level modeling, while analytical modeling can only be done for laboratory specimens.

Table 5. 2 Comparison between experimental and predicted (3D-FE modeling) fatigue lives.

Test ID	Amplitude type	Fatigue life unit	Experiment	FE Modeling				
				Fixed properties (tensile/half-life)	Time-based		APSE-based	
			Observed life	Predicted life	Predicted Life	Accuracy (%)	Predicted Life	Accuracy (%)
ET-F06	Constant	Cycles	4202	∞	4200	100.0	6151	89.3 [#]
ET-F41	Constant	Cycles	6914	∞	6925	99.8		
ET-F38	Variable	Blocks	1179	∞	1180	99.9	1091	92.5
ET-F40	Random	Time (s)	215900	∞	N/A	N/A	204947	94.9

* Time-based modeling is not possible for random amplitude loading. # APSE-based FE simulation was not performed for ET-F38 test.

An average experimental life (5558 cycles) based on observation from ET-F06 and ET-F41 tests is used to calculate the accuracy in predicted life.

Table 5. 3 Comparison of APSE-based predicted fatigue lives between analytical modeling and 3D-FE modeling results.

Fatigue test type (amplitude)	Fatigue life unit	Experimental	Analytical modeling		FE modeling	
		Observed life	Predicted life	Accuracy (%)	Predicted Life	Accuracy (%)
Constant	Cycles	5558*	5860	94.6	6151	89.3
Variable	Blocks	1179	1090	92.5	1091	92.5
Random	Time (s)	215900	204400	94.6	204947	94.9

* An average experimental life (5558 cycles) based on observation from ET-F06 and ET-F41 tests is used.

6 Stress-Controlled Tensile/Fatigue Tests of 316 SS

Under realistic loading conditions, nuclear reactor components are subjected to stress loading rather than strain loading, as in the case of conventional strain-controlled fatigue tests. In the low cycle fatigue regime, the life of reactor components is conventionally estimated by using S~N (strain~life) curves, which are estimated from strain-controlled fatigue test data. Cyclic stress-controlled loading may result in ratcheting of strain-induced failure modes. Ratcheting can be defined as the progressive directional accumulation of permanent strain due to stress cycling [38, 39]. The difference in peak true stress levels during tension and compression can lead to non-closure of the hysteresis loop, which causes the shifting of the loop along the direction of the strain axis [40, 41]. Ratcheting strain is a secondary deformation process that proceeds cycle by cycle. During stress cycling, the cumulative effect of fatigue damage and progressive ratcheting strain accumulation in a particular direction can severely deteriorate the performance of a component by continuous thinning out the cross-sectional area [38]. Ratcheting strain not only depends on the material but also the loading factors, such as stress level, loading history, loading rate, and loading path [40]. Thus, it is important to investigate material behavior under stress-controlled loading. It is also important to investigate how the reactor coolant environment affects the ratcheting behavior of materials, such as 316 SS. In U.S. PWRs, 316 SS and other similar stainless steel grades are primarily used in the construction of hot leg, cold leg, and SL pipes. In this section, we present some preliminary experimental results related to stress-controlled tensile and fatigue testing of 316 SS base metal. The discussed results are based on few test data sets and require many more tests to draw any firm conclusion.

We performed stress-controlled fatigue experiments on 316 SS base metal under air at 300 °C and a PWR water coolant environment at 300 °C. Two loading rates were employed during the fatigue tests to determine the impact of loading rate on material behavior under air and PWR environment conditions. All the tests were conducted with small hourglass specimens. Experiments under air and PWR environment were conducted in separate test setups containing hydraulic-controlled MTS test frames. For the PWR environment fatigue experiments, a specially designed pressurized water loop was used to create the PWR coolant water condition. The pressurized water test loop consists of various subsystems such as feed water supply tank, circulating water pump, pre-heater, autoclave, heat exchanger, hydrogen and other cover gas supply systems, etc. The details of the test setups and environmental control can be found in a previous Argonne report[24]. For the in-air fatigue tests, a precision high-temperature extensometer was used to measure the gauge-area strain. For the PWR environment tests, an extensometer couldn't be used for gauge-area strain measurement due to a water-tight autoclave in the experimental assembly. To determine the strain of the specimens during the PWR environment tests, actuator position measurements from PWR water tests were used along with the position-strain mapping functions generated from the in-air fatigue tests. One stress-controlled tensile test in air at 300 °C was also performed to investigate material behavior under stress-controlled tensile loading. Results from strain-controlled fatigue test ET-F41 (see Section 3) and strain-controlled tensile test ET-T04 [37] are also used. The test conditions along with Test IDs are presented in Table 6.1.

Table 6. 1 Test conditions for 316 SS base metal tensile and fatigue tests.

Test ID	Test Condition
ET-T04	In air, 300 °C, strain control, tensile test [37].
ET-T11	In air, 300 °C, stress control, tensile test.
ET-F41	In air, 300 °C, strain control, constant amplitude = 0.5%, fatigue test [see Section 3].
ET-F43	In air, 300 °C, stress control, one block gradually increasing stress amplitude (106 MPa to 216 MPa) with slow loading rate (0.0432 MPa/s) followed by constant amplitude (216 MPa, equivalent to stress amplitude observed during stabilized cycles of ET-F41 test) with fast loading rate (43.2 MPa/s), fatigue test.
EN-F44	PWR water, 300 °C, stress control, one block gradually increasing stress amplitude (106 MPa to 216 MPa) with slow loading rate (0.0432 MPa/s) followed by constant amplitude (216 MPa, equivalent to stress amplitude observed during stabilized cycles of ET-F41 test) with fast loading rate (43.2 MPa/s), fatigue test.
ET-F45	In air, 300 °C, stress control, one block gradually increasing stress amplitude (106 MPa to 216 MPa) with slow loading rate (0.0432 MPa/s) followed by constant amplitude (216 MPa, equivalent to stress amplitude observed during stabilized cycles of ET-F41 test) with slow loading rate (0.0432 MPa/s), fatigue test.
EN-F46	PWR water, 300 °C, stress control, one block gradually increasing stress amplitude (106 MPa to 216 MPa) with slow loading rate (0.0432 MPa/s) followed by constant amplitude (216 MPa, equivalent to stress amplitude observed during stabilized cycles of ET-F41 test) with fast loading rate (0.0432 MPa/s), fatigue test.

6.1 Tensile Test

Figure 6.1 depicts the engineering stress-strain plot (up to 2% strain) estimated from stress-controlled tensile test ET-T11. The engineering stress-strain plot from strain-controlled test ET-T04 is also shown in Figure 6.1 for comparison. The stress-strain plots indicate no significant difference in material behavior under the different loading conditions. Stress-controlled tensile test data were further analyzed to estimate fixed material parameters and model the fatigue test cases, as discussed in Section 7.

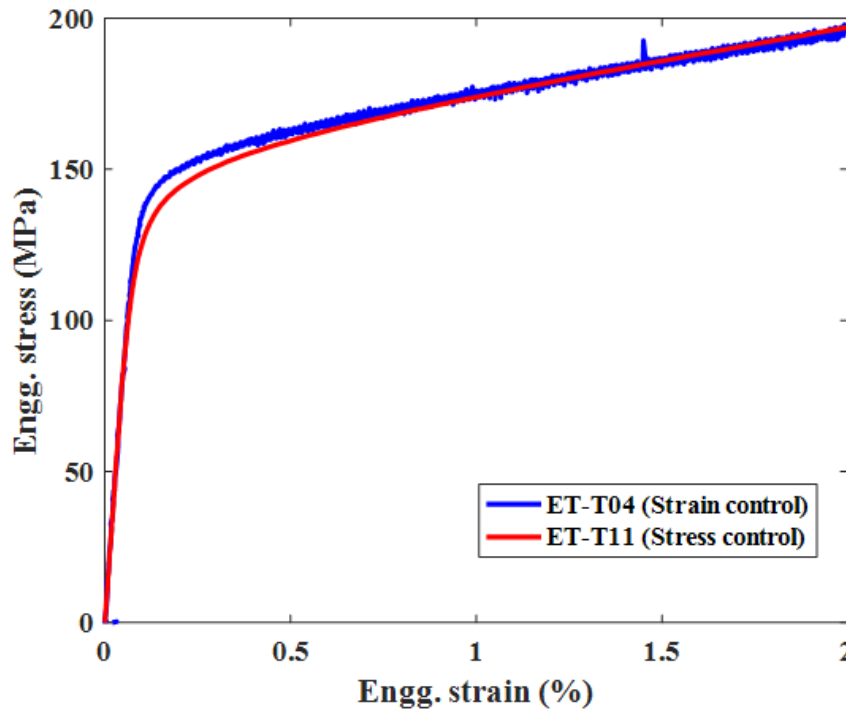


Figure 6. 1 Engineering stress-strain curve estimated from ET-T04 [37] and ET-T11 data.

6.2 Fatigue Test

6.2.1 Test Procedures

Two different stress inputs were used to perform fatigue tests on 316 SS. Figure 6.2 shows the stress input during ET-F43 and EN-F44 tests. As seen in the figure, stress input consists of an initial variable-amplitude block loading comprising 12 fatigue cycles with gradually increased stress amplitude followed by repeated cycles of constant-amplitude loading. A magnified plot of constant-amplitude stress input is shown in Figure 6.3. The stress amplitude for the constant-amplitude loading was equal to the maximum stress amplitude (last cycle) during the variable-amplitude loading. This amplitude was decided based on the stress amplitude during stabilized cycles of strain-controlled fatigue test ET-F41, as shown in Figure 6.4. The stress rate during constant-amplitude loading was 43.2 MPa/s, which was selected such that the time period is the same as that of ET-F41 test. Note that the stress rate during variable-amplitude loading was 0.0432 MPa/s, which is 1000 times lower than the stress rate during constant-amplitude loading. This was done to mimic the initial slow heat-up of the nuclear reactor components during operation. The high stress rate (during constant-amplitude loading) after the initial variable-amplitude loading at low rate was done to complete the test within a reasonable time frame. The initial variable-amplitude block loading with gradually increased stress was applied to ensure that the test material does not deform too much within the first quarter cycle. As shown in Figure 6.1, a 2% deformation is observed after application of 197 MPa stress during tensile test ET-T11.

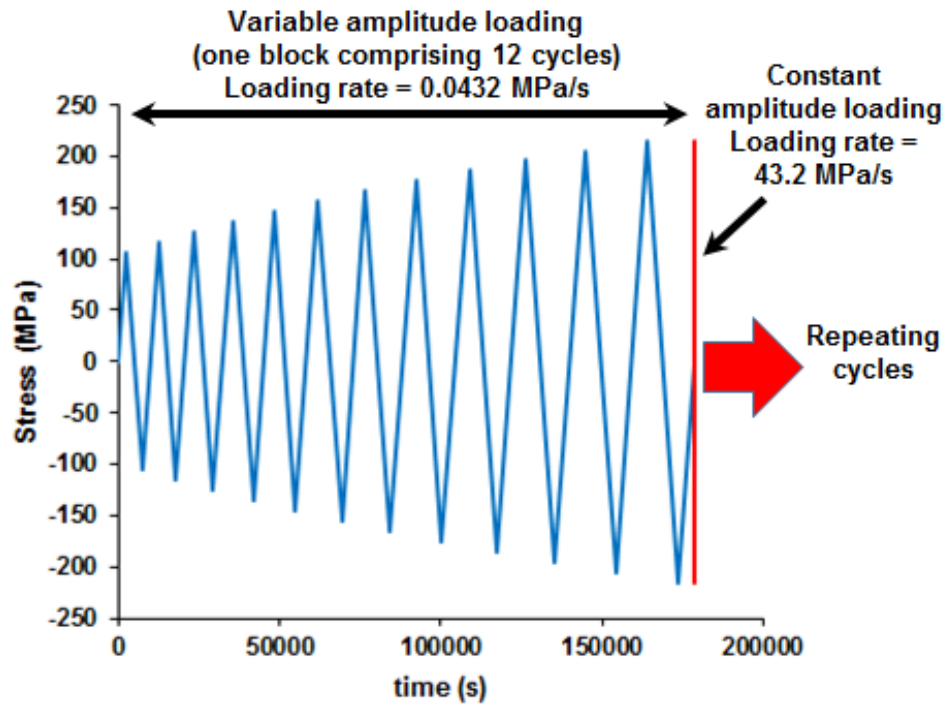


Figure 6. 2 Stress input during ET-F43 and EN-F44.

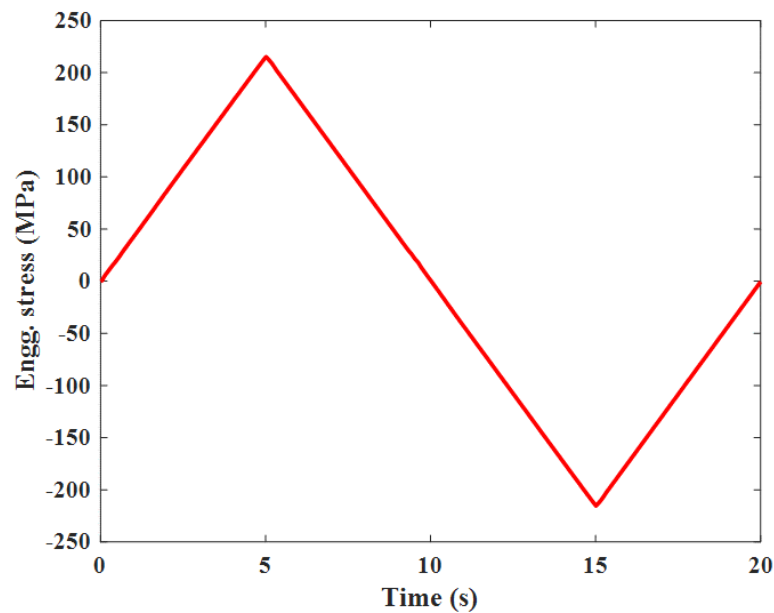


Figure 6. 3 Repeating constant-amplitude stress input at high rate (after low-rate variable-amplitude stress input in first block) during ET-F43 and EN-F44.

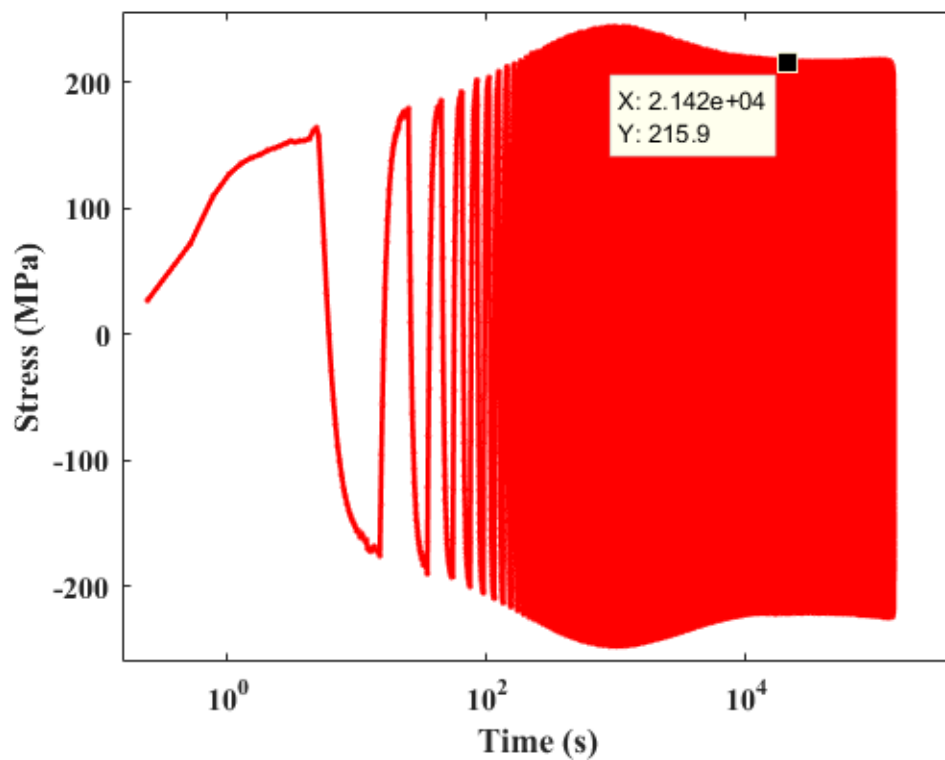


Figure 6. 4 Observed stress during the ET-F41. Data point shows stress amplitude during stabilized cycle.

Another set of stress-controlled tests (ET-F45 and EN-F46) was conducted, where the stress rate was the same for both variable- and constant-amplitude loading. The employed stress rate was 0.0432 MPa/s. The stress input during ET-F45 and EN-F46 tests is shown in Figure 6.5. These low stress rate tests were performed to examine the impact of loading rate on material behavior during constant-amplitude stress loading cycles. The time period was 20000 s during low-rate constant-amplitude loading (ET-F45 and EN-F46), but only 20 s during high-rate constant-amplitude loading (ET-F43 and EN-F44).

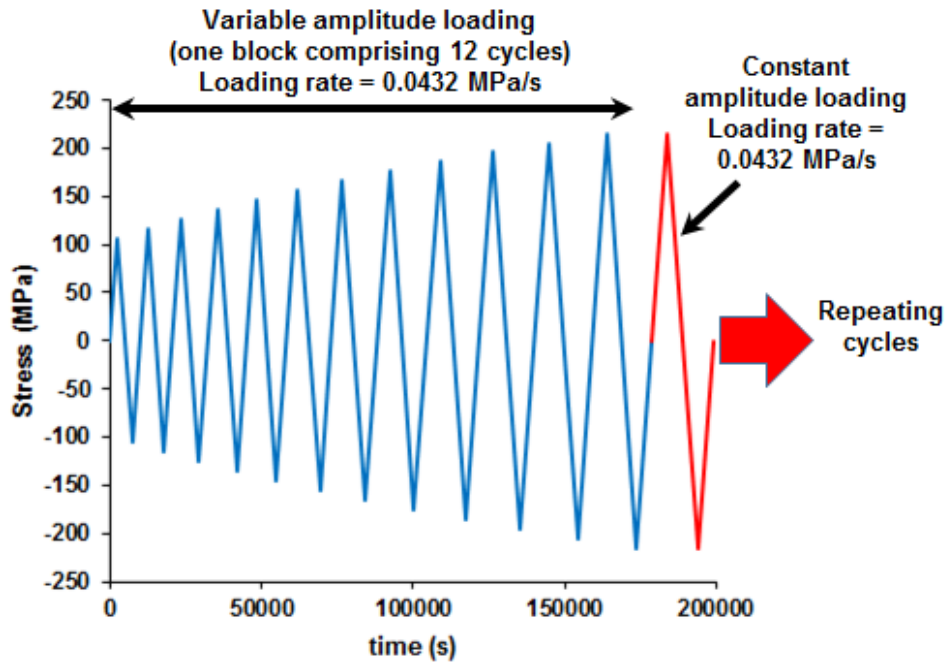


Figure 6. 5 Stress input during ET-F45 and EN-F46.

6.2.2 Experimental Observations

6.2.2.1 In-air Tests

Figure 6.6 shows the observed engineering strain during the entire ET-F43 test. The figure indicates that a significant amount of ratcheting strain occurs during the stress-controlled fatigue experiment with 316 SS. Although no mean stress was applied, the specimen still ratcheted up to 3% in the tensile direction. To determine the driving force behind ratcheting of the specimen, the mean true stresses during variable- and constant-amplitude loading of ET-F43 are plotted in Figures 6.7 and 6.8, respectively. These figures show that the mean true stress during ET-F43 is in the tensile direction, which might have caused the material to ratchet in that direction.

Figure 6.6 suggests that the rate of ratcheting was much higher during the initial phase (variable-amplitude loading) of the experiment. Careful observation also indicates that the observed strain amplitude was much higher during the last cycle of variable-amplitude loading than the first cycle of constant-amplitude loading. Note that the applied stress amplitude is same for both cases. This finding suggests that 316 SS shows rate-dependent behavior, particularly when the rate of loading changes. For example, the strain ratcheting rate was higher when the applied stress rate was lower during initial-variable loading, but when the applied stress rate was changed to a higher rate (during constant-amplitude loading), the observed strain ratcheting rate decreased. The slower strain ratcheting during higher rate constant-amplitude loading could be also due to work hardening associated with the higher rate strain ratcheting

during the initial variable loading. This finding is very important for fatigue modeling of nuclear reactor components, as they are subjected to variable-rate stress-strain reversal, leading to a load-sequence effect on material performance. Also, this test result signifies the importance of stress analysis and fatigue modeling of reactor components based on both stress- and strain-controlled fatigue test data.

The observed actuator position during ET-F43 is shown in Figure 6.9. The actuator position data were used to generate position-strain mapping, which was used to predict the strain from position data during PWR water tests EN-F44 and EN-F46.

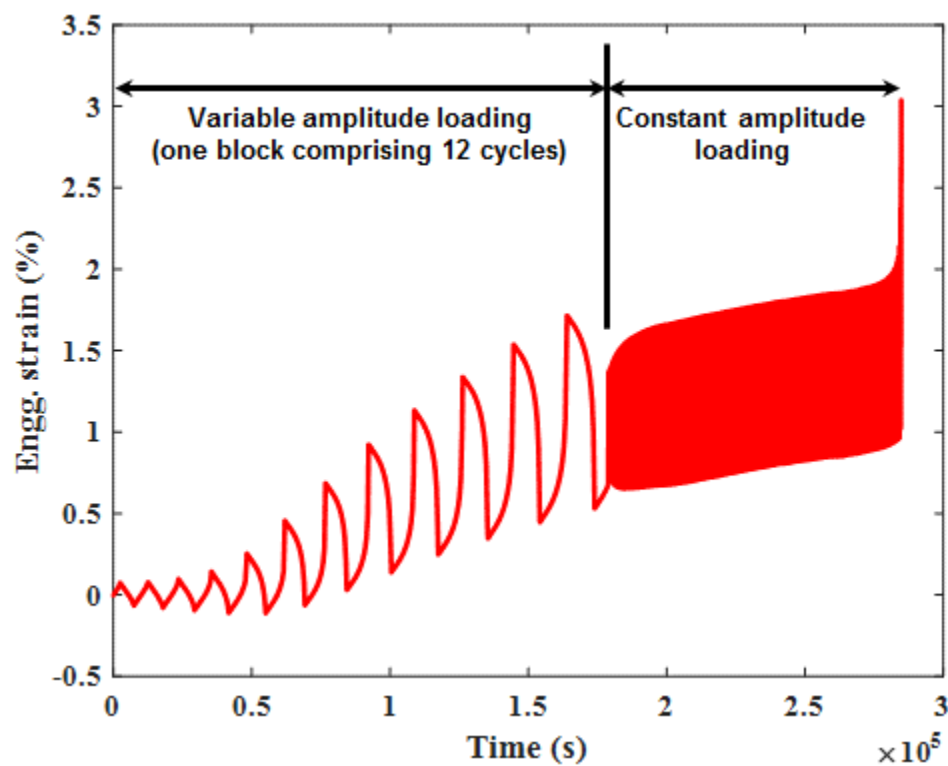


Figure 6. 6 Observed strain during ET-F43.

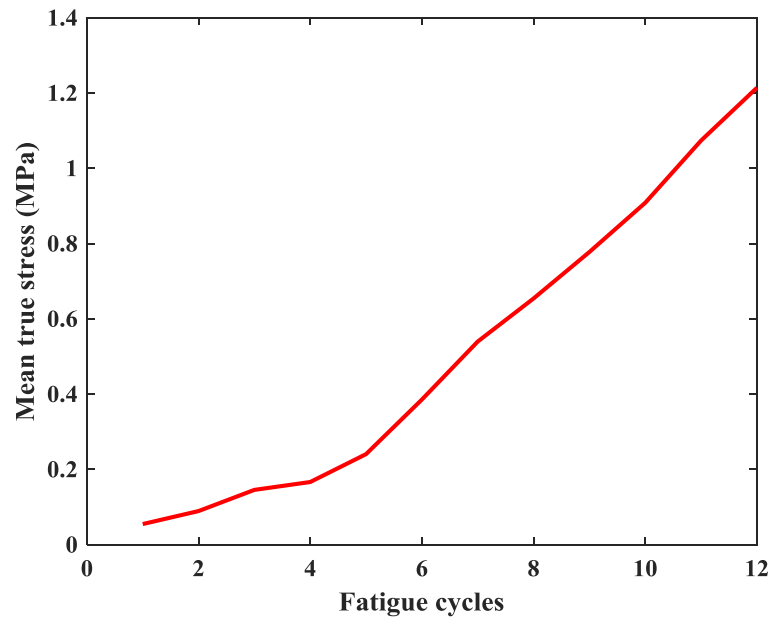


Figure 6. 7 Mean true stress during variable-amplitude loading of ET-F43.

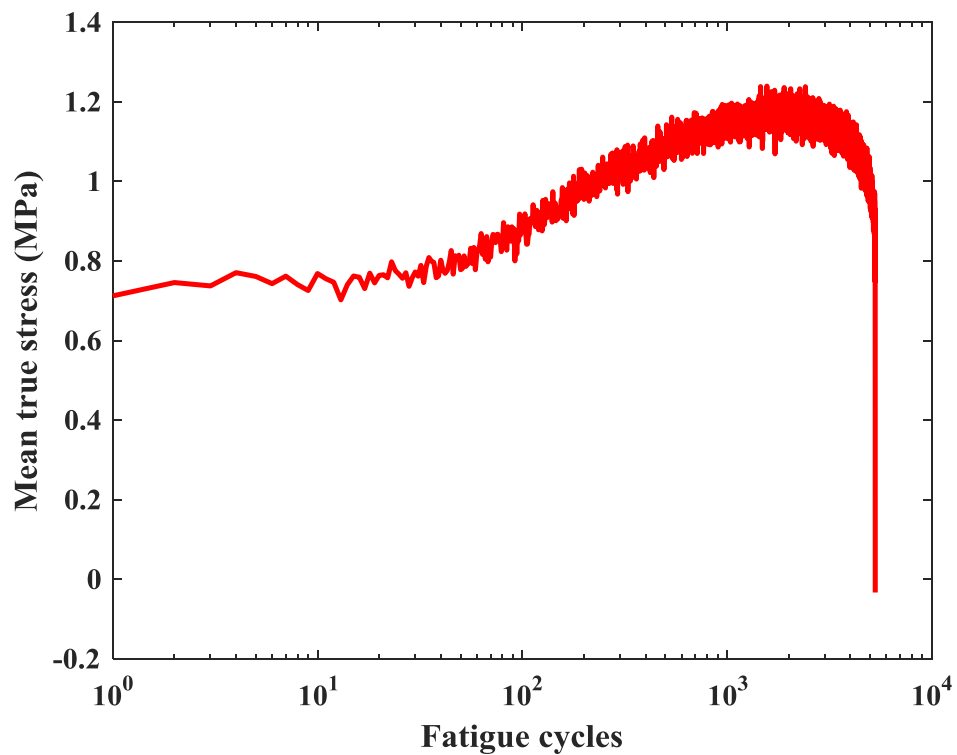


Figure 6. 8 Mean true stress during constant-amplitude loading of ET-F43.

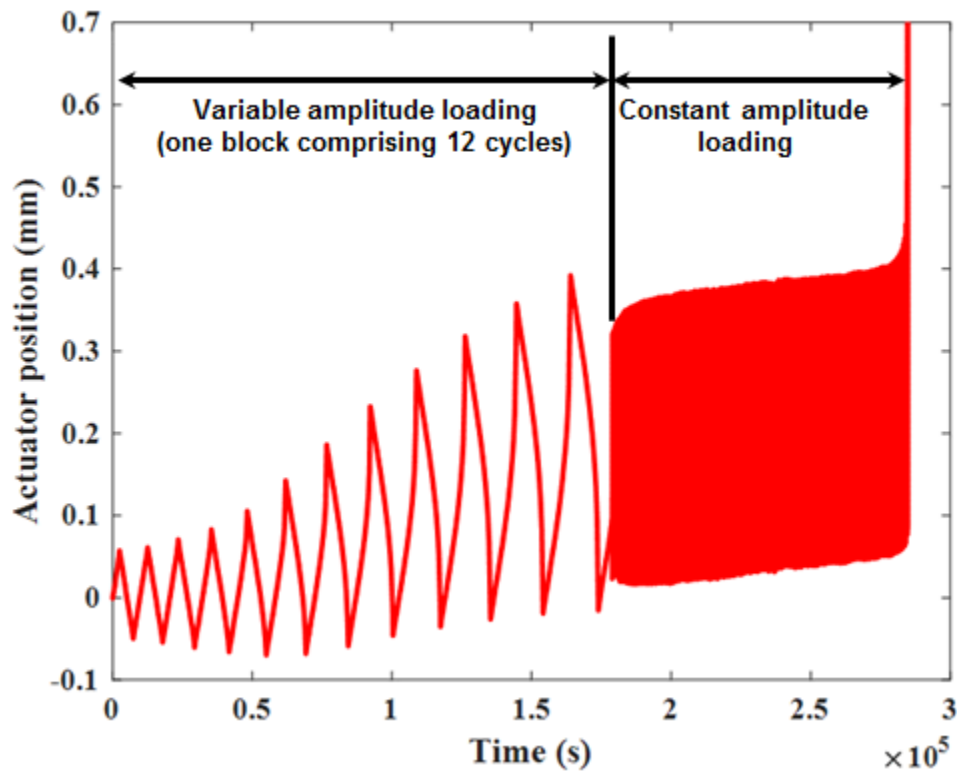


Figure 6. 9 Observed actuator position during ET-F43.

The observed strain and actuator position during the ET-F45 test are shown in Figures 6.10 and 6.11, respectively. As the stress rate during constant-amplitude loading of ET-F45 test was 1000 times lower than that of ET-F43, the experiment took exceptionally long, and the sample did not break even after 48 days. The experiment was stopped after 200 constant-amplitude loading cycles.

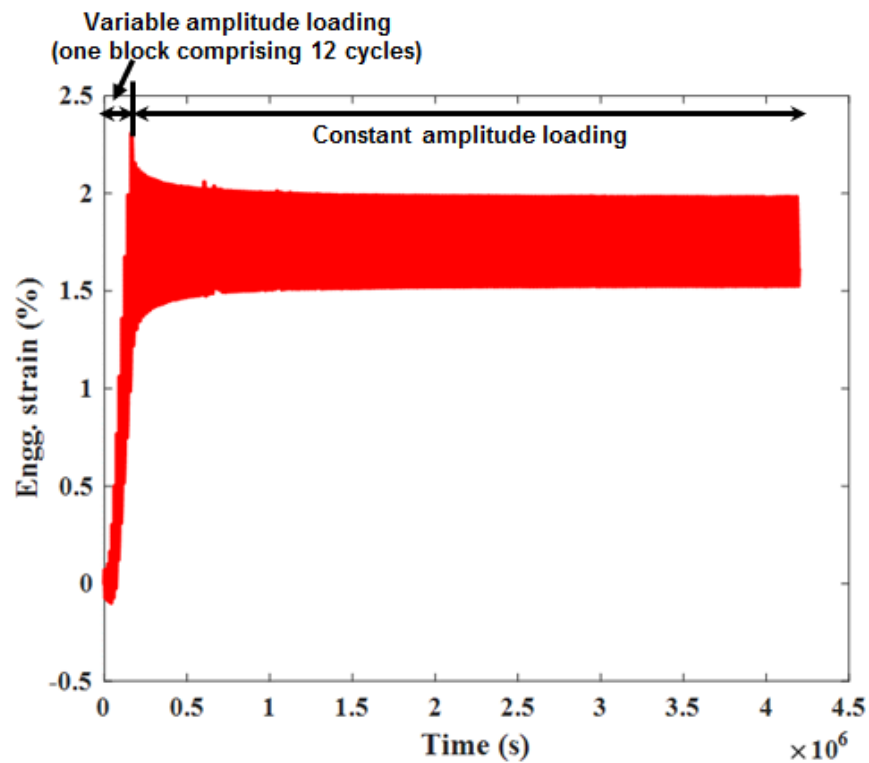


Figure 6. 10 Observed strain during ET-F45 fatigue test.

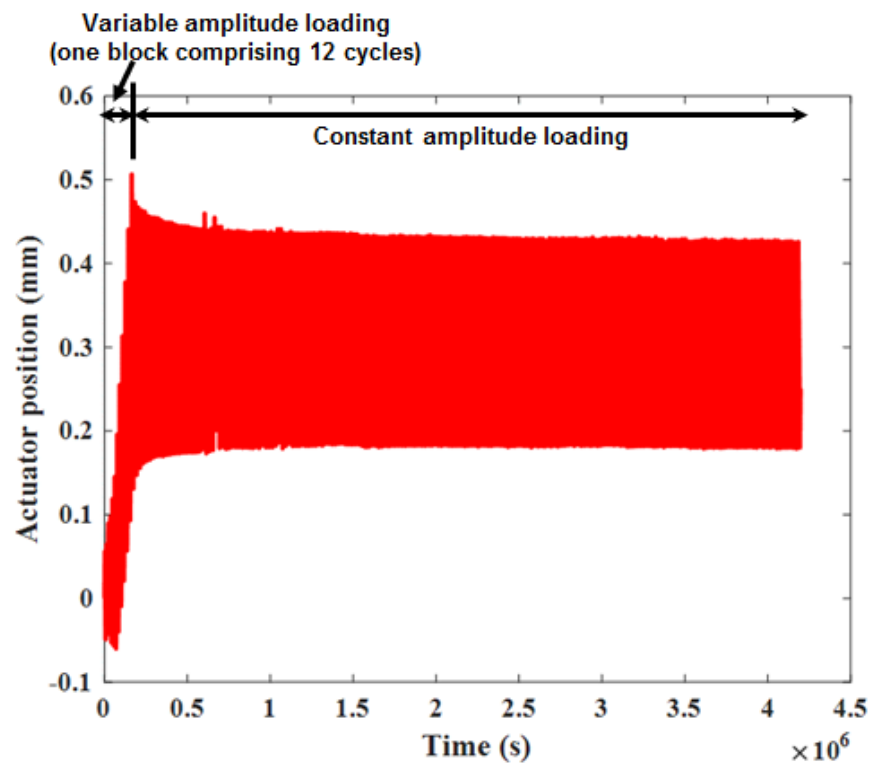


Figure 6. 11 Observed actuator position during ET-F45 fatigue test.

Comparisons between material behavior during variable-amplitude loading of in-air tests ET-F43 and ET-F45 are shown in Figures 6.12 and 6.13, respectively. Figure 6.12 shows the engineering stress-strain hysteresis plots while Figure 6.13 shows the ratcheting strain during variable-amplitude block loading. From these figures, a significant difference can be seen in ratcheting strain, although the loading conditions (stress amplitude and stress rate) were the same for both tests (during variable-amplitude loading). This finding indicates that the test material can behave very differently under the same stress cyclic loading. As can be seen in the tensile stress-strain plot in Figure 6.1 and stress-strain hysteresis plot in Figure 6.12, during plastic deformation, material strain response becomes asymptotic at higher stress loading. A small amount of stress perturbation can cause huge plastic strain, which can further drive the ratcheting by increasing the mean true stress in the following loading cycle. These findings show the importance of conducting several stress-controlled fatigue tests under the same condition so that the variation in material behavior under stress loading can be incorporated into the material properties with a statistically good level of confidence. These findings also signify the complexity of conducting stress-controlled fatigue experiments. Reports of related stress-controlled tests are rare in the open literature. The different material behaviors under different stress rate during constant-amplitude loading is discussed in Section 6.2.5.

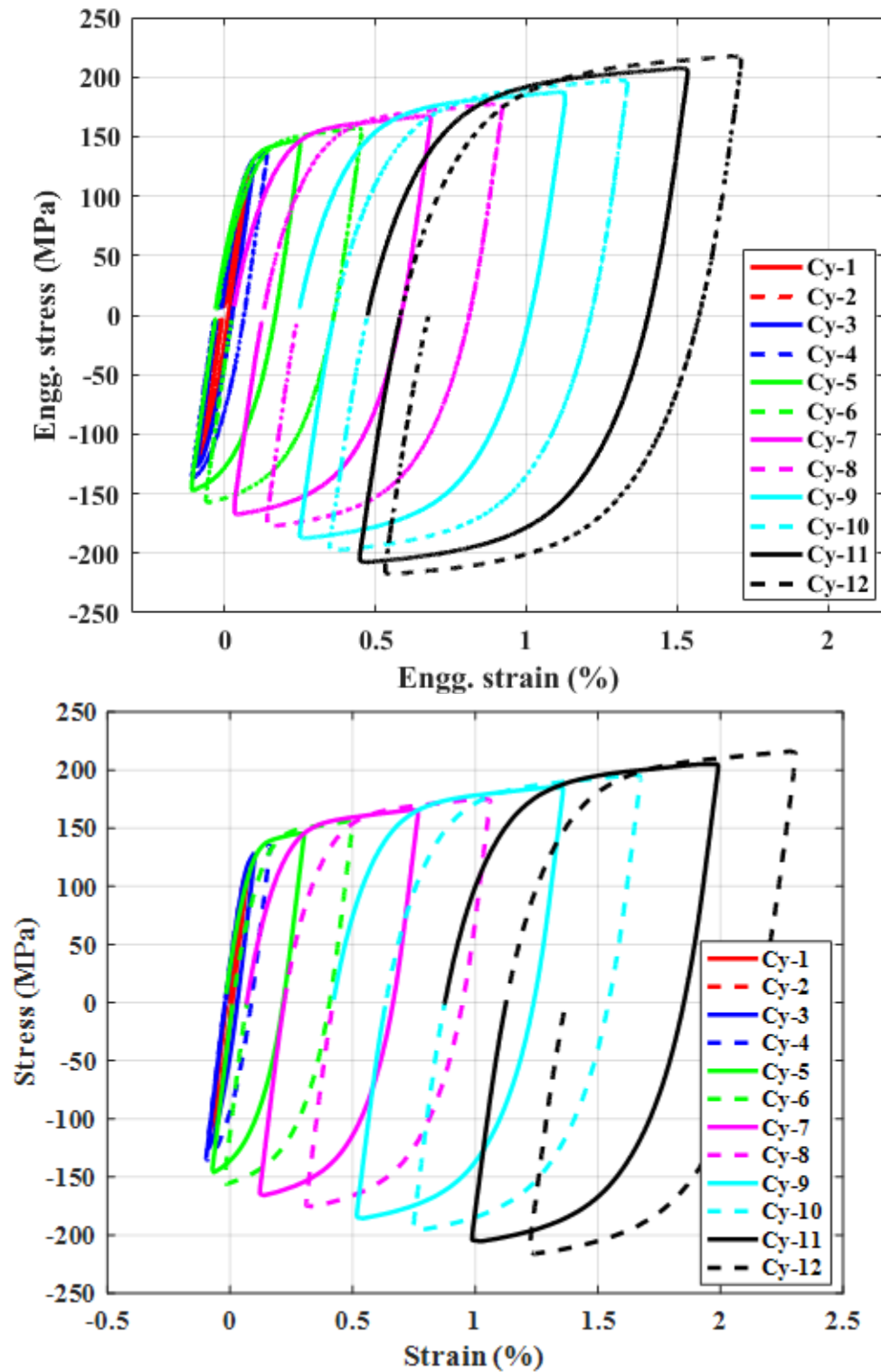


Figure 6. 12 Comparison of ratcheting strain during variable-amplitude block loading of ET-F43 (top) and ET-F45 (bottom).

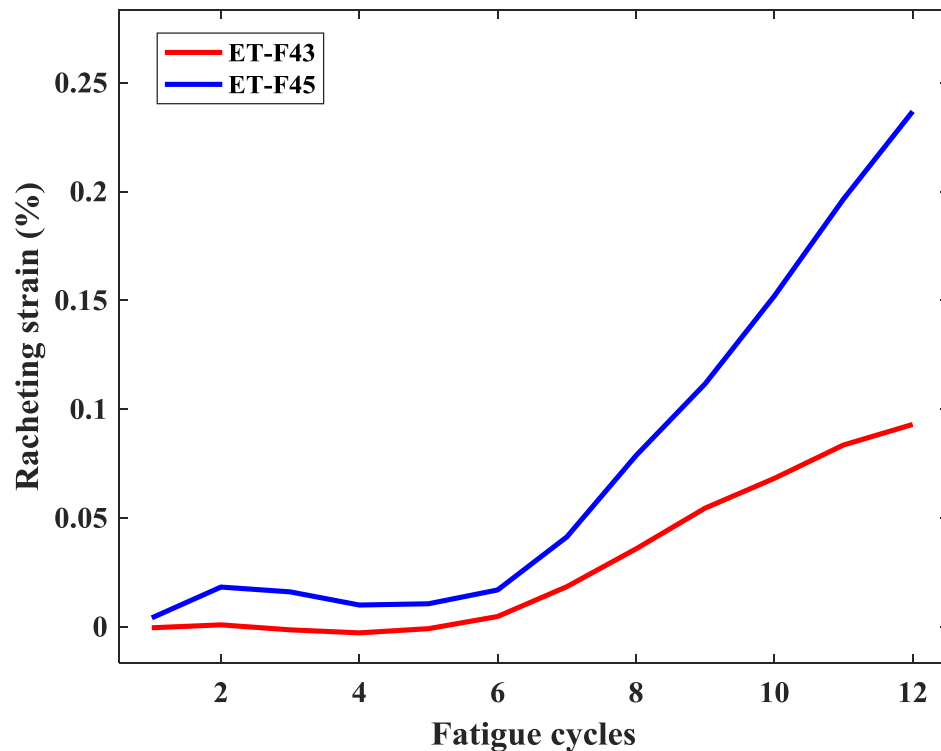


Figure 6. 13 Comparison of ratcheting strain during variable-amplitude loading of ET-F43 and ET-F45.

6.2.2.2 PWR Tests

Figure 6.14 shows the observed actuator position for the entire test EN-F44. The stress input during the PWR water test EN-F44 was the same as for the in-air test ET-F43. Initial observation of the actuator position data between ET-F43 (Figure 6.9) and EN-F44 (Figure 6.14) suggests that ratcheting is much higher in PWR water than in air. However, strain must be predicted from actuator position data for the PWR water test to get a better picture of the impact of the PWR environment on ratcheting strain. The position-strain mapping functions obtained from air tests ET-F43 and ET-F45 were used to predict strain from observed actuator position data during PWR tests, which are discussed in Section 6.2.3.

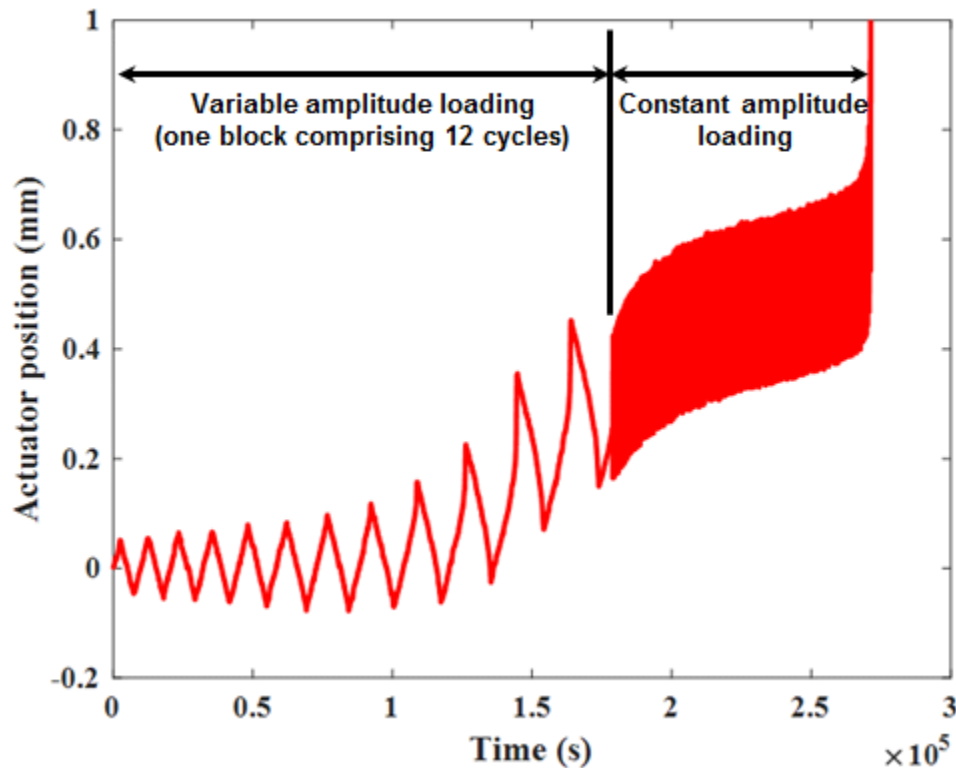


Figure 6. 14 Observed actuator position during PWR water test EN-F44.

The observed actuator position from PWR water test EN-F46 is shown in Figure 6.15. The stress input during this test was the same as that of the in-air test ET-F45, where the stress rate was 0.0432 MPa/s during both variable- and constant-amplitude loading. For EN-F44, the stress rate was 0.0432 MPa/s during variable-amplitude loading and 43.2 MPa/s during constant-amplitude loading. Due to the low (1000 times) stress rate during constant-amplitude loading of EN-F46, the experiment took exceptionally long, and the sample did not break even after 34 days. The test was stopped after 139 cycles. As seen in the comparison of the observed actuator position data between ET-F43 and EN-F44, the comparison between ET-F45 (Figure 6.11) and EN-F46 (Figure 6.15) also indicates higher ratcheting in the case of the PWR water test.

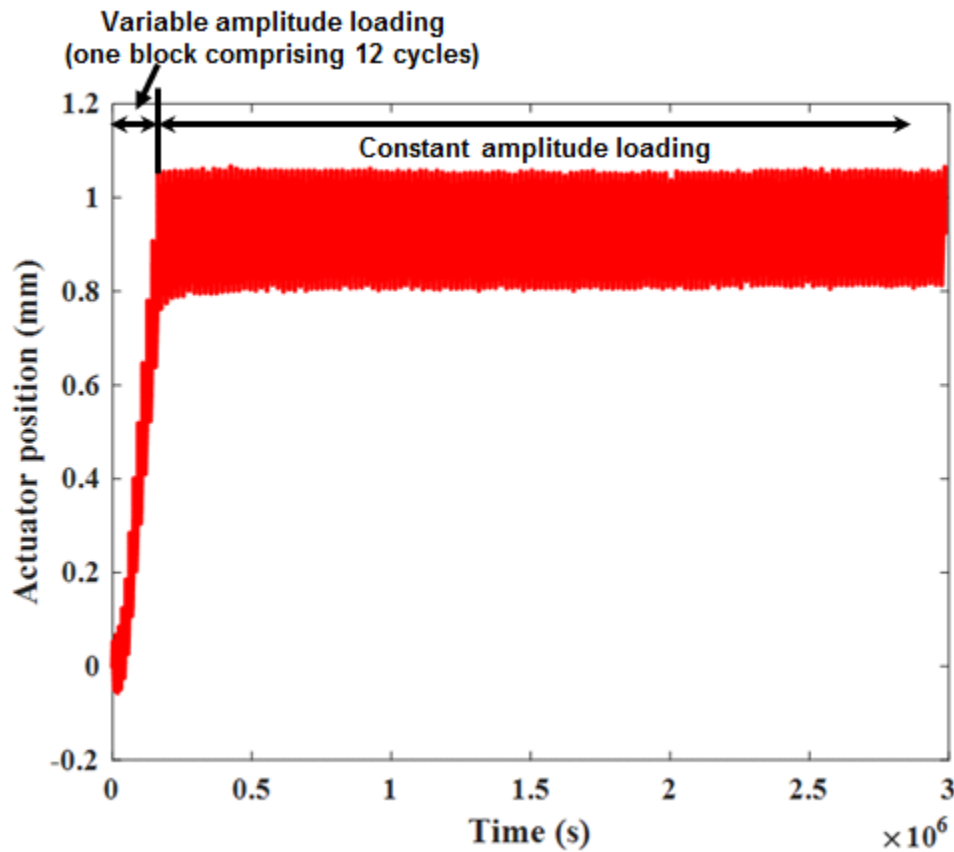


Figure 6. 15 Observed actuator position during PWR water test EN-F46.

The observed actuator positions during variable-amplitude loading of ET-F44 and ET-F46 tests are shown in Figure 6.16. The curves indicate a significant difference in material ratcheting during variable-amplitude loading between the two tests, although the loading conditions (stress amplitude and stress rate) were the same for both tests during variable-amplitude loading. A similar observation was also made for the in-air tests (Figure 6.13). As discussed in Section 6.2.2.1, this kind of variation in material behavior under the same experimental condition could be due to the asymptotic plastic strain response at high stress level.

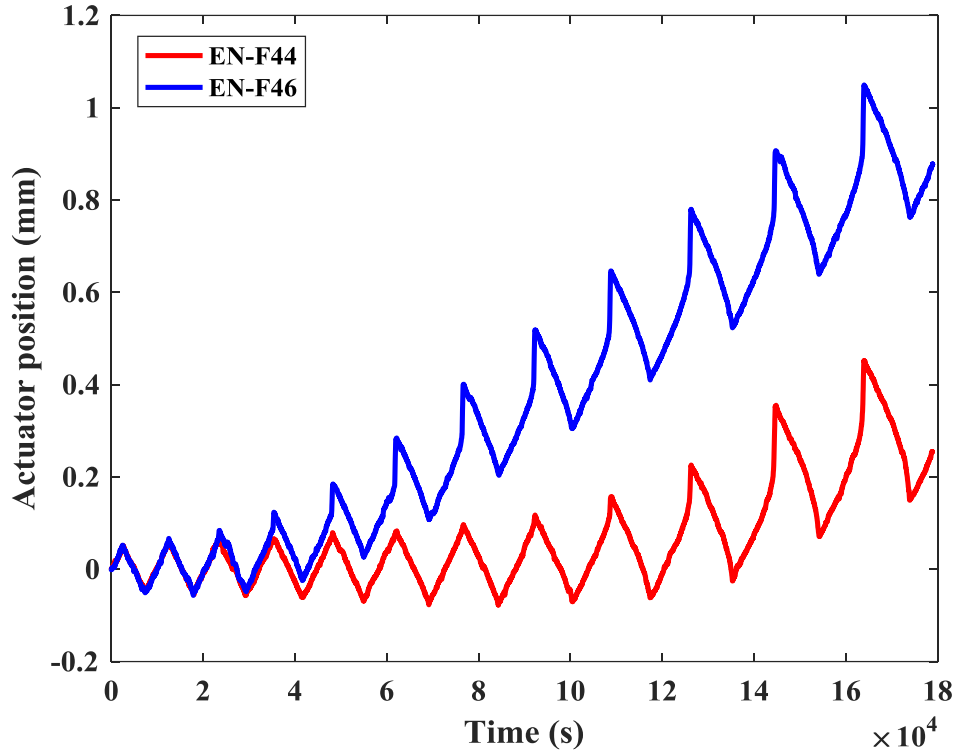


Figure 6. 16 Comparison of observed actuator position during variable-amplitude block loading of ET-F43 and ET-F45.

6.2.3 Prediction of Strain from Actuator Position Data of PWR Tests

During PWR environment tests, an extensometer could not be placed inside the water-tight autoclave for strain measurement. Thus, the axial deformation of the specimen must be measured or controlled by either frame crosshead displacement (i.e., stroke) or frame actuator position. Previously [37, 42, 43], we conducted PWR environment tests by controlling the crosshead displacement. To predict the strain from the crosshead displacement data of the PWR tests, we used stroke-strain mapping functions generated from in-air tests data, where the in-air tests were controlled by the same crosshead displacement used for PWR tests. The stroke-strain mapping functions from stroke-controlled in-air test data were generated by using the 7th-order polynomial given below [37]:

$$\varepsilon = a_0 + a_1 d_s + a_2 d_s^2 + a_3 d_s^3 + a_4 d_s^4 + a_5 d_s^5 + a_6 d_s^6 + a_7 d_s^7 \quad (6.1)$$

where ε and d_s represent strain and crosshead displacement, respectively, and a 's are constants. An example comparison of actual strain and regenerated strain from crosshead displacement (using stroke-strain mapping functions) of an in-air test is shown in Figure 6.17. The plot indicates that the regenerated strain from stroke measurements is well matched with the actual gauge-area strain measurements.

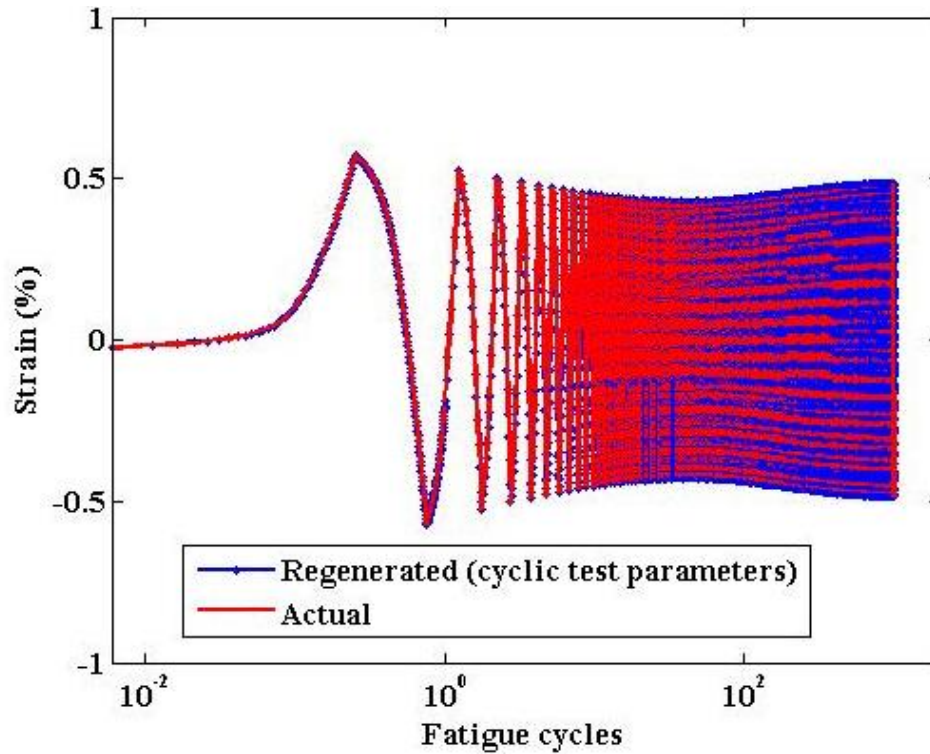


Figure 6. 17 A comparison between actual strain and regenerated strain from stroke measurements of a stroke-controlled in-air test [42].

In this work, we used actuator position measurements to predict strain during the PWR environment tests. We used actuator position measurements instead of stroke measurements because, during stress-controlled testing, a significant amount of axial ratcheting of the specimen occurs in the tension direction, which is beyond the measurement range of the stroke sensor. To generate position-strain mapping functions during in-air stress controlled tests, we used the following 7th-order polynomial, similar to Eq. 6.1.

$$\varepsilon = a_o + a_1 d_a + a_2 d_a^2 + a_3 d_a^3 + a_4 d_a^4 + a_5 d_a^5 + a_6 d_a^6 + a_7 d_a^7 \quad (6.2)$$

where d_a represents the actuator position. However, Eqs. 6.1 or 6.2 can only accurately predict the strain from stroke or actuator position measurements if there is no axial ratcheting of the specimen. Note that no ratcheting (shifting of mean-strain axis) occurred in the specimen during the stroke-controlled test (originally intended to mimic a typical strain-controlled test), as can be seen from Figure 2.17. The 7th-order polynomial was able to predict the shape of the stress-strain hysteresis plots within a cycle, but only after removal of the ratcheting portion of the overall specimen deformation. Thus, ratcheting deformation of the specimen must be predicted separately.

To generate the position-strain mapping for the ratcheting portion of the overall specimen deformation, we plotted ratcheting strain (i.e., strain measurements at the end of each cycle) against the position measurements at the end of each cycle for both in-air stress-controlled tests ET-F43 and ET-F45. The plots, shown in Figure 6.18, indicate that the ratcheting strain follows a linear relationship with end-of-cycle position measurements. The slopes of the linear relationship between ratcheting strain and end-of-cycle position measurements from ET-F43 and ET-F45 are found to be 6.5809 and 5.7499, respectively. We used an average value (6.1654) of the slopes as position-strain mapping function to predict ratcheting strain from the end-of-cycle position data from PWR water tests EN-F44 and EN-F46. However, before predicting the overall strain of the PWR tests, we checked whether the combination of linear position-strain mapping for ratcheting strain and the 7th-order polynomial position-strain mapping for strain within a cycle can predict the strain from the position data. To verify this, we regenerated the strain from the position data of in-air tests ET-F43 and ET-F45. The comparison between regenerated strain and actual measured strain from ET-F43 are shown in Figures 6.19 and 6.20. Figure 6.19 shows the data from the variable-amplitude loading while Figure 6.20 shows the data from the constant-amplitude loading of ET-F43. As seen in the figures, the regenerated strain through position-strain mapping match the actual strain measurements with good accuracy. Thus, the two position-mapping functions, one for ratcheting strain and one for the strain within a cycle, can be used to predict the overall strain from actuator position data of PWR tests.

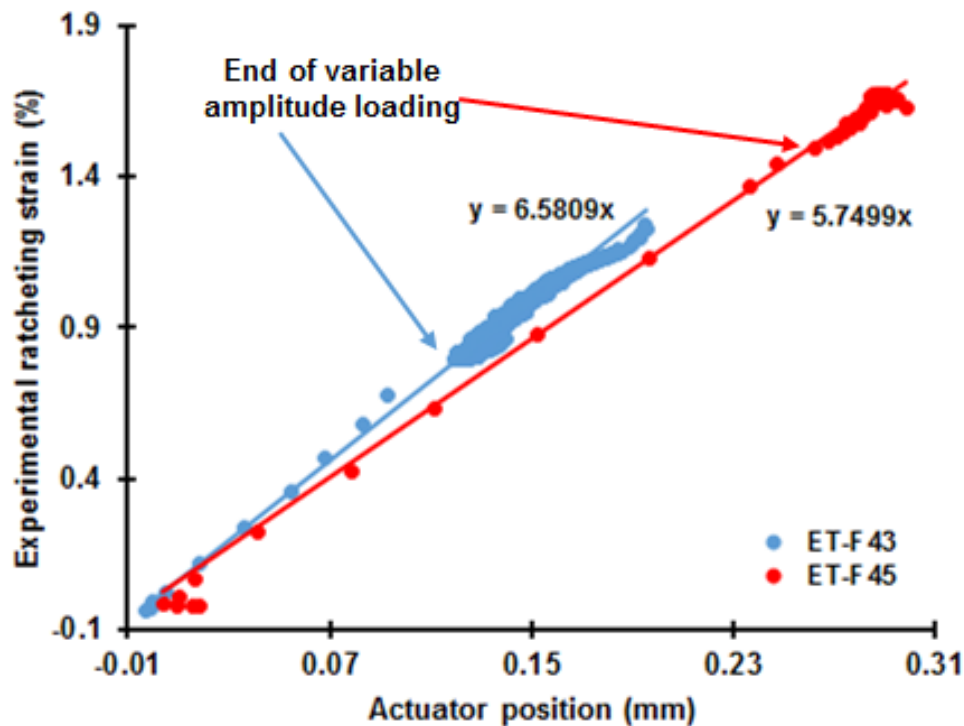


Figure 6. 18 Ratcheting strain as function of actuator position measurements at the end of each cycle from ET-F43 and ET-F45.

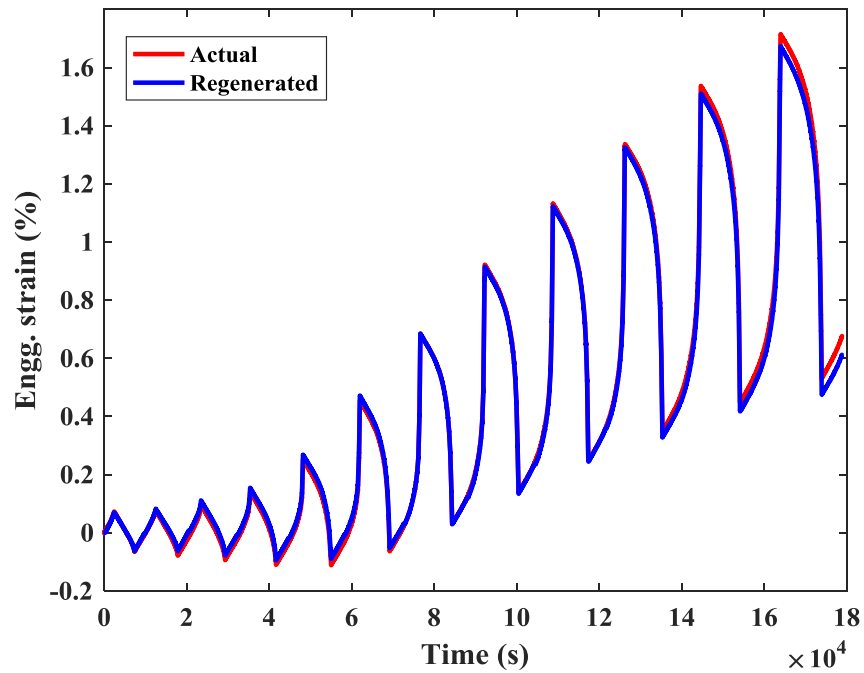


Figure 6. 19 Actual strain measured by strain gauge vs. predicted strain regenerated from position data of ET-F43 during variable-amplitude loading.

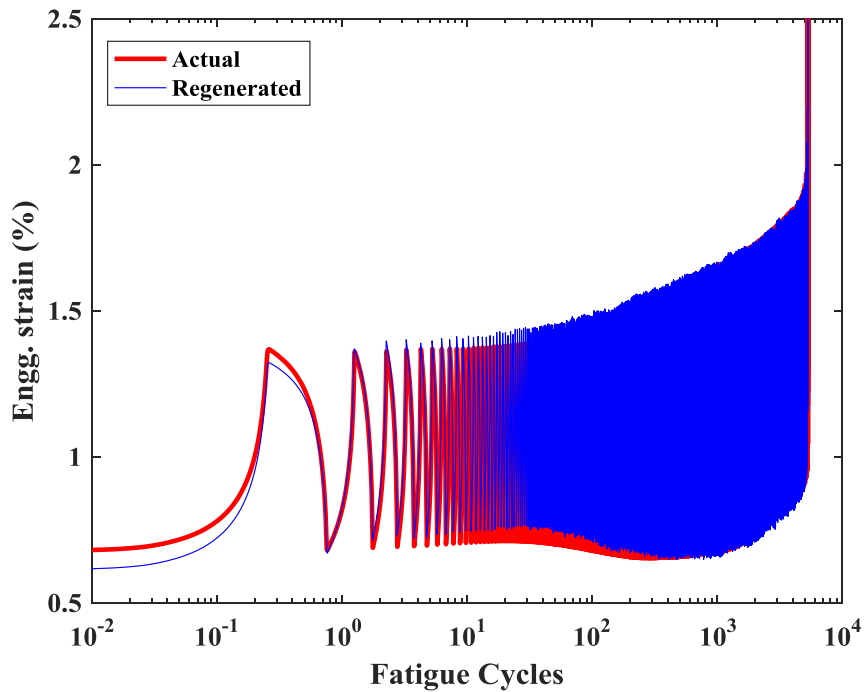


Figure 6. 20 Actual strain measured by strain gauge vs. predicted strain regenerated from position data of ET-F43 during constant-amplitude loading.

We used the position-strain mapping functions discussed in this section to predict strain from position data of PWR environment tests EN-F44 and EN-F46. As shown in Figures 6.21 and 6.22, ratcheting strain during variable-amplitude loading of EN-F46 is much higher than EN-F44, although in the both cases the stress input was the same. The ratcheting strain after variable-amplitude loading was found to be 1.68% for EN-F44 and 5.75% for EN-F46. This 3.42 times higher value in the predicted ratcheting for EN-F46 (after variable-amplitude loading) can be well justified if the position data at the end of variable-amplitude loading are compared (refer to Figure 6.16). The position measurement at the end of variable-amplitude loading during EN-F46 was 0.874 mm, which is 3.43 times higher than the position data (0.255 mm) from EN-F44.

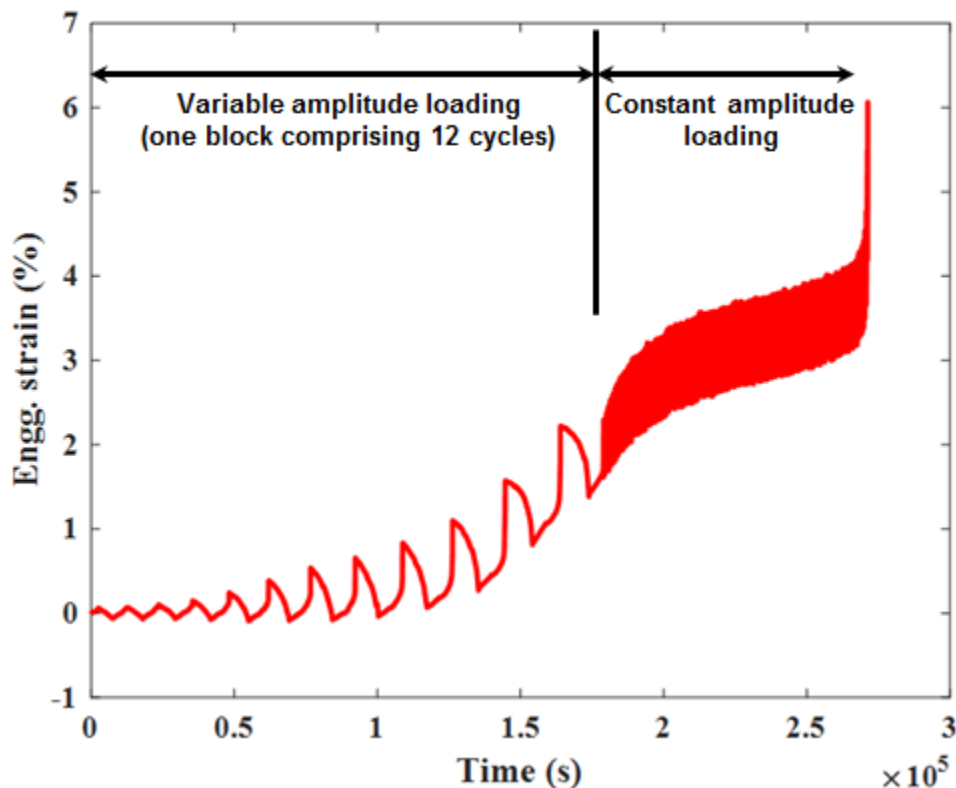


Figure 6. 21 Predicted engineering strain from actuator position data during EN-F44.

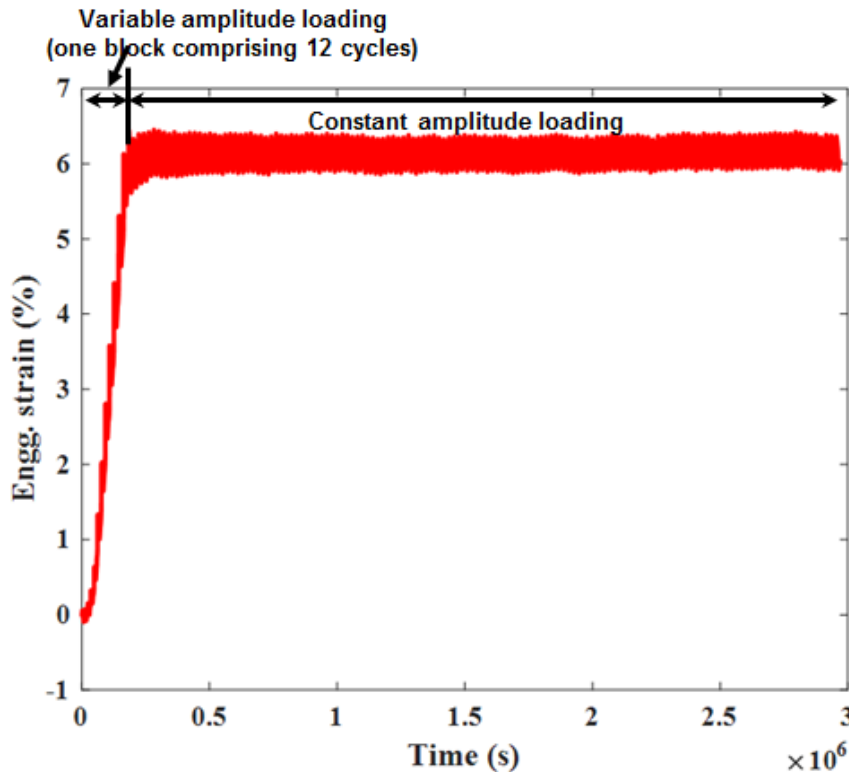


Figure 6. 22 Predicted engineering strain from actuator position data during EN-F46.

6.2.4 Effect of Stress Rate on Material Behavior

As discussed in Section 6.2.1, the applied stress rate was the same during the variable-amplitude loading for all the tests while it was different during constant-amplitude loading. The stress rate during constant-amplitude loading of ET-F43 and EN-F44 was 43.5 MPa/s, while a 1000 times lower stress rate (0.0432 MPa/s) was employed during constant-amplitude loading of ET-F45 and EN-F46 tests. To compare the effect of stress rate on material behavior, the engineering strain responses during constant-amplitude loading of ET-F43 and ET-F45 tests are plotted in Figure 6.23. As seen in the figure, the strain at the beginning of the constant-amplitude loading was different. This finding is due to the difference in ratcheting strain after the initial variable-amplitude loading (see Figure 6.13). To get a better picture of the effect of stress rate during constant-amplitude loading, the strain data were normalized by subtracting the initial strain. Figure 6.24 plots the normalized engineering strain vs. fatigue cycles of ET-F43 and ET-F45. Similarly, Figure 6.25 plots the same factors from constant-amplitude loading of PWR tests EN-F44 and EN-F46. From both figures, it can be concluded that under lower stress rate as well as for longer fatigue cycles, material hardens more. The normalized ratcheting strain as a function of fatigue cycles is plotted in Figures 6.26 and 6.27 for in-air and PWR tests, respectively. The plots indicate that material ratchets at a higher rate under lower stress rate, a finding that is somewhat conflicting if the conclusion is made only based on the material hardening observed from Figures 6.24 and 6.25. One would expect slower ratcheting as material hardens, as in the case of the low stress rate test, but it is not always the case.

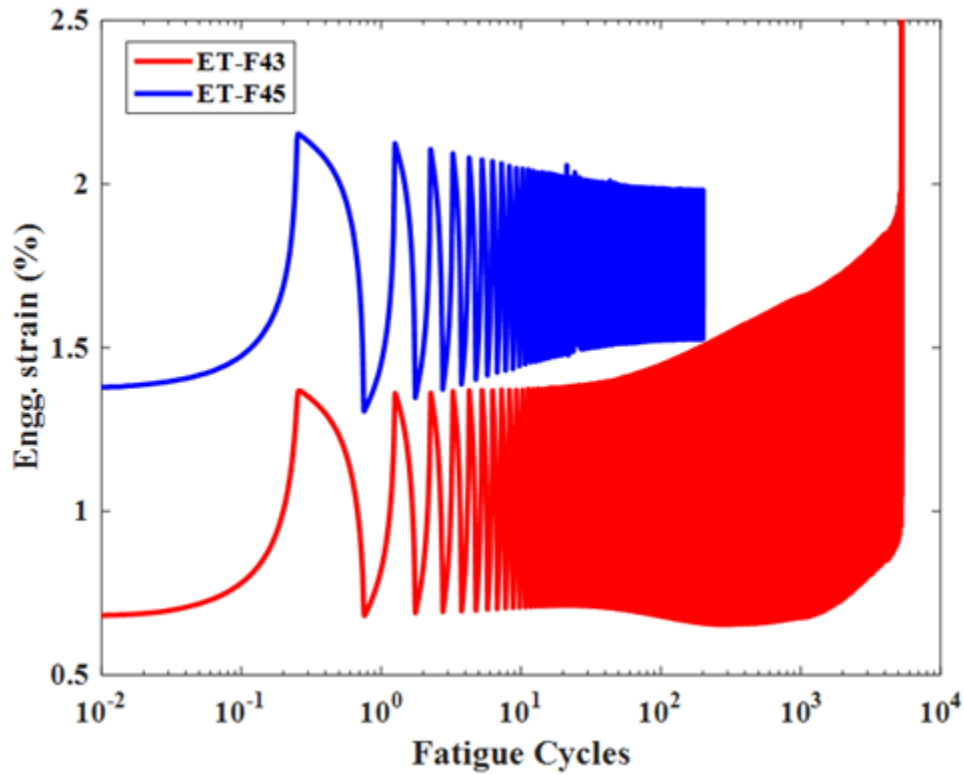


Figure 6. 23 Engineering strain vs. fatigue cycles during constant-amplitude loading of ET-F43 and ET-F45.

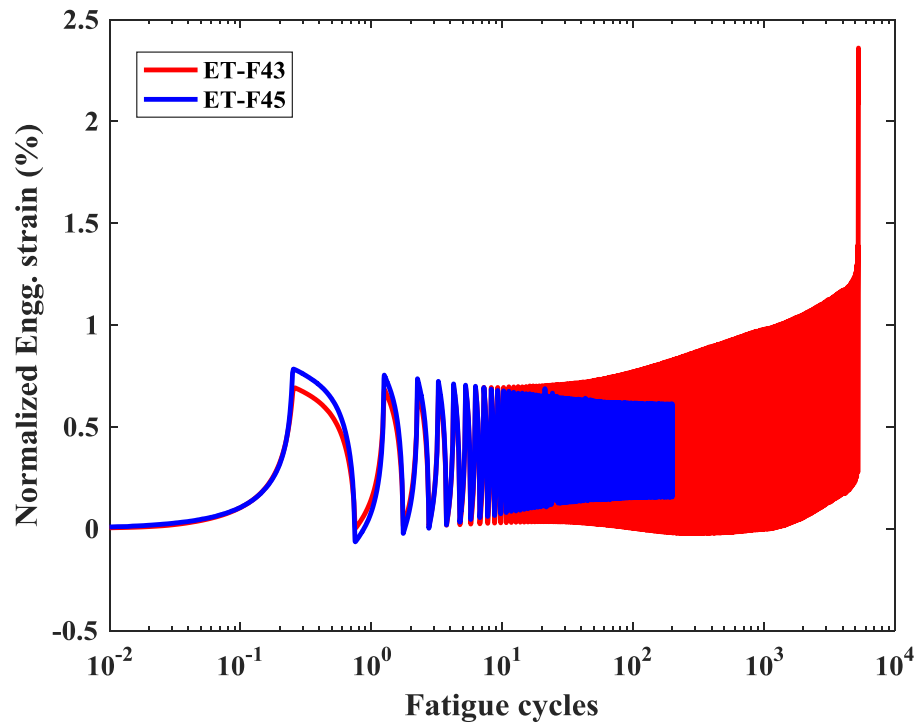


Figure 6. 24 Normalized engineering strain vs. fatigue cycles during constant-amplitude loading of ET-F43 and ET-F45.

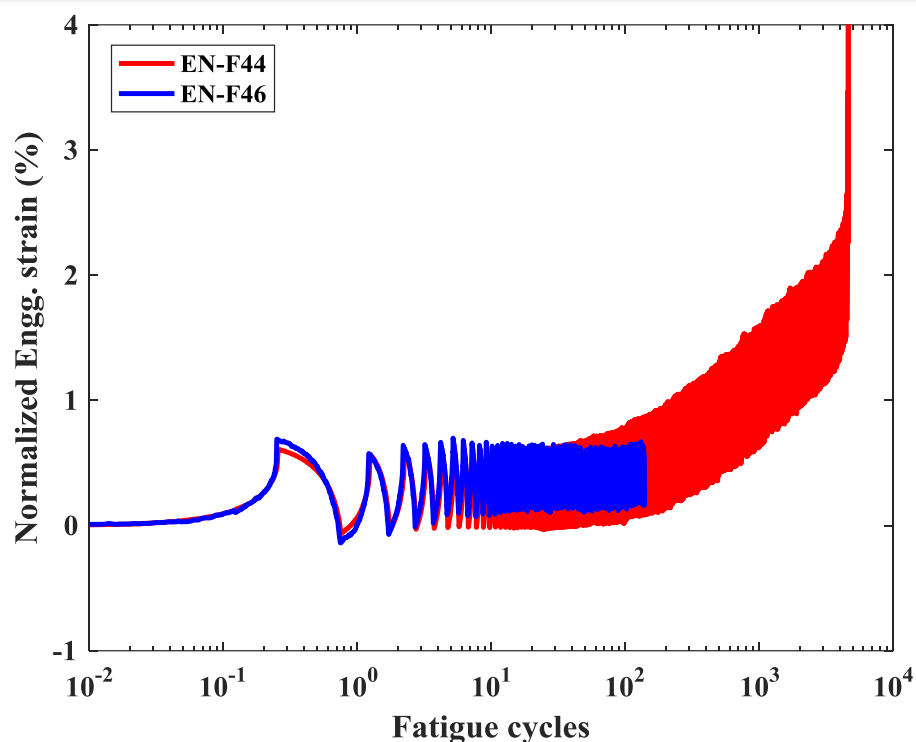


Figure 6. 25 Normalized engineering strain vs. fatigue cycles during constant-amplitude loading of EN-F44 and EN-F46.

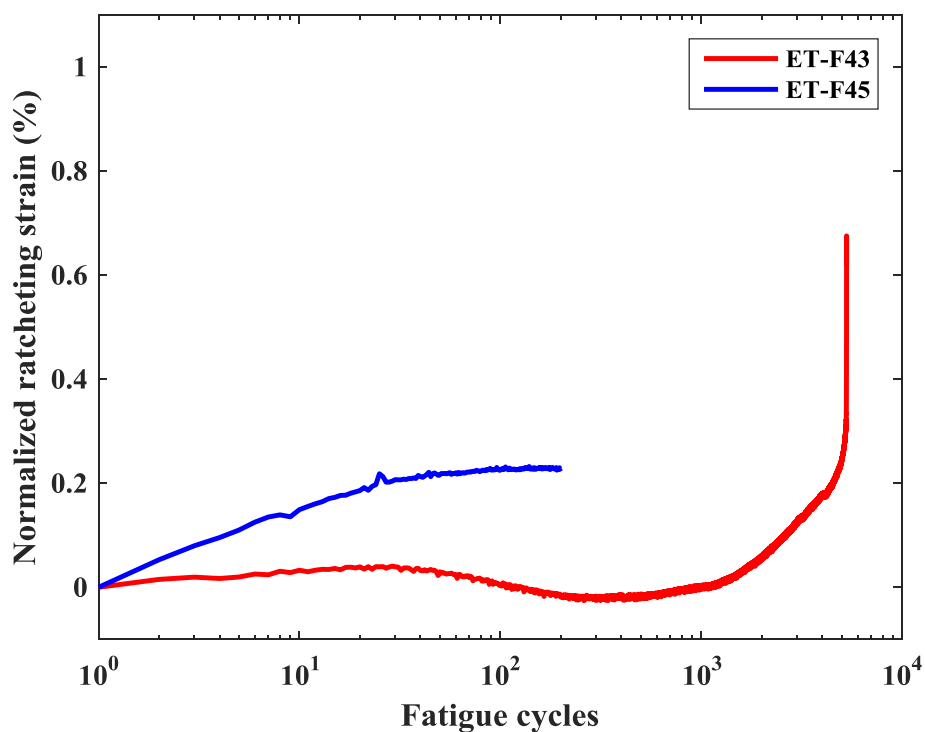


Figure 6. 26 Normalized ratcheting strain vs. fatigue cycles during constant-amplitude loading of ET-F43 and ET-F45.

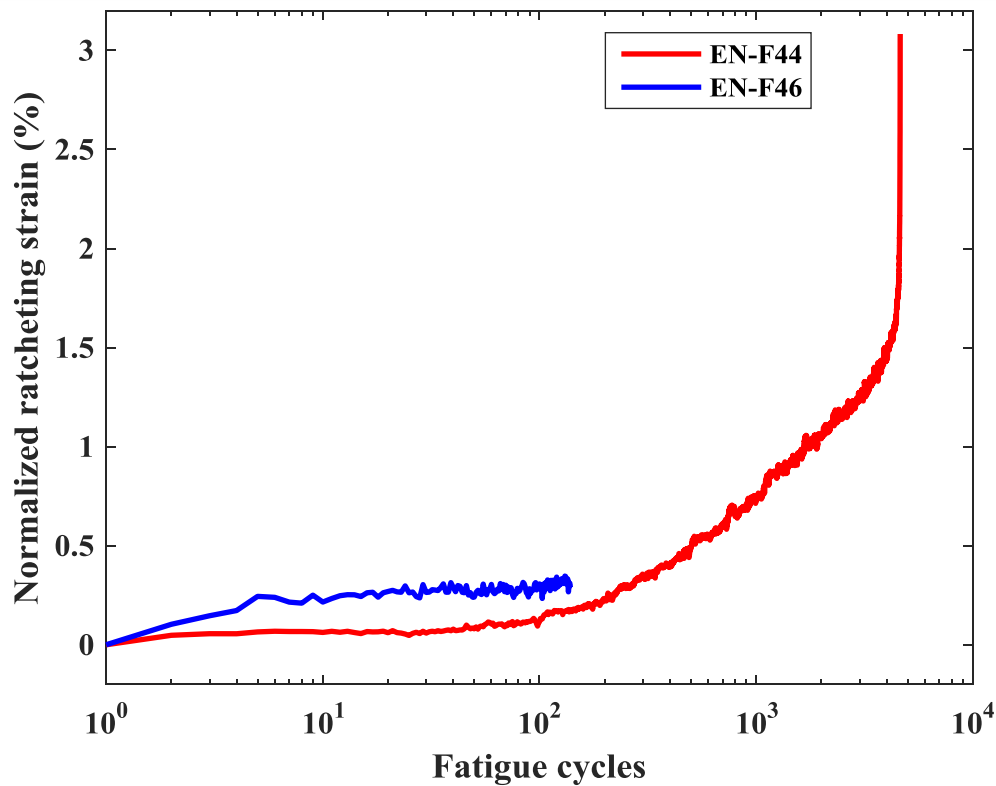


Figure 6. 27 Normalized ratcheting strain vs. fatigue cycles during constant-amplitude loading of EN-F44 and EN-F46.

6.2.5 Effect of PWR Environment on Material Behavior

To investigate the effect of the PWR environment on material behavior, ratcheting strain during variable-amplitude loading of all four stress-controlled tests is plotted as a function of fatigue cycles in Figure 6.28. Note that the stress input for all four cases is the same during variable-amplitude loading. As seen in Figure 6.28, the ratcheting strain at the end of variable-amplitude loading is higher for the two PWR tests (EN-F44 and EN-F46) than the two in-air tests (ET-F43 and ET-F45). However, there is a huge variation in the ratcheting strain values irrespective of the environment. Ratcheting strain for ET-F45 (in-air) is 2.65 times higher than ET-F43 (in-air), while ratcheting strain for EN-F46 (PWR) is 3.43 times higher than EN-F44 (PWR). There is also significant variation in material response at the initial stage of the stress-controlled fatigue test.

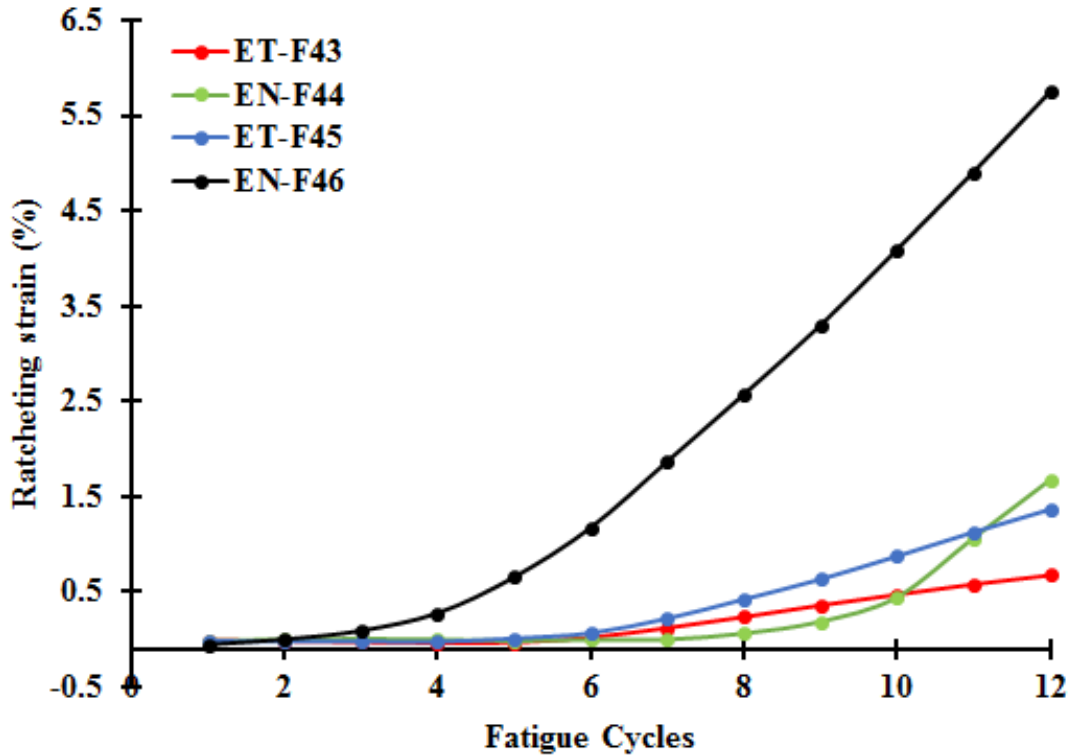


Figure 6. 28 Comparison of ratcheting strain during variable-amplitude loading of in-air tests (ET-F43 and ET-F45) and PWR tests (EN-F44 and EN-F46).

The effect of the PWR environment on material behavior during constant-amplitude loading was also investigated. Figure 6.29 compares the normalized ratcheting strain between ET-F43 and EN-F44, which are high stress rate tests (43.2 MPa/s), while Figure 6.30 gives the results for ET-F45 and EN-F46, low stress rate (0.0432 MPa/s) tests. In both cases, the test material experiences higher ratcheting under the PWR environment. The life of the EN-F44 (PWR) specimen is also reduced by 13% compared to the ET-F43 specimen (in-air).

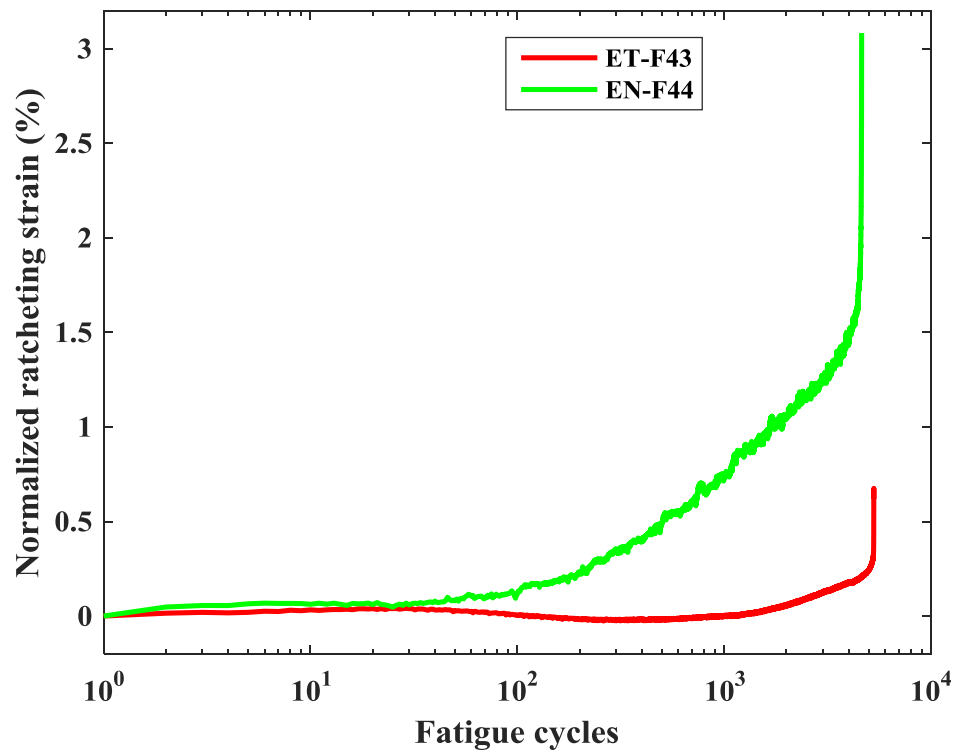


Figure 6. 29 Comparison of normalized ratcheting strain during constant-amplitude loading of ET-F43 and EN-F44.

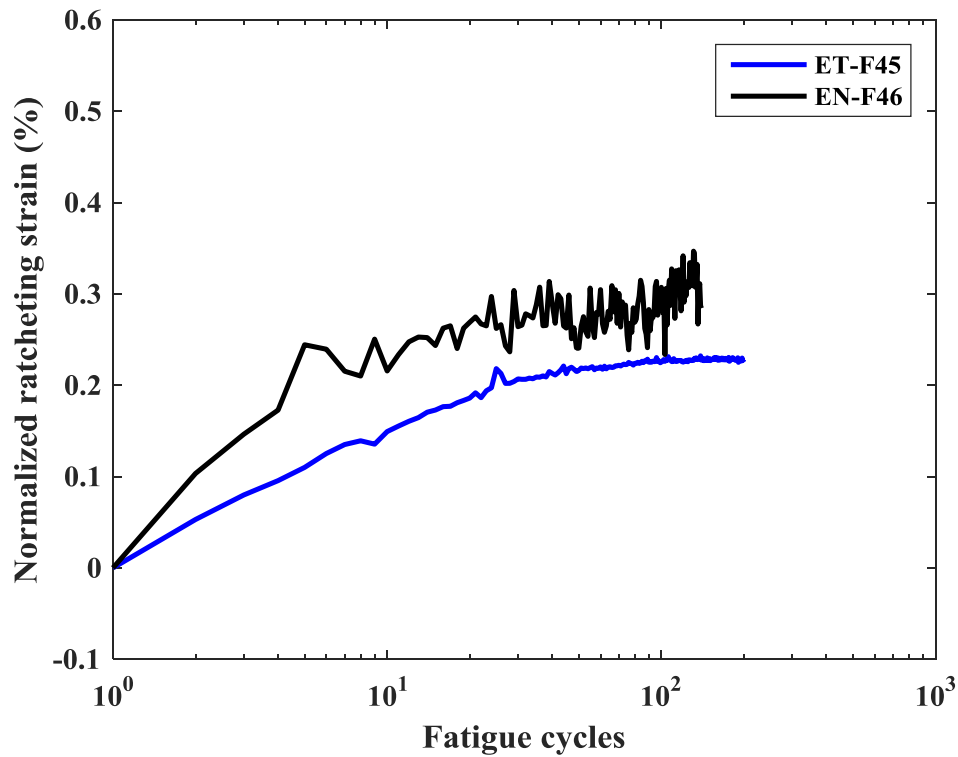


Figure 6. 30 Comparison of normalized ratcheting strain during constant-amplitude loading of ET-F45 and EN-F46.

7 Results from Analytical Modeling of Stress-Controlled Fatigue Tests of 316 SS

As discussed in Section 6, ratcheting strain-induced failure may occur in nuclear reactor components due to cyclic stress loading. The conventional modeling approach for strain-controlled fatigue testing may not accurately predict material behavior under realistic loading conditions. Moreover, fatigue life evaluation of nuclear reactor components requires component-level cyclic stress analysis, where stress rather than strain is controlled. To develop a more accurate fatigue model for 316 SS, stress-controlled fatigue tests were performed, as discussed in Section 6. In this section, results from a mechanistic-based analytical model of stress-controlled fatigue tests are presented. In Section 4, it is shown that the ANL-developed evolutionary cyclic plasticity model can accurately model strain-controlled fatigue tests. However, the model should also be able to predict material behavior under stress-controlled fatigue loading before it can be further used for component-level thermal-mechanical stress analysis under cyclic loading. We, therefore, examine the capability of the model in predicting the behavior of 316 SS under stress-controlled fatigue loading. Note that all the results presented here are preliminary, and more work is required for further improvement of stress-controlled fatigue modeling. Nevertheless, the ultimate aim of this project is to develop a framework for ratcheting-strain-dependent finite element modeling (based on an evolutionary cyclic plasticity model) that can be used alongside ratcheting strain-based failure criteria to estimate the life of nuclear reactor components through thermal-mechanical cyclic stress analysis.

7.1 Analytical Modeling of In-air Test Cases

Modeling of the initial variable-amplitude loading at low stress rate during ET-F43 was done using two sets of material parameters: constant material parameters based on tensile test ET-F11 and cycle-dependent material parameters. Figure 7.1 shows the experimental vs. predicted true strain simulated with the constant tensile-test parameters and the Chaboche model. The curves indicate that the Chaboche model based on constant tensile-test parameters cannot predict the cyclic deformation of 316 SS under stress-controlled loading. Figure 7.2 shows the experimental vs. predicted true strain simulated using cycle-dependent material properties and the evolutionary cyclic plasticity model. The comparison between experimental and predicted strain shows that the evolutionary cyclic plasticity model can predict the material deformation of 316 SS under stress-controlled cyclic loading. Note that the magnitude of the applied up and down engineering stress amplitudes are the same within a cycle; as a result, the mean engineering stress is zero. However, the magnitudes of the up and down true stress amplitudes are different, which creates a mean true stress within a cycle. The mean true stress for initial variable-amplitude loading of ET-F43 is shown in Figure 6.7. As discussed in Section 6.2.2.1, the mean true stress is the driving force behind the non-recoverable deformation (i.e., ratcheting strain) of the specimen. As true stress-strain is used for calculation, the simulation results for stress-controlled tests are presented in true quantity. Also note that the modeling results presented in Section 4 (strain-controlled tests) are based on engineering stress-strain calculation, as there is no (or very negligible amount of) mean stress in a strain-controlled test with equal magnitude of up and down amplitudes.

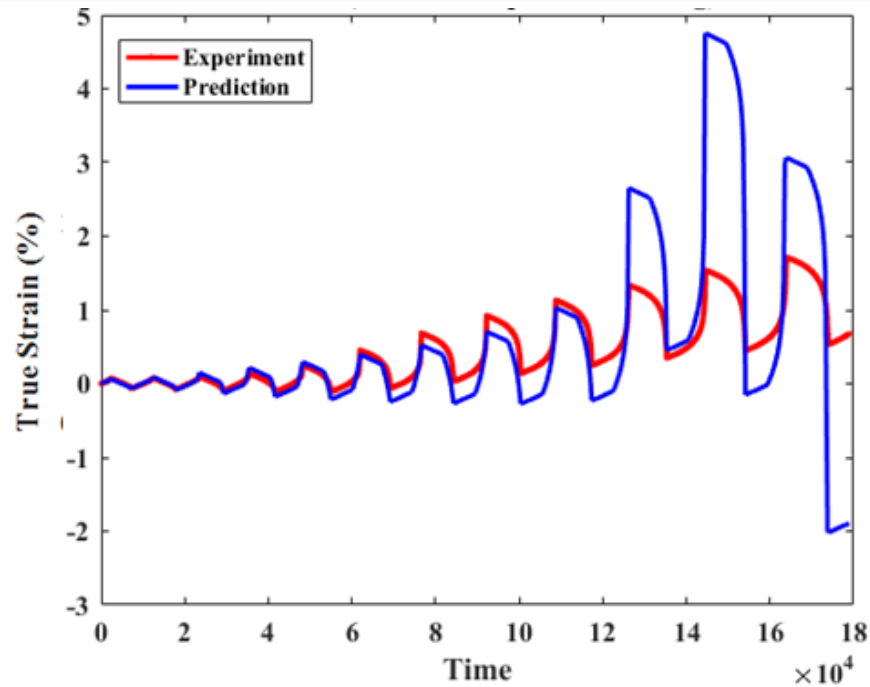


Figure 7. 1 Experimental vs. predicted true strain during initial variable-amplitude loading of ET-F43. Prediction is based on tensile-test-based constant parameters and the Chaboche model.

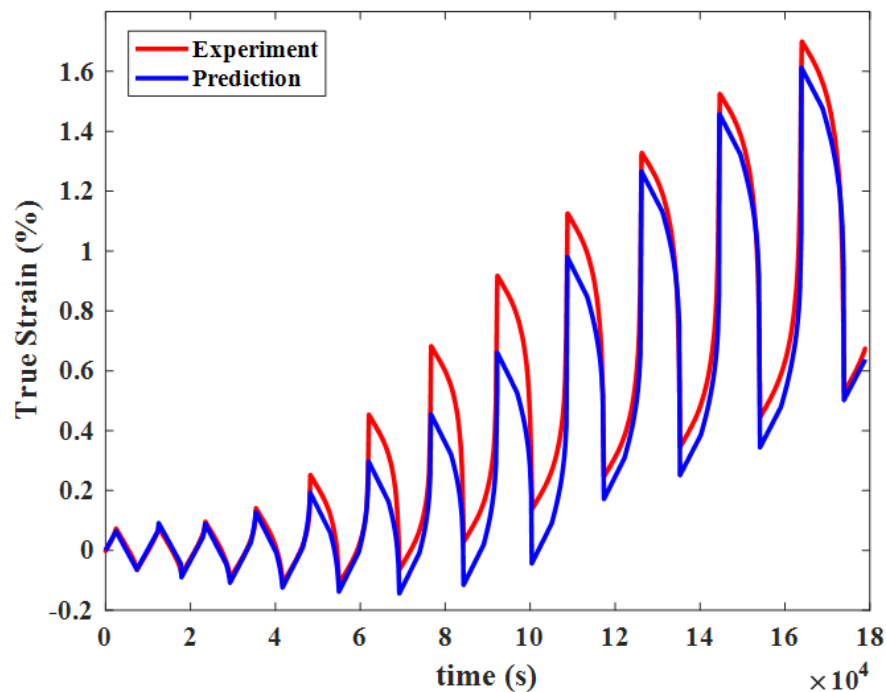


Figure 7. 2 Experimental vs. predicted true strain during initial variable-amplitude loading of ET-F43. Prediction is based on cycle-dependent parameters and the evolutionary cyclic plasticity model.

Modeling of ET-F43 during the constant-amplitude loading at high stress rate was also done with cycle-dependent material parameters and the evolutionary cyclic plasticity model. A comparison between experimental and simulated true strain is shown in Figure 7.3. The curves indicate reasonable accuracy in the predicted true strain.

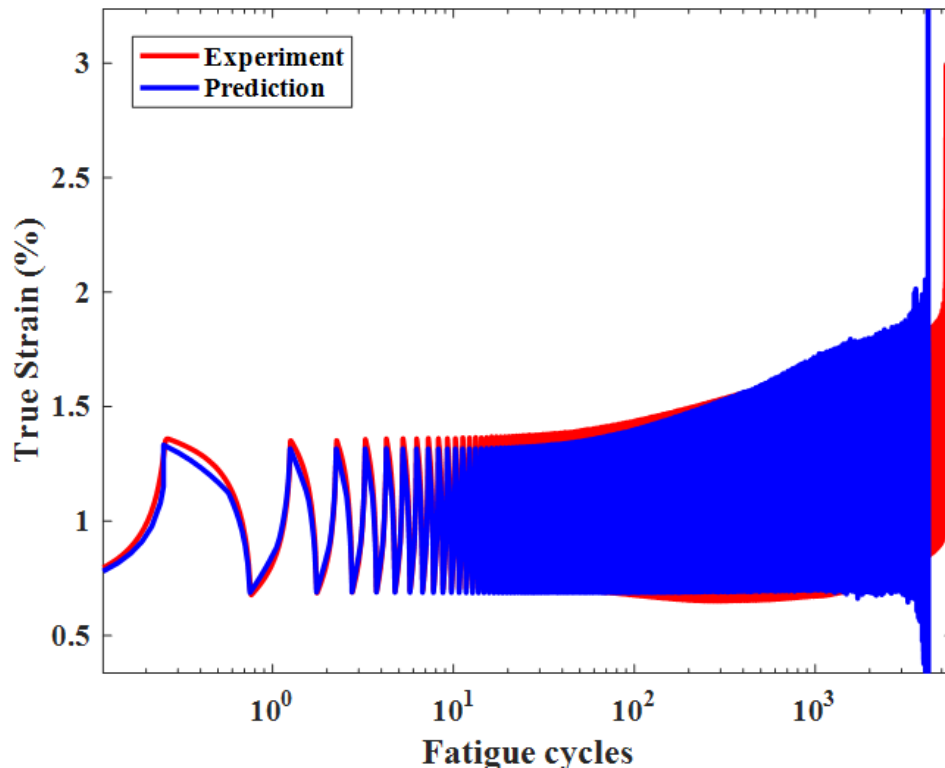


Figure 7. 3 Experimental vs. predicted true strain during constant-amplitude loading of ET-F43. Prediction is based on cycle-dependent parameters and ANL-developed evolutionary cyclic plasticity model.

Similarly, the ET-F45 fatigue test was modeled for both initial variable-amplitude and following constant-amplitude loadings. The results are shown in Figures 7.4 and 7.5, respectively. The comparison between experimental and simulated true strains shown in the figures indicates that the predictions with the evolutionary cyclic plasticity model are in good agreement with the experimental observation. Also, note that the stress rates during constant-amplitude loading of ET-F43 and ET-F45 are very different. The rate is 1000 times higher for ET-F43 compared to ET-F45. This signifies that the model can also capture the effect of loading rate on material behavior.

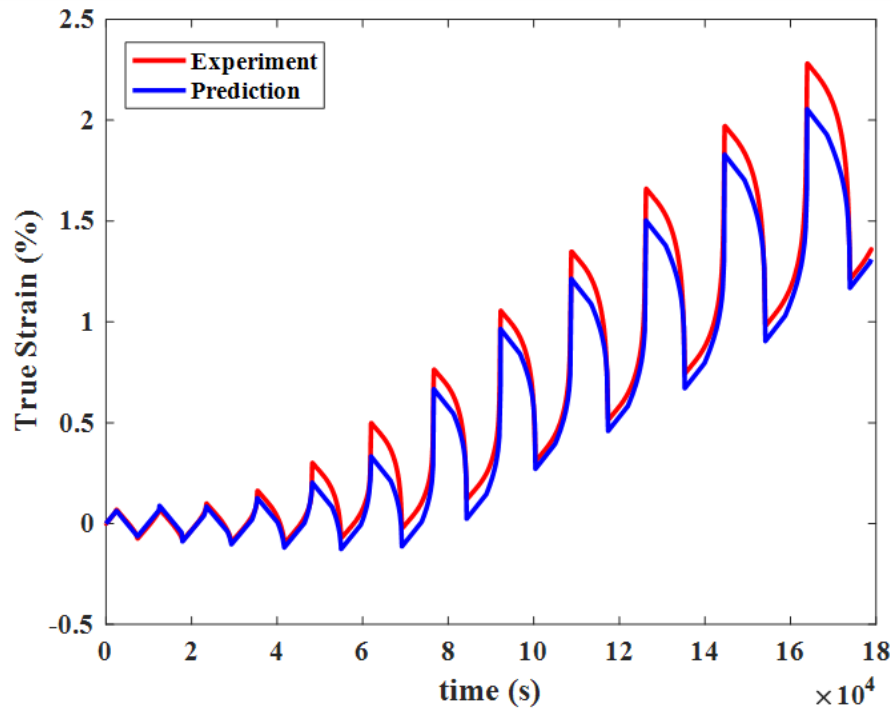


Figure 7. 4 Experimental vs. predicted true strain during initial variable-amplitude loading of ET-F45. Prediction is based on cycle-dependent parameters and the evolutionary cyclic plasticity model.

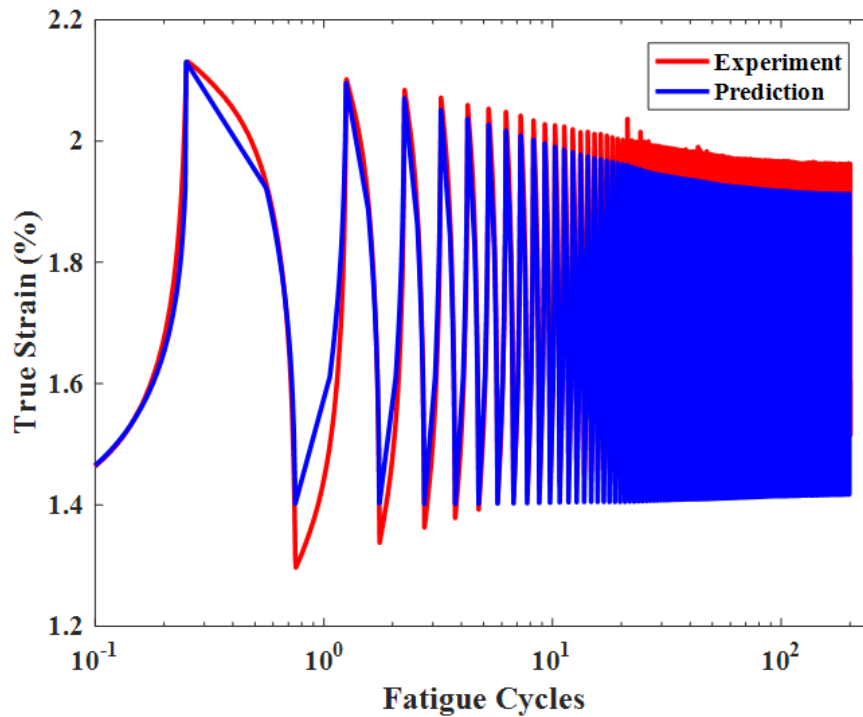


Figure 7. 5 Experimental vs. predicted true strain during constant-amplitude loading of ET-F45. Prediction is based on cycle-dependent parameters and the evolutionary cyclic plasticity model.

7.2 PWR Test

The PWR environment test EN-F44 was analytically modeled with the cycle-dependent material properties and the evolutionary cyclic plasticity model. Figure 7.6 shows the experimental and simulated true strain for the initial variable-amplitude loading. It can be seen that the evolutionary cyclic plasticity model can predict the behavior of 316 SS under variable-amplitude loading in the PWR environment. The experimental and simulated true strain during constant-amplitude loading (first 50 cycles) of EN-F44 is shown in Figure 7.7

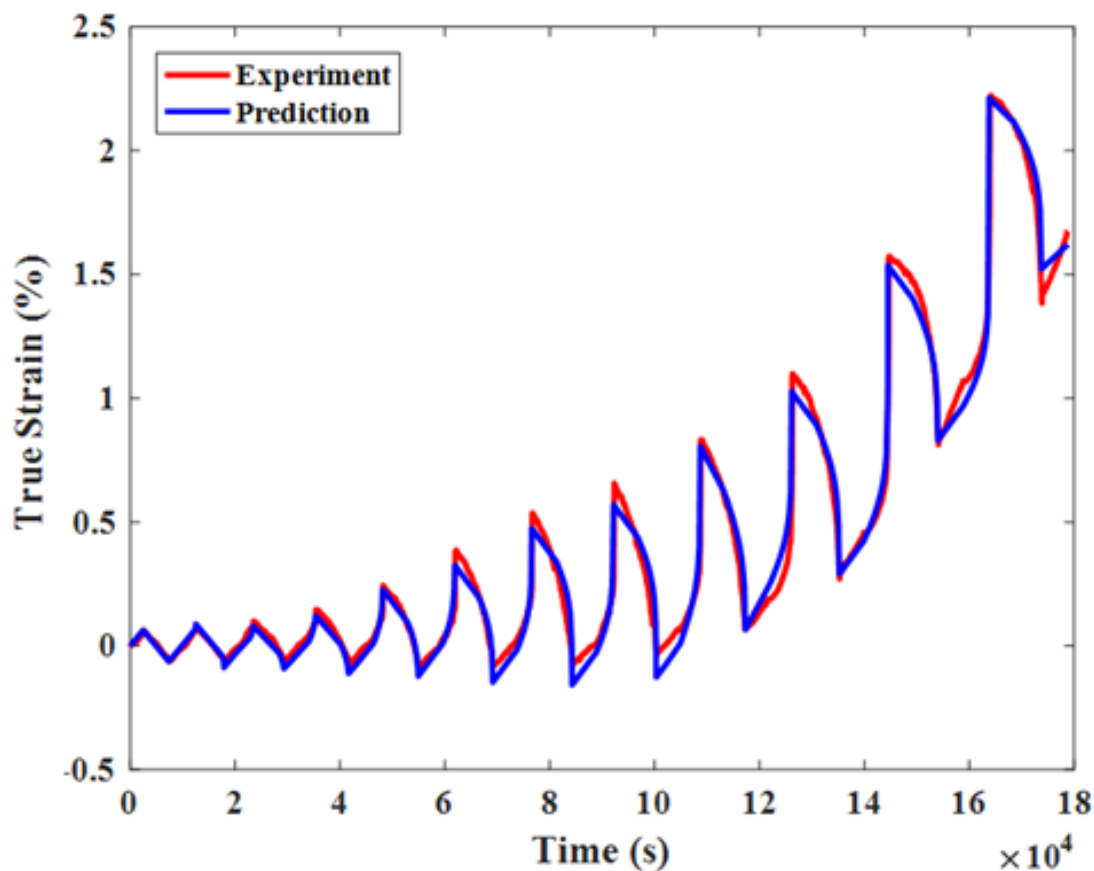


Figure 7. 6 Experimental vs. predicted true strain during initial variable-amplitude loading of EN-F44. Prediction is based on cycle-dependent parameters and the evolutionary cyclic plasticity model.

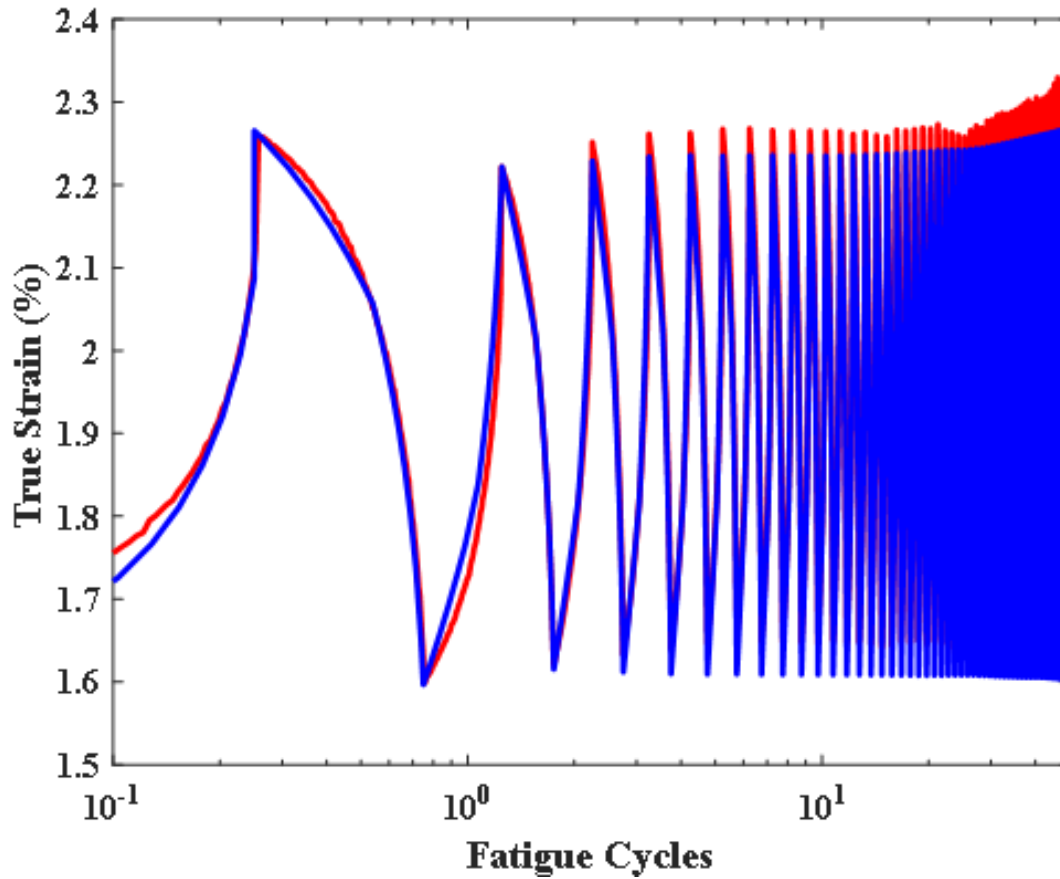


Figure 7. 7 Experimental vs. predicted true strain during constant-amplitude loading (first 50 cycles) of ET-F46. Prediction is based on cycle-dependent parameters and the evolutionary cyclic plasticity model.

8 CFD and Thermal-Mechanical Stress Analysis under Transient Conditions

In general, the design lives of light water reactors (LWR) are 40 years. In US efforts are being made to extend the life of LWRs from original design life of 40 years to extended life of 80 years or more. However, environmental fatigue of the reactor components are one of the major issues for extended service of these reactors. Different components of reactor experience different type of thermal-mechanical loading, which along with the reactor environment govern the degradation mechanism in that particular component. Many research organizations around the world are involved in studying the effect of reactor environment and associated damage mechanism on reactor material. However, majority of the related research works are focused on testing and material characterization using small-scale specimen under uniaxial loading conditions. However, failure of a component is, not only depend on material interaction with reactor environment but also on the multiaxial loading conditions of components. However, laboratory testing of a component to study the effect of environmental fatigue is not always an easy option. This is due to replicating the reactor fluid-thermal-mechanical loading is not an easy task. Also component scale experiment is extremely time-consuming and cost prohibitive. The alternate approach for component level structural integrity evaluation is through computational modeling. For example use of 3D finite element tools are increasingly becoming popular for component level structural integrity analysis of reactor components [44-48]. In this report we present component level fatigue evaluation such as of surge line (SL) pipe. Most of the pressurized water reactor (PWR) has SL that is used for controlling the primary loop pressure. For evaluating fatigue of SL it is required to perform the stress analysis. In turn stress analysis of SL requires to perform the computational fluid dynamics analysis to estimat the thermal boundary condition of SL. The thermal boundary condition of SL is highly complex due to the thermal stratification [49]. Development of computational fluid dynamics (CFD) model required to model the thermal condition of SL. There are many researchers contributed for CFD modeling of SL or similar component for modeling complex flow mixing and associated thermal stratification [50-63]. In this section we present a detailed parametric study of standalone CFD and coupled CFD and heat transfer (CFD-HT) analysis of SL. The models have been developed for estimating the temperature boundary condition and stratification of the SL pipe. Both standalone CFD and coupled CFD heat transfer (CFD-HT) fluid structure interaction (FSI) models are developed. The resulting temperature data are then used for stress analysis (ST) of the SL pipe. Analysis regarding the standalone CFD, and CFD-HT, models with representative results is presented below. The related ST and fatigue analysis results are discussed in Sections 9 and 10, respectively.

8.1 CFD and CFD-HT Theoretical Background

In the reported work, commercially available ABAQUS software was used for the CFD and CFD-HT simulations. The details of the CFD theoretical background and its implementation to ABAQUS code can be found in the ABAQUS user manual [64] or other relevant literature. However, in this subsection, we briefly describe the theoretical information for completeness and easy reference of the terminology and material constants used in the model. The related conservation of mass, momentum, turbulence, and energy equations are briefly described below.

The conservation of mass or continuity equation can be given as:

$$\frac{\partial \rho}{\partial t} + \nabla \cdot (\rho \mathbf{u}) = 0 \quad (8.1)$$

where ∇ , ρ , and \mathbf{u} are, respectively, the del operator, density, and velocity vector of the fluid. Then, the conservation of momentum or the Navier-Stokes (NS) equation can be given as:

$$\frac{\partial}{\partial t} (\rho \mathbf{u}) + \nabla \cdot (\rho \mathbf{u} \otimes \mathbf{u}) = -\nabla \cdot p \mathbf{I} + \nabla \cdot \boldsymbol{\tau} + \rho \mathbf{g} \quad (8.2)$$

where \otimes , p , \mathbf{I} , $\boldsymbol{\tau}$, and \mathbf{g} are, respectively, the outer product, pressure, identity matrix, deviatoric (shear) stress tensor, and body accelerations, e.g., acceleration due to gravity. In the present work, commercially available ABAQUS software was used for the CFD simulation. The ABAQUS/CFD code only allows the incompressible flow type models. For the incompressible flows the momentum equation given in Eq. (8.2) has the equivalent form as:

$$\frac{\partial}{\partial t} (\rho \mathbf{u}) + \nabla \cdot (\rho \mathbf{u} \otimes \mathbf{u}) = -\nabla \cdot p \mathbf{I} + \mu \nabla^2 \mathbf{u} + \rho \mathbf{g} \quad (8.3)$$

In general, the flow conditions in the SL are highly turbulent, particularly during transient in-surge or out-surge conditions (which are discussed in this work). The simulation of turbulent flows in the SL requires numerically solving the NS equation given in Eq. (8.3). This, in turn, requires resolving a very wide range of length and time scales. One of the approaches for solving turbulent NS equations is through using a Large Eddy Simulation (LES) type solver. The LES solvers are based on the principles of ignoring the computationally expensive smaller length scales, e.g., near-wall flows via low-pass filtering of NS equations. This helps in increased computational economy of LES solvers, which are popular for large industrial applications. ABAQUS/CFD offers an implicit large eddy simulation (ILES) type solver, which is automatically chosen for high Reynolds number flow. In LES/ILES type solver, large eddies smaller than the mesh size are resolved. To resolve smaller eddies requires finer mesh, leading to higher computational requirement. So an ILES type solver may or may not capture the flow behavior in the SL. In this work, the efficacy of an ILES solver was checked along with turbulence models such as Reynolds Averaged Navier-Stokes (RANS) models. In the RANS model, the fluid velocity components in the NS equation (Eq. 8.3) are decomposed into two parts: ensemble-averaged (or time-averaged) mean velocity components and fluctuating velocities components due to turbulence. For the RANS model, the instantaneous velocity component with respect to space and time, $u_i(\mathbf{X}, t)$ can be expressed as:

$$u_i(\mathbf{X}, t) = \bar{u}_i(\mathbf{X}, t) + \acute{u}_i(\mathbf{X}, t) \quad (8.4)$$

In Eq. (8.4) \bar{u}_i and \acute{u}_i represent time-averaged mean and fluctuating velocity component. To solve the NS equations (Eq. 8.3) along with Eq. (8.4) requires the introduction of an additional term, called Reynolds stress R_{ij} . The corresponding RANS momentum equation can be given as:

$$\rho \frac{\partial \bar{u}_i}{\partial t} + \rho \bar{u}_j \frac{\partial \bar{u}_i}{\partial x_j} = -\frac{\partial \bar{p}}{\partial x_i} + \frac{\partial}{\partial x_j} \left(\mu \frac{\partial \bar{u}_i}{\partial x_j} \right) + \rho \bar{g}_i + \frac{\partial R_{ij}}{\partial x_j} \quad (8.5)$$

In Eq. (8.5) μ , \bar{u}_i , \bar{p} , and \bar{g}_i are, respectively, the dynamic viscosity, mean pressure field, mean velocity field, and mean body force or gravity field to model the mean flow. Reynolds stress R_{ij} components represent the fluctuating velocity (with respect to mean velocity) component and can be expressed in terms of fluctuating velocity component \bar{v}_i as:

$$R_{ij} = -\rho \overline{\bar{u}_i \bar{u}_j} \quad (8.6)$$

The RANS equation (Eq. 8.5) requires solution of Reynolds stress tensor R_{ij} in addition to the mean pressure and velocity components in a typical LES/ILES type solver. The RANS equations require solution of additional nonlinear Reynolds stress terms, leading to creation of different turbulence models. For example, using the Boussinesq hypothesis the additional term in Eq. (8.5), i.e., Reynolds stress R_{ij} , can be modeled in terms of eddy or turbulent kinematic viscosity ν_t . The Reynolds stress R_{ij} tensor in terms of ν_t , can be expressed as:

$$R_{ij} = -\rho \overline{\bar{u}_i \bar{u}_j} = \nu_t \left(\frac{\partial \bar{u}_i}{\partial x_j} + \frac{\partial \bar{u}_j}{\partial x_i} \right) - \frac{2}{3} (\rho k + \nu_t \frac{\partial \bar{u}_k}{\partial x_k}) \delta_{ij} \quad (8.7)$$

In Eq. (8.7) $k = \overline{\bar{u}_i \bar{u}_i} / 2$ is the turbulent kinetic energy, and the turbulent viscosity ν_t has to be solved. There are different turbulence models to solve turbulent viscosity ν_t . In this work in addition to the ILES solver, another two RANS type solvers, such as Spalart-Allmaras and $k - \epsilon$ turbulence models, were investigated for modeling the SL flow. The Spalart-Allmaras is a one-equation turbulence model used to solve the turbulent kinematic viscosity ν_t , which can be expressed as:

$$\nu_t = \tilde{\nu} f_\nu, \quad f_\nu(\chi) = f(\chi = \frac{\tilde{\nu}}{\nu}) \quad (8.8)$$

In Eq. (8.8), the ν_t has to be estimated by solving the differential equation of $\tilde{\nu}$. The details of the differential equation associated with $\tilde{\nu}$ can be found in the ABAQUS manual or other CFD literature. Compared to the one-parameter Spalart-Allmaras equation, in which the transport equation is solved to estimate the turbulent viscosity, in $k - \epsilon$ turbulence models, the transport equation is solved to estimate two parameters, such as turbulence kinematic energy (k) and turbulence dissipation rate (ϵ). This requires an additional two equations for solving $k - \epsilon$ turbulence models. These are given as follows:

$$\rho \frac{\partial k}{\partial t} = \frac{\partial}{\partial x_j} \left[\left(\mu + \frac{\nu_t}{\sigma_k} \right) \frac{\partial k}{\partial x_j} \right] + \nu_t S^2 - \rho \epsilon \quad (8.9)$$

and

$$\rho \frac{\partial \epsilon}{\partial t} = \frac{\partial}{\partial x_j} \left[\left(\mu + \frac{v_t}{\sigma_\epsilon} \right) \frac{\partial \epsilon}{\partial x_j} \right] + \frac{\epsilon}{k} (C_{1\epsilon} v_t S^2 - \rho C_{2\epsilon} \epsilon) \quad (8.10)$$

In Eq. (8.9) and (8.10) σ_k and σ_ϵ are, respectively, the turbulent Prandtl number for kinematic energy (k) and turbulence dissipation rate (ϵ). $C_{1\epsilon}$ and $C_{2\epsilon}$ are two constants. Also in Eq. 8.9 and 8.10 the term S can be expressed in terms of the mean strain rate S_{ij} as:

$$S = \sqrt{2S_{ij}S_{ij}} \quad , \quad S_{ij} = \frac{1}{2} \left(\frac{\partial \bar{u}_i}{\partial x_j} + \frac{\partial \bar{u}_j}{\partial x_i} \right) \quad (8.11)$$

Once Eqs. 8.10 and 8.11 are solved for kinematic energy (k) and turbulence dissipation rate (ϵ), the turbulent kinematic or eddy viscosity v_t in Eq. 8.7 can be estimated using:

$$v_t = \rho C_\mu \frac{k^2}{\epsilon} \quad (8.12)$$

In Eq. 8.12 C_μ is a constant.

In the PWR SL pipe, thermal stratification is a major issue, which is being investigated in this work. The thermal stratification is a phenomenon mainly associated with flow mixing and differential fluid densities associated with differential fluid temperatures. However, the ABAQUS/CFD solver doesn't allow using temperature-dependent densities as input material/fluid properties. To address this, the Boussinesq approximation is used. According to this equation, the density variation in the momentum equation is neglected except in the gravity or buoyancy term $\rho \mathbf{g}$. Accordingly, Eq. 8.3 can be rewritten as

$$\rho_0 \left[\frac{\partial}{\partial t} \mathbf{u} + \nabla \cdot (\mathbf{u} \otimes \mathbf{u}) \right] = -\nabla \cdot p \mathbf{I} + \mu \nabla^2 \mathbf{u} + \rho \mathbf{g} \quad (8.13)$$

In Eq. 8.13 the variable density ρ associated with the buoyancy term $\rho \mathbf{g}$ is estimated through a variable volumetric thermal expansion coefficient, β . Using the Boussinesq approximation, the thermal expansion coefficient β can be estimated from the following expression:

$$(\rho - \rho_0) \mathbf{g} \approx -\rho_0 \beta (\theta - \theta_0) \mathbf{g} \quad (8.14)$$

In Eqs. 8.13 and 8.14, ρ_0 and ρ represent fluid density at a reference and given temperature. Also, θ_0 and θ represent the fluid temperature at reference and a given time.

For CFD simulation involving non-isothermal (variable temperature) conditions (such as in the present case of SL temperature stratification), the energy equation has to be solved in addition to the continuity, momentum, and turbulence equations. The corresponding energy conservation equation for the fluid media is given as:

$$\frac{\partial}{\partial t} (\rho C_p \theta) + \nabla \cdot (\rho C_p \theta \mathbf{u}) = Q + \kappa \nabla^2 \theta \quad (8.15)$$

where C_p , θ , Q , and κ are, respectively, the fluid specific heat or heat capacity at constant pressure, temperature, external heat supplied, and the coefficient of thermal conductivity. Equations 8.1 to 8.15 are for solving standalone CFD problems, for which the effect of energy transfer through a solid boundary is assumed negligible. However, to consider the effect of energy transfer through a solid boundary (for example, in the case of a surge line, the metal pipe is the solid boundary), the energy equation for solid has to be solved coupled with the energy equation for a fluid (Eq. 8.15). The energy equation for metallic solid is given as:

$$\frac{\partial}{\partial t}(\rho^s C_p^s \theta^s) = Q^s + \kappa^s \nabla \theta^s \quad (8.16)$$

In Eq. 8.16, ρ^s , C_p^s , θ^s , Q^s , and κ^s are, respectively, the density, specific heat capacity, solution-dependent temperature, external heat applied, and coefficient of thermal conductivity of a solid, in this case, of SL pipe. ABAQUS through its fluid structure interaction (FSI) feature simultaneously solves the fluid and solid energy equations (Eqs. 8.15 and 8.16) along with CFD-related continuity, momentum, and turbulence equations. Throughout this report, we use the abbreviations “CFD-HT” to refer to the coupled CFD- and FSI-based heat transfer analysis.

8.2 Finite Element Model Information

8.2.1 Finite element model

ABAQUS software was used for modeling the flow behavior, heat transfer, and stress-strain state of a PWR SL pipe. The overall aim of ANL’s environmental fatigue work is to extend the ANL-developed fully mechanistic approach (discussed in the Sections 2 to 7) to component-level fatigue evaluation. For component-level fatigue evaluation and stress analysis, it is essential to know the thermal-mechanical boundary condition. In this work, we have selected the PWR SL pipe as a benchmark component, since it is one of the most vulnerable components in the context of environmental fatigue. The stainless steel SL pipe experiences a higher fatigue usage factor due to thermal stratification associated with temperature difference between its pressurizer (PRZ) end nozzle and hot leg (HL) end nozzle. For stress analysis it is essential to model the complex thermal stratification and then to estimate the nodal temperature in the SL pipe. The stress analysis and fatigue evaluation of SL pipes require CFD, heat transfer (HT), and structural analysis of the SL pipe. In this section three types of ABAQUS finite element models are developed.

- a) Standalone CFD models for preliminary parametric study on CFD solver selection, mesh size effects, etc.
- b) Conjugate or coupled CFD-HT model for SL pipe nodal temperature estimation.
- c) Thermal mechanical stress or structural (ST) analysis for stress-strain estimation.

Figure 8.1 shows the ABAQUS model of the SL and its connection locations with respect to the PRZ and HL. The dimensions of the SL pipe selected based on the data are given in [49]. Schedule 160 pipe with OD = 14 in. (355.6 mm) and thickness = 1.406 in. (35.712 mm) was considered for the SL pipe model. ABAQUS was used for the CFD, HT, and ST analyses. ABAQUS/CFD elements (either hexahedral FC3D8, i.e., 8-noded linear fluid brick element or tetrahedral FC3D4, i.e., 4-node linear fluid tetrahedron element) were used for modeling the inside fluid. ABAQUS/standard hexahedral elements (for ST: eight-noded linear brick element C3D8, and for HT: eight-noded linear brick element DC3D8) were used for outside pipe HT and ST analysis. To avoid longer computations, only the SL pipe and inside fluid between PRZ and HL were considered. Figures 8.2a and 8.2b show the example hexahedral mesh for the inside fluid and pipe, respectively. Figure 8.2a shows typical observation locations, and these results will be discussed in the later part of this section.

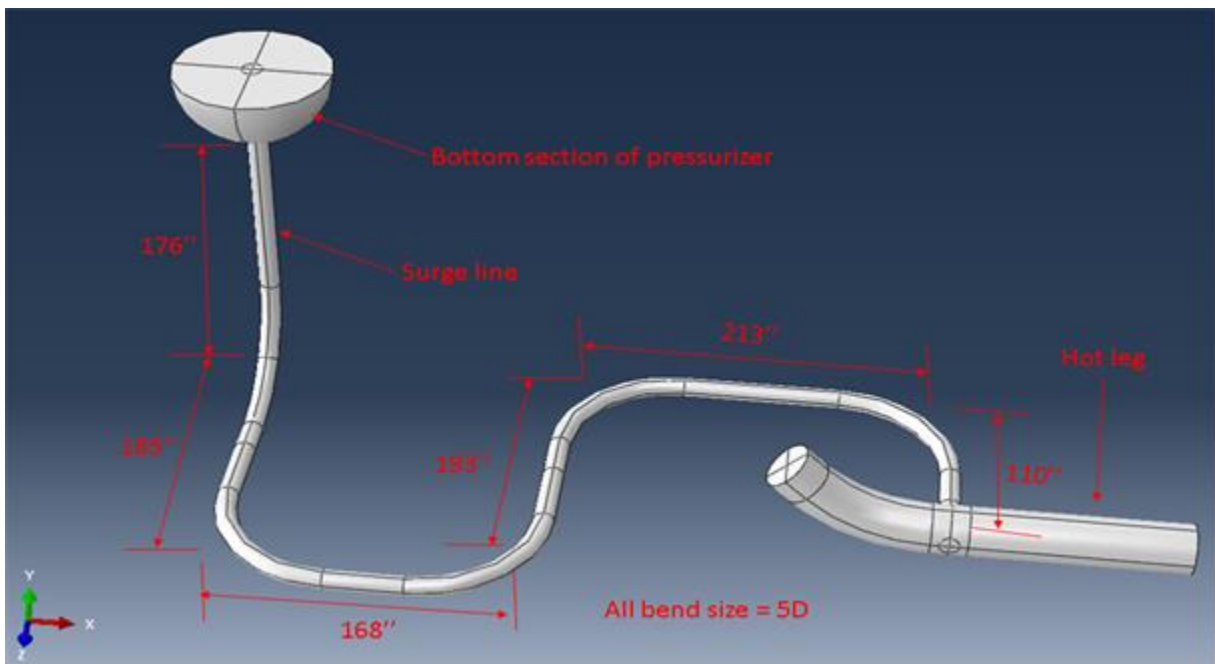


Figure 8. 1 ABAQUS model of surge line that connects the hot leg and pressurizer.

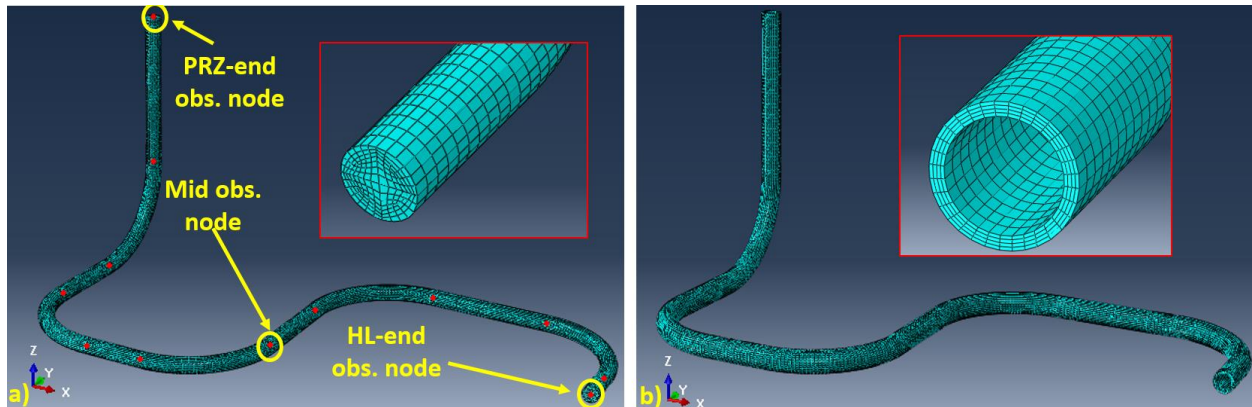


Figure 8. 2 Example hexahedral mesh of (a) SL inside fluid with highlighted observation nodes for which the related results are presented (b) SL outside pipe.

8.2.2 Thermal-mechanical boundary conditions

The SL pipe of a four-loop type PWR was CFD modeled to estimate the wall temperature and thermal stratification (if any) along the length of the SL line. In a PWR the SL pipe connects the hot leg and pressurizer. The major aim of the SL along with the pressurizer is to maintain the primary loop pressure of the PWR. The SL pipe may experience thermal stratification during various stages of plant heat-up, cool-down, and normal operation. To simulate the stratification condition during plant heat-up, cool-down, and normal operation, the flow for entire flow cycles must be modeled. Figure 8.3 shows an example of the PRZ and HL end temperature boundary condition of SL pipe for heat-up, cool-down, and normal operation (only for a few hours). Because this is a preliminary effort, we have not considered the detailed heat-up, cool-down, and normal operation sequences. Rather, only a transient condition is simulated, with the primary aim of performing a parametric study for selecting the appropriate CFD solver, mesh size, CFD-HT modeling capability, etc. This is to save computational time. The full cycle simulation is one of our future tasks. For the discussed model, a simulated situation during the transition from mode-5 (cold shutdown) to mode-4 (hot shutdown) is considered. During this transition, it is assumed that the HL and pressurizer would be at 55 °C and 218.1 °C, respectively. During this period, the temperature difference between the HL and pressurizer is assumed to be highest and can result in a higher thermal stratification effect, which can lead to a higher fatigue usage factor. The mode-5 to mode-4 transition regime is highlighted in Figure 8.3. During this transition, an upset event can lead to in-surge and out-surge flow in the SL, leading to a higher stratification-related fatigue usage factor. In-surge and out-surge conditions can occur during any time, such as plant heat-up, cool-down, and normal operation. However, the temperature difference between the pressurizer and HL governs the extent of thermal stratification and associated increased fatigue usage factor. The CFD, CFD-HT, and ST analysis were performed for the following out-surge and/or in-surge conditions:

- a) *Out-surge condition:* The temperatures of the HL and pressurizer were assumed to be 55 °C and 218.1 °C, respectively. The SL fluid and pipe temperatures were assumed to be 55 °C at initial condition. Due to an upset event, hotter pressurizer water would suddenly flow into the SL.
- b) *In-surge condition:* The temperatures of the HL and pressurizer were assumed to be 55 °C and 218.1 °C, respectively. The SL fluid and pipe temperatures were assumed to be 218.1 °C at the initial condition. Due to an upset event, cooler HL water would suddenly flow into the SL.

The above information was used for setting the thermal boundary condition of the CFD, CFD-HT, and ST models. During the transient conditions, the pressure in the coolant primary circuit is assumed equal to 2.2406 MPa. This is based on the full-cycle pressure information shown in Figure 8.4 (and also based on the temperature versus water saturation pressure curve shown in Figure 8.11). Also, note that prior to the start of the reactor coolant pumps during plant heat-up, the temperature of the coolant in the HL is approximately 55 °C. At that time, the temperature of pressurizer water would be as high as the saturation temperature, which corresponds to the pressure at which the reactor coolant pump can be started [49]. This is approximately 2.2406 MPa. The corresponding coolant temperature of the pressurizer would be 218.1 °C (424.6 °F). During this time, the difference in temperature of the HL and pressurizer would be 163.1 °C, which would be the highest compared to other instances of plant heat-up, cool-down, and normal operation. Because of this higher temperature gradient, the potential and extent of thermal stratification would be highest compared to any other non-accident condition events during plant heat-up, cool-down, and normal operations [49]. For the discussed CFD and CFD-HT models, a water pressure of 2.2406 MPa was set as the reference pressure; however, for the ST model this pressure was set as internal pressure. For the CFD model it is also essential to provide inlet and outlet velocity conditions. The inlet and outlet velocity of SL selected based on the assumed SL and HL mass flow rate. A detail parametric study with different SL and HL flow rates was performed; the details of the related mass flow rate can be found in the later part of this section. For most of the simulations except the parametric study on the effect of different SL flow rates (refer to section 8.3.5), the SL mass flow rate was assumed equal to 50 gpm. However, the actual SL flow rate depends on the plant type and the particular steps followed during the heat-up and cool-down operations. For the HL, the maximum flow rate was assumed to be equal to 69,020 gpm. Note that for a typical 4-loop Westinghouse type reactor [65], the total mass flow rate in the reactor is approximately 869,020 gpm. With this value, the approximate mass flow rate in a HL at 100 % power is assumed equal to $869,020/4=69,020$ gpm. For most of simulation cases except the parametric study on effect of different HL flow rates (refer section 8.3.6), the HL mass flow rate was assumed equal to 3451 gpm (i.e., 5 % of the HL flow rate at 100% power).

In addition to above-mentioned temperature/pressure/velocity boundary conditions for CFD and CFD-HT models, it is also essential to model the displacement boundary condition of the SL pipe for ST analysis. For ST analysis, both the HL and pressurizer end of the SL pipe were constrained in all directions, with all translational and rotational components assumed to be zero. Also, for simplicity the intermediate supports and seismic restraints of the SL are not modeled.

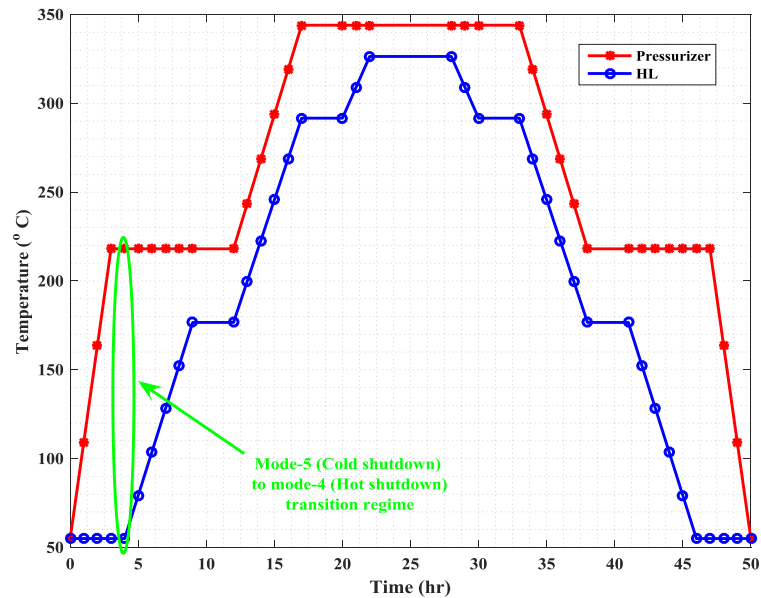


Figure 8. 3 Pressurizer and HL temperature during plant heat-up, cool-down, and normal operation. Mode-5 to Mode-4 transition regime (which is considered in the discussed results) is also highlighted.

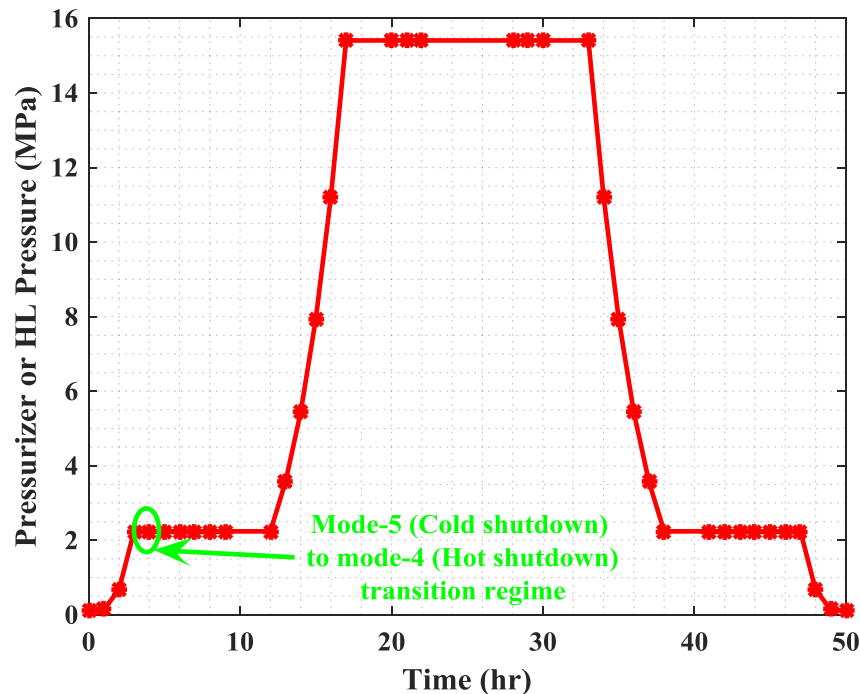


Figure 8. 4 Example pressure history of the primary loop during plant heat-up, cool-down, and normal operation. Mode-5 to Mode-4 transition regime (which is considered in the discussed results) is also highlighted.

8.2.3 Material properties

The CFD model requires values of water properties (Eqs. 8.1-6.15) such as density (ρ), dynamic viscosity (μ), specific heat capacity at constant pressure (C_p), and thermal conductivity (k). Note that we assume an incompressible flow condition with constant density. However, temperature-dependent densities were modeled with the Boussinesq approximation (Eq. 8.14). Figure 8.5 shows a comparison of the temperature-dependent density (ρ) of water determined from the original IAEA data base [66] and Boussinesq approximation-based estimated densities. The Boussinesq approximation-based densities were estimated by considering fixed and variable volume expansion coefficients. The fixed or temperature-dependent (variable) volume expansion coefficients (β) of water were estimated with the Boussinesq approximation (Eq. 8.14) and original temperature-dependent density shown in Figure 8.5. Note that, for estimating the expansion coefficients (β) the reference temperature was considered to be 55 °C. The corresponding density was considered as the reference density. The fixed expansion coefficients (β) was estimated as at a temperature of 136.55 °C, which is the mid temperature between 55 °C and 218.1 °C. Figure 8.6 shows the estimated temperature-dependent volume expansion coefficients (β) of water. Figures 8.7 to 8.11 show other required water properties such as dynamic viscosity (μ), heat capacity (C_p), thermal conductivity (k), Prandtl number, and water saturation pressure, respectively. For coupled CFD-HT it is also required to provide the thermal properties of SL metallic pipe (refer to Eq. 8.16). The respective temperature-dependent solid/pipe properties [1], such as thermal conductivity (κ^S) and specific heat capacity (C_p^S), are shown in Figures 8.12 and 8.13. Note that 316 SS is considered as the SL pipe material. The solid/pipe density (ρ^S) was assumed fixed and equal to 8000 kg/m³. The ST analysis requires other properties, such as thermal expansion coefficients and elastic-plastic properties of 316 SS pipe material. Figure 8.14 shows the temperature-dependent expansion coefficient (α^S) of 316 SS pipe material. The elastic-plastic material used for the transient stress analysis under out-surge and in-surge conditions (refer section 8.5) is based on the ANL-conducted tensile tests. The related elastic-plastic properties are given in Table 8.1. We also used ANL's cyclic tests based on elastic-plastic properties for the cyclic stress analysis (discussed in Section 9). The related input material properties are discussed in Section 9.

Table 8. 1 Elastic-plastic material properties for 316SS estimated from ANL tensile test data

Temp. (°C)	Elastic modulus (GPa)	Elastic limit as yield limit			0.05% offset strain limit as yield limit			0.1% offset strain limit as yield limit			0.2% offset strain limit as yield limit		
		σ_y (MPa)	C1 (MPa)	γ_1	σ_y (MPa)	C1 (MPa)	γ_1	σ_y (MPa)	C1 (MPa)	γ_1	σ_y (MPa)	C1	γ_1
22	175.1	183.61	34159	292.9	217.41	11927	100.71	233.63	7779.4	61.011	249.58	5420.6	39.88
300	157.92	130.73	10085	149.97	145.03	4673.3	52.043	150.72	3714.3	34.023	155.77	3234.2	25.038

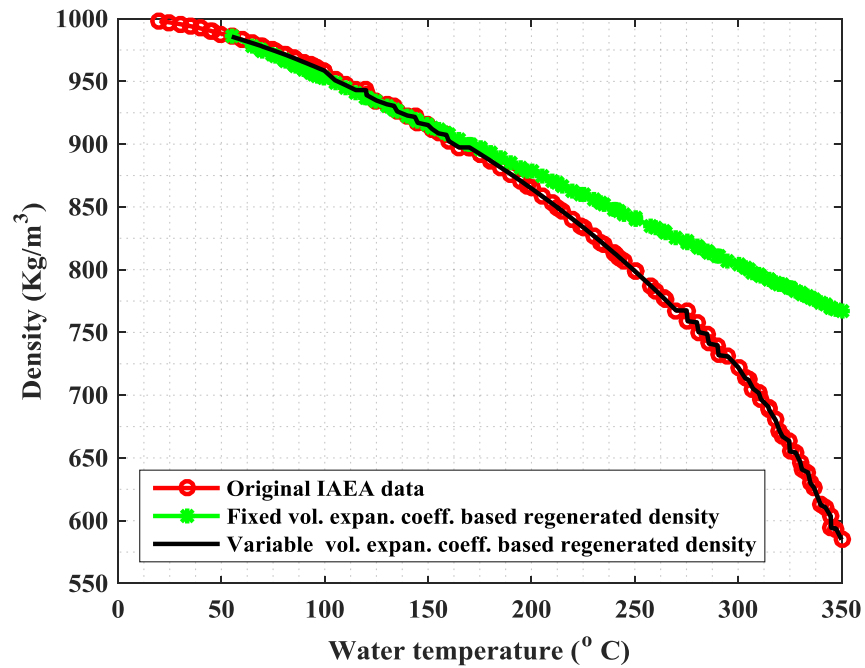


Figure 8. 5 Temperature-dependent density (ρ) of water.

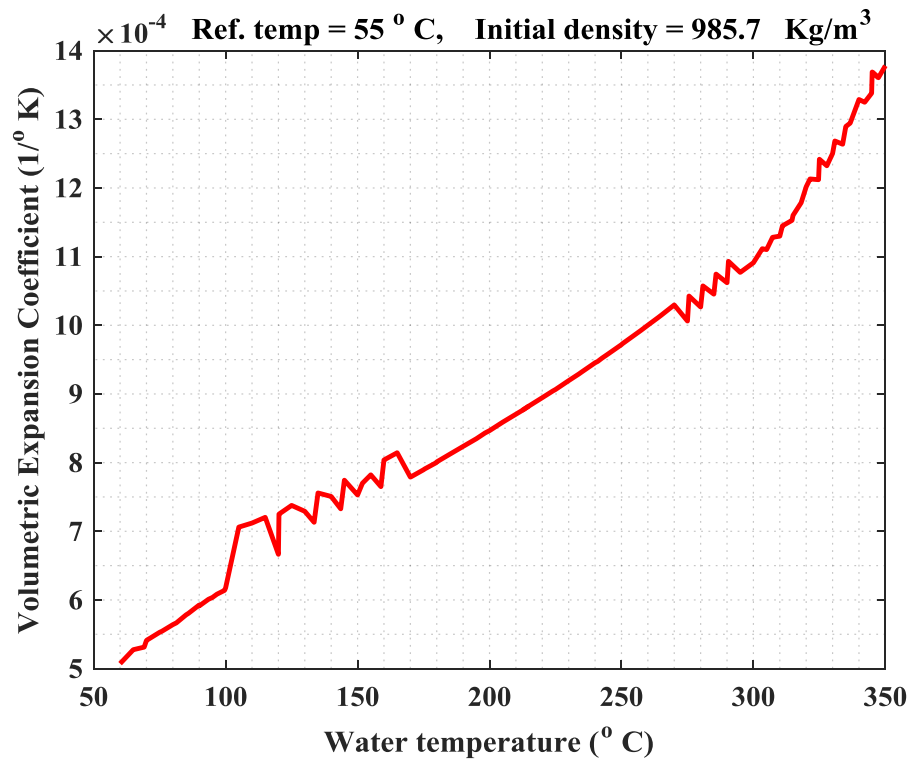


Figure 8. 6 Temperature-dependent volume expansion coefficient (β) of water. Estimated using Boussinesq approximation (Eq. 8.14) and temperature-dependent density.

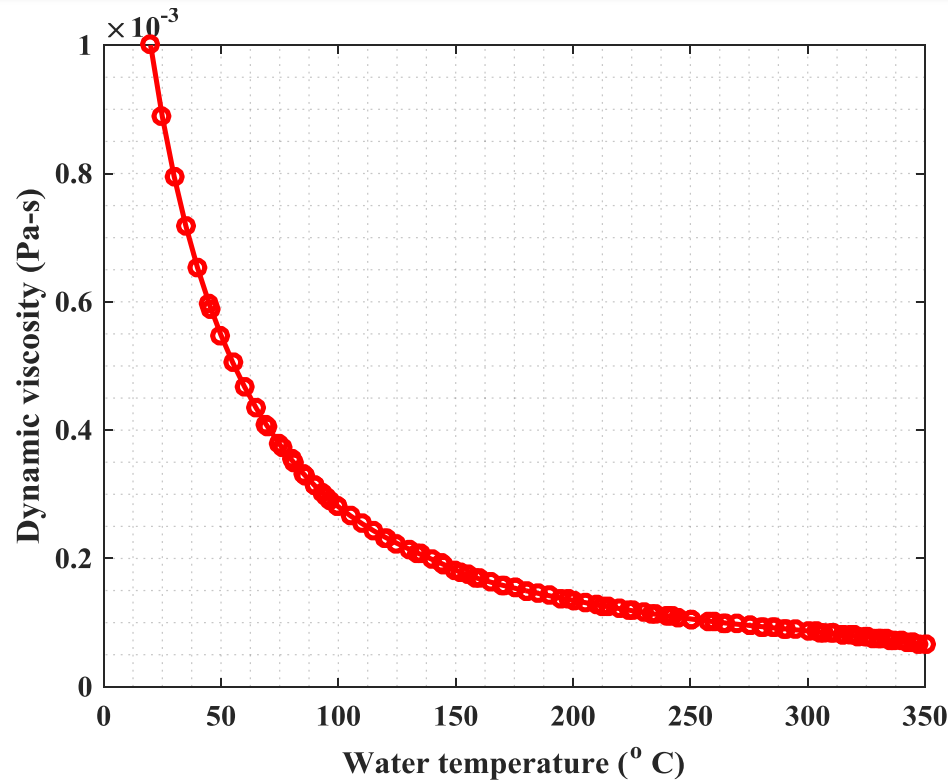


Figure 8. 7 Temperature-dependent dynamic viscosity (μ) of water.

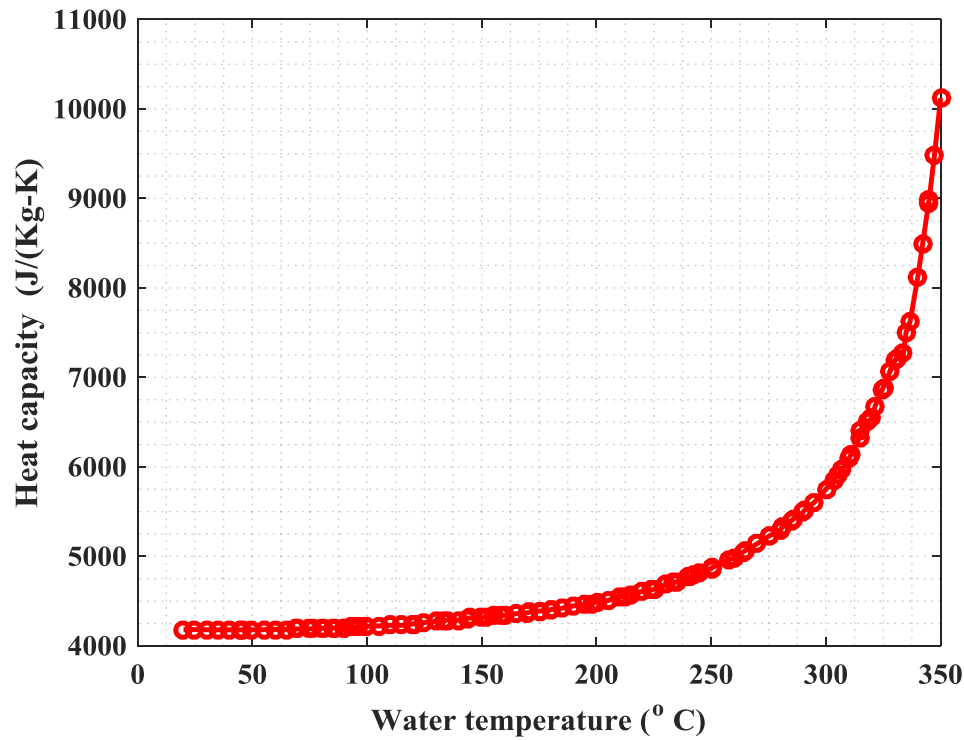


Figure 8. 8 Temperature-dependent heat capacity (C_p) of water.

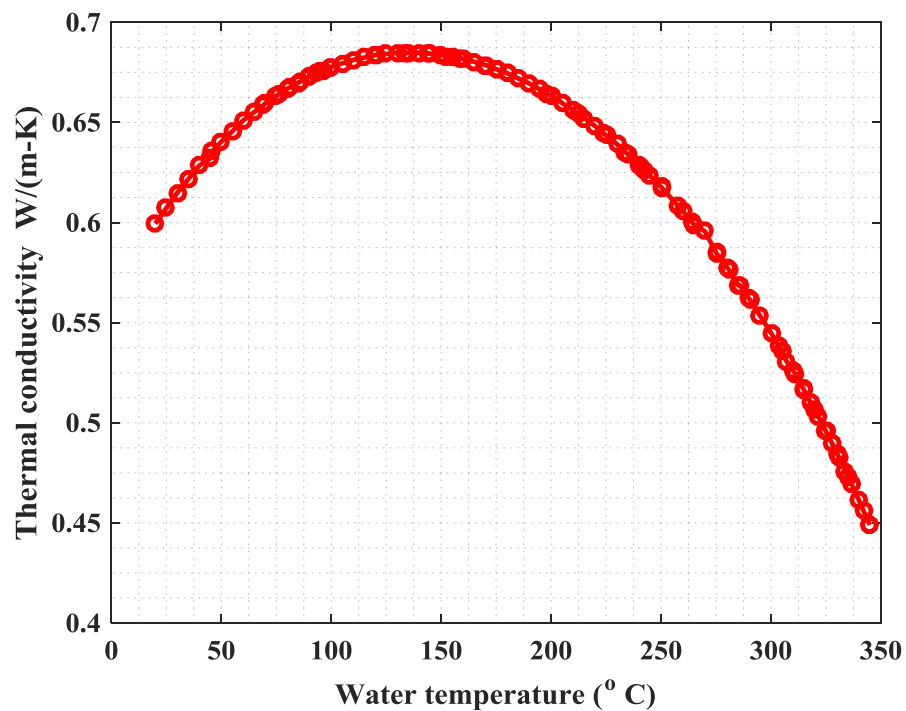


Figure 8. 9 Temperature-dependent thermal conductivity (k) of water.

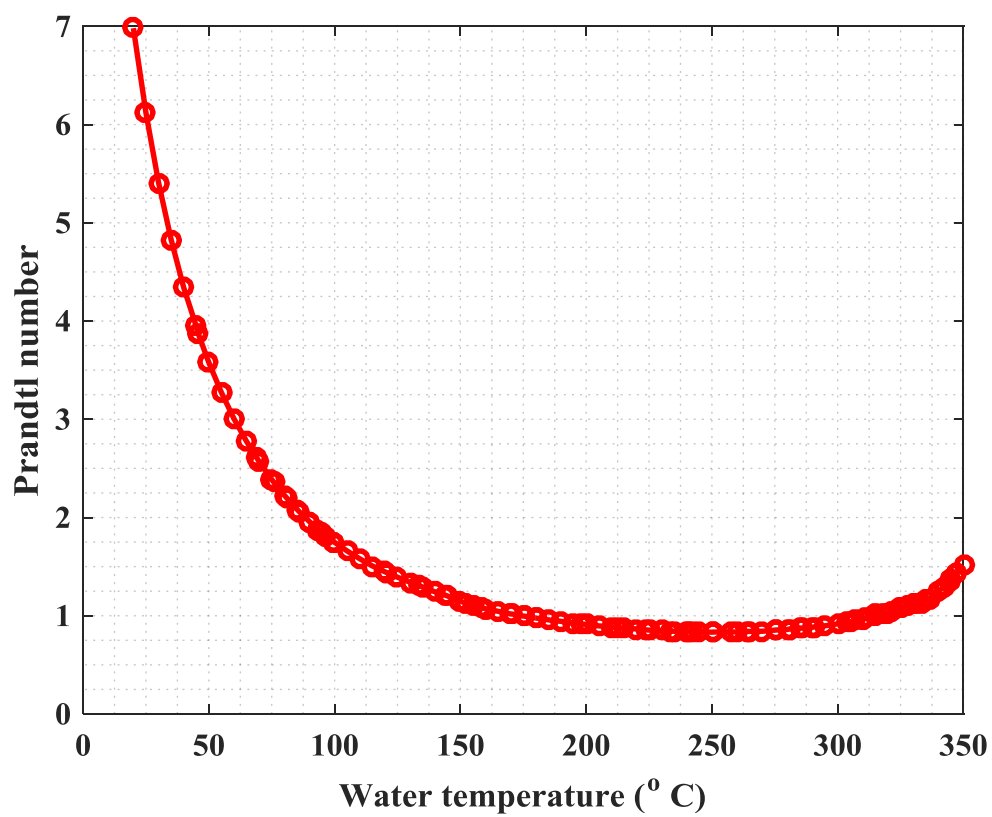


Figure 8. 10 Temperature-dependent Prandtl number.

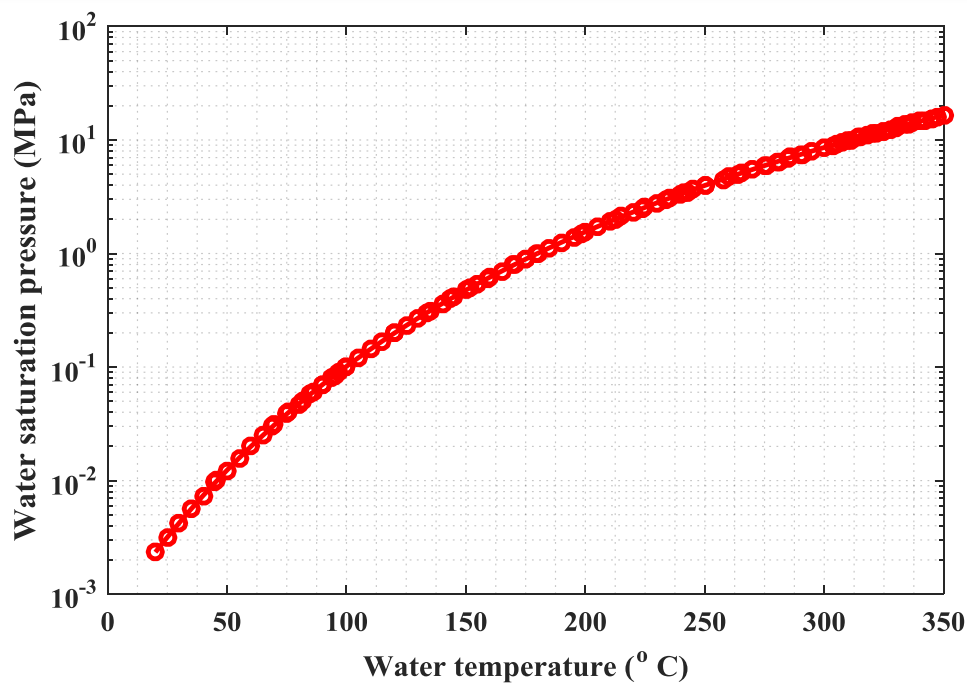


Figure 8. 11 Temperature-dependent water saturation pressure.

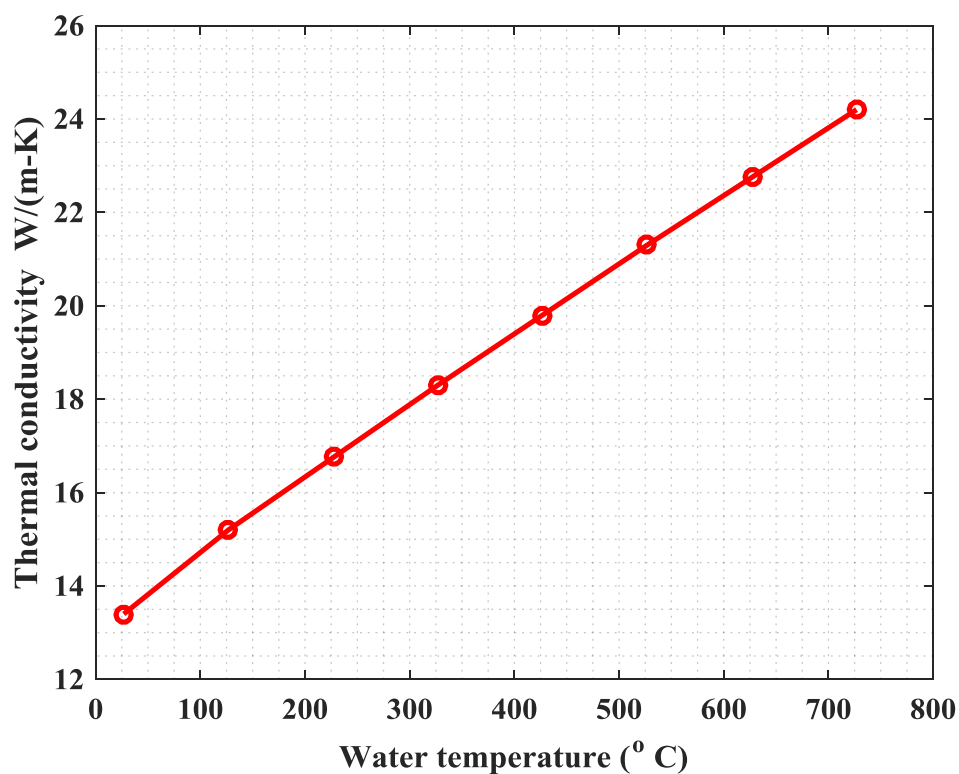


Figure 8. 12 Temperature-dependent thermal conductivity (κ^S) of 316 SS.

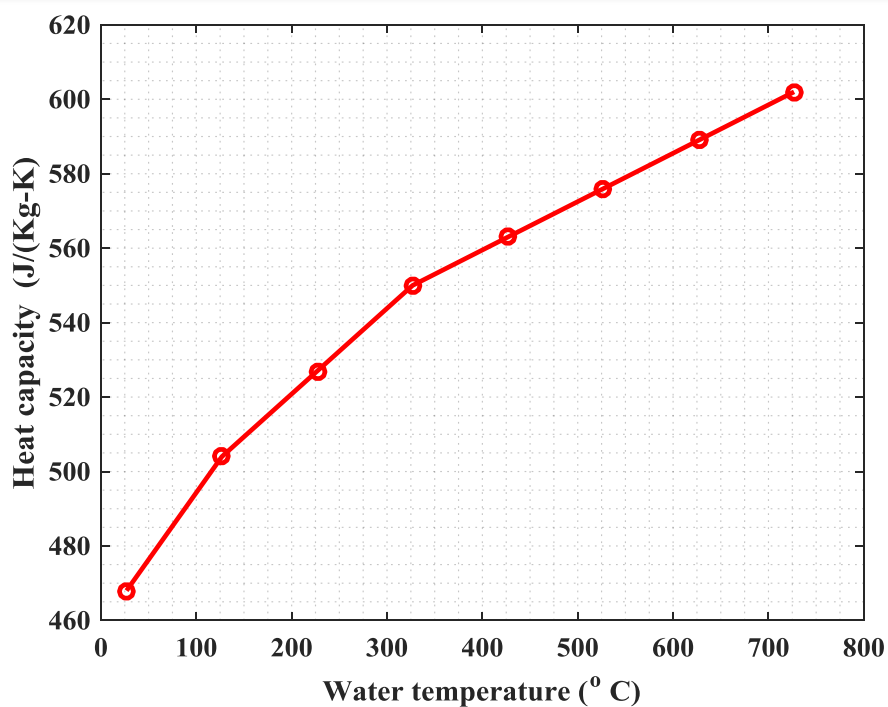


Figure 8.13 Temperature-dependent specific heat capacity (C_p^S) of 316 SS

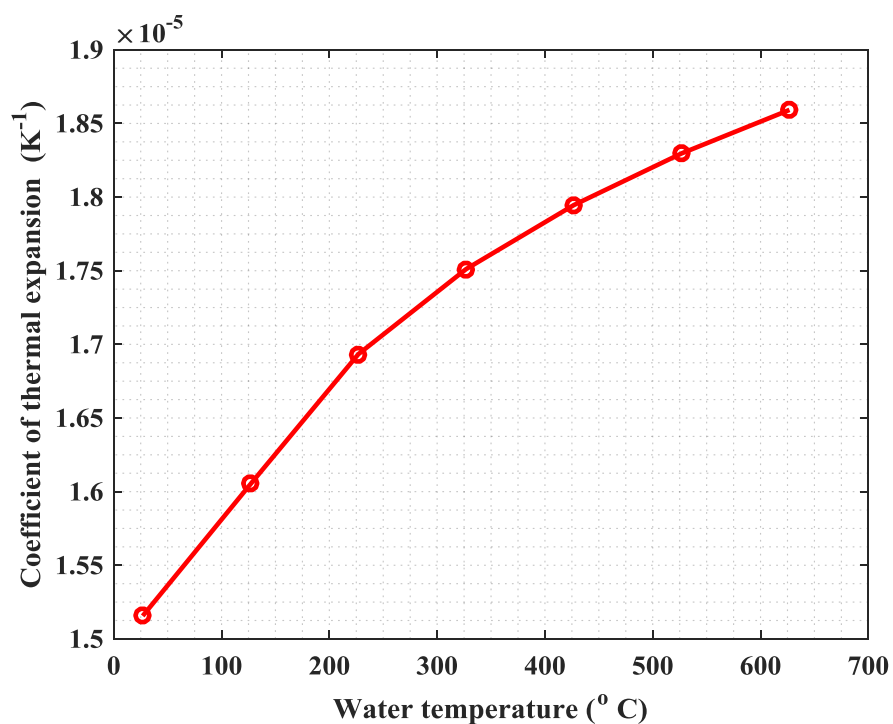


Figure 8.14 Temperature-dependent coefficient of thermal expansion (α^S) of 316 SS .

8.3 Stand-alone CFD Results

The first few stand-alone CFD simulations were performed for parametric evaluation of the CFD model under different conditions. Stand-alone CFD models are computationally less expensive compared to CFD-HT fluid-structure-interaction models. Parametric studies were performed for the following cases discussed below.

8.3.1 Effect of different type of CFD solver

In our last half yearly report we presented some preliminary CFD results using only the ILES type solver. Although ILES type solvers are used for industrial application, they may not capture the turbulence behavior of SL flow. In this work two additional CFD models (specifically designed to handle turbulence), such as Spalart-Allmaras (Eq. 8.8) and $k - \epsilon$ (Eq. 8.9 and 8.10) models, are studied. In our last report (ANL/LWRS-17/01) we presented preliminary CFD simulation results under a simulated full reactor cycle. However, we had decided to first perform the parametric study of different solvers and their efficacy under transient conditions. For the purpose of the CFD solver parametric study, the out-surge condition (refer to section 8.2.2 for boundary conditions) was simulated. Figure 8.15 shows the comparative results. For example, Figures 8.15a1 and a2, respectively, show the temperature contour from the $k - \epsilon$ model simulation (left inset figures show temperature iso-surfaces near the HL end of SL) at end of 500 s and the temperature-time history at different nodes (along the length of SL, as shown in Figure 8.2a). Figures 8.15(b1 and b2 and c1 and c2 show the corresponding results obtained by using the Spalart-Allmaras and ILES models. Figure 8.15 indicates that the ILES type solver gives completely different results compared to the $k - \epsilon$ and Spalart-Allmaras models. It also shows that both $k - \epsilon$ and Spalart-Allmaras models give similar results. Figure 8.16 shows a direct comparison of the temperature history at the PRZ-end node, mid node, and HL-end node of the SL, which are simulated using the $k - \epsilon$, Spalart-Allmaras, and ILES CFD models. Previous work [50-63] used $k - \epsilon$ or variant of $k - \epsilon$ type CFD models for the SL or pipe for simulations. Based on the results reported in this section (Figures 8.15 and 8.16) and literature data, it seems that the $k - \epsilon$ type solver is a better option compared to the ILES type solver. For the results discussed onward, only the $k - \epsilon$ type solver was used for obtaining the stand-alone CFD or CFD-HT fluid-structure interaction models. Note that with use of 8 CPU (in a Dell Precision Tower 7810 workstation), the approximate simulation time for the $k - \epsilon$, Spalart-Allmaras, and ILES solvers were 31.9, 23.9, and 29 min, respectively.

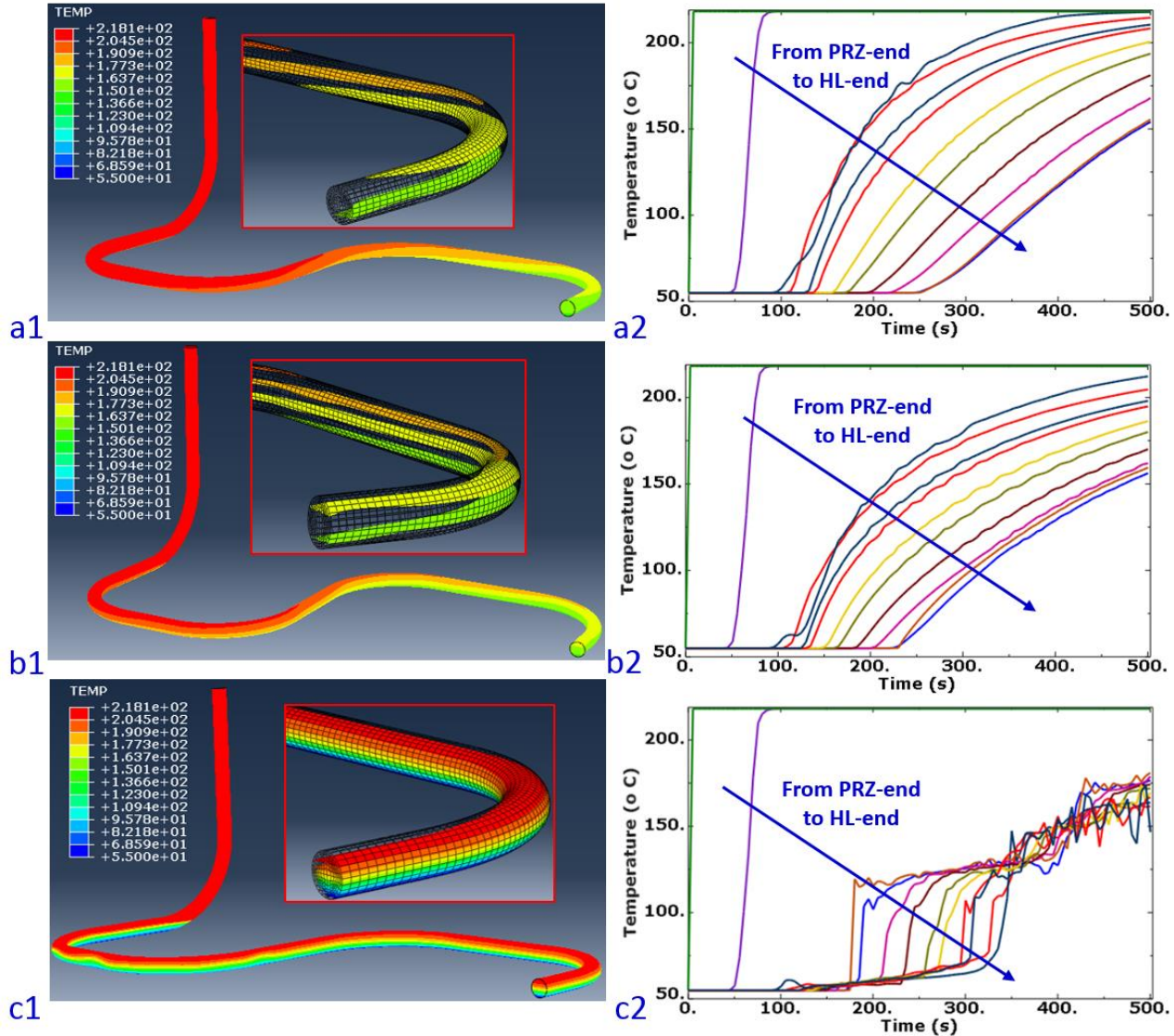


Figure 8. 15 CFD simulation results of SL for out-surge case. Sub figure pairs (a1 and a2), (b1 and b2), and (c1 and c2) show temperature contours (left inset figures show temperature iso-surfaces near HL end of SL) at end of 500 s and temperature-time history at different nodes (along the length of SL as shown in Figure 8.2a) for $k-\epsilon$, Spalart-Allmaras, and ILES models.

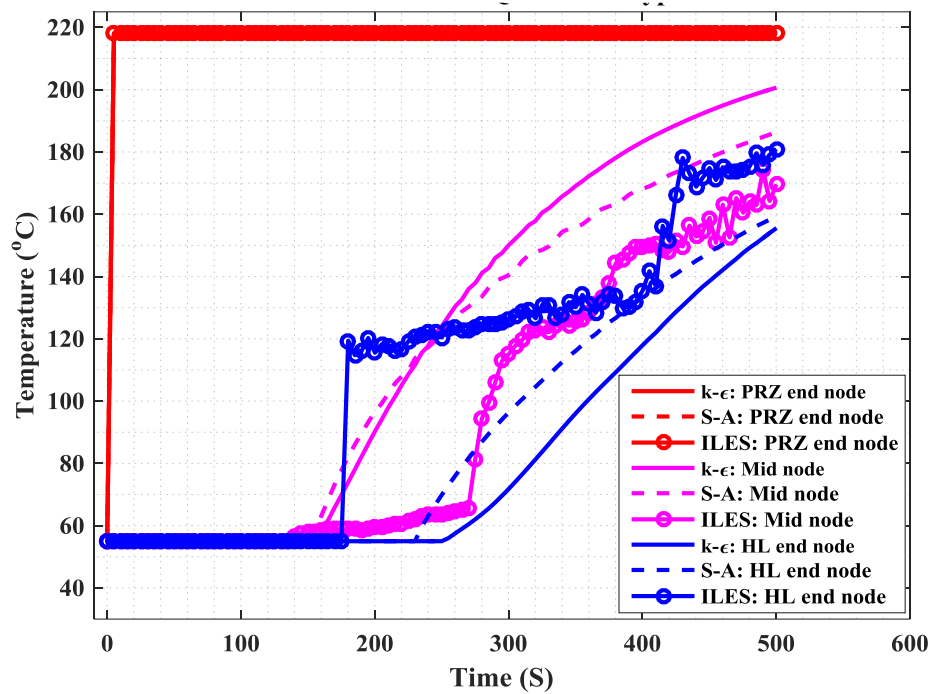


Figure 8. 16 Comparison of temperature history at PRZ-end node, mid node, and HL-end node of SL, which are simulated by using $k - \epsilon$, Spalart-Allmaras, and ILES stand-alone CFD models.

8.3.2 Effect of finite element type

All the results discussed in the above section were obtained from CFD models based on a hexahedral fluid element (FC3D8: 8-noded linear fluid brick element). To study the effect of finite element type on CFD results, we used a model that simulated a tetrahedral fluid element (FC3D4: a 4-node linear fluid tetrahedron). Both the hexahedral and tetrahedral meshes were generated using elements with the same maximum length of 35.71 mm and 62.492 mm along the circumferential and axial directions, respectively. The radial direction length was chosen between 8.9275 mm and 35.71 mm. These element size selections resulted in an average aspect ratio of 3.8 and 2.72 for the hexahedral and tetrahedral mesh, respectively. With this element size selection, the number of elements for hexahedral mesh was 55,480. For tetrahedral mesh the number of elements was 158,564. Figure 8.17 shows the temperature contour (left inset figures show temperature iso-surfaces near HL end of SL) at end of 500 s and temperature-time history at different nodes (along the length of SL, as shown in Figure 8.2a). Figure 8.18 shows a direct comparison of the temperature history at the PRZ-end node, mid node, and HL-end node of the SL, which are simulated by using hexahedral and tetrahedral FE meshes. Comparing Figure 8.17 (a1 and a2) with Figure 8.15 (a1 and a2) indicates that hexahedral and tetrahedral mesh produce similar results, although there is no exact match, as can be seen from Figure 8.18. However, while the hexahedral mesh-based model took 31.9 min of simulation time (in a Dell Precision Tower 7810 workstation), the corresponding tetrahedral mesh-based model took much longer, 11 h 45 min. This comparison shows that hexahedral mesh is economical in computation time compared to the tetrahedral mesh, at least for the discussed SL-CFD models. So for discussed model results in the remainder of the section, only the hexahedral mesh was used.

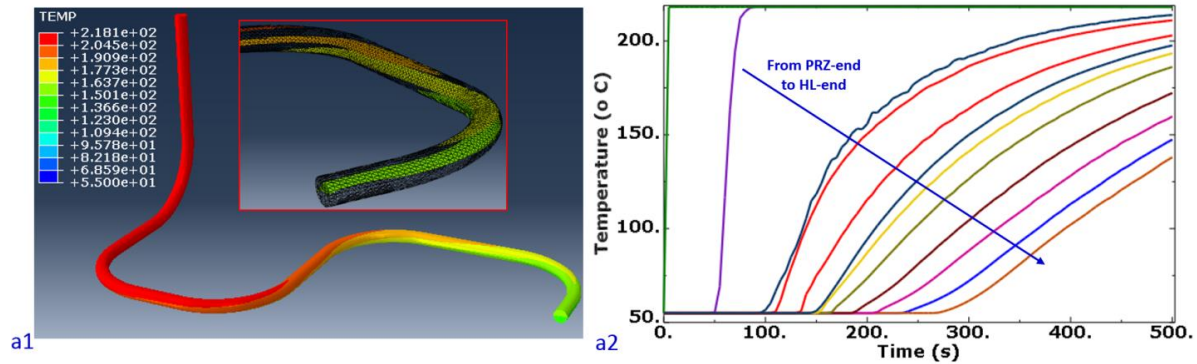


Figure 8. 17 CFD simulation results of SL with tetrahedral mesh: (a1) temperature contour (left inset figures show temperature iso-surfaces near HL end of SL) at end of 500 s, (a2) temperature-time history at different nodes (along the length of SL as shown in Figure 8.2a)

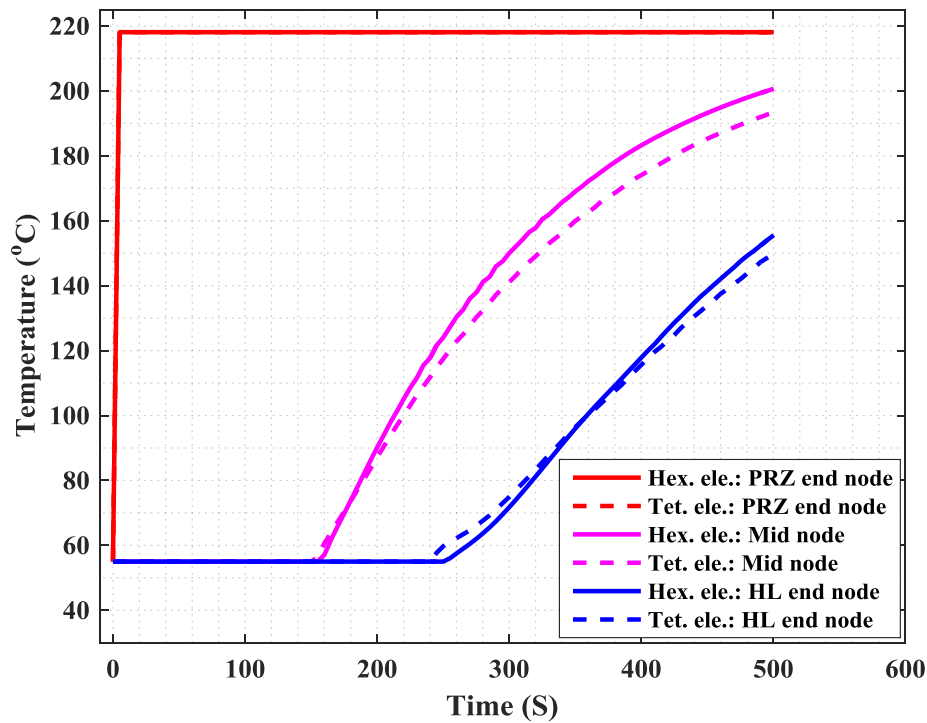


Figure 8. 18 Comparison of temperature history at PRZ-end node, mid node, and HL-end node of SL, which are simulated using hexahedral and tetrahedral meshes.

8.3.3 Effect of finite element size

3.8.), Figures 8.19a1 and a2 were obtained from a finer mesh model with total 167,640 hexahedral elements. (The maximum lengths along the circumferential and axial directions are 35.71 mm and 31.246 mm, respectively, and the radial direction length is between 8.9275 mm and 35.71 mm. The average aspect ratio of elements = 2.01.) Figure 8.20 shows a direct comparison of the temperature history at the PRZ-end node, mid node, and HL-end node of the SL, which are simulated by using the above-mentioned coarser mesh and finer mesh models. From Figures 8.15, 8.19, and 8.20, we concluded that the coarser and finer mesh model produce very similar results, although the finer mesh model took much more computational time (CPU time = 2.156 h) compared to the finer mesh model (CPU time = 31.9 min). With this observation, the coarser mesh model with 55,480 hexahedral elements was selected for both CFD and CFD-HT simulations for all further discussed results. Note that our overall aim was to perform computationally intensive CFD-HT simulations (results discussed in the later part of this section), and full-cycle CFD-HT and ST simulation is one of our future tasks. Hence, we tried to restrict the mesh size as much as possible, while maintaining the quality of the results.

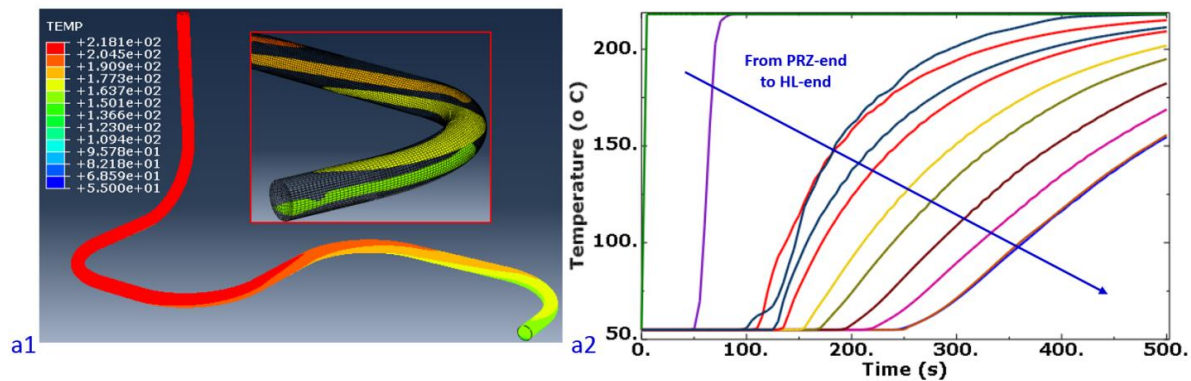


Figure 8. 19 CFD simulation results of SL with finer hexahedral mesh: (a1) temperature contour (left inset figures show temperature iso-surfaces near HL end of SL) at end of 500 s and (a2) temperature-time history at different nodes (along the length of SL as shown in Figure 8.2a).

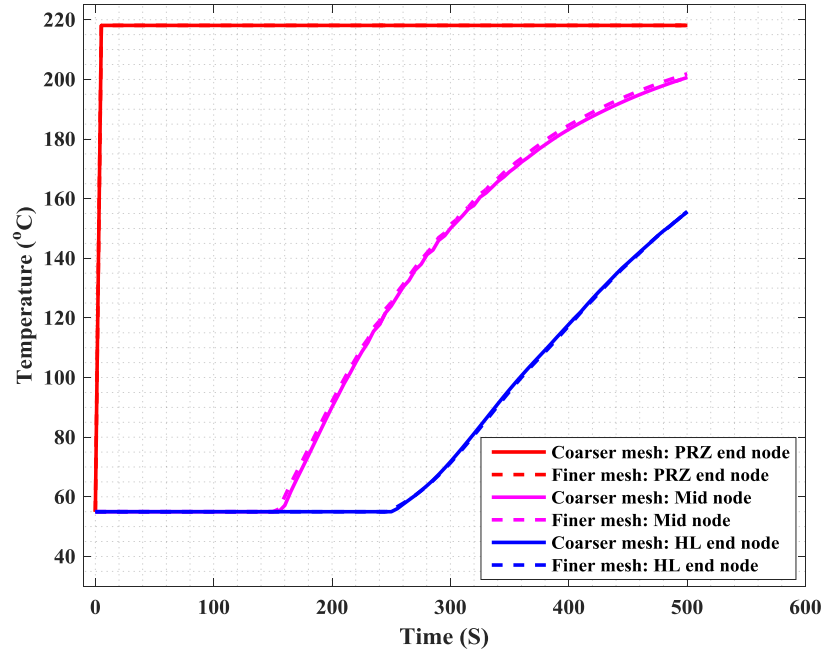


Figure 8. 20 Comparison of temperature history at PRZ-end node,, mid node, and HL-end node of SL, which are simulated by using coarser and finer hexahedral meshes.

8.3.4 Effect of buoyancy and variable density

Natural convection or buoyancy has a significant effect on SL flow, because the pressurizer that connects one end of the SL is at higher level compared to the majority of the SL pipes (refer Figure 8.1). Also, variable temperature associated with stratified flow can lead to variable density flow in SLs. However, ABAQUS/CFD software doesn't allow modelling of variable density as fluid properties. To alleviate this issue, variable or temperature-dependent density was modeled through use of temperature-dependent volumetric expansion coefficients. As mentioned in section 8.1, this is to model the buoyancy term $\rho \mathbf{g}$ in Eq. 8.13. The equivalent volumetric thermal expansion coefficients β were estimated with the Boussinesq approximation (Eq. 8.14). To study the effect of the buoyancy term $\rho \mathbf{g}$ in Eq. 8.13, three CFD model cases were examined: (1) variable β (which can equivalently model variable density), (2) constant β (which can equivalently model constant density), and (3) no value for β (which can equivalently model without modeling any buoyancy effect). Note that all the results discussed earlier in this section are based on using incompressible CFD models, but with variable β . For example, the results shown in Figure 8.15a1 and a2 are from a model using a variable β out-surge case. These figures show the temperature contour at the end of 500 s and the temperature-time history at different nodes (along the length of SL as shown in Figure 8.2a). Figure 8.21 a1 and a2 and b1 and b2 show the corresponding results obtained from a constant β CFD model and a model with no buoyancy effect ($\beta = 0$). Figure 8.22 shows a direct comparison of the temperature history at the PRZ-end node,, mid node, and HL-end node of the SL, which are simulated by using variable β , constant β , and $\beta = 0$, respectively. Figures 8.15, 8.21, and 8.22 show that temperatures simulated from the model with $\beta = 0$ are much different compared to mode-l with

variable and constant β . This difference is because the buoyancy effect is not modeled, although there is a significant effect of gravity or natural convection on the SL flow due to the high position of the pressurizer with respect to the HL.

Figures 8.15a1 and a2 and 8.21a1 and a2 indicate that the constant β model gives similar results as the variable β model. The similarity in results is due to the selected simulation temperature range (55 °C to 218.1 °C), for which variable β does not play much of a role. This is more evident from Figure 8.5, which shows a comparison of regenerated density using variable β with regenerated density using constant β . This figure indicates that, within the selected simulation temperature range of 55 °C to 218.1 °C, the density curve for temperature versus constant β is almost identical with that for temperature versus variable β . For the constant β case, the value of β was selected at a temperature of 136.55 °C, which is the mid temperature between 55 °C and 218.1 °C. Ideally, for this transient simulation with temperature range of 55 °C to 218.1 °C, selection of β at 136.55 °C would give similar results as variable β models. However, for better accuracy, the variable β model was selected for discussed results in the remainder of the section.

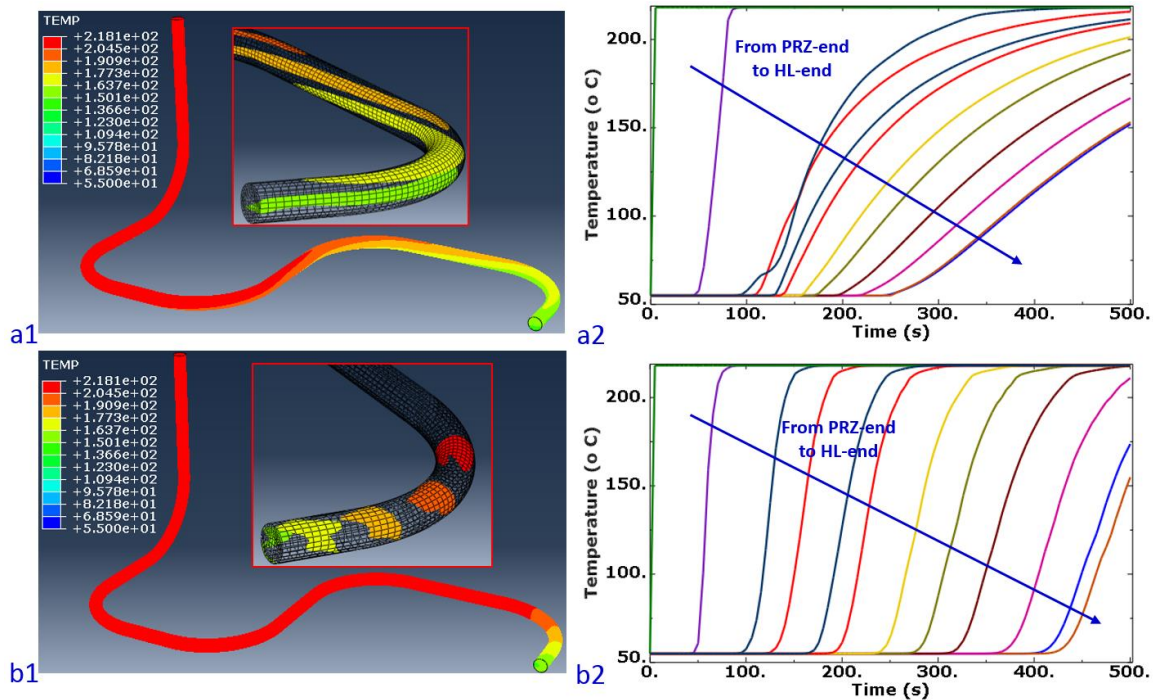


Figure 8. 21 CFD simulation results of SL for out-surge case. Figure pairs (a1 and a2), (b1 and b2), and (c1 and c2) show temperature contours (left inset figures show temperature iso-surfaces near HL end of SL) at end of 500 s and temperature-time-history at different nodes (along the length of SL, as shown in Figure 8.2a) for $\beta = \text{constant}$ and $\beta = 0$ models.

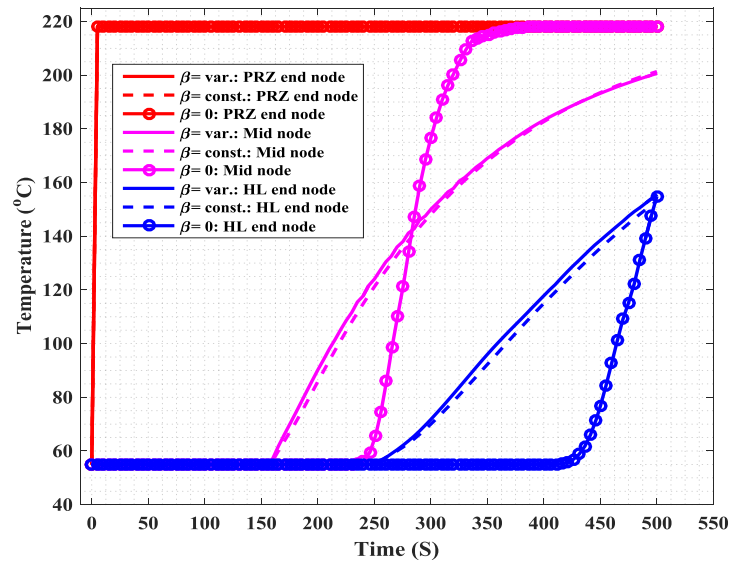


Figure 8. 22 Comparison of temperature history at PRZ-end node, mid node, and HL-end node of SL, which are simulated by using model with $\beta = f(\theta)$, $\beta = \text{constant}$, and $\beta = 0$.

8.3.5 Effect of SL mass flow rate

The SL flow rate can significantly affect the extent of thermal stratification. The flow rate in SL varies according to plant operating procedures and can vary widely from plant to plant. A flow rate of 25-100 gpm is reported in the literature [50-63]. We selected a similar flow rate for the parametric studies discussed in this section. To understand the effect of SL flow rate, stand-alone CFD simulations were performed with SL flow rates of 10 gpm, 50 gpm, 100 gpm, and 200 gpm. For this parametric study when the SL flow rate was varied, the HL flow rate was assumed to be 5% of the full power flow with a flow rate of 3451 gpm. Note that at 100% power, the flow rate at each HL is approximately 69,020 gpm (refer to section 8.2.2). A parametric study for the effect of HL flow rate follows.

Figures 8.23, 8.24, and 8.25 show the results related to the parametric study of SL mass flow rate. For example, Figure 8.23 shows the temperature contour of the SL obtained by considering different SL mass flow rates. Figure 8.24 shows the corresponding temperature history at selected nodes of the SL (as highlighted in Figure 8.2). From Figure 8.23 and 8.24, it clearly can be seen that a substantial effect is associated with SL mass flow rate. As the flow rate increases, the extent of stratification decreases. Figure 8.25 shows a direct comparison of temperature histories (at mid node of SL) obtained from different cases. The curves indicate that, as the mass flow rate of SL increases, the rate of the temperature rise increases. This leads to a faster spread of high temperature fluid (from pressurizer) along the length of the SL, leading to lesser stratification duration. This type of information can be used as a mitigation strategy to reduce thermal stratification related to fatigue damage in SL pipes. However, faster flow can lead to thermal shock that could be more dangerous than a lower flow rate. Exhaustive CFD, HT, and ST analyses are

required to ascertain the extent of associated thermal fatigue damage (or usage factor). However, this is not the main scope of the discussed work.

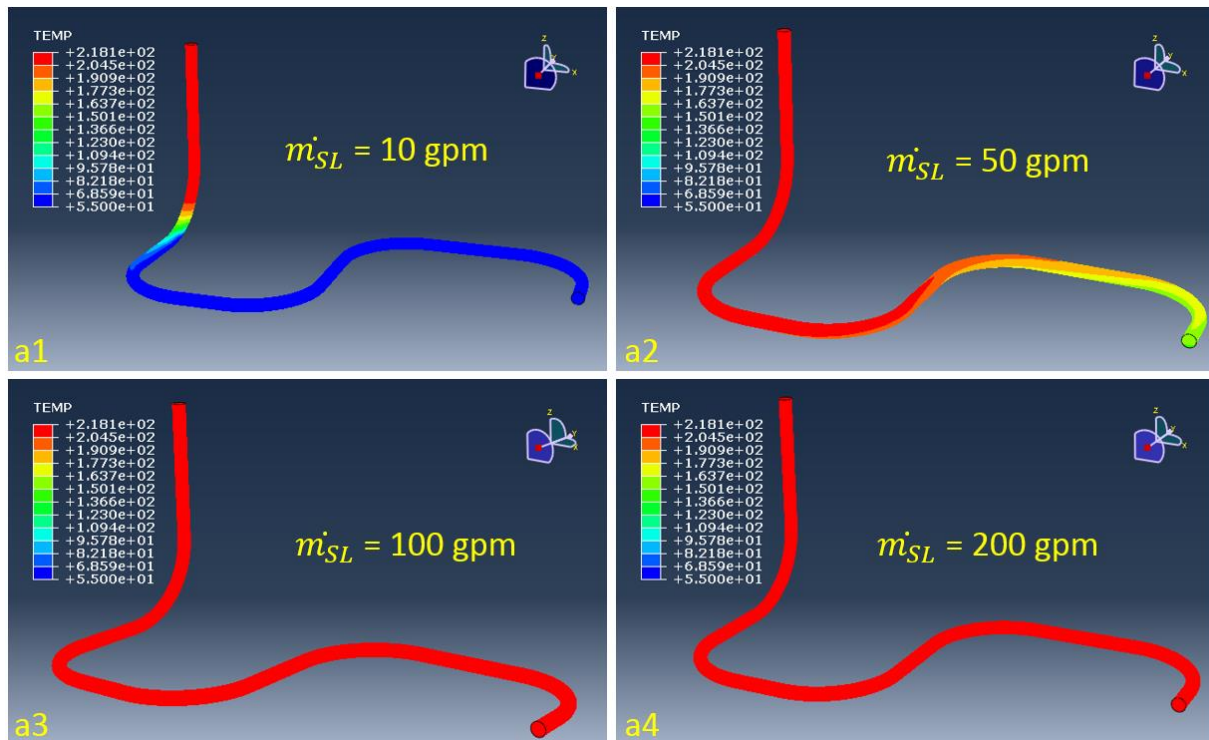


Figure 8. 23 SL temperature at end of 500 s for out-surge case with SL mass flow rate (a1) 10 gpm, (a2) 50 gpm, (a3) 100 gpm, and (a4) 200 gpm.

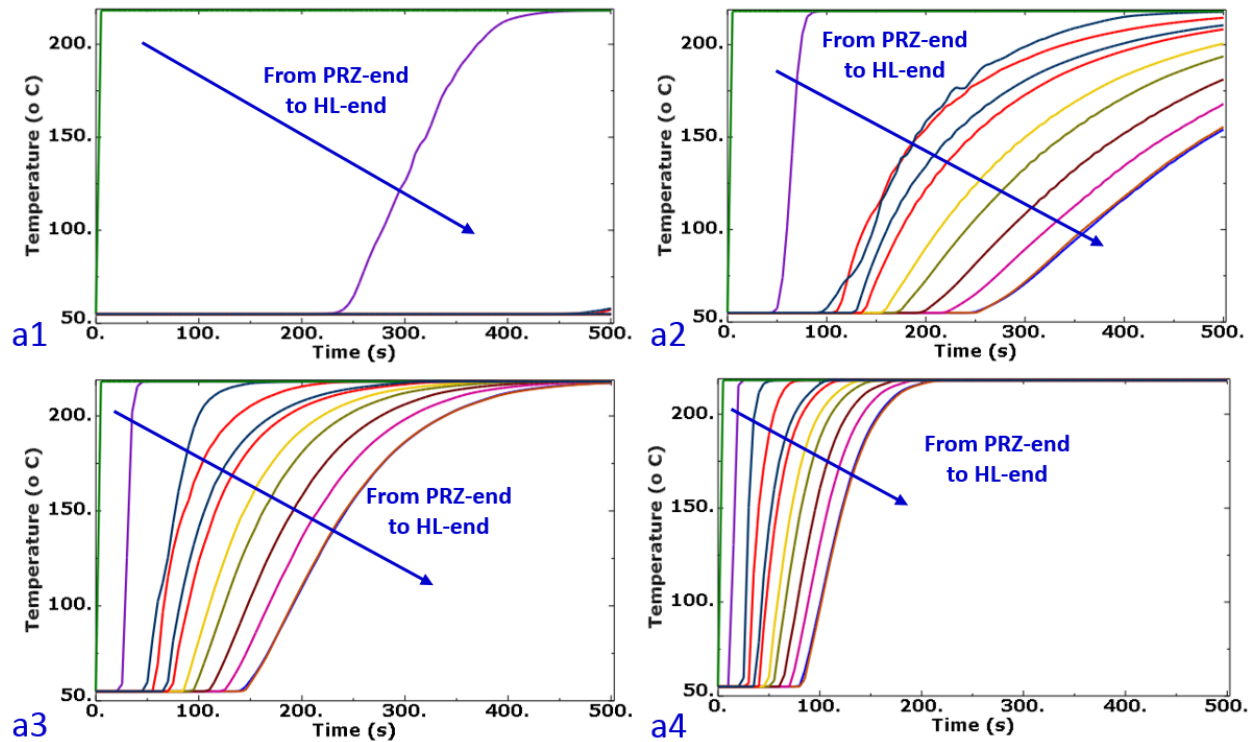


Figure 8. 24 SL temperature history for out-surge case with SL mass flow rate (a1) 10 gpm, (a2) 50 gpm, (a3) 100 gpm, and (a4) 200 gpm.

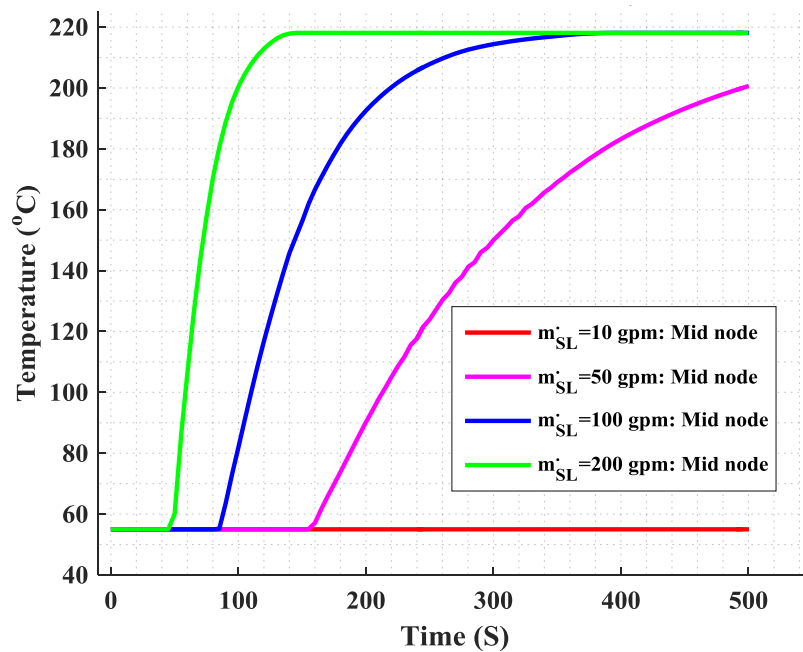


Figure 8. 25 Comparison of temperature history at a mid-node (refer to Figure 8.2a) of SL, which is simulated with 10 gpm , 50 gpm, 100 gpm, and 200 gpm of SL mass flow rate.

8.3.6 Effect of HL mass flow rate

In addition to the effect of the SL mass flow rate, the effect of the HL mass flow rate was studied. CFD models with HL flow rate equivalent to 0% power ($\dot{m}_{HL} = 0$ gpm), 5% power ($\dot{m}_{HL} = 3451$ gpm), 50% power ($\dot{m}_{HL} = 34,510$ gpm), and 100% power ($\dot{m}_{HL} = 69020$ gpm) were simulated. While the HL mass flow rate was varied (for the above discussed cases), the mass flow rate of SL was kept fixed at 50 gpm. Figures 8.26, 8.27, and 8.28 show the related simulation results. Figure 8.26 shows the temperature contour of the SL obtained by considering different HL mass flow rates. Figure 8.24 shows the corresponding temperature histories at selected nodes of the SL (as highlighted in Figure 8.2). Figure 8.28 shows a direct comparison of temperature histories (at mid-node of SL) obtained from the above-mentioned cases. These figures indicate that the HL flow rate has no significant effect on the extent of stratification. Note that, for the discussed model, the SL and HL junctions (refer to Figure 8.1) were kept perpendicular to each other. This condition could be a reason why there is not much effect of HL velocity on extent of thermal stratification in the SL pipe. Ideally, other cases could have been simulated with different SL-HL joining angles, but it is not our primary goal to study each and every case. Through the discussed work we want to make a case that different variables may or may not affect the extent of thermal stratification in SL pipes. Hence, it is required to consider those variables for more accurate stress analyses and fatigue evaluations.

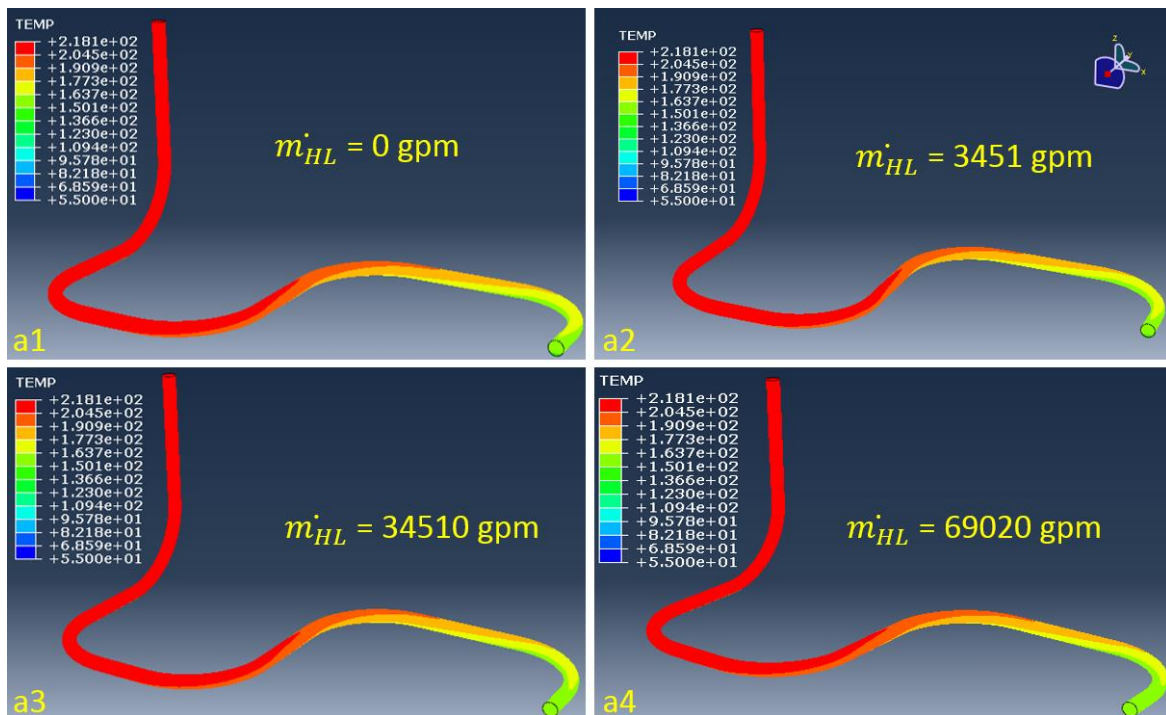


Figure 8. 26 SL temperature at end of 500 s for out-surge case with HL mass flow rate (a1) 0 gpm, (a2) 3451 gpm, (a3) 34,510 gpm, and (a4) 69,020 gpm.

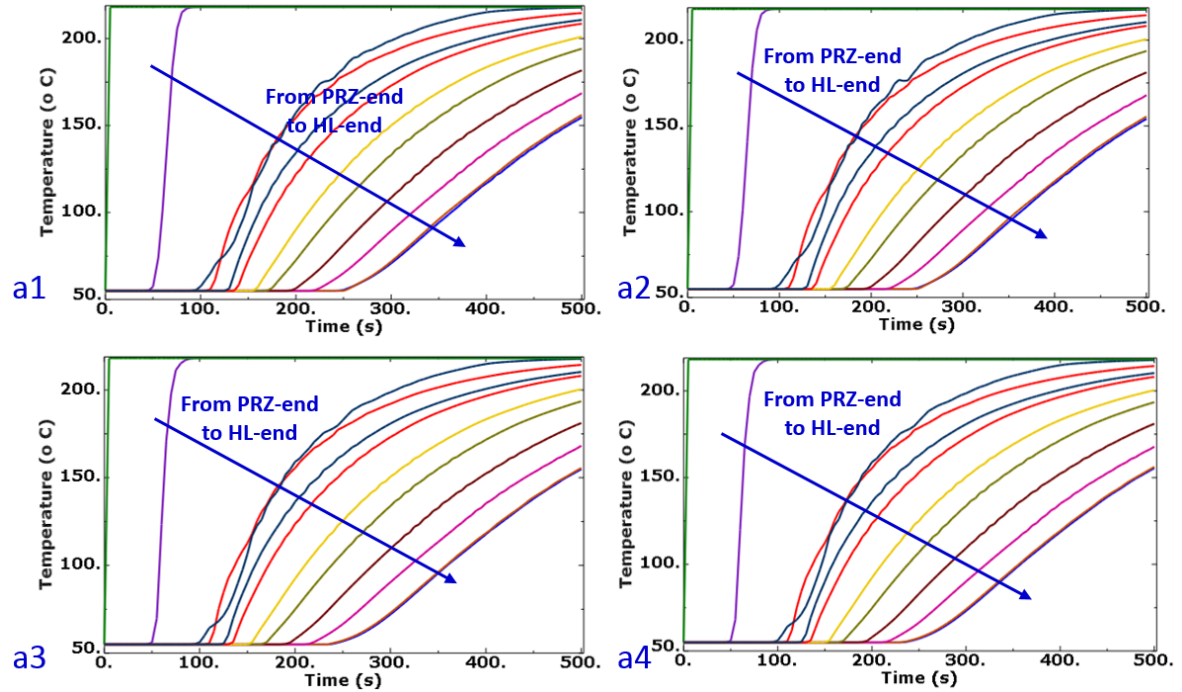


Figure 8.27 SL temperature history for out-surge case with HL mass flow rate (a1) 0 gpm, (a2) 3451 gpm, (a3) 34,510 gpm, and (a4) 69,020 gpm.

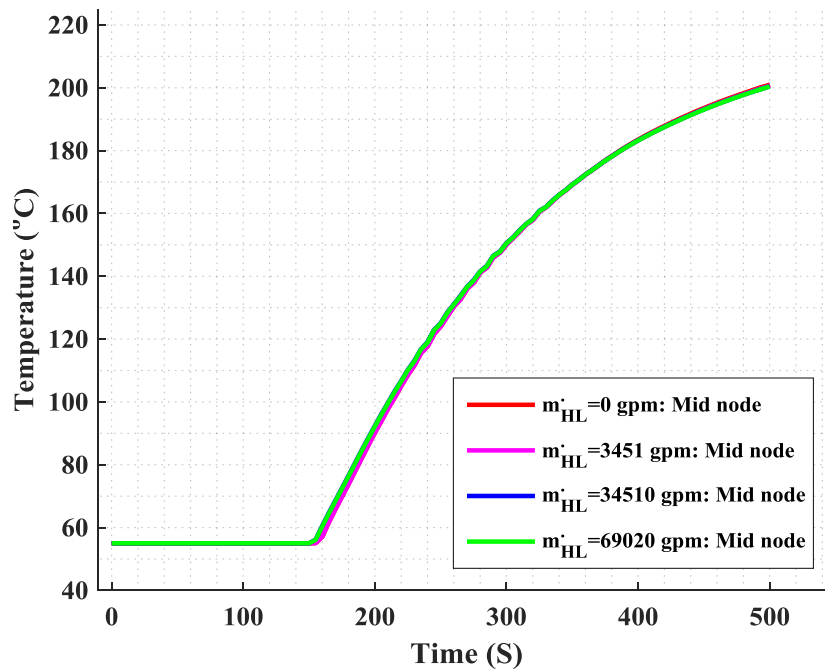


Figure 8.28 Comparison of temperature history at a mid-node (refer to Figure 8.2a) of SL, which are simulated with 0 gpm, 3451 gpm, 34,510 gpm, and 69,020 gpm of HL mass flow rate.

8.4 CFD-HT Fluid Structure Interaction Model Results

All the above discussed results were obtained with the ABAQUS stand-alone CFD code. For those models, only the inside fluid of the SL pipe was simulated. This is to save computational time while performing various parametric studies. However, the outer metallic pipe may affect the heat transfer in the SL fluid. Hence, it is essential to include the metallic pipe in the CFD simulation. For the purpose of ABAQUS, a co-simulation or FSI feature was used to model the heat transfer of both the inside fluid and outside pipe. Using this FSI capability of ABAQUS, CFD-HT was performed to simulate out-surge and in-surge flow conditions in the SL pipe. The resulting temperature distribution in the outer pipe was later used for stress analysis. These results are discussed in the following section. For both the out-surge and in-surge, a SL mass flow rate of 50 gpm and HL mass flow rate of 3451 gpm (equivalent of 5% of the full power mass flow rate) were considered. The details of the temperature and flow direction are given in section 8.2.2. Unlike the previous discussed results for which the simulations were conducted for 500 s, the simulations were for 2000 s in the cases discussed below.

8.4.1 CFD-HT fluid structure interaction model results for out-surge case

The out-surge case results obtained through the CFD-HT fluid structure interaction model are shown in Figures 8.29 to 8.32. Figure 8.29 shows a comparison of the temperature contour (at different times) of the OD surface of the SL fluid obtained from the stand-alone CFD and CFD-HT models. Figure 8.30 shows the SL fluid temperature history at selected nodes for the stand-alone CFD and CFD-HT fluid structure interaction models. Figure 8.31 shows a direct comparison of the temperature history at the PRZ-end node, mid node, and HL-end node of the SL fluid, simulated using stand-alone CFD and CFD-HT models. Figure 8.32 shows the OD surface temperature contour (at different times) generated by the CFD-HT model for the SL metallic pipe. Figures 8.29 to 8.31 clearly show that the inside fluid temperature, simulated by considering the metallic outer pipe, is significantly different compared to that simulated without considering the outer pipe. It also can be seen that the temperature rise in the stand-alone CFD model is faster compared to the CFD-HT model. Nevertheless, it is always better to consider computational models that are closer to the actual physical system. Hence, we considered the CFD-HT model for further stress analysis, although it took much more computational time compared to the stand-alone CFD model.

For the simulation time of 2000 s the 8 CPU (in a Dell Precision Tower 7810 workstation) CFD-HT model took 20.5 h, whereas the stand-alone CFD model took only 1 h. From this transient simulation case, it can be imagined how computationally expensive it would be if a full cycle (heat-up, cool-down, and normal operation, as shown in Figure 8.3) were modeled. Note that full-cycle CFD-HT and ST analysis of SLs under design-basis normal operating condition and the grid-load-following condition are future tasks.

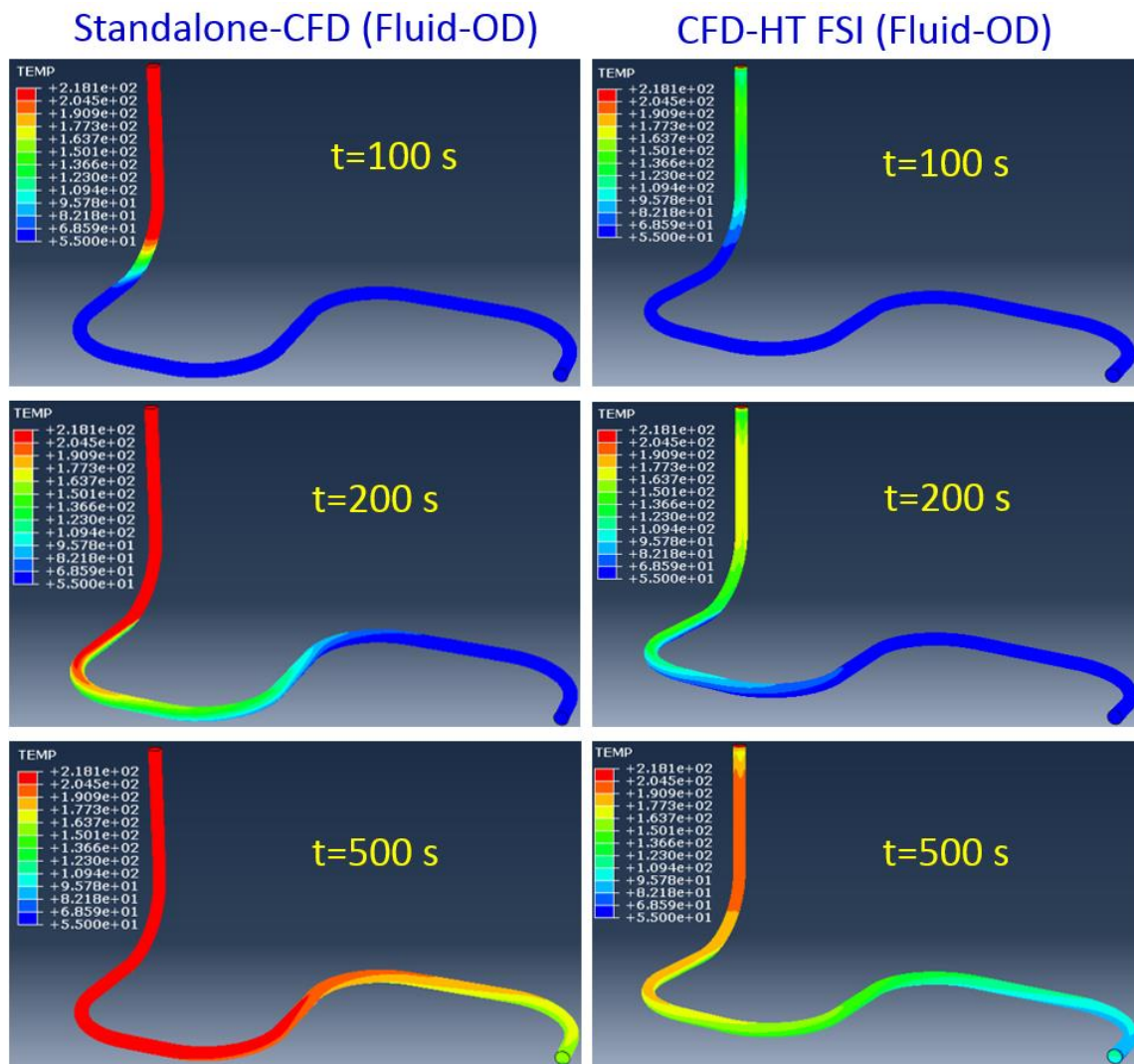


Figure 8.29 Comparison of temperature contour (at different times) of OD surface of SL fluid for stand-alone CFD and CFD-HT models (both under out-surge condition).

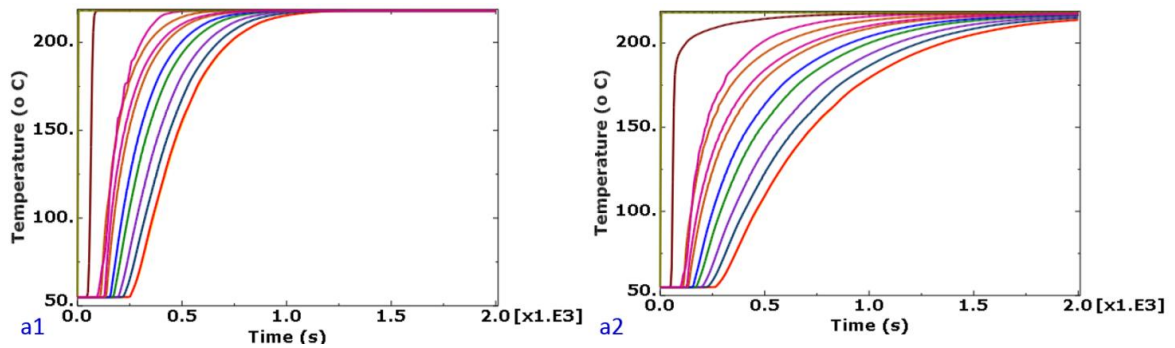


Figure 8. 30 Temperature history at selected nodes (refer to Figure 8.2a) under out-surge case for SL determined with (a1) standalone CFD model and (a2) CFD-HT model.

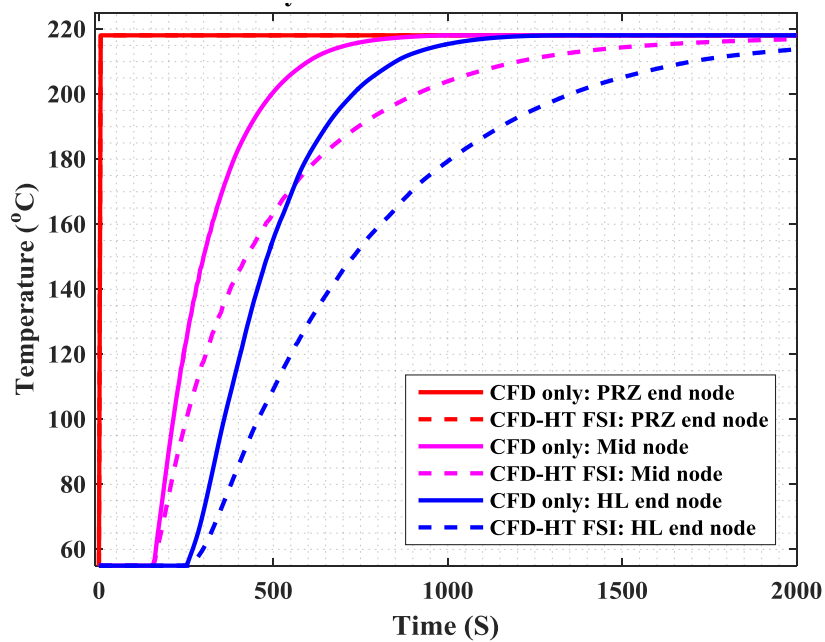


Figure 8. 31 Comparison of temperature history at PRZ-end node, mid node, and HL-end node of SL, simulated using stand-alone CFD and CFD-HT models (both under out-surge condition).

CFD-HT FSI (Pipe-OD)

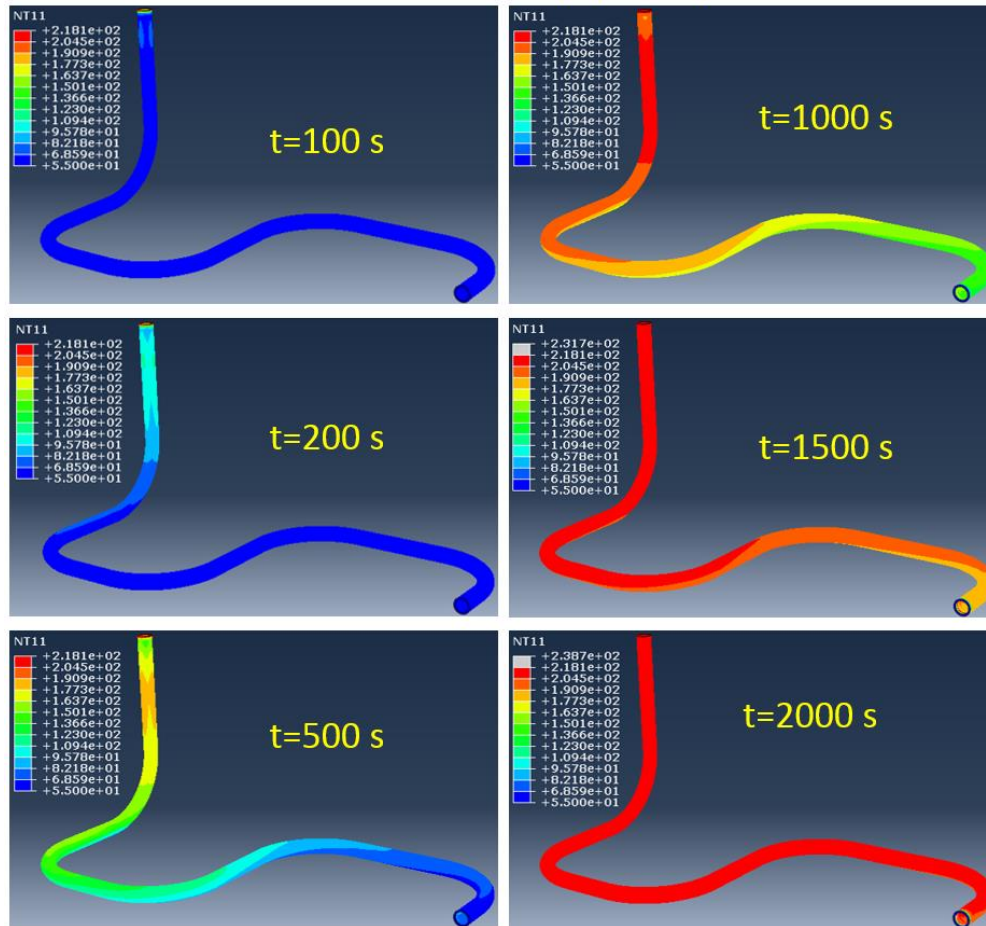


Figure 8.32 OD surface temperature contour (at different times) of SL metallic pipe under out-surge condition determined with CFD-HT model.

8.4.2 CFD-HT fluid structure interaction model results for in-surge case

The in-surge case simulation was conducted with the CFD-HT fluid structure interaction model only. Figures 8.33 to 8.35 show the related results. Figure 8.33 shows the OD surface temperature contour of SL fluid at different times. The corresponding OD surface temperature contours of SL metallic pipe at different instances are shown in Figures 8.34. Figure 8.35 shows the temperature history at selected nodes (refer to Figure 8.2a) of SL fluid. Note that for the in-surge case the simulation time of 2000 s took 29.93 h in an 8 CPU computer (in a Dell Precision Tower 7810 workstation).

CFD-HT FSI (Fluid-OD)

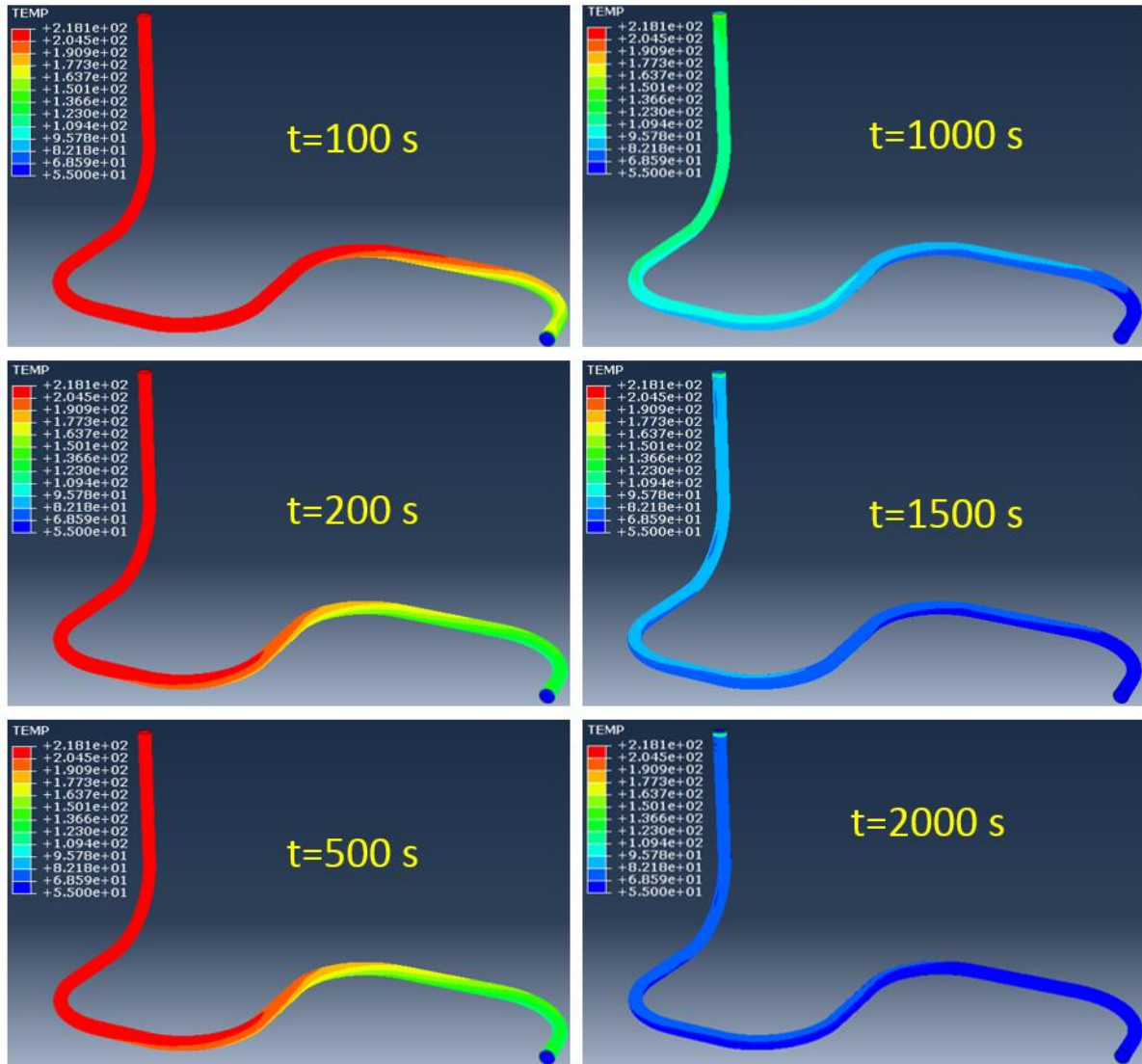


Figure 8. 33 OD surface temperature contours (at different times) of SL fluid under in-surge condition determined with the CFD-HT model.

CFD-HT FSI (Pipe-OD)

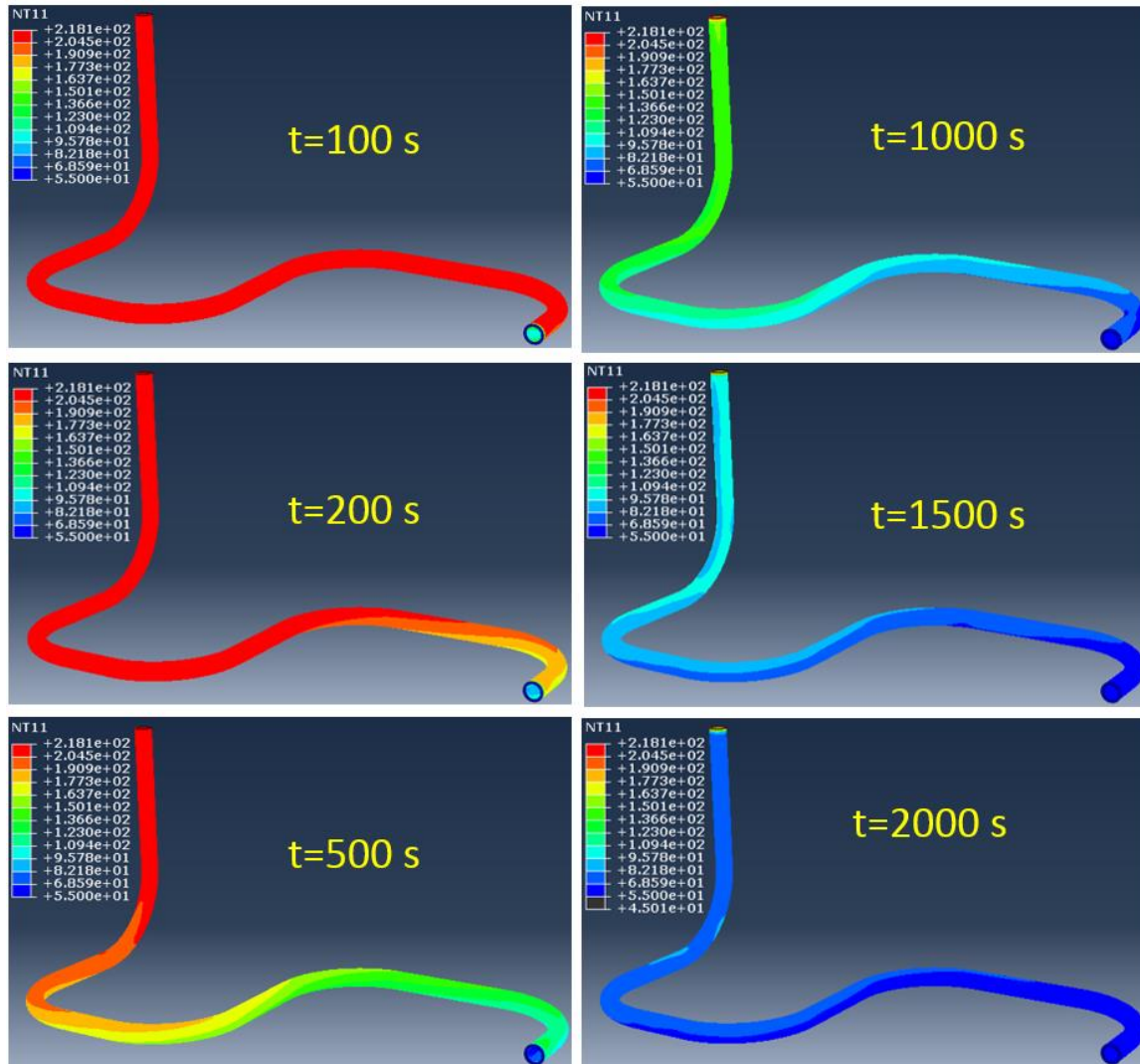


Figure 8. 34 OD surface temperature contours (at different times) of SL metallic pipe under in-surge condition determined with the CFD-HT model.

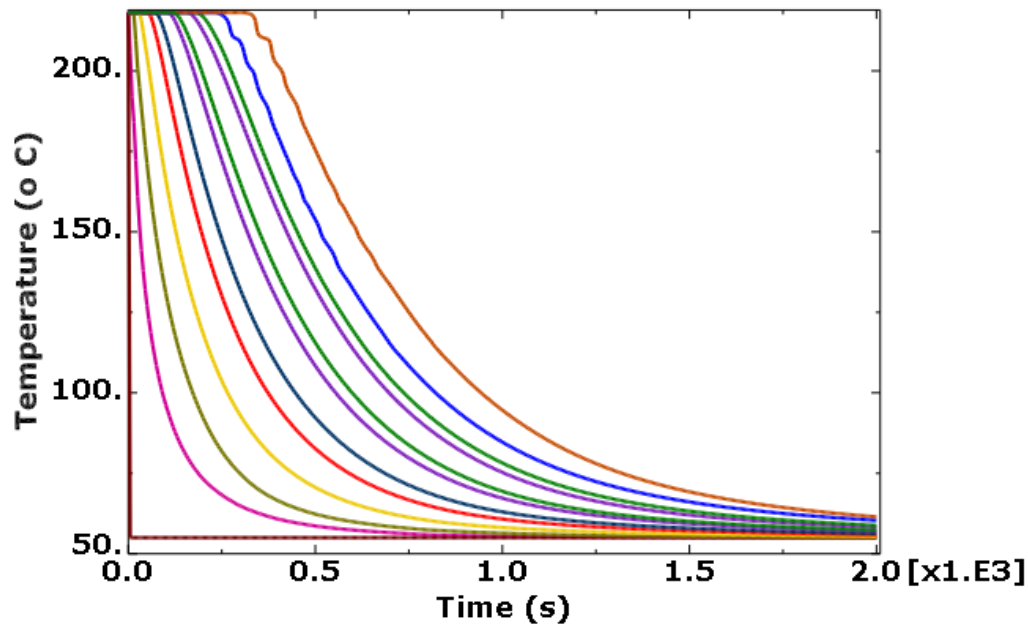


Figure 8. 35 SL temperature history at selected nodes (refer to Figure 8.2a) under in-surge case determined with the CFD-HT model.

8.5 Stress Analysis Results

The nodal temperature history generated through the CFD-HT model was further used in structural analysis (ST) models. The ST models were developed for both out-surge and in-surge cases. The related results are discussed below.

8.5.1 Structural analysis model results for out-surge case

The out-surge ST analyses were conducted for different cases with different material properties. The details of the material properties are given in section 8.2.3. Both elastic and elastic-plastic stress analyses were conducted. Different elastic-plastic analyses with different yield conditions (refer to Table 8.1) were considered, such as 0.05%, 0.1%, and 0.2% offset-strain limit stress as the yield stress. Related results are presented in Figures 8.36 to Figure 8.44. Figure 8.36 shows the (elastic limit as yield stress case) contour plots of von Mises stress, maximum principal total strain, maximum principal thermal strain, and maximum principal plastic strain. This figure indicates that the maximum von Mises stress is at the HL end of the SL pipe and is 232.1 MPa. The maximum principal total strain, maximum principal thermal strain, and maximum plastic strains are 0.726%, 0.282%, and 0.332 %, respectively. These results show that the observed strain, particularly the total strain and plastic strain, are significant for only one transient loading. This may be one of the major reason why the SL pipe experiences higher thermal fatigue usage factor. A detailed cyclic analysis will reveal more information on this, which is one of our future tasks.

For this simulation case (with elastic limit as yield limit), Figure 8.37 shows time-dependent von Mises stress, maximum principal total strain, maximum principal thermal strain, and plastic strain at the typical PRZ-end and HL-end nodes. This figure shows that the stress is higher at the HL end of the SL, whereas all the strain quantities are higher at the PRZ end of the SL pipe. In addition to elastic limit as yield limit, other cases of stress analysis such as pure elastic analysis and different elastic-plastic analysis (with 0.05%, 0.1%, and 0.2% offset strain limit as the yield limit) were simulated. The comparative results of the von Mises stress, maximum principal total strain, maximum principal thermal strain, and plastic strain magnitude are presented in Figures 8.38 to 8.41, respectively. Figure 8.42 shows (with magnification factor =10) the relative displacement of the SL pipe at different times with a maximum displacement of 45.21 mm. Figures 8.38 to 8.41 suggest that elastic stress analysis gives significantly different stress and strain compared to the elastic-plastic stress analysis results. An exception is the thermal strain, which is supposed to give same strain under both elastic and elastic-plastic analysis conditions, since thermal strains are linearly estimated for both elastic and elastic-plastic analysis. **The finding of totally different stress and strain in the case of elastic analysis compared to more realistic elastic-plastic conditions questions the accuracy of widely followed fatigue evaluation approaches based on elastic analysis.**

To check the accuracy of this component-level stress analysis, the finite-element simulated maximum principal strain versus von Mises stresses at two typical integration points (elements near the PRZ and HL end of the SL pipe) are compared with respect to strain versus stress curves based on the 22 °C and 300 °C tensile tests (elastic-plastic properties were used for discussed structural analysis models). The comparison can be seen in Figure 8.43. The curves indicate that the strain versus stress plot of the HL-end element (for which the temperature is approximately maintained at 55 °C, as shown in Figure 8.44) closely correlates with strain versus stress curve based on the 22 °C tensile test. Note that the input properties for yield stress at 22 °C and 300 °C were 183.61 and 130.730 MPa, respectively (for the present ST model with the elastic limit as yield limit). According to a linear interpolation, the corresponding yield stress at 55 °C is 177 MPa. From a close examination of Figure 8.43, the HL-end element strain versus stress curve crossed into the plastic regime (from the initial elastic regime) at very close yield stress of 170.8 MPa. . As shown in Figure 8.44, the PRZ-end element experiences large variation of temperature before it saturates toward 218.1 °C (which is the PRZ temperature during the entire simulation). A similar trend in the strain versus stress curve for the PRZ element was also observed before saturating towards the strain versus stress curve for the 300 °C tensile test. With unavailability of costly component-level results, this type of validation of multi-axially loaded component stress-strain with uni-axial test data is noteworthy.

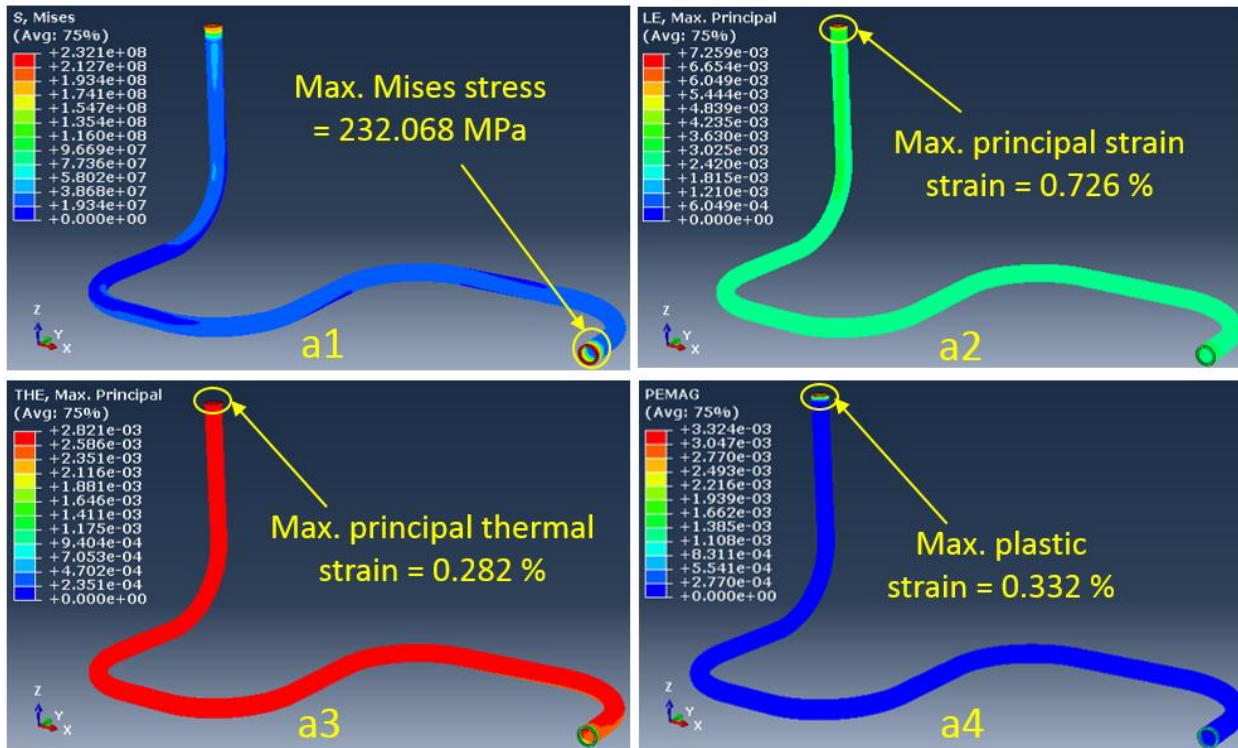


Figure 8.36 Stress analysis (with elastic limit as yield limit) results for SL pipe under out-surge conditions: contour plots at end of 2000 s for (a1) von Mises stress, (a2) maximum principal total strain, (a3) maximum principal thermal strain, and (a4) maximum principal plastic strain.

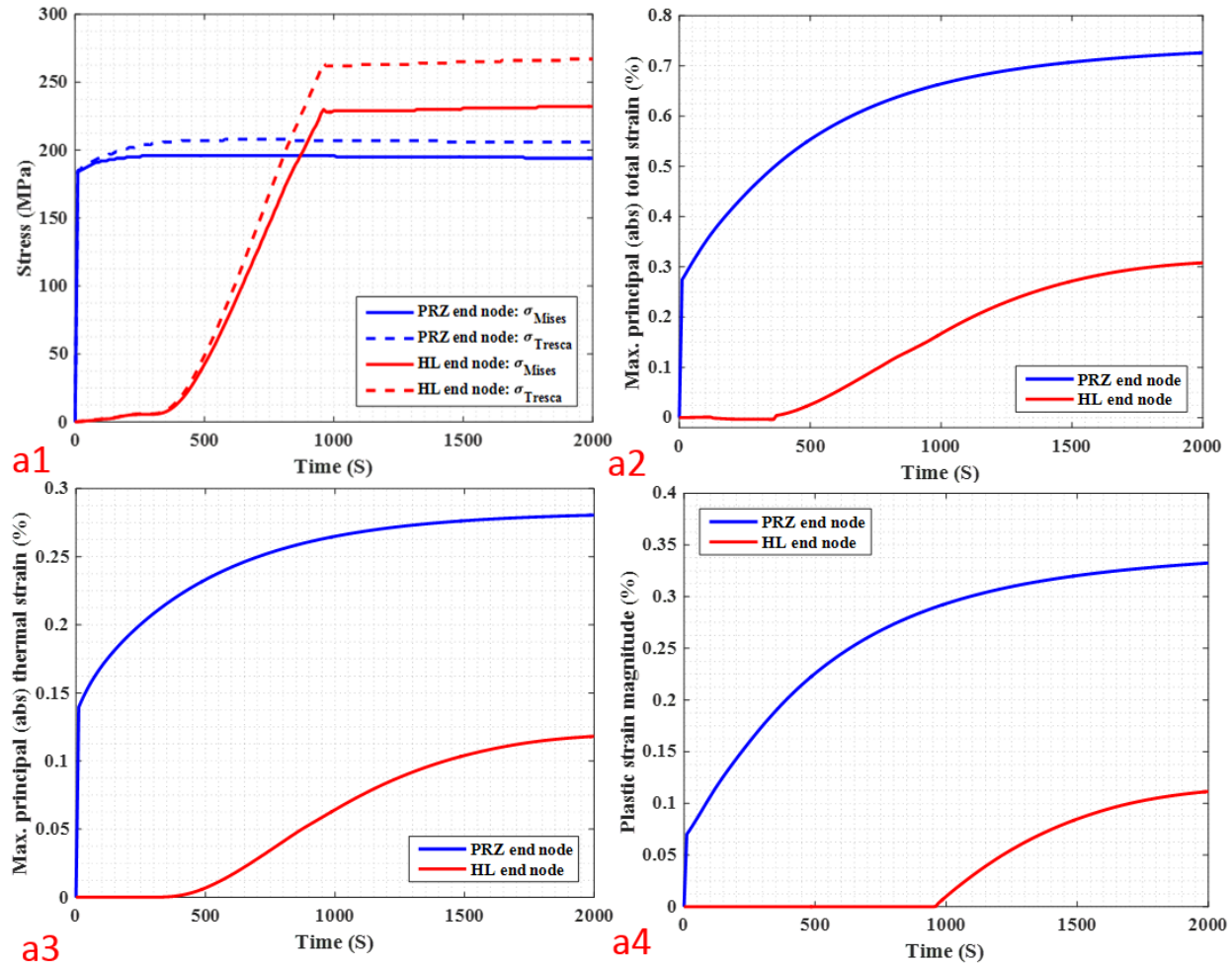


Figure 8.37 Stress analysis (with elastic limit as yield limit) results for SL pipe under out-surge conditions: PRZ-end versus HL-end node time-dependent results for (a1) von Mises stress, (a2) maximum principal total strain, (a3) maximum principal thermal strain, and (a4) plastic strain magnitude.

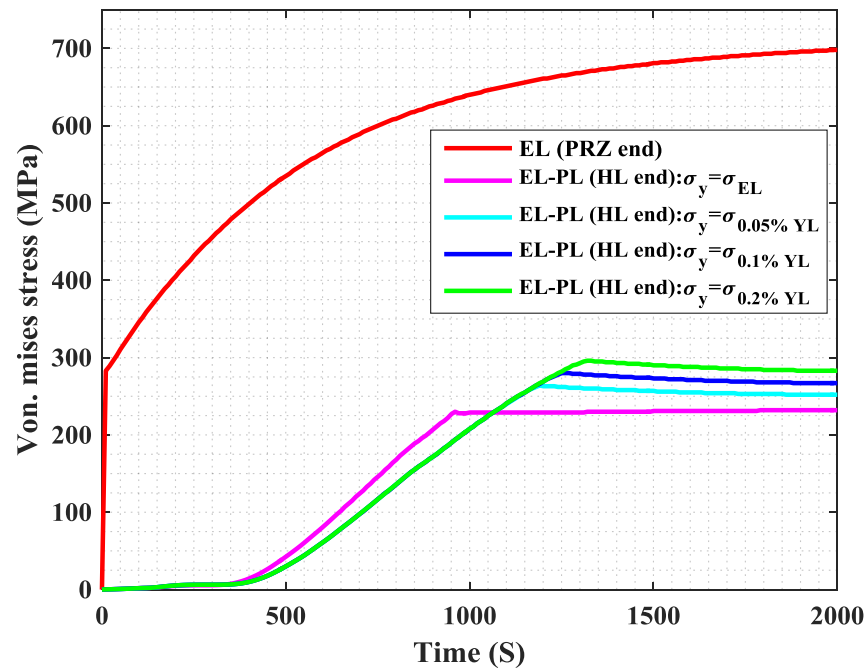


Figure 8. 38 Time variation of out-surge condition for maximum von Mises stress obtained using elastic (EL) and different elastic-plastic (EL-PL) yield conditions.

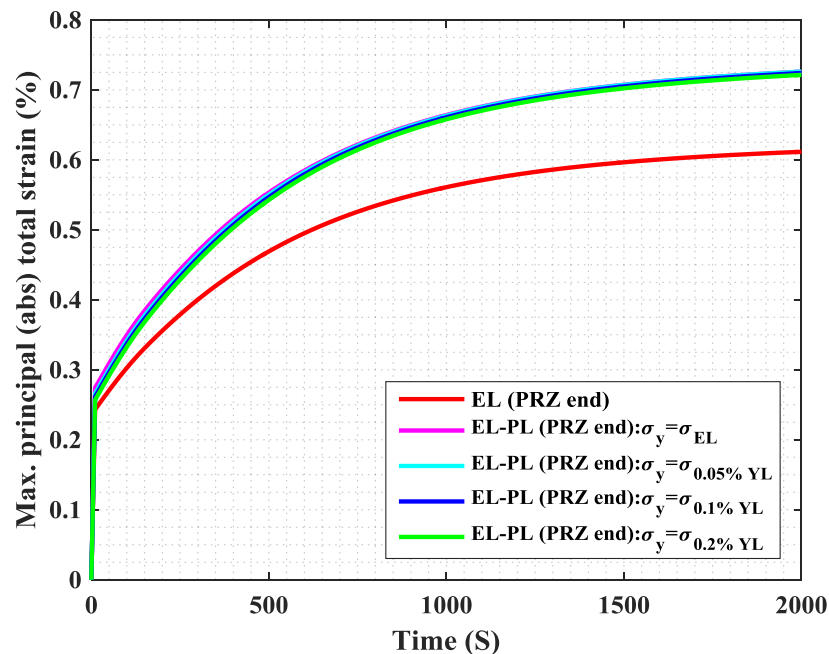


Figure 8. 39 Time variation of out-surge condition for maximum principal total strain obtained using elastic (EL) and different elastic-plastic (EL-PL) yield conditions.

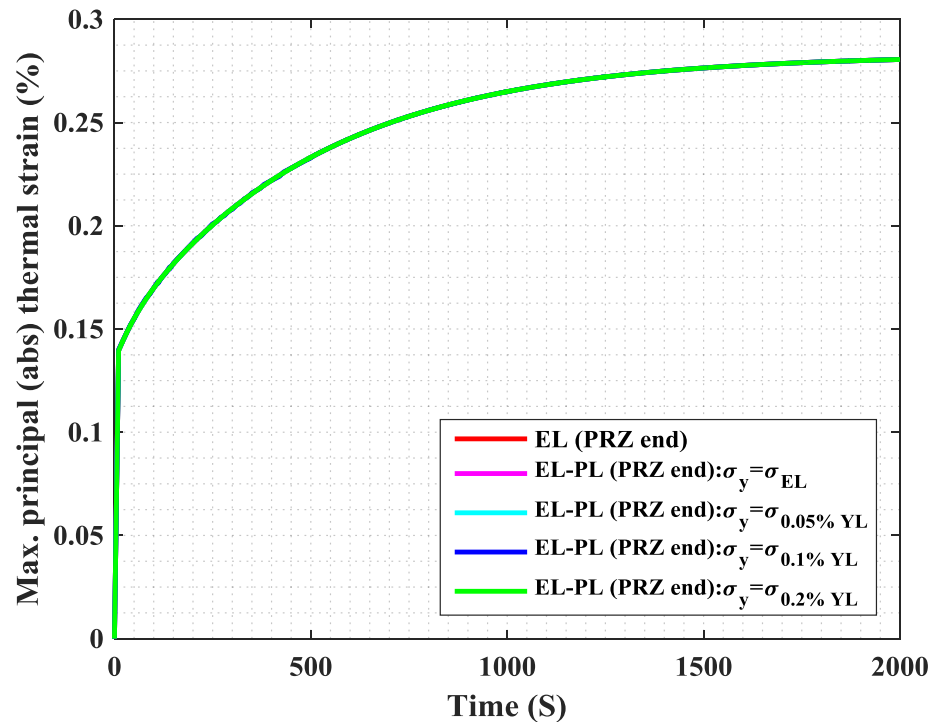


Figure 8. 40 Time variation of out-surge condition for maximum principal thermal strain obtained using elastic (EL) and different elastic-plastic (EL-PL) yield conditions.

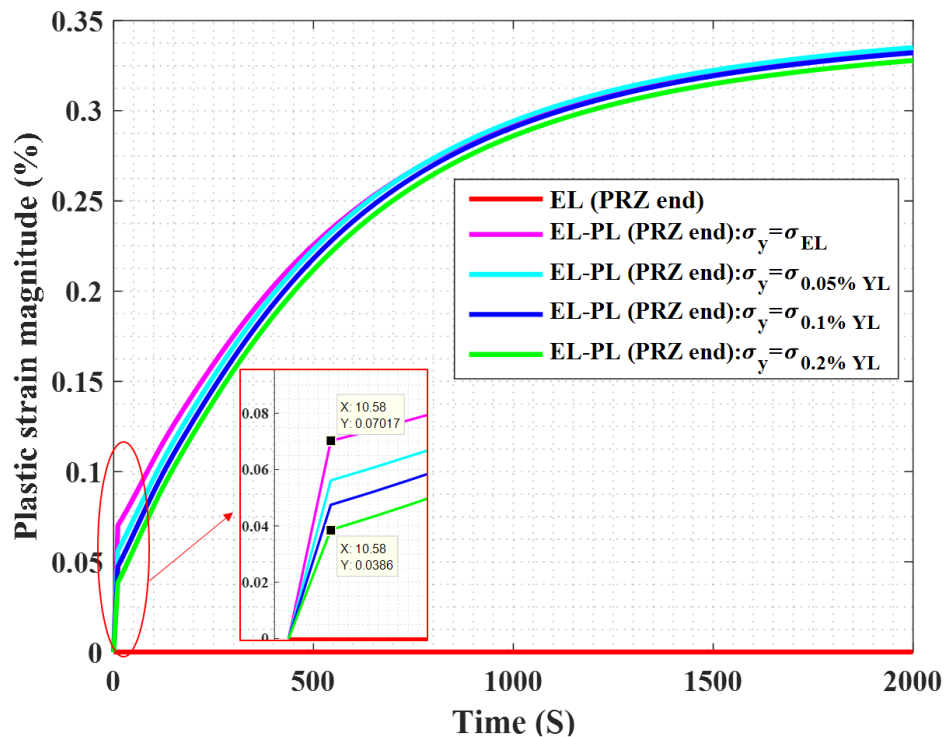


Figure 8. 41 Time variation of out-surge condition for plastic strain magnitude obtained using elastic (EL) and different elastic-plastic (EL-PL) yield conditions.

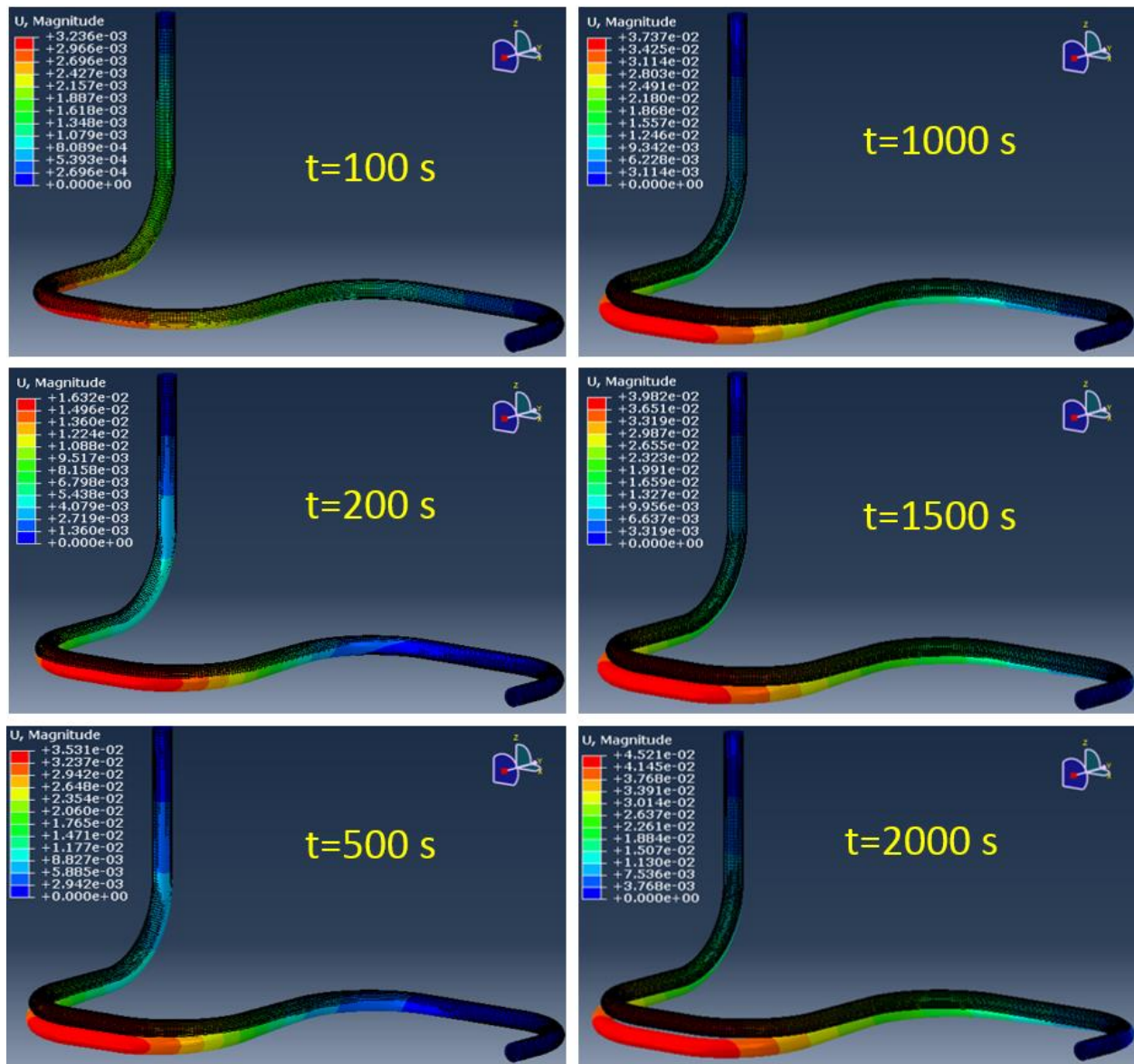


Figure 8.42 Relative displacement of SL pipe at different times for out-surge case (magnification factor =10).

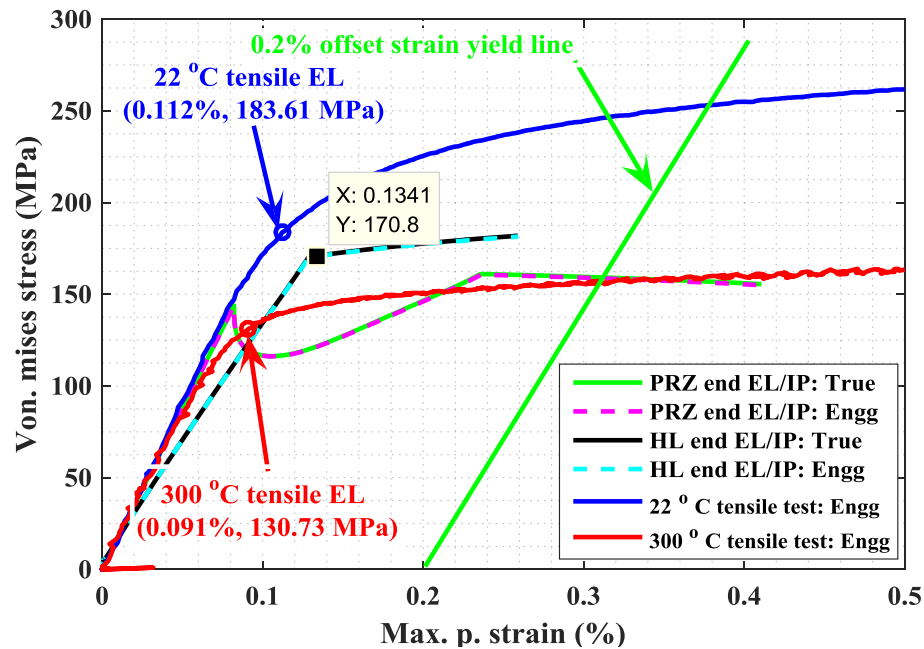


Figure 8. 43 Out-surge condition maximum principal strain versus von Mises stress at two typical integration points (of elements near PRZ and HL end of SL pipe) and their comparison with respect to 22 °C and 300 °C tensile test curves. Associated elastic-plastic properties were used for discussed structural analysis models.

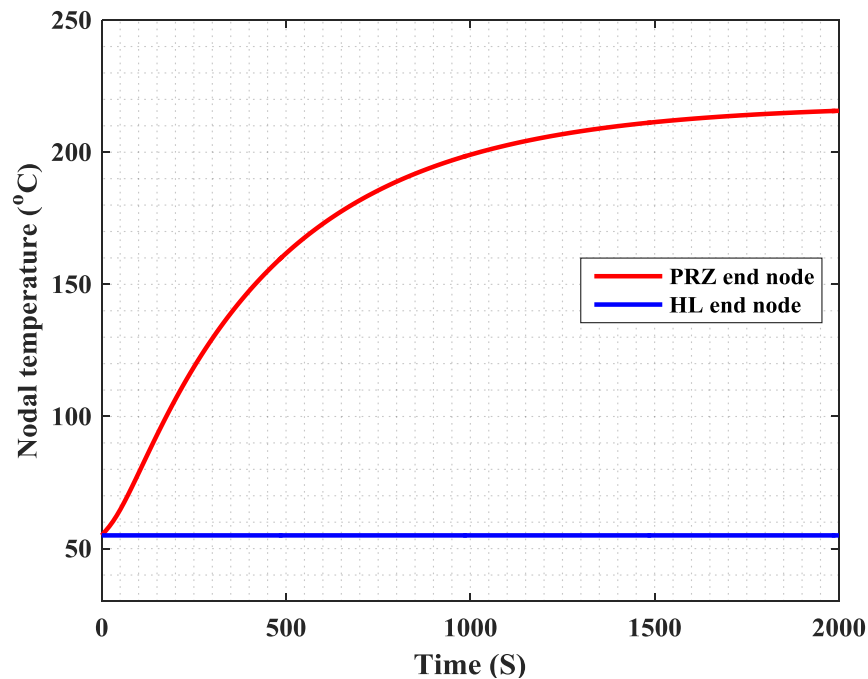


Figure 8. 44 Nodal temperature at the two elements near PRZ and HL end of SL pipe, where strain versus stress results are presented in Figure 8.43.

8.5.2 Structural analysis model results for in-surge case

An ST analysis was also performed for the in-surge case by using the nodal temperature obtained through the CFD-HT model (refer to section 8.4.2) simulated under in-surge flow condition. This analysis was conducted under the elastic-plastic condition with the elastic limit as the yield-limit stress. Figure 8.45 shows the corresponding contour plots of von Mises stress, maximum principal total strain, maximum principal thermal strain, and maximum principal plastic strain. Figure 8.46 shows time-dependent von Mises stress, maximum principal total strain, maximum principal thermal strain, and plastic strain at typical PRZ-end and HL-end nodes. Figure 8.47 shows the relative displacement of the SL pipe at different times (magnification factor =10), with a maximum displacement of 32.08 mm.

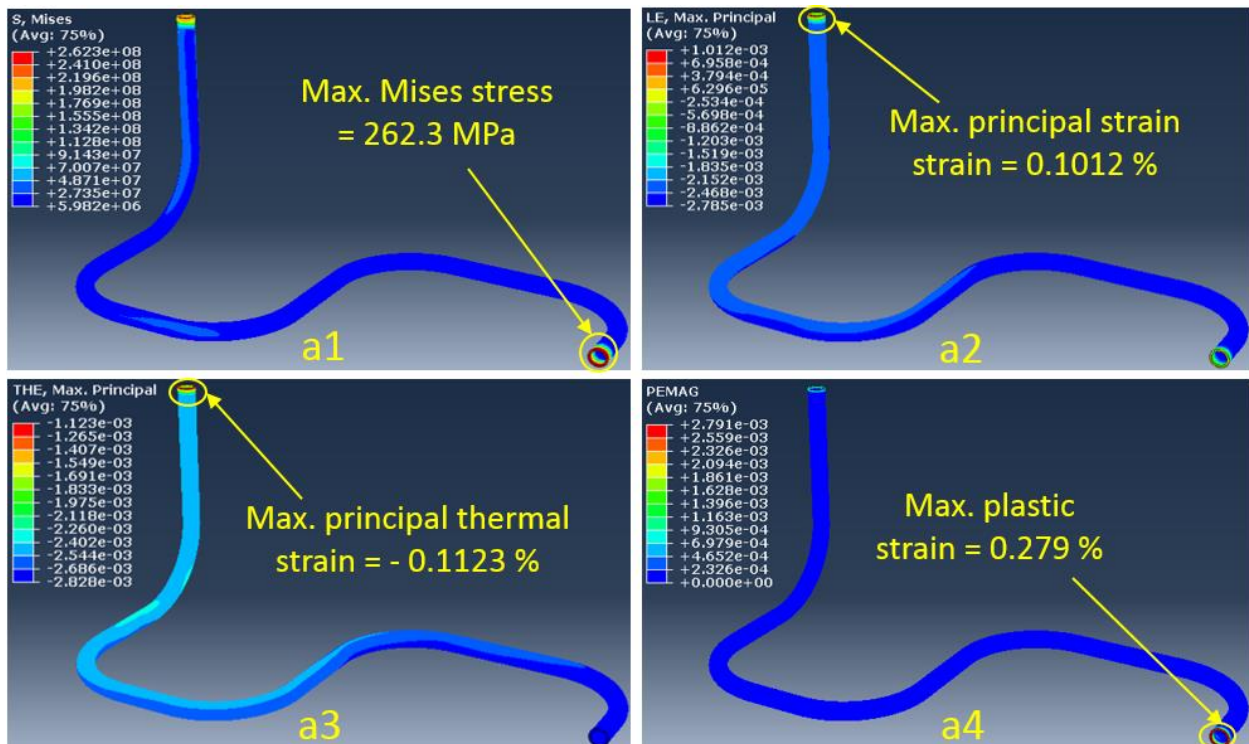


Figure 8. 45 Stress analysis (with elastic limit as yield limit) results for SL pipe under in-surge conditions: contour plots at end of 2000 s for (a1) von Mises stress, (a2) maximum principal total strain, (a3) maximum principal thermal strain, and (a4) maximum principal plastic strain.

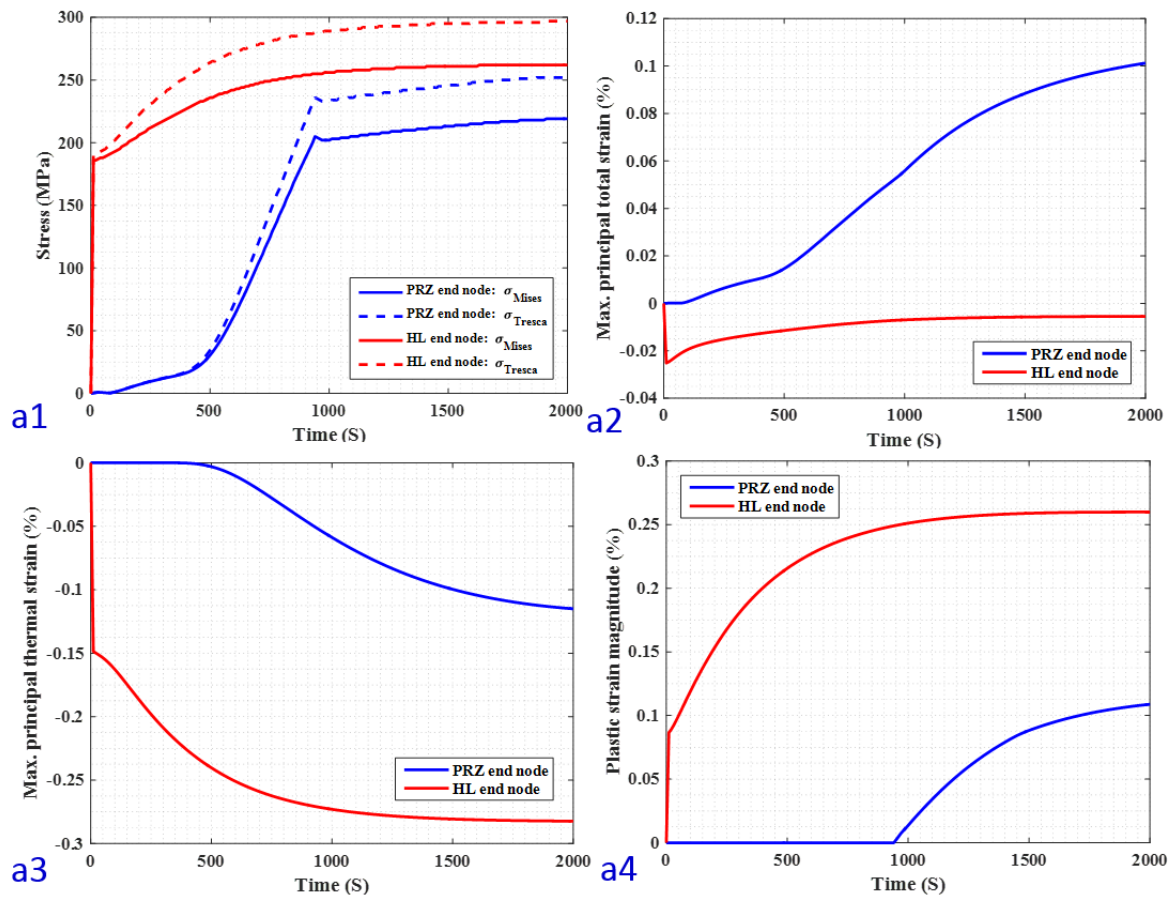


Figure 8.46 Stress analysis (with elastic limit as yield limit) results for SL pipe under in-surge conditions: PRZ-end versus HL-end node time-dependent results for (a1) von Mises stress, (a2) maximum principal total strain, (a3) maximum principal thermal strain, and a4) maximum principal plastic strain.

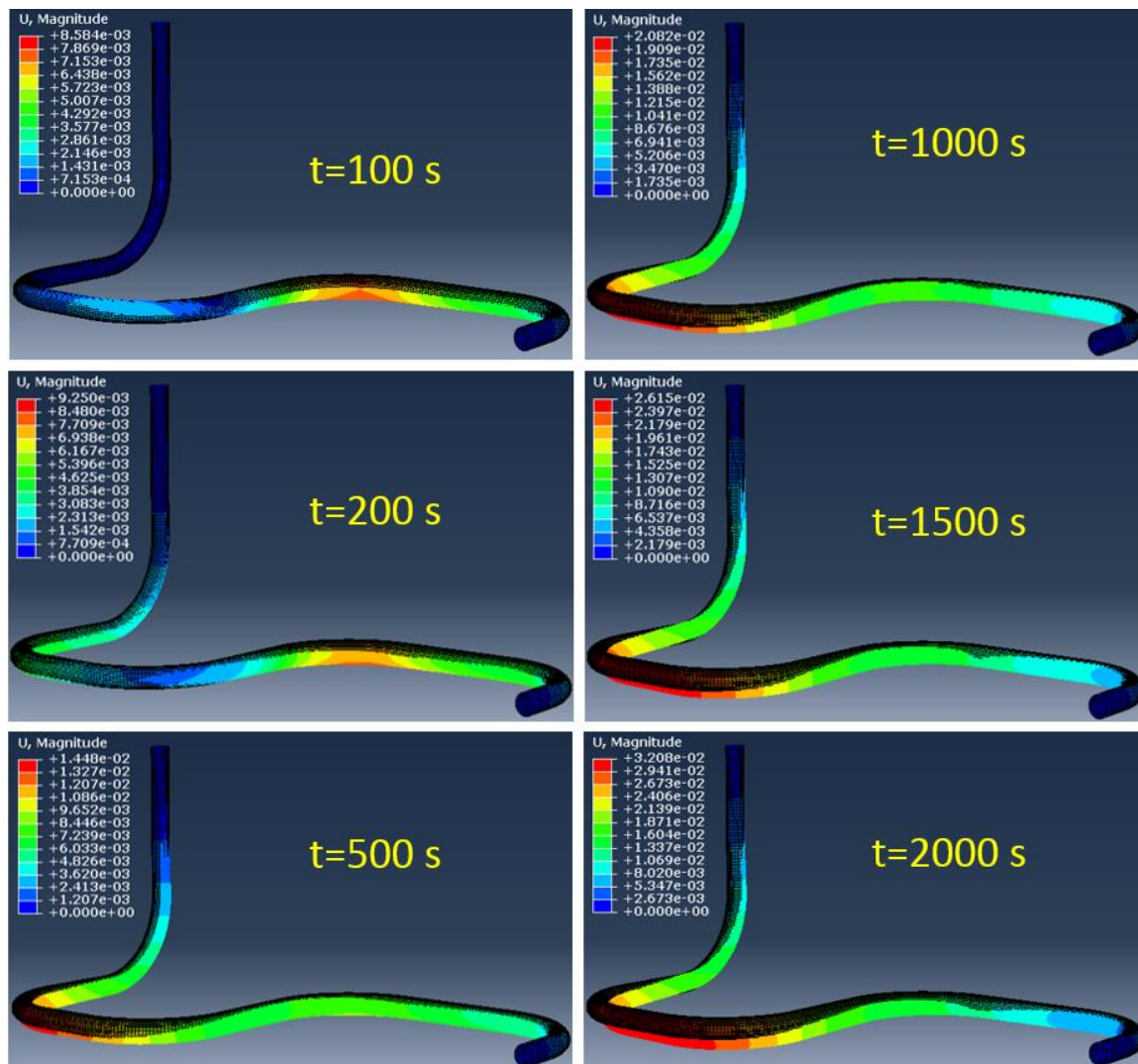


Figure 8.47 Relative displacement of SL pipe at different time for in-surge condition (magnification factor =10).

9 Fatigue Life Estimation of SL Pipe based on ANL Developed Fully Mechanistic Approach and ASME and NUREG-6909 Mandated S~N Curve based Approaches

In this section we present the results related to fatigue live evaluation of SL pipe. Based on the earlier discussed CFD-HT and ST (single cycle) models, fatigue evaluations are performed under two loading scenarios such as for:

- a) SL pipe subjected to an imaginary strain-controlled loading condition.
- b) SL pipe subjected to actual stress-controlled loading condition.

The related results are discussed below.

9.1 Fatigue Life Estimation of SL Pipe under Imaginary Strain-Controlled Loading Conditions

Fatigue evaluation under imaginary strain-controlled case performed using ANL developed cyclic-plasticity based fully mechanistic model and ASME [1, 3] and NUREG-6909 [2, 67] mandated S~N curve based approaches. Results from both the approaches are discussed below.

9.1.1 Strain-controlled case elastic-plastic analysis and fully mechanics based life estimation

In our mechanics-based fatigue-modeling project, we are trying to develop an FE model framework based on an ANL-developed evolutionary cyclic plasticity model to estimate the life of nuclear reactor critical safety components. The overall picture of this modeling framework is shown in Figure 9.1. As shown in the flowchart, mechanics-based fatigue modeling starts with uniaxial fatigue experiments followed by material model (based on an evolutionary cyclic plasticity model) development along with material model parameter estimations. The details of this work and related results are discussed in Sections 2 and 3. The next step is validation of the evolution cyclic plasticity model through analytical and 3D-FE modeling of the specimen. Results from the analytical and 3D-FE modeling of 316 SS specimens under uniaxial fatigue loading are presented in Sections 4 and 5, respectively. The 3D-FE implementation of evolutionary cyclic plasticity model is discussed in Section 2. In the final step, the developed FE model framework and material model parameters are utilized to extrapolate uniaxial fatigue test-based material behavior to a multiaxial domain for structural analysis of nuclear reactor components subjected to multiaxial fatigue loading. This section presents some preliminary results from the final step of proposed fully mechanistic fatigue evaluation framework.

We performed an elastic-plastic analysis of the PWR SL pipe under strain control fatigue loading. The FE mesh of the PWR SL along with the boundary conditions and the direction of applied displacement is shown in Figure 9.2. We used fixed boundary conditions at two ends of the SL. Cyclic displacements equivalent to $\pm 0.5\%$ constant strain amplitude in z-direction were applied to nodes

near one of the ends, as shown in Figure 9.2b. The profile of the applied cyclic displacement is shown in Figure 9.2c. The constant amplitude strain control fatigue experiment (ET-F41) was performed with 0.5% strain amplitude. However, application of 0.5% strain amplitude is not totally absurd. Rather the motivation of selecting the strain amplitude is based on the CFD-HT and subsequent ST analysis results of SL pipe under out-surge condition. The related structural analysis results are already discussed in section 8.5.1. As can be seen from Figure 8.36, due to instantaneous out-surge flow the pressurizer end of SL pipe experience a maximum principal strain magnitude of 0.726 %. The equivalent strain along the vertical direction (i.e. direction toward the pressurizer, refer Figure 8.1 and Figure 8.36 a2) is approximately in an order of 0.5%. However, unlike the actual case where the strain loading is multiaxial due to multiaxial actual thermal-mechanical loading, for the discussed fatigue evaluation case the strain was applied only along the vertical direction. There are two reasons for applying strain loading along only one direction: First, applying multiaxial strain loading at different nodes (according to actual loading conditions) in FE model is nearly impossible. Also, note that, no real-world structures are strain-controlled. Second, we wanted to compare the life of the SL with the experimentally observed life of the uniaxial specimen (ET-F41), so we decided to keep the similar loading condition for the component. Through this imaginary loading case, we are trying to determine whether the FE framework based on the evolutionary cyclic plasticity model can be utilized for component-level elastic-plastic analysis and studying how the stress profiles in components differ (if any) from those in uniaxial fatigue specimens.

We used the APSE-based modeling approach in which APSE-dependent material parameters are used to map the fatigue cycle/time-dependent material behavior under uniaxial to multiaxial loading conditions. The theoretical background of the APSE-based modeling approach is presented in Section 2. APSE-dependent material parameters estimated from ET-F41 are used for the structural simulation of the PWR SL. Figure 9.3 shows the contour plot of the von Mises stress at a typical instant. As shown in the figure, maximum stress concentration occurs in the elements that are directly subjected to the applied deformation at one side (in the z-axis direction) and constrained to deform (all directions) at the other side because of the fixed boundary conditions. One of these elements, as shown in the magnified inset in Figure 9.3, is selected as the element of interest for analyzing the results from simulation. All the simulated stress-strain results presented are at the centroid of this element.

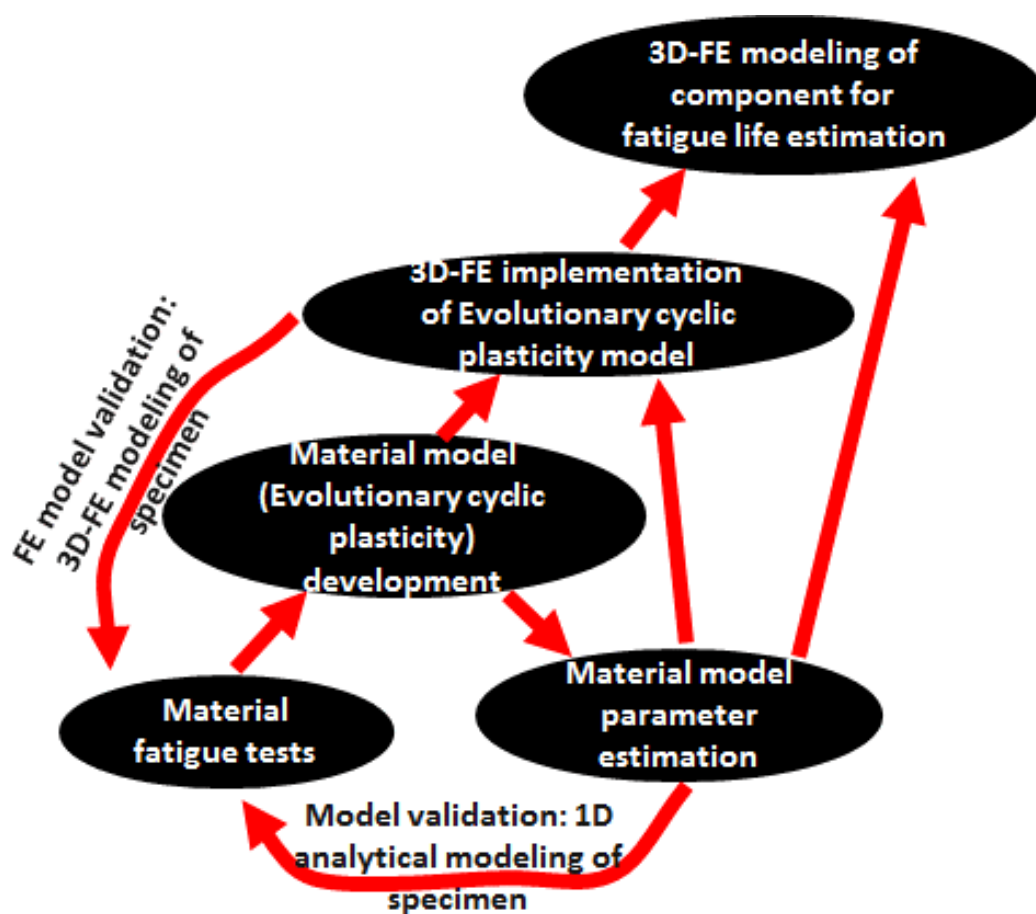


Figure 9. 1 Flowchart showing the steps in the ANL mechanics-based modeling.

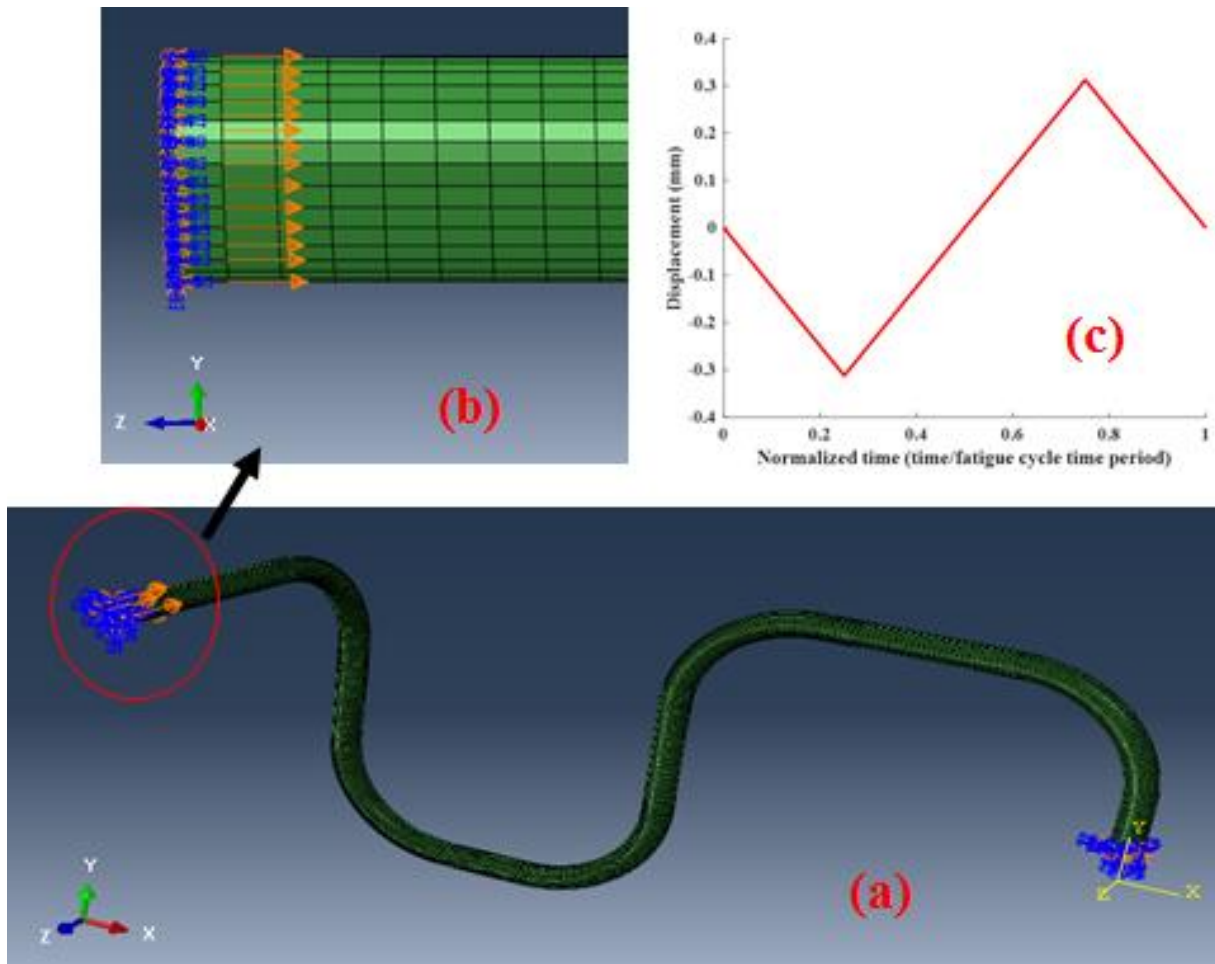


Figure 9. 2 (a) FE mesh of the PWR surge line. Blue arrows at two ends show the fixed boundary condition and yellow arrows indicate the location and direction of applied cyclic displacement. (c) Profile of the applied cyclic displacement.

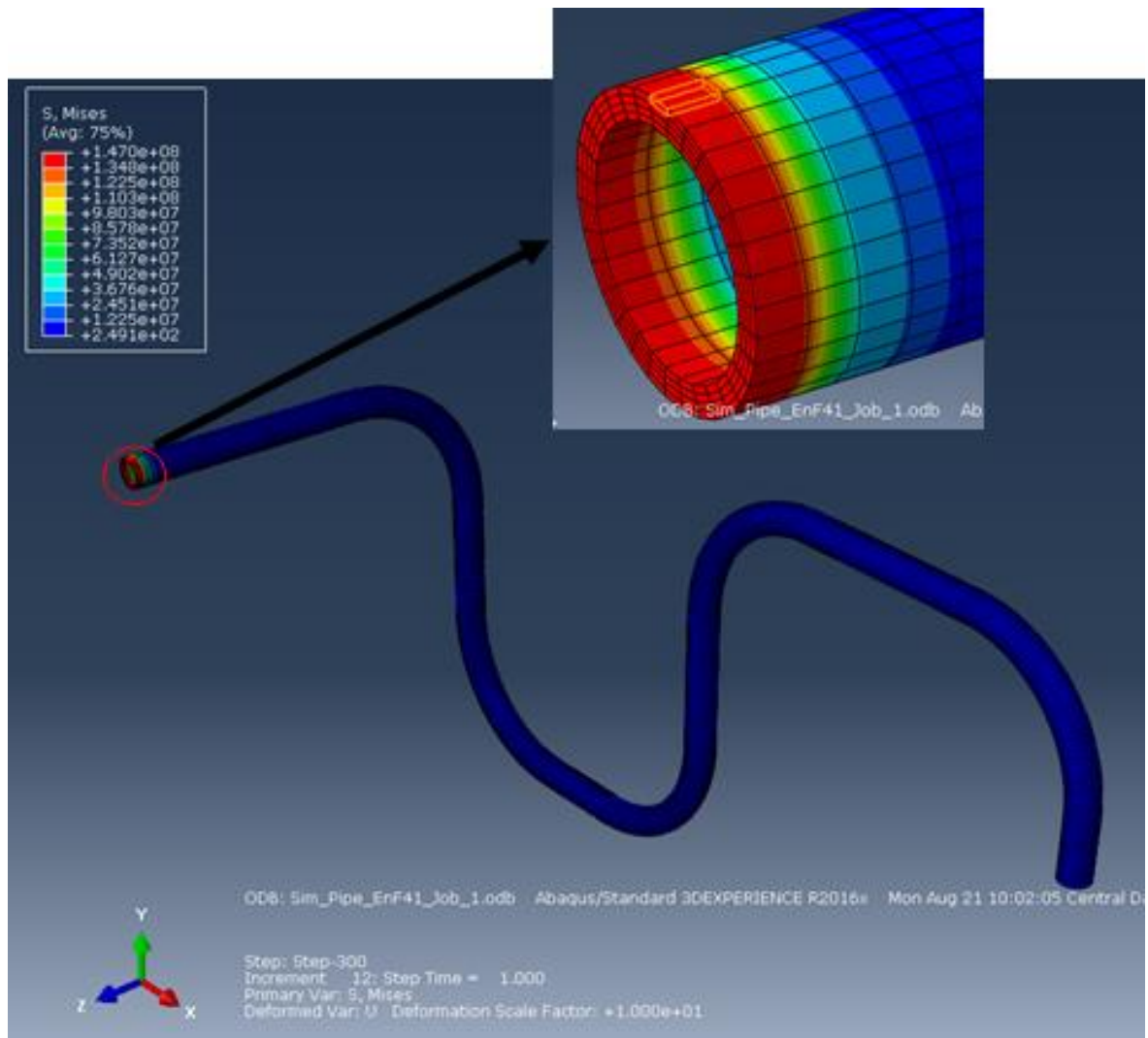


Figure 9.3 Contour plot of the von Mises stress at an instant during the strain control fatigue loading shown in Figure 9.1. The highlighted element in the magnified inset is the element of interest.

Figure 9.4 shows the simulated strain in the direction (z-axis) of applied displacement as a function of fatigue cycles. As shown in the figure, the strain amplitude is 0.5%. Note that the simulation was performed only for 100 fatigue cycles. The simulated stresses in the principal coordinate system are shown in Figures 9.5, 9.6, and 9.7 for maximum, mid, and minimum principal stress, respectively. The figures also compare the simulated principal stresses with the values calculated from the uniaxial fatigue experiment (ET-F41). Because of the multiaxiality, simulated principal stress amplitudes are very different from experimental amplitudes. However, because the evolutionary cyclic plasticity model uses von Mises stress for checking the yield criteria during elastic-plastic analysis, von Mises stress should be used for comparing simulation results with experimental observations.

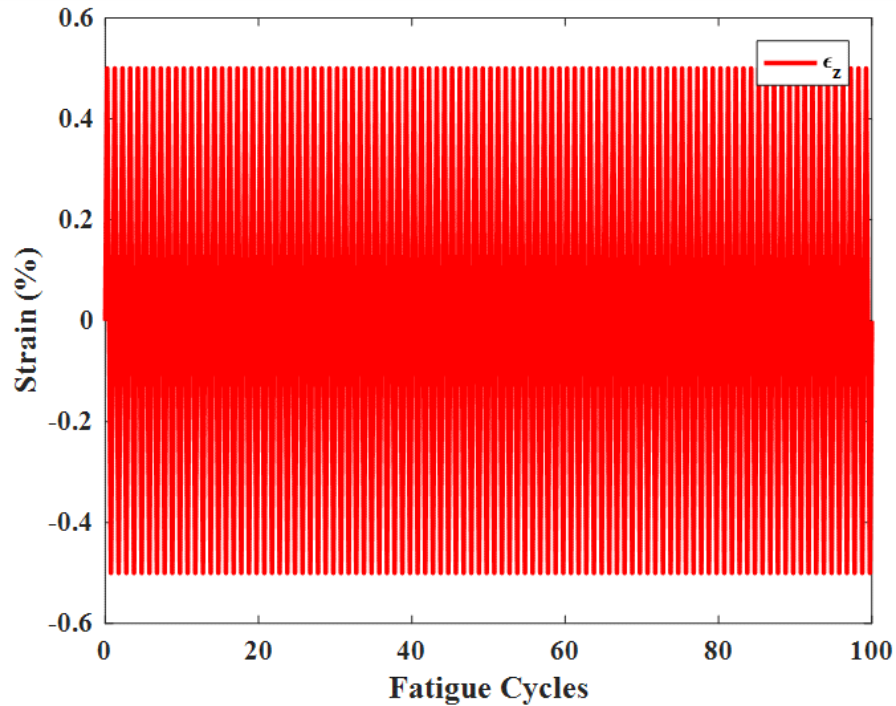


Figure 9. 4 Simulated (elastic-plastic analysis) ϵ_z as function of fatigue cycles.

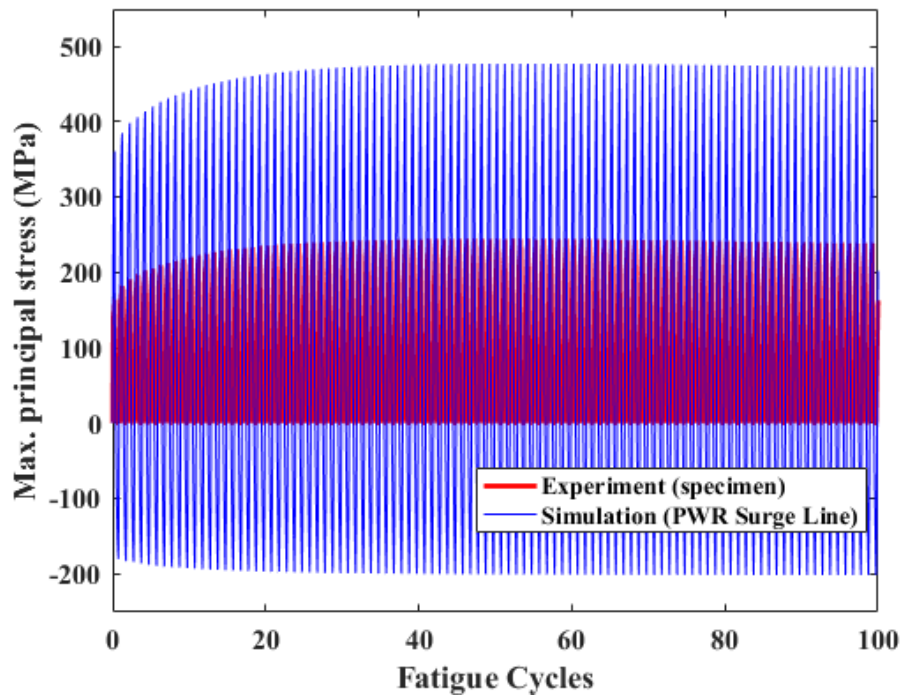


Figure 9. 5 Simulated (elastic-plastic analysis) vs experimental maximum principal stress as function of fatigue cycles. Experimental results are shown for first 100 cycles. Simulation was performed for only 100 cycles.

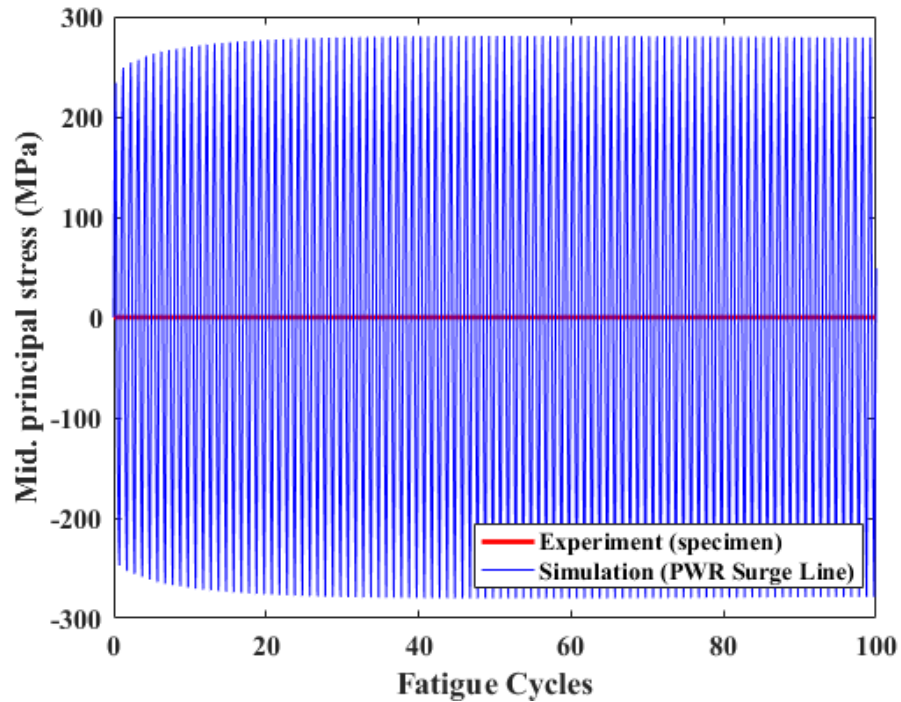


Figure 9. 6 Simulated (elastic-plastic analysis) vs experimental mid principal stress as function of fatigue cycles. Experimental results are shown for first 100 cycles. Simulation was performed for only 100 cycles.

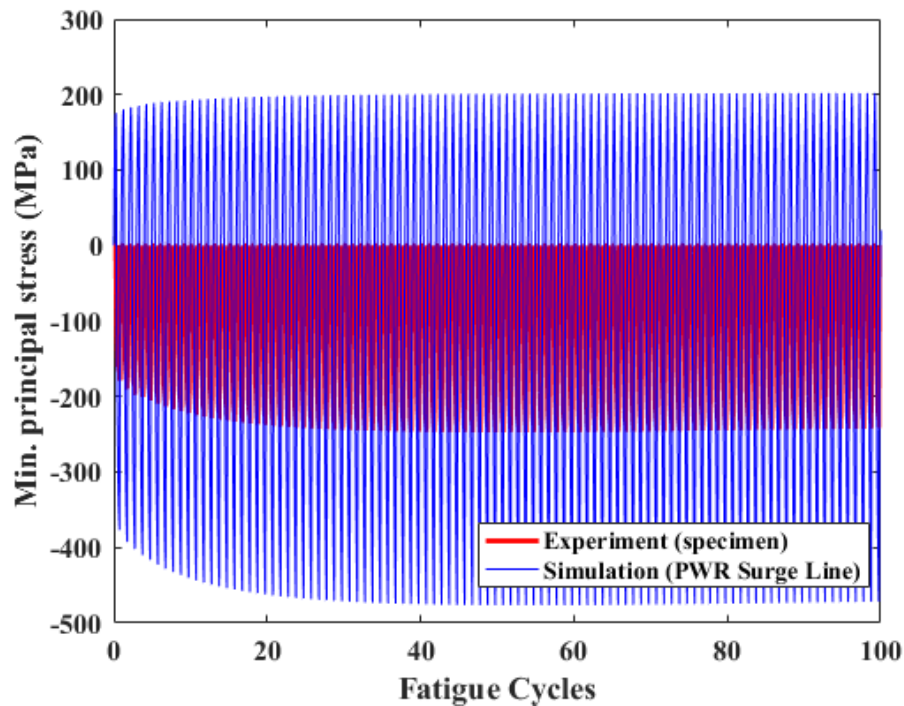


Figure 9. 7 Simulated (elastic-plastic analysis) vs experimental minimum principal stress as function of fatigue cycles. Experimental results are shown for first 100 cycles. Simulation was performed for only 100 cycles.

The comparison between von Mises stress amplitudes of experimental observation and those of simulation is shown in Figure 9.8. In Figure 9.9, von Mises stress amplitudes during compression and tensile cycles are plotted separately, but the values of compression amplitudes are shown as negative for better visualization. Both figures indicate material hardening followed by softening in the simulated stress profile; this behavior is typical of 316 SS as observed during uniaxial fatigue tests. The value of maximum hardening von Mises stress from simulation is found to be 245.7 MPa, which is very close to the experimentally observed value (244.2 MPa). The simulated Tresca stress as function of fatigue cycles is shown in Figure 9.10. The maximum hardening Tresca stress is found to be 275.7 MPa, which is 1.13 times the maximum hardening von Mises stress. Note that, the purpose of the discussed component level cycle-by-cycle stress analysis model is to check whether the ANL's proposed evolutionary cyclic plasticity based approach can be used for component level cycle-by-cycle stress analysis or not. For the discussed results, the simulation was conducted for first 100 cycles. Although, the component level stress analysis shown in Figures 9.8 and 9.9 closely match with uniaxial test results, it is to be noted that the strain amplitude applied to the component is very similar, the way it is applied to the uniaxial specimen. Also note that to compare the simulation results with experiment, the observed Von-Mises stress (shown in Figures 9.8 and 9.9) are considered only from one of the elements (refer Figure 9.2b) to which the strain inputs were applied. For the discussed ideal or imaginary loading condition, the stress profile at other locations (other than the applied strain locations) can be much different compared to the simulated and experimental cyclic stress profile shown in Figures 9.8 and 9.9. This is due to the multi-axial effect. Furthermore, this type of idealistic strain-controlled loading conditions may not representative of the loading conditions under actual thermal-mechanical loading scenarios. Actual thermal-mechanical loading condition will be multi-axial loading and may lead to very different Von-Mises stress profile, and associated cyclic stress hardening/softening rate. Nevertheless, the purpose of the discussed exercise is to demonstrate the feasibility of cycle-by-cycle stress analysis of a realistic reactor component.

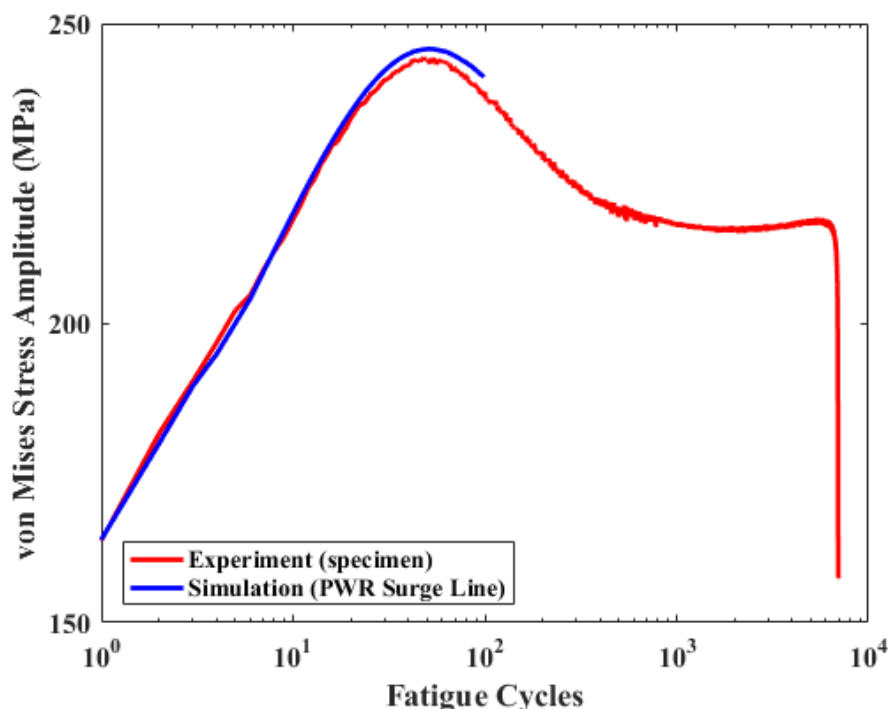


Figure 9. 8 Simulated (elastic-plastic analysis) vs experimental von Mises stress amplitudes as function of fatigue cycles.

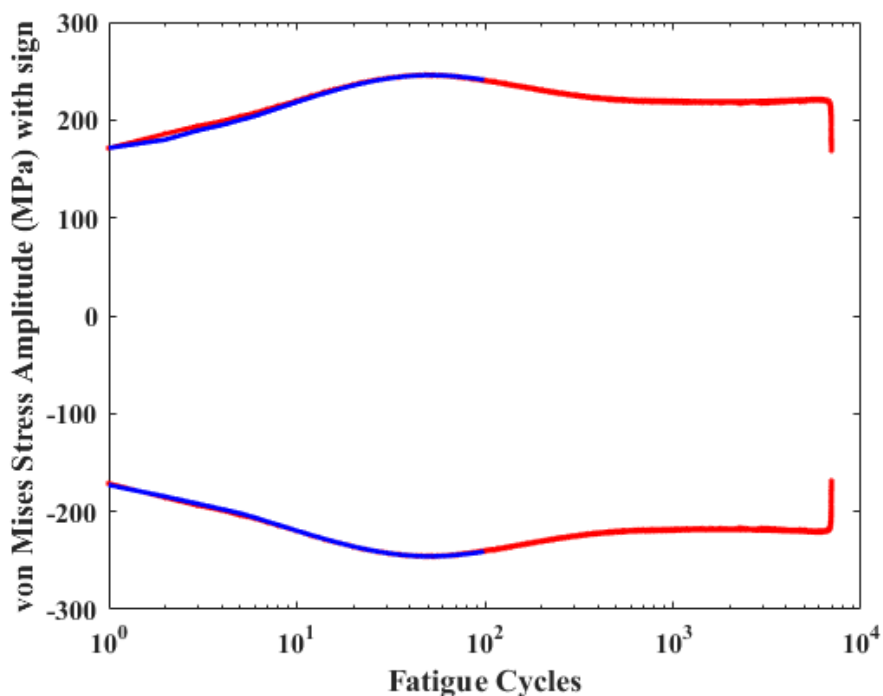


Figure 9. 9 Simulated (elastic-plastic analysis) vs experimental von Mises stress amplitudes (with negative sign during compression cycle) as function of fatigue cycles.

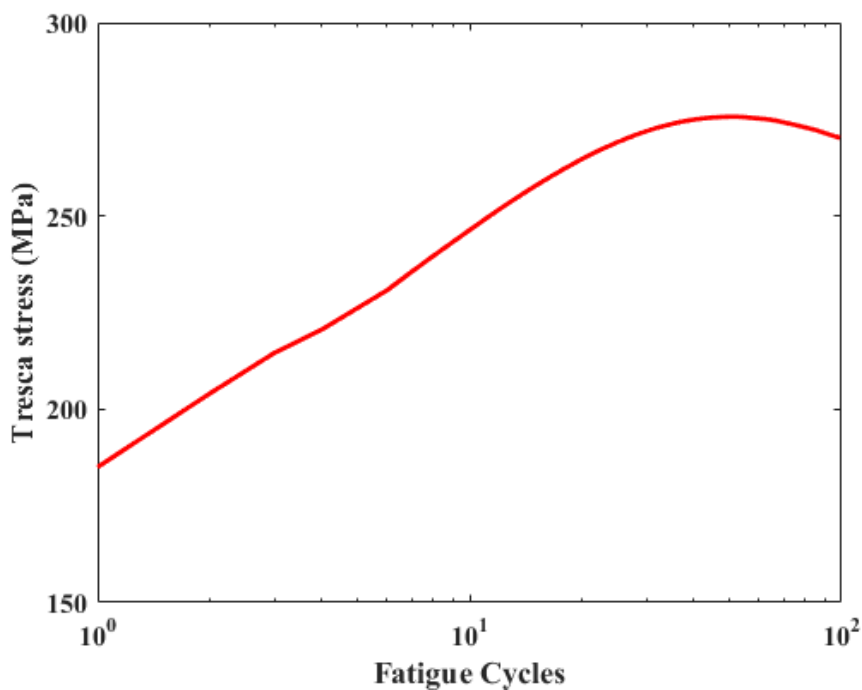


Figure 9. 10 Simulated (elastic-plastic analysis) Tresca stress amplitudes as function of fatigue cycles.

The comparison between the APSE calculated from experimental data (ET-F41) and from simulation is shown in Figure 9.11. Because the material properties used for structural simulation of the SL are APSE dependent and estimated from the uniaxial fatigue test (ET-F41), the APSE can be attributed as the mapping between material behavior under uniaxial fatigue loading and in the component under multiaxial loading. As shown in Figure 9.11, the APSE increases linearly with the number of fatigue cycles in both experiment and simulation. By using the slope of the APSE-vs-fatigue cycles plot and the maximum APSE value (16344 MJ/m³) at the end of fatigue life of the specimen, we can predict the life of the component. Note that, due to long simulation time (for example 29 hrs for 20 fatigue cycles using 1cpu and 1gpu) the PWR SL component was simulated for only 100 fatigue cycles. Based on the slope of APSE-vs-fatigue cycles curve the life of the SL pipe can be predicted as 6796. We believe that the component would have failed at around similar number of cycles if the simulation had been continued.

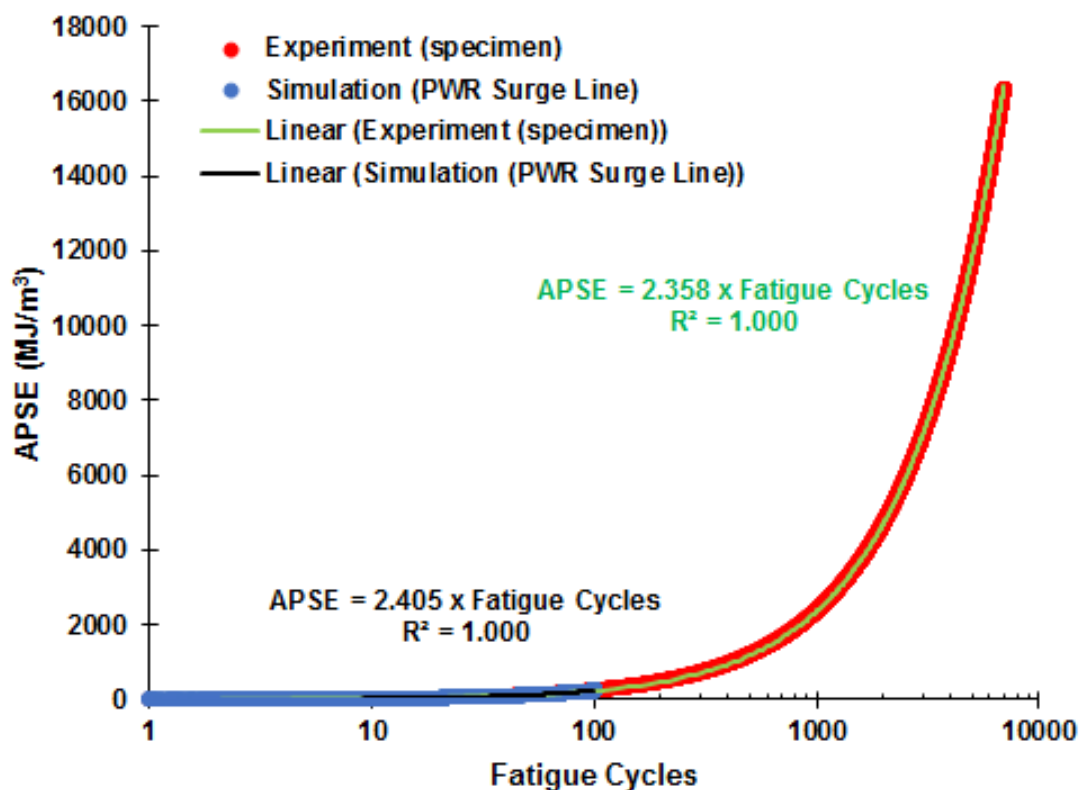


Figure 9. 11 Simulated (elastic-plastic analysis) vs experimental APSE as function of fatigue cycles.

9.1.2 Strain-controlled case ASME code and NUREG based life estimation

We also performed elastic analysis of PWR SL under strain control loading to estimate the fatigue life under in-air and PWR environment at 300 °C. We used ASME [1, 3] criteria for fatigue life evaluation in air. Then, we used the environmental fatigue correction factor, described in Ref [2, 47, 67], to estimate the PWR environment fatigue life from the in-air fatigue life.

For elastic analysis, we used the same FE mesh and boundary conditions as used for elastic-plastic analysis. The applied displacement amplitude and locations were also same. However, during elastic analysis cyclic displacement was applied only for one cycle. Since fixed elastic material properties are used for elastic analysis, it is expected that stress-strain would not evolve over time. Thus, it is justified to use stress-strain results from one fatigue cycle to evaluate fatigue life of the component. The FE mesh along with boundary conditions and applied displacement are shown in Figure 9.2. Similar to elastic-plastic analysis (see Section 9.1), the elastic analysis was also done at 300 °C. The elastic modulus (316 SS at 300 °C) used for analysis is given in Table 8.1. Figure 9.12 shows the contour plot of maximum principal stress distribution at an instant. Similar to the results from elastic-plastic analysis, the highest stress concentration is found to occur in the elements that are directly subjected to the applied deformation at one side and constrained to deform (all direction) at the other side due to the fixed boundary conditions. One of these elements, as shown in the magnified inset in Figure 9.12, is selected as the element of interest for analyzing the results from simulation. All the simulated stress-strain results presented here are at the centroid of this element. The simulated maximum, mid, and minimum principal stresses are shown in Figure 9.13.

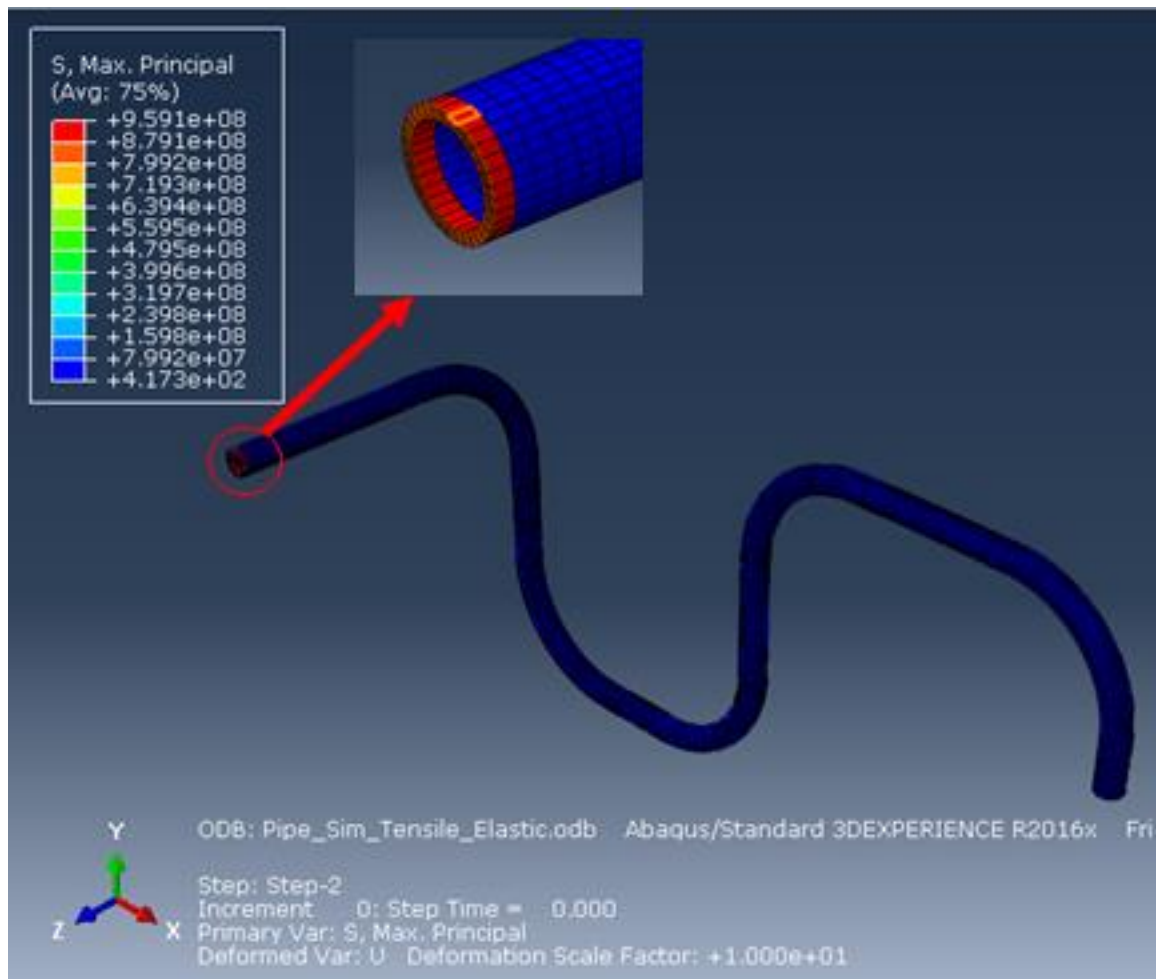


Figure 9. 12 Contour plot (from elastic analysis) of the maximum principal stress at an instant during the strain control fatigue loading shown in Figure 9.1. The highlighted element shown in the magnified inset is the element of interest.

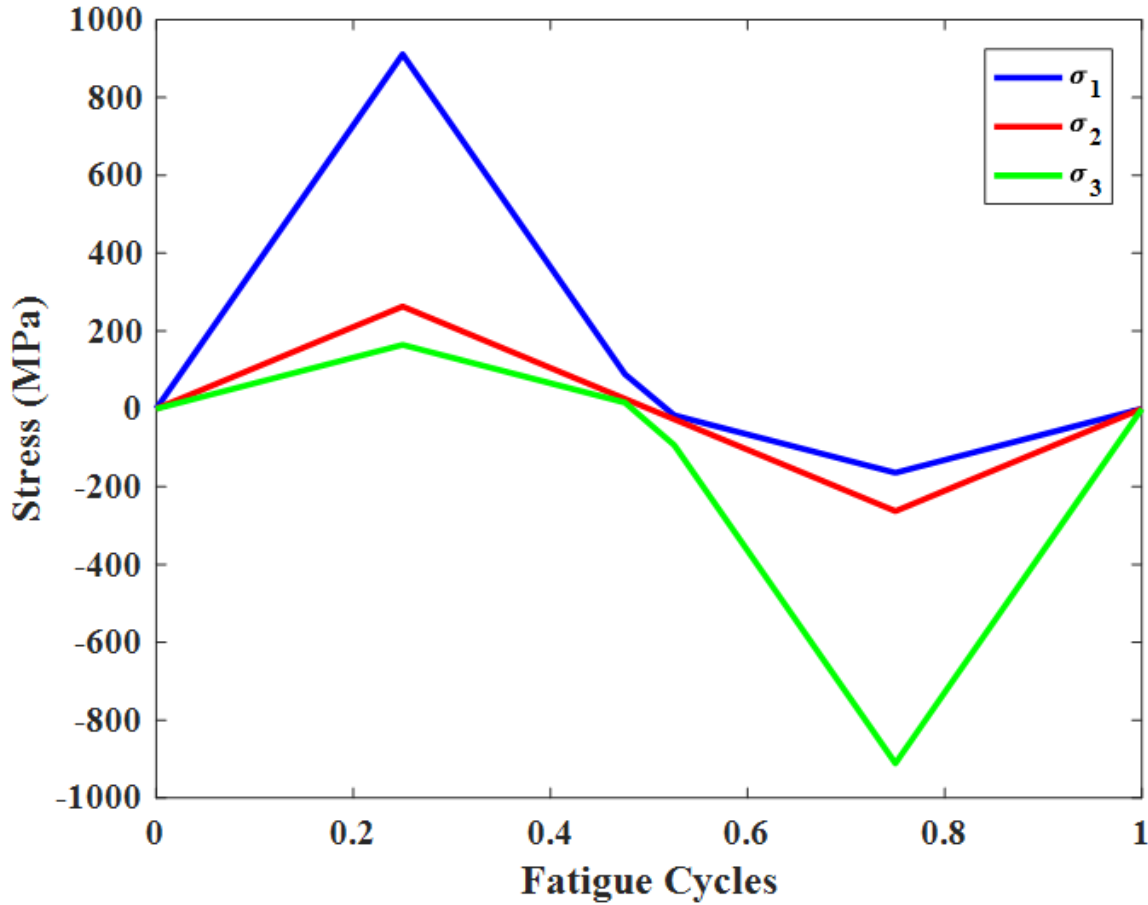


Figure 9. 13 Simulated (elastic analysis) maximum (σ_1), mid (σ_2), and minimum (σ_3) principal stresses.

We used the maximum (σ_1) and minimum (σ_3) principal stress histories, plotted in Figure 9.13, to estimate the equivalent cyclic stress amplitude σ_a at a given instant, i using the following expression:

$$\sigma_{a,i} = \frac{1}{2} [\sigma_{1,i} - \sigma_{3,i}] \quad (9.1)$$

ASME code design by analysis rules (NB-3200) uses Tresca criterion for fatigue life estimation. According to Tresca criterion, the maximum shear stress at a point is equal to one-half the difference between the algebraically largest (σ_1) and the algebraically smallest (σ_3) of the three principal stresses at that point. Hence the estimation of stress amplitude $\sigma_{a,i}$ using Eq. 9.1 would result in estimating the shear stress at a given instant, i . Figure 9.14 shows the stress amplitude history using Eq. 9.1. We then calculated the maximum stress amplitude (σ_a^{max}) using Eq. 9.2.

$$\sigma_a^{max} = \max[\sigma_{a,i}] - \min[\sigma_{a,i}] \quad (9.2)$$

According to ASME code [1, 3], the following equation needs to be used to calculate the allowable stress (\hat{S}_a) which would be used to determine the in-air fatigue life at 300 °C from the ASME fatigue life curve for RT.

$$\hat{S}_a = K_r K_e S_a \frac{E(\text{curve})}{E(\text{analysis})} \quad (9.3)$$

where S_a is the calculated stress from analysis which in our case is σ_a^{\max} . $E(\text{curve})$ is the modulus of elasticity given on the Design Fatigue curve, $E(\text{analysis})$ is the elastic modulus used for analysis. K_r is the roughness correction factor which is assumed to be 1. K_e is the fatigue penalty factor. According to ASME code (equation KD-323.1 in Ref. [3]), K_e can be calculated using following equation.

$$K_e = \frac{(\Delta \varepsilon_t)_{ep}}{(\Delta \varepsilon_t)_e} \quad (9.4)$$

where $(\Delta \varepsilon_t)_{ep}$ is the equivalent total strain range from elastic-plastic analysis, while $(\Delta \varepsilon_t)_e$ is the equivalent total strain range from elastic analysis. Using the maximum and minimum principal strain histories from elastic-plastic and elastic analyses, we determined the respective equivalent total strain range as follows:

$$K_e = \frac{\max[\varepsilon_1 - \varepsilon_3]_{ep}}{\max[\varepsilon_1 - \varepsilon_3]_e} \quad (9.5)$$

where ε_1 and ε_3 are maximum and minimum principal strains, respectively. Note that, the elastic-plastic analysis (see Section 9.1.1) was performed for 100 fatigue cycles but we considered the results from only 1st fatigue cycle to estimate $(\Delta \varepsilon_t)_{ep}$. Using the data from elastic-plastic and elastic analyses and Eq. 9.5, the value of K_e was found 1.32.

Using Eq. 9.3, the allowable stress, \hat{S}_a was found. Introducing this stress into ASME fatigue life curve (Figure 9.15) for RT, the in-air fatigue life at 300 °C is estimated. The estimated in-air fatigue life at 300 °C is given in Table 9.1. We also determined the fatigue life assuming K_e equal to 1 and the results are presented in Table 9.2.

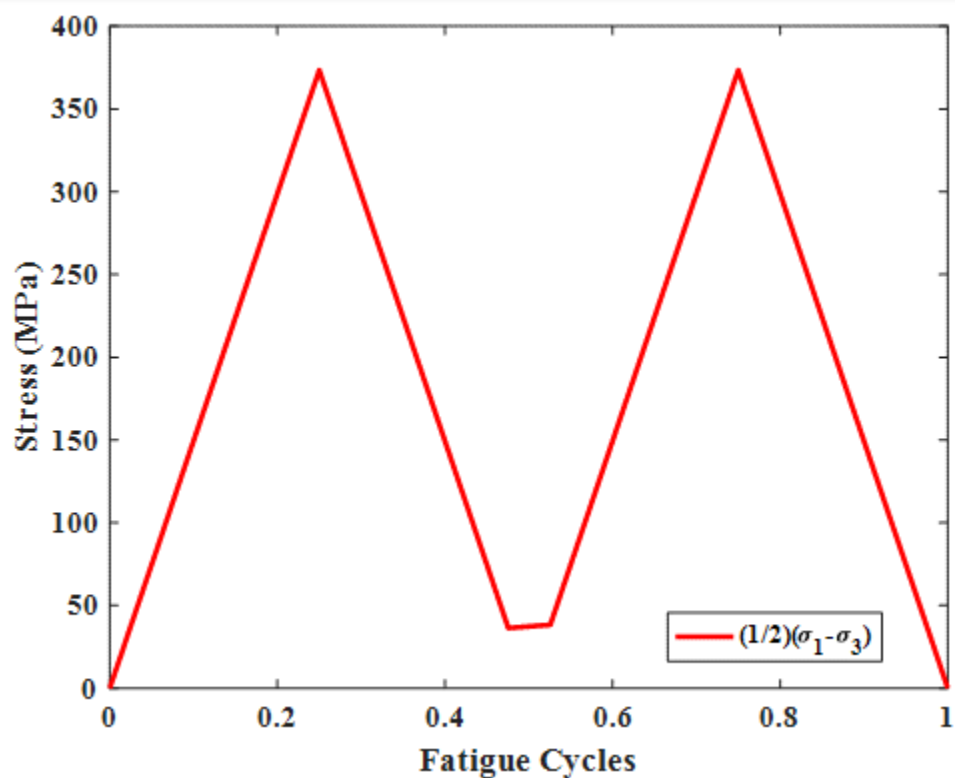


Figure 9. 14 Stress amplitude history according to Eq. 9.1.

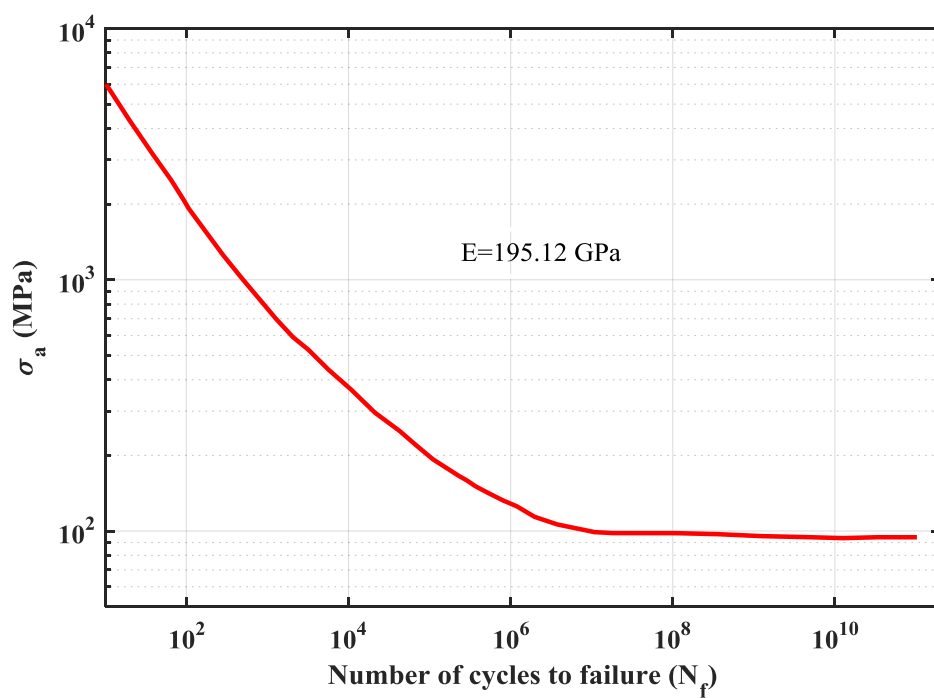


Figure 9. 15 ASME code fatigue design curve for austenitic steel [1].

We determined the fatigue live in PWR environment (N_{PWR}) from in-air fatigue life (N_{air}) by applying necessary environmental fatigue correction factor (F_{en}) using following equation.

$$N_{PWR} = \frac{N_{air}}{F_{en}} \quad (9.6)$$

According to NUREG-6909, Rev.1 [67], F_{en} for austenitic steel can be determined using:

$$F_{en} = \exp(0.734 - \theta' O' \epsilon') \quad (9.7)$$

where θ' , O' , and ϵ' are transformed temperature, dissolved oxygen (DO), and strain rate, respectively, as follows:

$$\begin{aligned} \theta' &= 0 & (\theta < 150 \text{ }^{\circ}\text{C}) \\ \theta' &= \frac{(T-150)}{175} & (150 \text{ }^{\circ}\text{C} \leq \theta < 325 \text{ }^{\circ}\text{C}) \\ \theta' &= 1 & (\theta \geq 325 \text{ }^{\circ}\text{C}) \end{aligned} \quad (9.8)$$

$$\begin{aligned} \epsilon' &= 0 & (\epsilon' > 0.4\%/s) \\ \epsilon' &= \ln\left(\frac{\dot{\epsilon}}{0.4}\right) & (0.0004 \leq \epsilon' \leq 0.4\%/s) \\ \epsilon' &= \ln\left(\frac{0.0004}{0.4}\right) & (\epsilon' < 0.0004\%/s) \end{aligned} \quad (9.9)$$

$$O' = 0.281 \quad (\text{all DO levels}) \quad (9.10)$$

We used the method described in NUREG/CR-6909 [2] to determine the maximum strain rate ($\dot{\epsilon}$). NUREG/CR-6909 suggests estimating the strain amplitude from the estimated principal stress histories. Based on the NUREG/CR-6909, the strain amplitude ($\epsilon_{a,i}$) at a given instant can be found using:

$$\epsilon_{a,i} = \frac{1}{2E(\text{analysis})} [\sigma_{1,i} - \sigma_{3,i}] \quad (9.11)$$

The strain amplitude history estimated according to Eq. 9.11 is given in Figure 9.16. From the strain amplitude history, we determined the maximum strain amplitude (ϵ_a^{max}) as follows:

$$\epsilon_a^{max} = \max[\epsilon_{a,i}] - \min[\epsilon_{a,i}] \quad (9.12)$$

Using ϵ_a^{max} and fatigue cycle time period, we determined $\dot{\epsilon}$ ($= 0.2364\%$) which was plugged in Eq. 9.9 to estimate the transformed strain rate (ϵ'). Using the values of θ ($= 300 \text{ }^{\circ}\text{C}$), ϵ' ($= 0.04728\%$), and O' , the environmental fatigue correction factor (F_{en}) was determined from Eq. 9.7. The estimated PWR environment fatigue life at $300 \text{ }^{\circ}\text{C}$ was then estimate using Eq. 9.6, and the value is given in Tables 9.1 and 9.2. Tables 9.1 and 9.2 also compare the estimated fatigue lives based on elastic analysis and code

(S~N curve) with those estimated based on elastic-plastic analysis and ANL's mechanistic fatigue evaluation method.

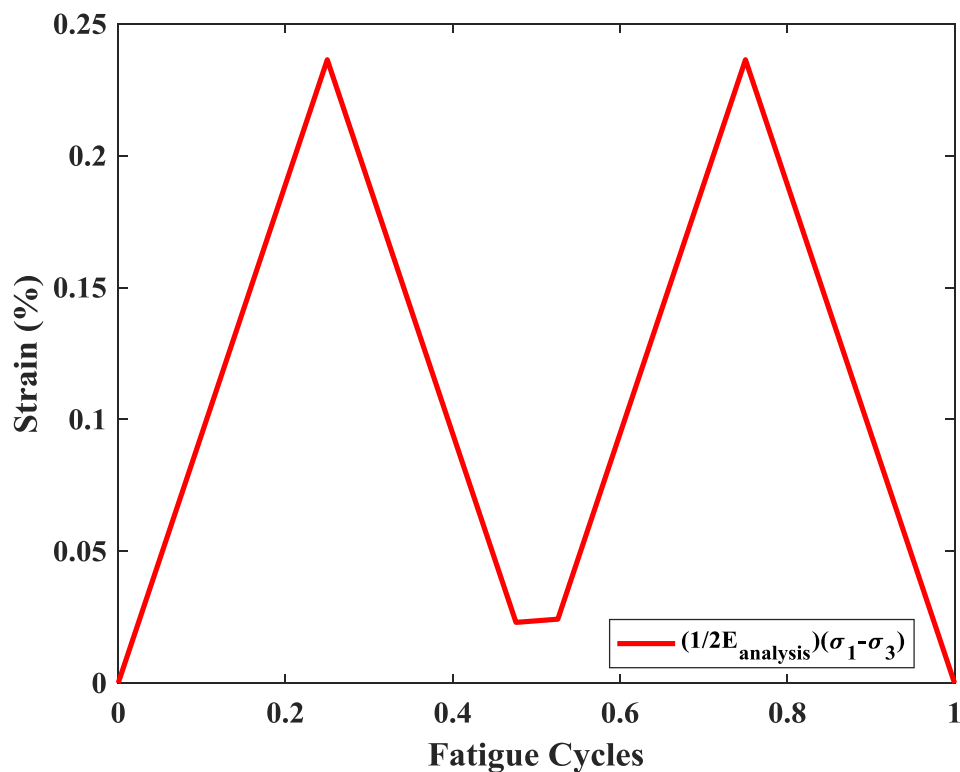


Figure 9. 16 Strain amplitude history estimated using Eq. 9.11.

Table 9. 1 Estimated in-air and PWR environment fatigue lives at 300 °C (using $K_e=1.32$ in Eq. 9.3)

Environment	Temperature	Environmental Correction Factor, F_{en}	Fatigue life (cycles)	Uniaxial Experiment or Multiaxial Analysis
Air	300 °C	N/A	6970	Uniaxial experiment
			2070	Single cycle-multiaxial elastic analysis and ASME code
			6796	Multicycle-multiaxial elastic-plastic analysis using ANL evolutionary approach
PWR	300 °C	3.469	597 (=2070/3.469)	Single cycle-multiaxial elastic analysis and ASME code and NUREG-6909
			1959 [#] (=6796/3.469)	Multicycle-multiaxial elastic-plastic analysis using ANL [£] evolutionary approach and NUREG-6909

Fatigue life is calculated by dividing in-air fatigue life estimated by elastic-plastic analysis ((based on ASME and NUREG-6909 based single cycle stress analysis approach and ANL's multi-cycle stress analysis approach) by environmental correction factor ($F_{en}=3.469$) estimated using Eq. 9.5.

£ ANL approach does not require to use NUREG-6909 F_{en} correction if PWR water condition evolutionary material model is used for multiaxial transformation of uniaxial data (as in present in-air case).

Table 9. 2 Estimated in-air and PWR environment fatigue lives at 300 °C (using $K_e=1$ in Eq. 9.3)

Environment	Temperature	Environmental Correction Factor, F_{en}	Fatigue life (cycles)	Uniaxial Experiment or Multiaxial Analysis
Air	300 °C	N/A	6970	Uniaxial experiment
			5668	Single cycle-multiaxial elastic analysis and ASME code
			6796	Multicycle-multiaxial elastic-plastic analysis using ANL evolutionary approach
PWR	300 °C	3.469	1634 (=5668/3.469)	Single cycle-multiaxial elastic analysis and ASME code and NUREG-6909
			1959 [#] (=6796/3.469)	Multicycle-multiaxial elastic-plastic analysis using ANL [£] evolutionary approach and NUREG-6909

Fatigue life is calculated by dividing in-air fatigue life estimated by elastic-plastic analysis (based on ASME and NUREG-6909 based single cycle stress analysis approach and ANL's multi-cycle stress analysis approach) by environmental correction factor ($F_{en}=3.469$) estimated using Eq. 9.5.

£ ANL approach does not require to use NUREG-6909 F_{en} correction if PWR water condition evolutionary material model is used for multiaxial transformation of uniaxial data (as in present in-air case).

From the results shown in Tables 9.1 and 9.2, it can be found that ANL's evolutionary plasticity based models predicts fatigue lives, which are much closer to the experiment (at least for the discussed in-air condition ideal loading case) compared to the predicted lives based on ASME's penalty factor based elastic-plastic stress analysis approach. Also these results show that ANL's method predict less conservative results than the predicted lives based on ASME and NUREG-6909 based approach. In summary, ANL's approach not only predict fatigue lives closer to experiment, but also predict less conservative results. Hence, ANL's model may help to provide simulated data those can be used for extended service evaluation of LWR components. However, the discussed results are preliminary and require further evaluation both under in-air and PWR water conditions.

9.2 Fatigue Life Estimation of SL Pipe under Actual Stress-Controlled or Thermal-Mechanical Loading Conditions

In this section we discuss the fatigue life estimation of SL pipe under actual stress-loading condition. In previous section we demonstrated the fatigue life estimation of SL pipe under an imaginary uniaxial and strain-controlled cyclic loading. This was to verify the ANL developed fully mechanistic model for

component life estimation against the experimental data, those are generated under same condition of uniaxial and strain-controlled cyclic loading. However, under realistic conditions, components experiences multiaxial stress loading associated with thermal-mechanical loading conditions. To apply the ANL developed fully-mechanistic (cycle-by-cycle stress analysis) model for life estimation of components under realistic stress-controlled type loading condition (associated with actual thermal-mechanical loading), it requires the use of material models developed under very similar loading conditions, in which strain is a dependent/observed variable not a controlling variable as in the case of strain-controlled testing cases. Although we have presented some of the stress-controlled related material test and material model data in Section 6 & 7, still the stress-controlled material model is in its infancy stage. In addition, it requires to be implemented to ABAUQS, which is one of our future task. Hence, in this section we only shows the fatigue life estimation of out-surge and in-surge condition based on ASME and NUREG-6909 based fatigue life estimation approaches using single-cycle stress analysis results. Related CFD-HT and a detailed stress analysis results are already disused in Section 7 and 8, respectively. Note that according to ASME code section III, NB3228.5 elastic analysis is required for life estimation of class 1 and components. Hence in this section only life estimation relevant elastic stress analysis results are presented. Also the same ASME and NUREG-6909 based methods discussed above (refer section 9.1.2) is used for the present fatigue live estimation under actual thermal-mechanical loading condition. Only the related out-surge and in-surge condition results are presented below.

9.2.1 In-air and environmental fatigue lives estimation of SL pipe under out-surge flow condition discussed in Section 8.4.1.

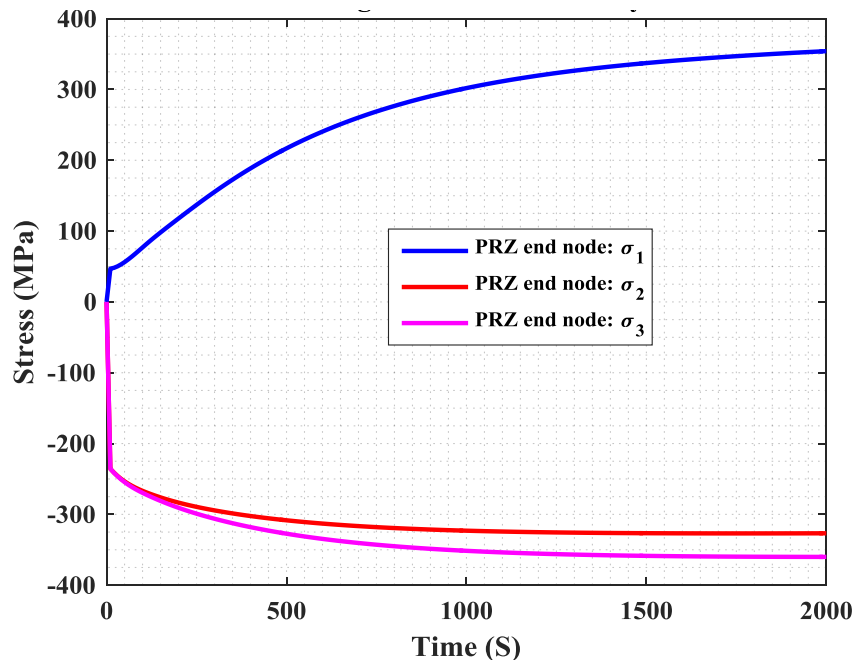


Figure 9. 17 Simulated (elastic analysis) maximum (σ_1), mid (σ_2), and minimum (σ_3) principal stresses at pressurizer-end of SL pipe under out-surge flow condition discussed in section 8.4.1.

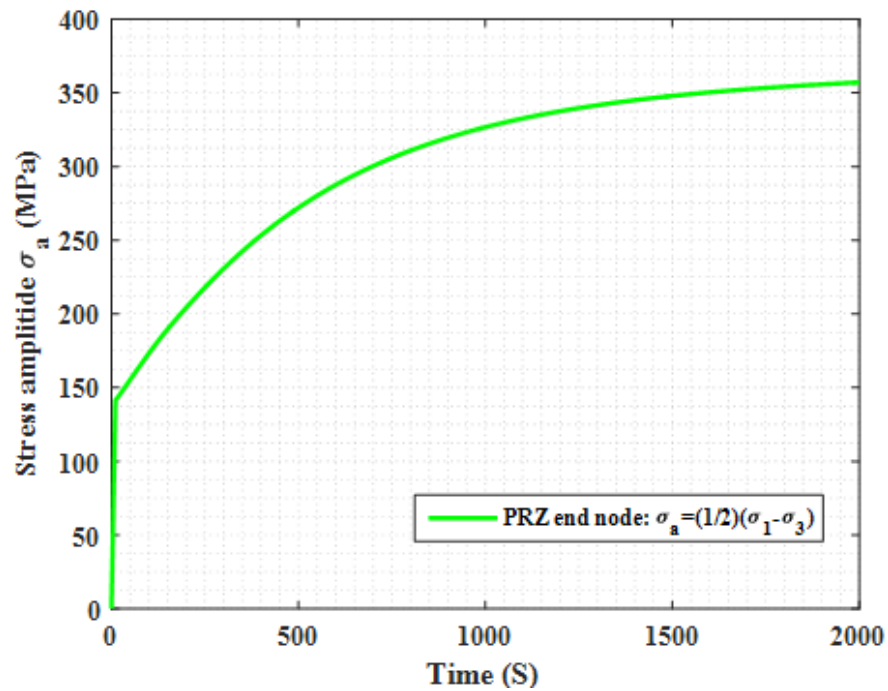


Figure 9. 18 Stress amplitude history according to Eq. 9.1 and at pressurizer-end of SL pipe under out-surge flow condition discussed in section 8.4.1.

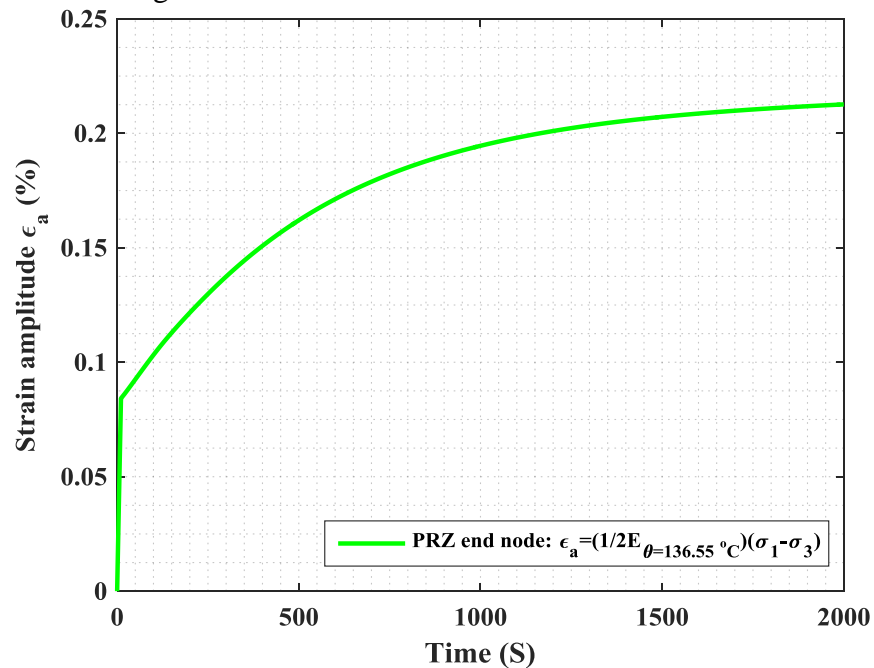


Figure 9. 19 Strain amplitude history according to Eq. 9.9 and at pressurizer-end of SL pipe under out-surge flow condition discussed in section 8.4.1.

Table 9. 3 Fatigue lives of SL pipe, estimated under out-surge flow condition discussed in section 8.4.1.

Environment (K_e value)	θ_{av} (°C)	E_{av} (GPa)	E_{curve} (GPa)	$E_{Correction}$	σ_a (MPa)	$\dot{\sigma}_a$ (MPa)	F_{en}	N_f
Air ($K_e = 1$)	136.55	167.95	195.12	1.1618	357.1	414.87	1	7332
PWR water ($K_e = 1$)							2.0834	3519
Air ($K_e = 1.22$) [#]						506.14	1	3777
PWR water ($K_e = 1.22$) [#]							2.0834	1813

$$^{\#} K_e = \frac{(\epsilon_1 - \epsilon_3)_{ep}}{(\epsilon_1 - \epsilon_3)_e} = 1.22 \text{ (Refer Eq. 9.5)}$$

9.2.2 In-air and environmental fatigue lives estimation of SL pipe under in-surge flow condition discussed in Section 8.4.2.

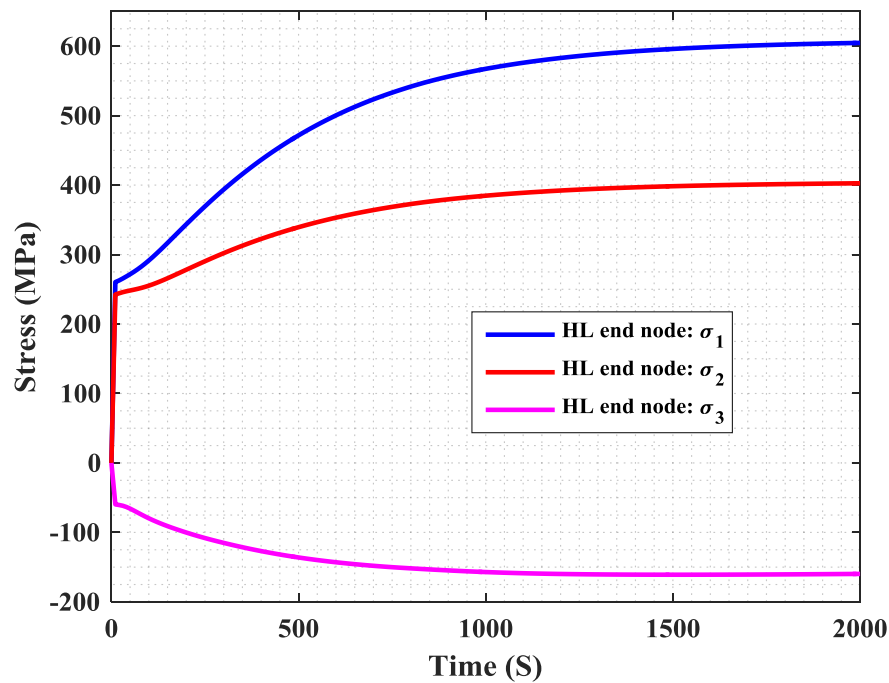


Figure 9. 20 Simulated (elastic analysis) maximum (σ_1), mid (σ_2), and minimum (σ_3) principal stresses at pressurizer-end of SL pipe under in-surge flow condition discussed in section 8.4.2.

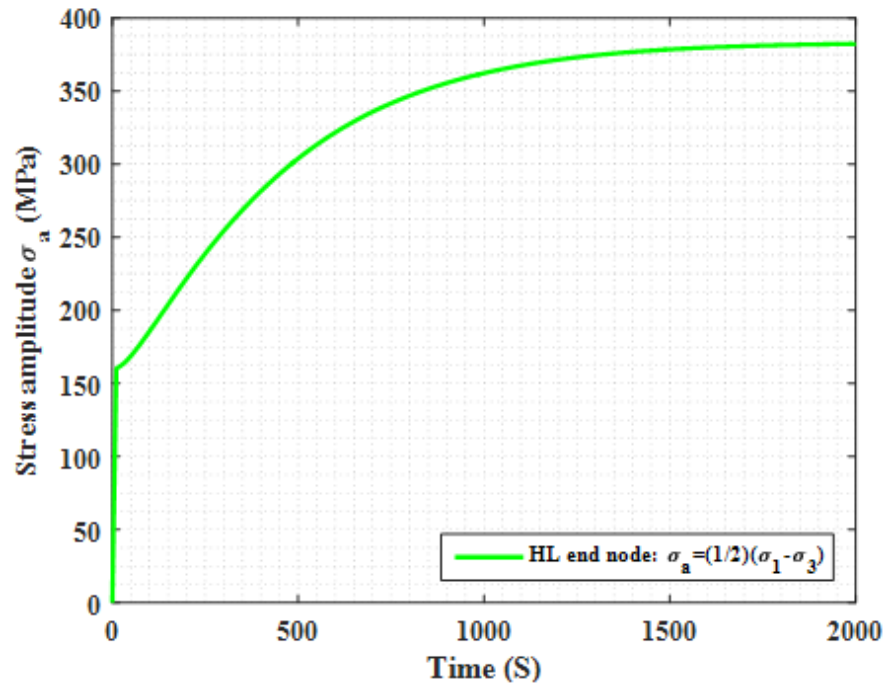


Figure 9. 21 Stress amplitude history according to Eq. 9.1 and at pressurizer-end of SL pipe under in-surge flow condition discussed in section 8.4.2.

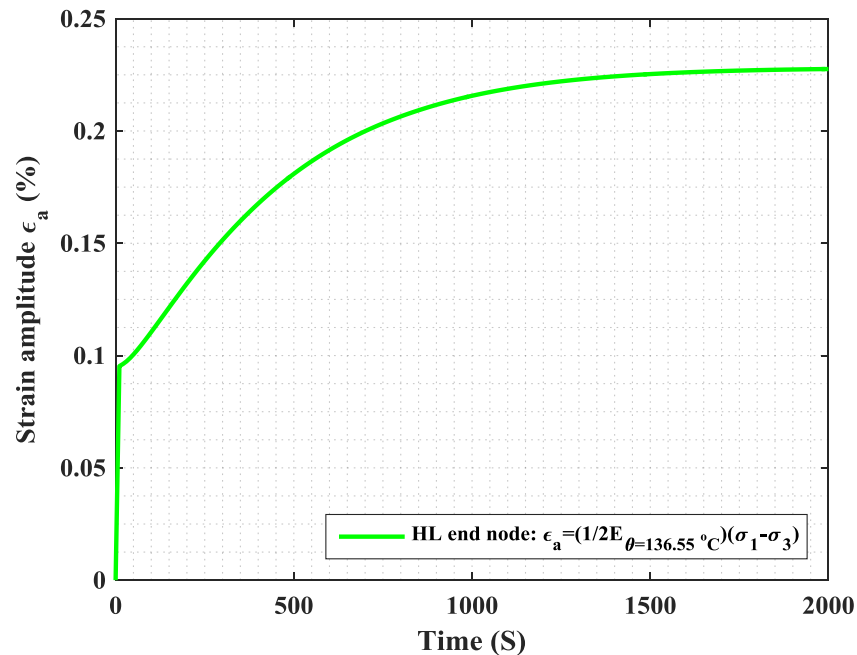


Figure 9. 22 Strain amplitude history according to Eq. 9.9 and at pressurizer-end of SL pipe under in-surge flow condition discussed in section 8.4.2.

Table 9. 4 Fatigue lives of SL pipe, estimated under in-surge flow condition discussed in Section 8.4.2.

Environment (K_e value)	θ_{av} (°C)	E_{av} (GPa)	E_{curve} (GPa)	$E_{Correction}$	σ_a (MPa)	$\dot{\sigma}_a$ (MPa)	F_{en}	N_f
Air ($K_e = 1$)	136.55	167.95	195.12	1.1618	382.2	444.03	1	5519
PWR water ($K_e = 1$)							2.0834	2649
Air ($K_e = 1.153$) [#]						511.97	1	3614
PWR water ($K_e = 1.153$) [#]							2.0834	1734

$$^{\#} K_e = \frac{(\epsilon_1 - \epsilon_3)_{ep}}{(\epsilon_1 - \epsilon_3)_e} = 1.153 \quad (\text{refer Eq. 9.5})$$

10 Summary and Future Study

10.1 Summary

In this report, a complete framework of ANL developed evolutionary cyclic plasticity based fatigue life estimation approach is demonstrated. Experimental data for 316 SS presented under both strain-controlled and stress-controlled loading conditions. Using the resulting test data different material models are developed. The accuracy of material models under both the strain-controlled and stress-controlled conditions is verified through evolutionary cyclic-plasticity based 1-D analytical models. The strain-controlled material models are implemented in commercially available ABAQUS FE software for component level modeling. The 3D FE implementation of evolutionary cyclic-plasticity in ABAQUS is verified through uniaxial test data under constant, variable and random amplitude fatigue loading. The transformation of uniaxial material model to multiaxial loading domain is demonstrated through fatigue life estimation of reactor component such as of 316 SS PWR surge line (SL) pipe. For component level fatigue life estimation of SL, different CFD analyses are performed to evaluate the thermal stratification condition. A detailed parametric study performed using both standalone CFD and fluid-structure-interaction (FSI) based coupled CFD and heat transfer (CFD-HT) models. Both out-surge and in-surge transient conditions are modeled to estimate the thermal boundary conditions for stress analysis and subsequent fatigue evaluation. Fatigue lives of the SL pipe under out-surge and in-surge flow conditions are estimated based on ASME approach (for in-air life estimation) and NUREG-6909 approach (for environmental correction factor estimation and corresponding PWR environmental fatigue life estimation). Finally, ANL developed fully mechanics based (evolutionary cyclic-plasticity) approach is demonstrated for fatigue life estimation of the SL pipe without using conventional S~N curve based approach. Followings are the major conclusions from the presented research work:

1. The simulated results demonstrate that the evolutionary cyclic plasticity model can mechanistically capture all the important stages of material behavior (initial hardening, softening, stabilized cycles, and finally rapid crack propagation followed by failure) during the entire fatigue life of the specimens with great accuracy.
2. Evolutionary cyclic plasticity model can capture the load-sequence effect such as under variable and random amplitude loading with great accuracy.
3. Stress-controlled test results show substantial effect of PWR water condition and loading rate on ratcheting strain.
4. CFD simulations show that there is a substantial effect of mass flow rate on the extent of thermal stratification in SL.
5. ANL's fully mechanistic or cycle-by-cycle stress analysis model can be used for cycle-by-cycle stress analysis and associated fatigue life prediction of actual reactor component. Although the discussed

component model (under the idealistic or imaginary strain controlled loading condition) predicted closely matching results (e.g. cyclic stress hardening/softening) comparable to the results obtained from the corresponding condition uniaxial experiment, under actual thermal-mechanical loading case the stress analysis results would be much dependent on multi-axial loading effect associated with actual thermal-mechanical loading conditions of reactor component. Nevertheless, the purpose of the discussed component-level fully mechanistic model is to demonstrate the feasibility of cycle-by-cycle stress analysis of a realistic reactor component.

10.2 Future Work

Followings are some of the future work envisioned:

1. Conduct more constant amplitude stress-controlled tests (with different mean stress conditions) to ascertain the observed higher rate of strain ratcheting under PWR water conditions.
2. Conduct stress-controlled tests under variable and random amplitude loading to develop more generic material models, which can be used for capturing the load-sequence effect under stress-controlled loading.
3. Extend the ANL developed fully mechanistic fatigue evaluation framework for use in high performance computing system.
4. Extend the transient condition based component-level CFD, stress, and fatigue analysis approach for full reactor cycles both under design basis conditions and grid-load-following conditions.
5. Extend the developed approach for modeling the nozzle welds.

References

1. The American Society of Mechanical Engineers (2010) *ASME Boiler and Pressure Vessel Code*.
2. O.K. Chopra, W.J. Shack (2007) *Effect of LWR Coolant Environments on the Fatigue Life of Reactor Materials*, U.S. Nuclear Regulatory Commission, Report no. NUREG/CR-6909, ANL-06/08. (<https://www.nrc.gov/docs/ML0706/ML070660620.pdf>).
3. The American Society of Mechanical Engineers (2013) *ASME Boiler and Pressure Vessel Code*, Section VIII, Division 3.
4. BSi (2012) BS EN 13445-3:2009+A1:2012, Unfired Pressure Vessels. Part 3: Design.
5. BSi (2012) PD 5500:2012, Specification for Unfired Fusion Welded Pressure Vessels.
6. EDF Energy Generation (2003) R5-Assessment Procedure for the High Temperature Response of Structures, Issue 3, Revision 1.
7. AFCEN (2007) RCC-M- Edition 2007 –Addendum December 2008: Design and Construction Rules for Mechanical Components of PWR Nuclear Islands.
8. N. Platts, D.R. Tice, J. Nicholls (2015) *Study of Fatigue Initiation of Austenitic Stainless Steel in a High Temperature Water Environment and in Air Using Blunt Notch Compact Tension Specimens*, ASME Pressure Vessels and Piping Conference, Paper no. PVP2015-45844.
9. J. Shi, L. Wei, C. Faidy, A. Wasylyk, N. Prinja (2016) *A Comparison of Different Design Codes on Fatigue Life Assessment Methods*, ASME Pressure Vessels and Piping Conference, Paper no. PVP2016-63040.
10. J. Shit, S. Dhar, S. Acharyya (2013) *Modeling and Finite Element Simulation of Low Cycle Fatigue Behaviour of 316 SS*, Procedia Engineering, 55, pp. 774-779.
11. Y.F. Dafalias, E.P. Popov (1975) *A Model of Nonlinearly Hardening Materials for Complex Loading*, Acta mechanica, 21, pp. 173-192.
12. P.J. Armstrong, C.O. Frederick (1966) *A Mathematical Representation of the Multiaxial Bauschinger Effect*, Central Electricity Generating Board and Berkeley Nuclear Laboratories, Research & Development Department.
13. J.L. Chaboche (1986) *Time-independent Constitutive Theories for Cyclic Plasticity*, International Journal of Plasticity, 2, pp. 149–188.
14. J.L. Chaboche (1991) *On Some Modifications of Kinematic Hardening to Improve the Description of Ratchetting Effects*, International Journal of Plasticity, 7, pp. 661–678.
15. J.L. Chaboche, G. Rousselier (1983) *On the Plasticity and viscoplasticity Constitutive Equations—part II: Application of Internal Variable Concepts to the 316 Stainless Steel*, Journal of Pressure Vessel Technology, 105, pp. 159-164.
16. N.N. Ohno Y.Y. Takahashi, K.K. Kuwabara (1989) *Constitutive Modeling of Anisothermal Cyclic Plasticity of 304 Stainless Steel*, Journal of Engineering and Materials Technology, 111, pp.106-114.
17. G. Kang (2006) *Finite Element Implementation of Visco-plastic Constitutive Model with Strain-range-dependent Cyclic Hardening*, International Journal for Numerical Methods in Biomedical Engineering, 22, pp. 137-153.
18. G. Kang, N. Ohno, A. Nebu (2003) *Constitutive Modeling of Strain Range Dependent Cyclic Hardening*, International journal of plasticity, 19, pp. 1801-1819.
19. N. Ohno, J.D. Wang (1993) *Kinematic Hardening Rules with Critical State of Dynamic Recovery, part I: Formulation and Basic Features for Ratchetting Behavior*, International journal of plasticity, 9, 375-390.

20. S.M Syed, T. Hassan, E. Corona (2008) *Evaluation of Cyclic Plasticity Models in Ratcheting Simulation of Straight Pipes under Cyclic Bending and Steady Internal Pressure*, International Journal of Plasticity, 24, pp. 1756-1791.
21. G. Sumit, S.K. Gupta, S. Sivaprasad, S. Tarafder, V. Bhasin, K.K. Vaze, A.K. Ghosh (2013) *Low Cycle Fatigue and Cyclic Plasticity Behavior of Indian PHWR/AHWR Primary Piping Material*, Procedia Engineering, 55, pp. 136-143.
22. S. Mohanty, W.K. Soppet, S. Majumdar, K. Natesan (2015) *Effect of Pressurized Water Reactor Environment on Material Parameters of 316 Stainless Steel: A Cyclic Plasticity Based Evolutionary Material Modeling Approach*, ASME Pressure Vessels and Piping Conference, Paper no. PVP2015-45701.
23. S. Mohanty, W.K. Soppet, S. Majumdar, K. Natesan (2016) *Chaboche-Based Cyclic Material Hardening Models for 316 SS–316 SS Weld under In-air and Pressurized Water Reactor Water Conditions*, Nuclear Engineering and Design, 305, pp 524-530.
24. S. Mohanty, W.K. Soppet, S. Majumdar, K. Natesan (2015) *Tensile and Fatigue Testing and Material Hardening Model Development for 508 LAS Base Metal and 316 SS Similar Metal Weld under In-air and PWR Primary Loop Water Conditions*, Argonne National Laboratory, Report no. ANL/LWRS-15/02. (<https://www.osti.gov/scitech/biblio/1224989>).
25. S. Mohanty, W.K. Soppet, S. Majumdar, K. Natesan (2016) *In-Air and Pressurized Water Reactor Environment Fatigue Experiments of 316 Stainless Steel to Study the Effect of Environment on Cyclic Hardening*, Journal of Nuclear Materials, 473, pp. 290-299.
26. S. Mohanty, B. Barua, W.K. Soppet, S. Majumdar, K. Natesan (2016) *Study the Cyclic Plasticity Behavior of 508 LAS under Constant, Variable and Grid-Load-Following Loading Cycles for Fatigue Evaluation of PWR Components*, Argonne National Laboratory, Report no. ANL/LWRS-16/03. (<https://www.osti.gov/scitech/biblio/1331616>).
27. M.L. Wilkins (1963) *Calculation of elastic-plastic flow*, California University Livermore Radiation Lab, Report no. UCRL-7322.
28. S.K. Koh (2002) *Fatigue Damage Evaluation of a High Pressure Tube Steel using Cyclic Strain Energy Density*, International Journal of Pressure Vessels and Piping, 79, pp. 791-798.
29. X. Lin, G. Halcheng (1998) *Plastic Energy Dissipation iVJodel for Lifetime Prediction of Zirconium and Zircaloy-4 Fatigued at RT and 400°C*, Journal of Engineering Materials and Technology, 120, pp. 114-118.
30. T. Łagoda (2001) *Energy Models for Fatigue Life Estimation under Uniaxial Random Loading. Part I: The Model Elaboration*, International Journal of Fatigue, 23, pp. 467-480.
31. B. Fekete (2015) *New Energy-based Low Cycle Fatigue Model for Reactor Steels*, Materials & Design, 79, pp. 42-52.
32. A.N. Kadhimi, M. Mustafa, A. Varvani-Farahani (2015) *Fatigue Life Prediction of Low-alloy Steel Samples Undergoing Uniaxial Random Block Loading Histories based on Different Energy-based Damage Descriptions*, Fatigue & Fracture of Engineering Materials & Structures, 38, pp. 69-79.
33. J. Morrow (1965) *Cyclic Plastic Strain Energy and Fatigue of Metals*, ASTM International, Internal Friction, Damping, and Cyclic plasticity.
34. G.R. Halford (1966) *The Energy Required for Fatigue (Plastic Strain Hysteresis Energy Required for Fatigue in Ferrous and Nonferrous Metals)*, Journal of materials, 1, pp. 3-18.
35. B.N. Leis (1977) *An Energy-based Fatigue and Creep-fatigue Damage Parameter*, Journal of Pressure Vessel Technology, 99, pp. 524-533.
36. Systèmes, Dassault. (2016) *"Abaqus Theory Guide"*.

37. S. Mohanty, W.K. Soppet, S. Majumdar, K. Natesan (2014) *Environmental Effect on Evolutionary Cyclic Plasticity Material Parameters of 316 Stainless Steel: An Experimental & Material Modeling Approach*, Argonne National Laboratory, Report no. ANL/LWRS-14/01. (<https://www.osti.gov/scitech/biblio/1168233>).
38. S.K. Paul, S. Sivaprasad, S. Dhar, S. Tarafder (2011) *Key issues in cyclic plastic deformation: experimentation*, Mechanics of Materials, 43, pp 705-720.
39. A.Sarkar, A. Nagesha, R. Sandhya, M.D. Mathew (2013) *Effect of Temperature on Ratcheting Behaviour of 316LN SS*, Procedia Engineering, 55, pp. 650-654.
40. S.K. Paul, S. Sivaprasad, S. Dhar, S. Tarafder (2010) *True stress control asymmetric cyclic plastic behavior in SA333 C-Mn steel*, International Journal of Pressure Vessels and Piping, 87, pp. 440-446.
41. S.K. Paul, S. Sivaprasad, S. Dhar, S. Tarafder (2012) *True stress-controlled ratcheting behavior of 304LN stainless steel*, Journal of Materials Science, 47, pp. 4660-4672.
42. S. Mohanty, W.K. Soppet, S. Majumdar, K. Natesan (2015) *Pressurized Water Reactor Environment Effect on 316 Stainless Steel Stress Hardening/Softening: An Experimental Study*, ASME Pressure Vessels and Piping Conference, Paper no. PVP2015-45694.
43. S. Mohanty, W.K. Soppet, B. Barua, S. Majumdar, K. Natesan (2017) *Modeling the Cycle-Dependent Material Hardening Behavior of 508 low Alloy Steel*, Experimental Mechanics, 57, pp. 847-855.
44. O.C. Garrido, L. Cizelj, I. Simonovski (2012) *Modular 3-D solid finite element model for fatigue analyses of a PWR coolant system*, Nuclear Engineering and Design, 246, pp. 115-122.
45. T. Zhang, F.W. Brust, G. Wilkowski, C.C. Huang, R.F. Liu, S. Ranganath, L. Wang, Y.L. Tsai (2012) *Weld Residual Stress Analysis and the Effects of Structural Overlay on Various Nuclear Power Plant Nozzles*, Journal of Pressure Vessel Technology, 134, pp. 061205.
46. A. Maekawa, A. Kawahara, H. Serizawa, H. Murakawa (2016) *Prediction of Weld Residual Stress in a Pressurized Water Reactor Pressurizer Surge Nozzle*, Journal of Pressure Vessel Technology, 138, pp. 021401.
47. D.J. Dewees, P. Hirschberg, W. Reinhardt, G.L. Stevens, D.H. Roarty, S. Gosselin, K. Wright, T.M. Damiani (2014) *ASME Section III Flaw Tolerance Sample Problem for Fatigue Design of Nuclear System Components*, ASME Pressure Vessels and Piping Conference, Paper no. PVP2014-28788.
48. S. Mohanty, W.K. Soppet, S. Majumdar, K. Natesan (2015) *System-Level Heat Transfer Analysis, Thermal-Mechanical Cyclic Stress Analysis, and Environmental Fatigue Modeling of a Two-Loop Pressurized Water Reactor, A Preliminary Study*, Argonne National Laboratory, Report no. ANL/LWRS-15/01. (<https://www.osti.gov/scitech/biblio/1179020>).
49. V.N. Shah, P.E. MacDonald (1993) *Aging and life extension of major light water reactor components*, Elsevier Science Publishers B.V., Amsterdam, The Netherland, ISBN: 0-444-89448-9.
50. Y. Zhang, T. Lu, P.X. Jiang, Y.H. Zhu, J. Wu, J., C.L. Liu (2016) *Investigation on thermal stratification and turbulent penetration in a pressurizer surge line with an overall out-surge flow*, Annals of Nuclear Energy, 90, pp. 212-233.
51. Y.J. Yu, S.H. Park, G.H. Sohn, W.J. Bak (1997) *Structural evaluation of thermal stratification for PWR surge line*, Nuclear engineering and design, 178, pp. 211-220.
52. J.C. Jo, D.G. Kang (2010) *CFD analysis of thermally stratified flow and conjugate heat transfer in a PWR pressurizer surgeline*, Journal of Pressure Vessel Technology, 132, pp. 021301.

53. J.C. Jo, S.J. Kim, Y.H. Choi, H.J. Kim (2002) *Transient Response of Thermal Stress at a PWR Pressurizer Surge Line Pipe Subjected to Internally Thermal Stratification*, Korean Nuclear Society Conference.
54. C. Ensel, A. Colas, M. Barthez (1995) *Stress analysis of a 900 MW pressurizer surge line including stratification effects*, Nuclear Engineering and Design, 153, pp. 197-203.
55. Y. Zhang, T. Lu, P.X. Jiang, Y.H. Zhu, J. Wu, C.L. Liu (2016) *Investigation on thermal stratification and turbulent penetration in a pressurizer surge line with an overall out-surge flow*, Annals of Nuclear Energy, 90, pp. 212-233.
56. I. Boros, G. Petőfi, A. Aszódi (2005) *CFD analysis of thermal stratification in the primary circuit*, International Atomic Energy Agency.
57. S.H. Kim, J.B. Choi, J.S. Park, Y.H. Choi, J.H. Lee (2013) *A coupled CFD-FEM analysis on the safety injection piping subjected to thermal stratification*, Nuclear Engineering and Technology, 45, pp. 237-248.
58. K.C. Kim, J.H. Lim, J.K. Yoon (2008) *Thermal fatigue estimation due to thermal stratification in the RCS branch line using one-way FSI scheme*, Journal of mechanical science and technology, 22, pp. 2218-2227.
59. S.W. Webb, J.T. Cook (2006) *LES data-model comparisons for flow over a tube bundle including heat transfer*, International Heat Transfer Conference.
60. J.C. Jo, Y.H. Choi, S.K. Choi (2003) *Numerical analysis of unsteady conjugate heat transfer and thermal stress for a curved piping system subjected to thermal stratification*, Journal of Pressure Vessel Technology, 125, pp. 467-474.
61. J.U. Jeong, Y.S. Chang, J.B. Choi, Y.J. Kim, J.S. Kim, J. H. Lee, H.D. Chung (2008) *Parametric CFD Analyses to Simulated Stratified Flows*, ASME Pressure Vessels and Piping Conference, Paper no. PVP2008-61659.
62. T. Lu, D. Attinger, S.M. Liu (2013) *Large-eddy simulations of velocity and temperature fluctuations in hot and cold fluids mixing in a tee junction with an upstream straight or elbow main pipe*, Nuclear Engineering and Design, 263, pp. 32-41.
63. B. Cai, H. Gu, Y. Weng, X. Qin, Y. Wang, S. Qiao, H. Wang (2017) *Numerical investigation on the thermal stratification in a pressurizer surge line*, Annals of Nuclear Energy, 101, pp. 293-300.
64. ABAQUS user manual (2011) and (2016).
65. G. Meyer, E. Stokke (1997) *Description of Sizewell B Nuclear Power Plant, Institutt for energiteknikk (IFE)*, Report no. NKS/RAK-2(97) TR-C4.
(http://www.iaea.org/inis/collection/NCLCollectionStore/_Public/29/010/29010110.pdf).
66. V.P. Bobkov, L.R. Fokin, E.E. Petrov, V.V. Popov, V.N. Rumiantsev, A.I. Savvatimsky, (2008) *Thermophysical Properties of Materials for Nuclear Engineering: A Tutorial and Collection of Data*, IAEA, Vienna.
(<http://www-pub.iaea.org/books/iaeabooks/7965/Thermophysical-Properties-of-Materials-for-Nuclear-Engineering-A-Tutorial-and-Collection-of-Data>).
67. O.K. Chopra, G.L. Stevens (2014) *Effect of LWR Coolant Environments on the Fatigue Life of Reactor Materials: Draft Report for Comment*, U.S. Nuclear Regulatory Commission, Report no. NUREG/CR-6909, Rev. 1 (ANL-12/60).
(<https://www.nrc.gov/docs/ML1408/ML14087A068.pdf>).

Appendices

The appendices contain additional experimental and material modeling results of the **strain-controlled** tensile (ET-T04) and fatigue (constant-amplitude: ET-F06, ET-F41; variable-amplitude: ET-F38; and random-amplitude: ET-F40) tests discussed in this report. The supplementary experimental results include observed actuator position and crosshead stroke data. The supplementary material modeling results for the tensile test (ET-T04) include estimated material parameters considering yield stress at elastic limit and at 0.05%, 0.1%, and 0.2% offset strain limit. Tensile test based (time-independent or fixed) both linear (C1 only) and nonlinear (C1 and γ_1) kinematic hardening parameters are provided. For fatigue test based material properties (time/cycle/block-dependent), nonlinear kinematic hardening parameters (C1 and γ_1) were estimated considering yield stress at elastic limit and 0.05% offset strain limit, while linear (C1 only) kinematic hardening parameters were estimated considering yield stress at 0.2% offset strain limit. In this work, however, nonlinear kinematic hardening parameters (C1 and γ_1) considering yield stress at the elastic limit were only used for both analytical and 3D-FE modeling. Other material parameters are provided in the appendices in case readers are interested in using those; however, authors do not have data on accuracy of the predictions using those parameters.

Appendix-3A: Supplementary Results for ET-T04 Tensile Test

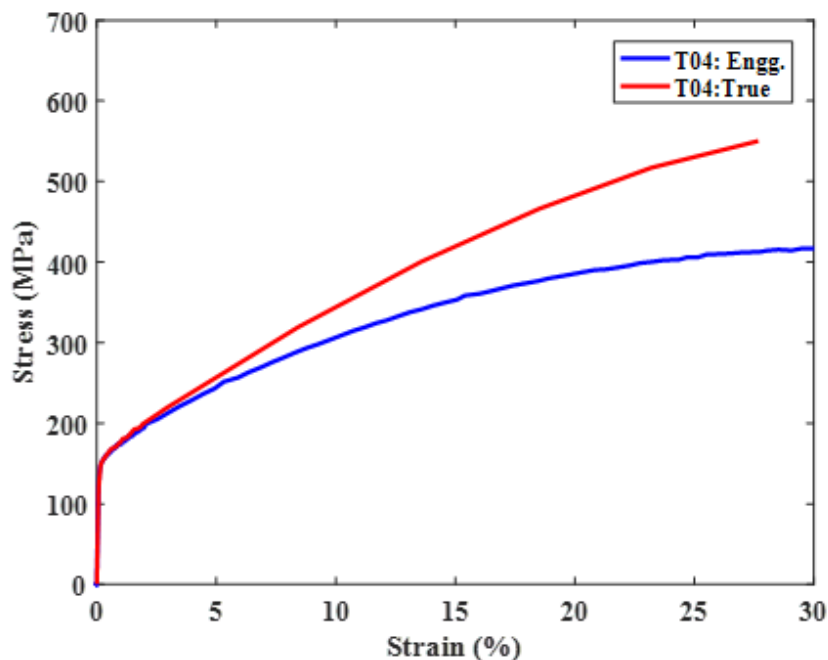


Figure 3A. 1 Engineering and true stress-strain curve estimated from T04 tensile test data.

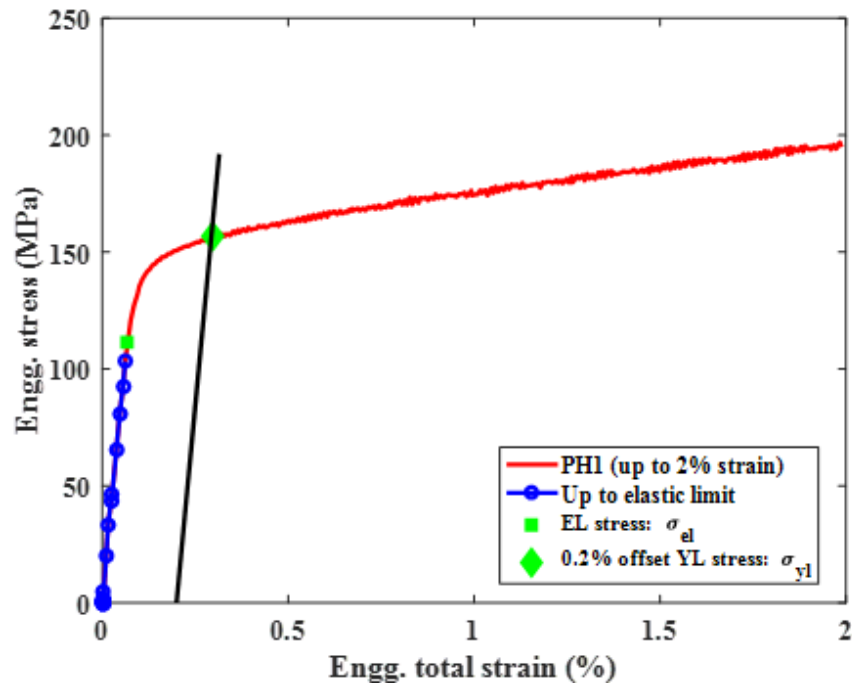


Figure 3A. 2 Engineering stress-strain curve (up to 2% strain) estimated from T04 tensile test data showing assumed elastic limit (EL) and estimated 0.2% offset yield limit (YL).

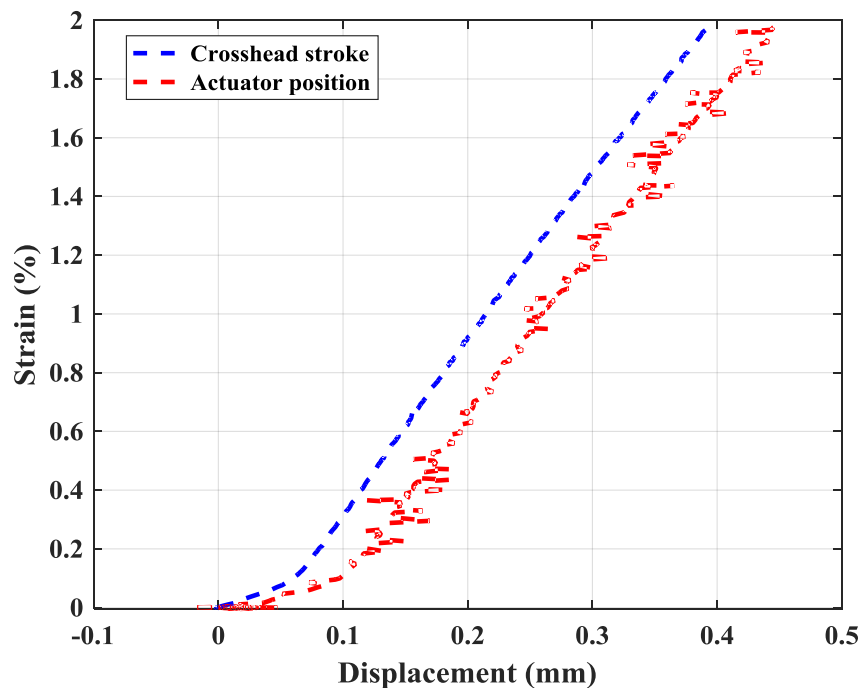


Figure 3A. 3 Frame crosshead displacement (stroke) and actuator position versus strain (up to 2% strain), estimated from ET-T04 tensile test data. These types of results will be used for selecting test parameters for stroke control and position control fatigue tests.

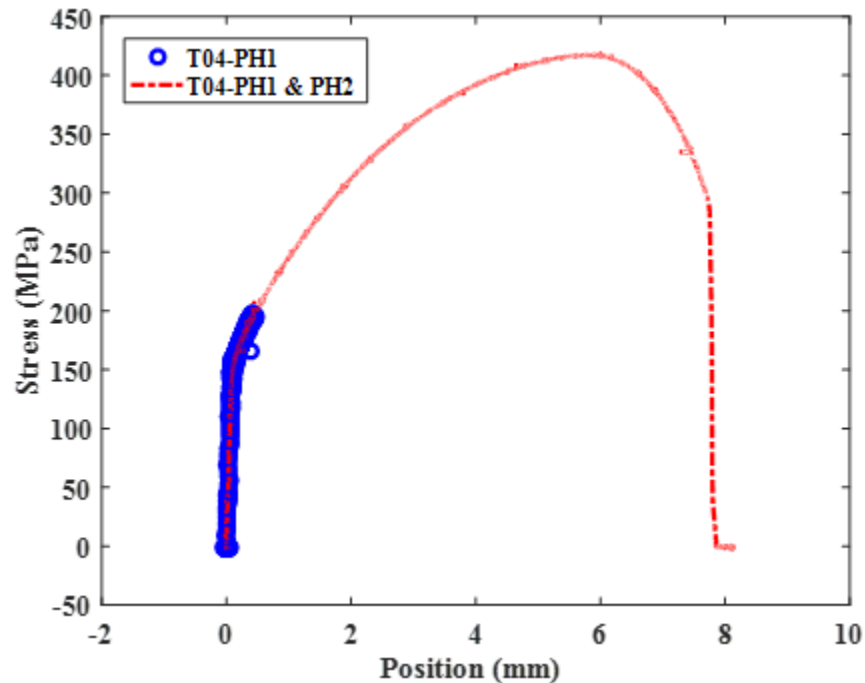


Figure 3A. 4 Stress vs position data from ET-T04. PH1: strain-controlled, PH2: position-control. Strain was predicted from position in PH2. This type of result will be used to estimate ratcheting strain from a stress-controlled fatigue test.

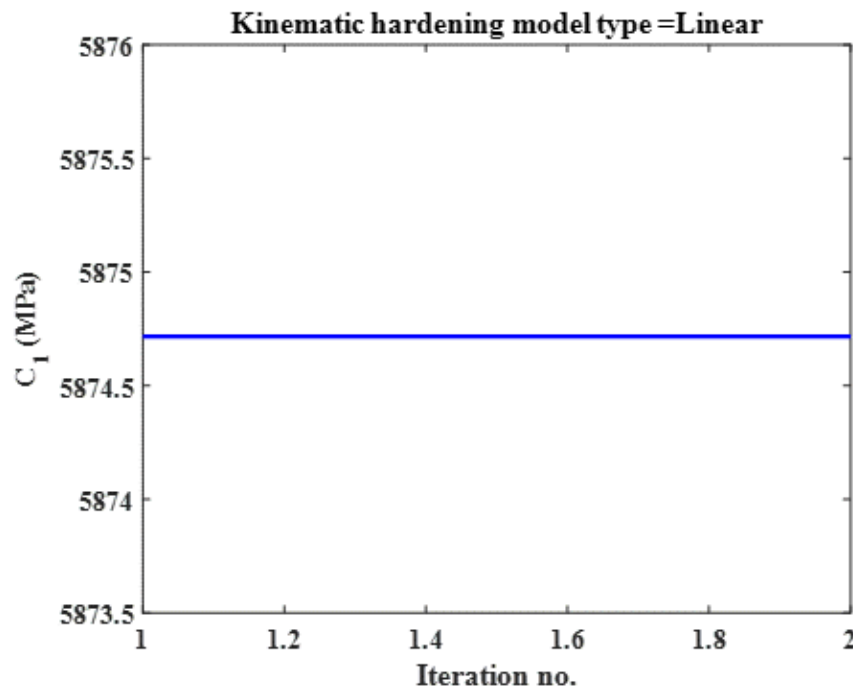


Figure 3A. 5 Linear kinematic hardening parameter C_1 with respect to number of iteration during parameter estimation using gradient based optimization scheme and using ET-T04 stress-strain data (from elastic limit to 2% true total strain).

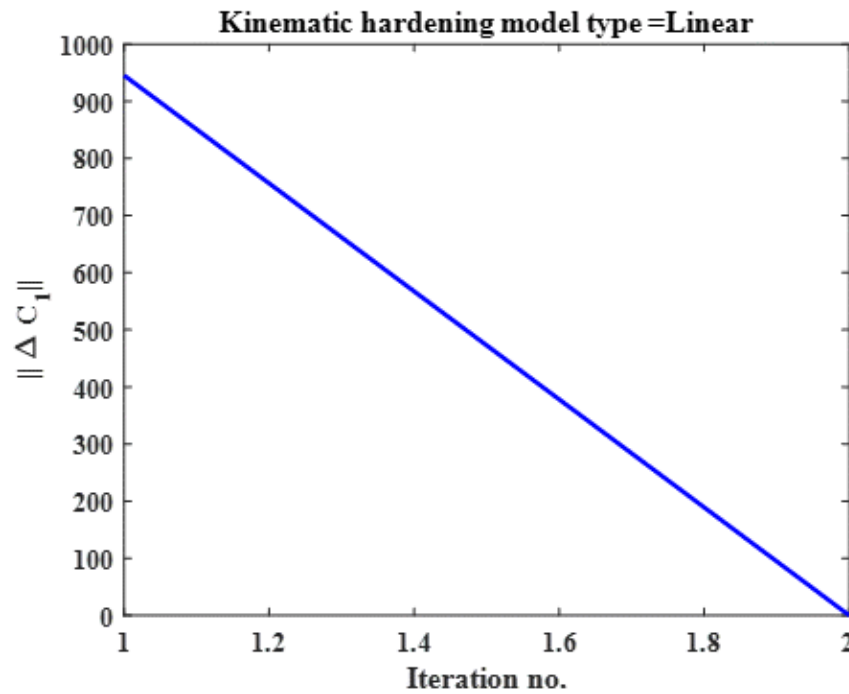


Figure 3A. 6 L2 norm (of incremental kinematic hardening constant C_1) with respect to number of iteration during parameter estimation using gradient based optimization scheme and using ET-T04 stress-strain data (from elastic limit to 2% true total strain).

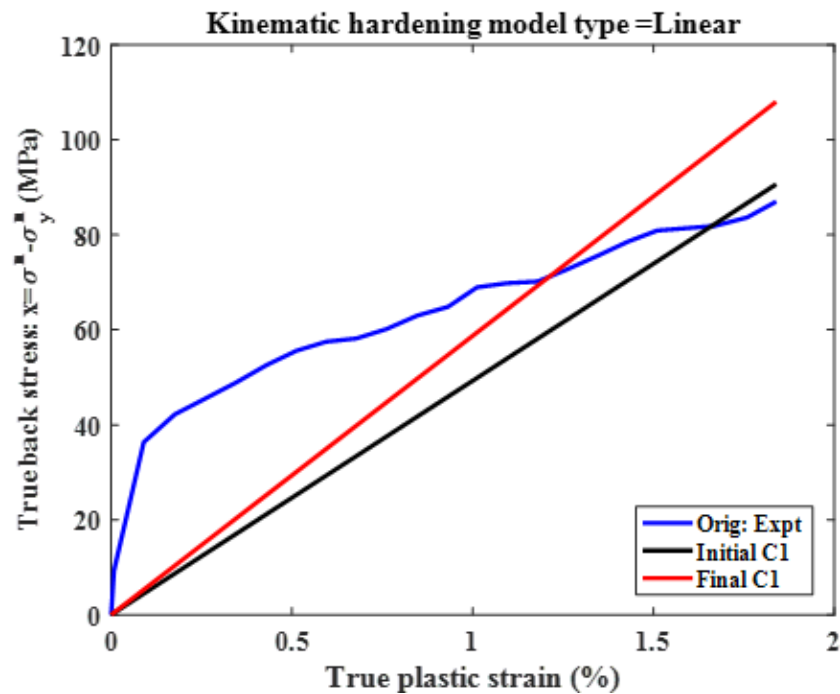


Figure 3A. 7 Comparison of predicted true back stress (using linear kinematic hardening parameter C_1 and considering elastic limit as yield limit) with experimental true back stress for ET-T04 tensile test.

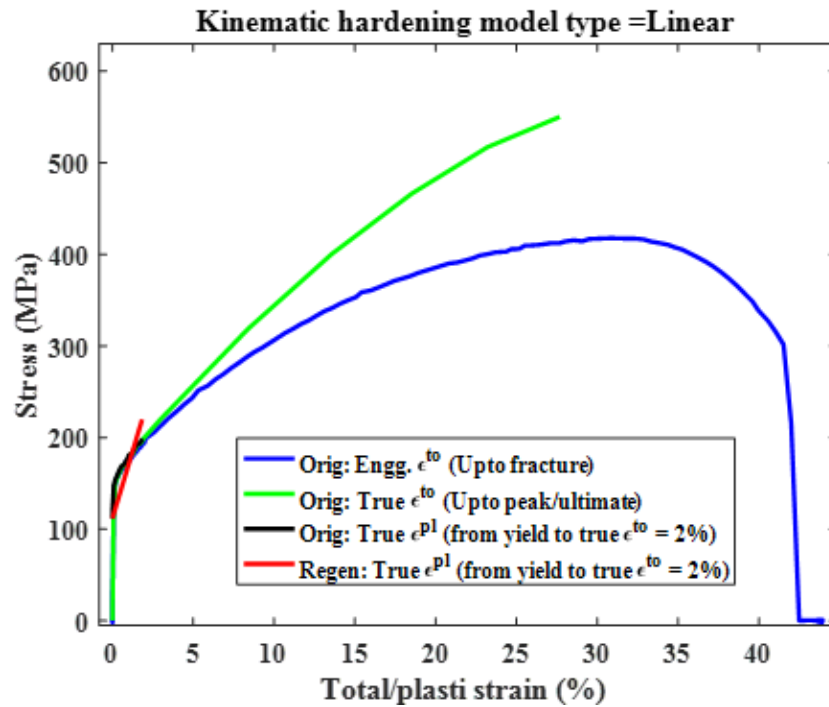


Figure 3A. 8 Comparison of predicted true total stress (using linear kinematic hardening parameter C1 and elastic limit as yield limit) with experimental true total stress for ET-T04 tensile test.

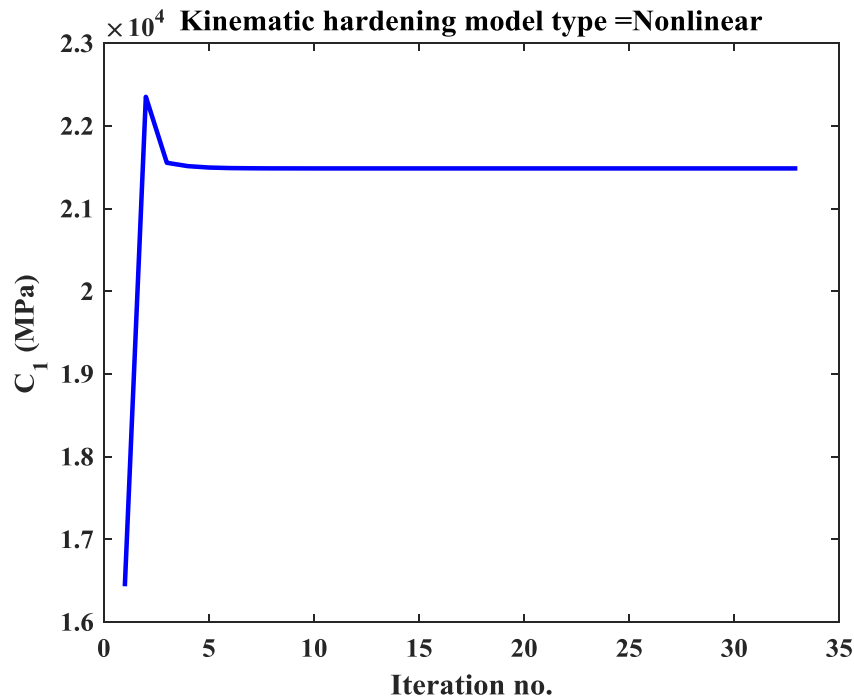


Figure 3A. 9 Nonlinear kinematic hardening constant C1 with respect to number of iteration during parameter estimation using gradient based optimization scheme and using ET-T04 stress-strain data (from elastic limit to 2% true total strain).

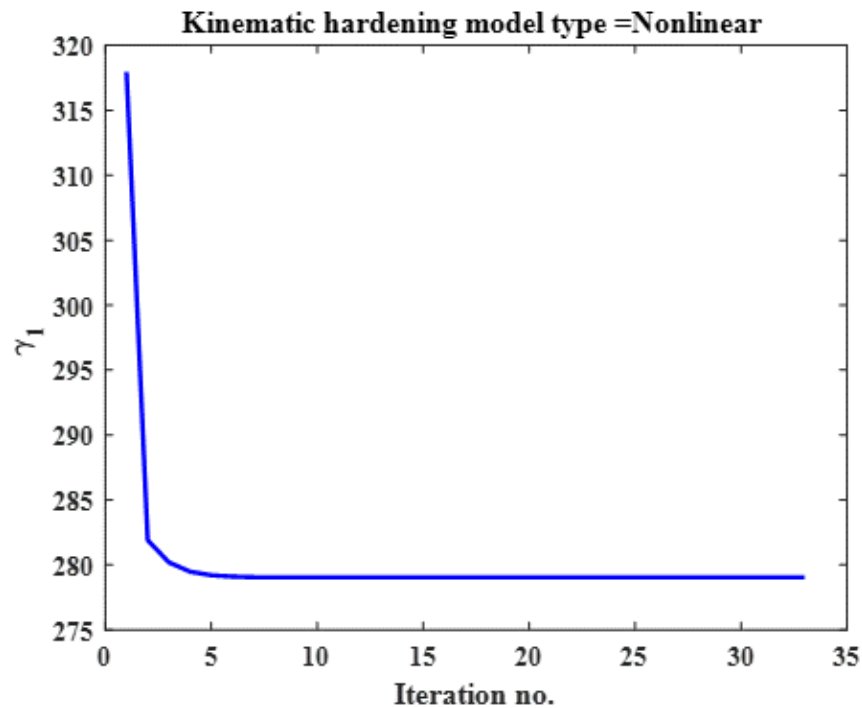


Figure 3A. 10 Nonlinear kinematic hardening constant γ_1 with respect to number of iteration during parameter estimation using gradient based optimization scheme and using ET-T04 stress-strain data (from elastic limit to 2% true total strain)

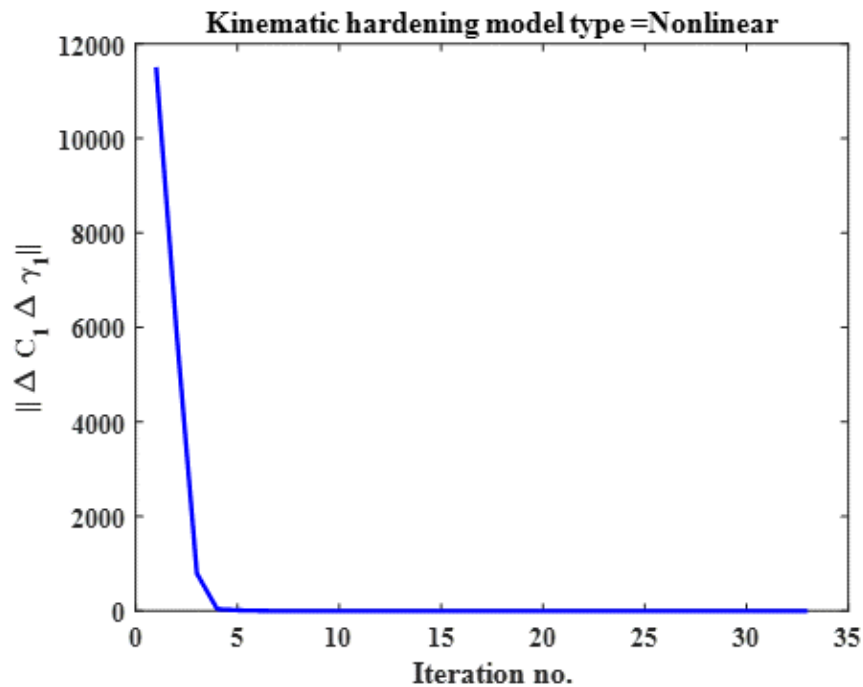


Figure 3A. 11 L2 norm (of incremental kinematic hardening constant C_1 and γ_1) with respect to number of iteration during parameter estimation using gradient based optimization scheme and using ET-T04 stress-strain data (from elastic limit to 2% true total strain).

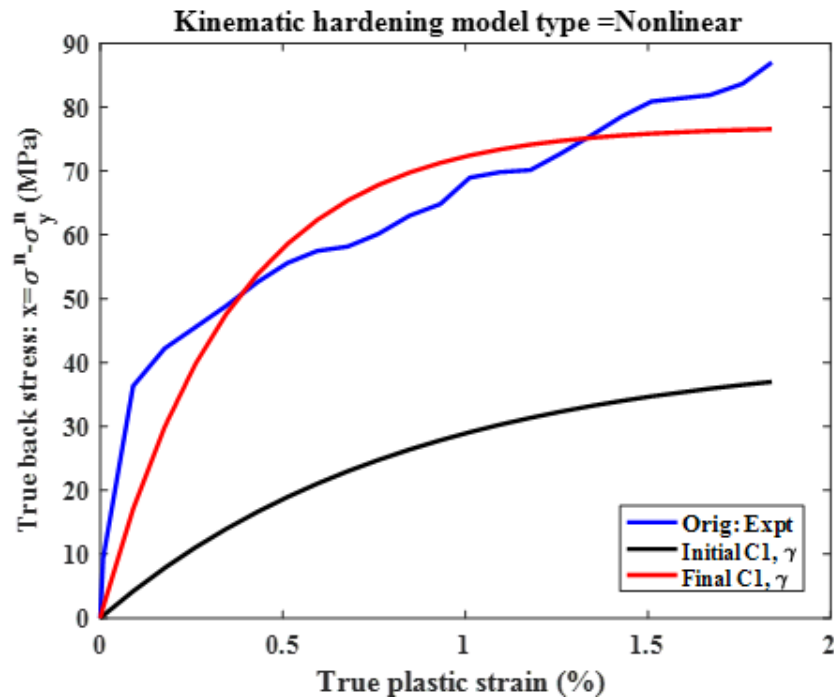


Figure 3A. 12 Comparison of predicted true back stress (using nonlinear kinematic hardening parameter C1 and γ 1 and considering elastic limit as yield limit) with experimental true back stress for ET-T04 tensile test.

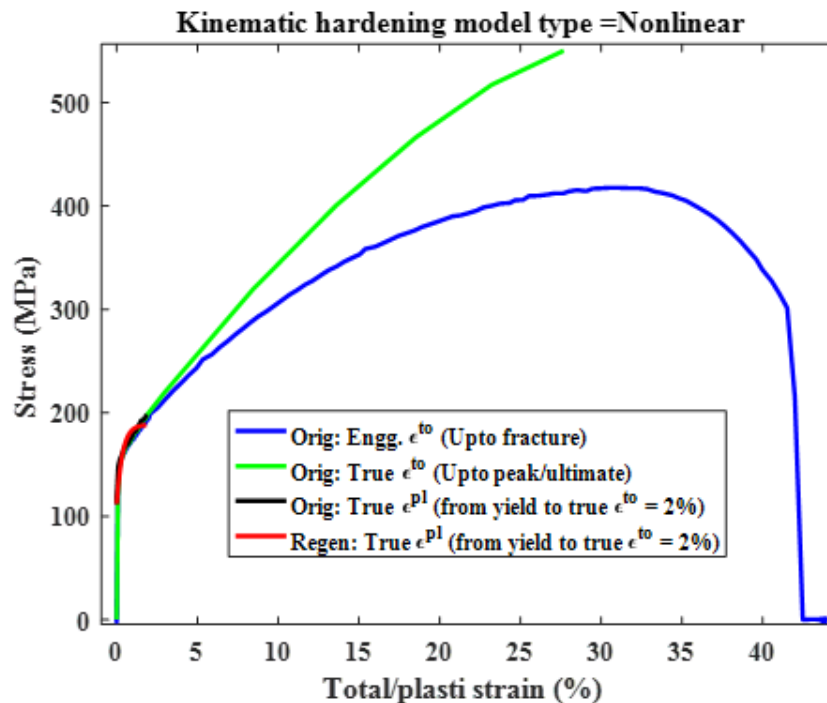


Figure 3A. 13 Comparison of predicted true total stress (using nonlinear kinematic hardening parameter C1 and γ 1 and considering elastic limit as yield limit) with experimental true total stress for ET-T04 tensile test.

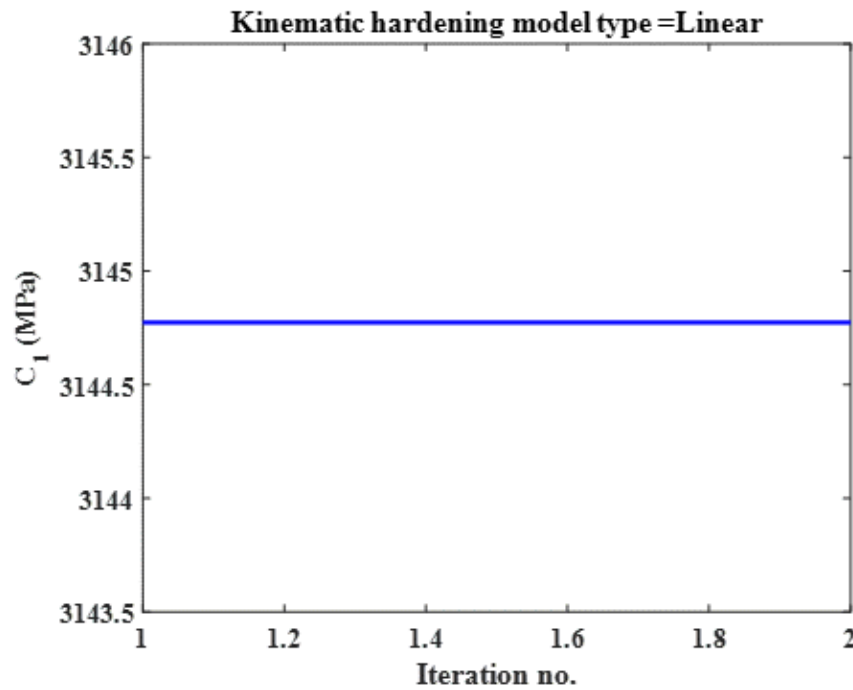


Figure 3A. 14 Linear kinematic hardening parameter C_1 with respect to number of iteration during parameter estimation using gradient based optimization scheme and using ET-T04 stress-strain data (from 0.05% offset strain yield limit to 2% true total strain).

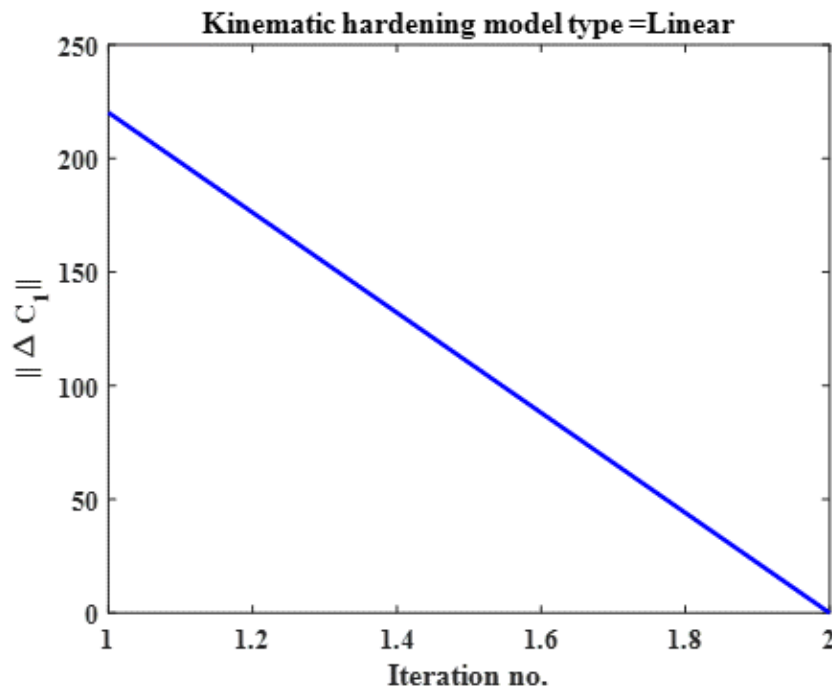


Figure 3A. 15 L2 norm (of incremental kinematic hardening constant C_1) with respect to number of iteration during parameter estimation using gradient based optimization scheme and using ET-T04 stress-strain data (from 0.05% offset strain yield limit to 2% true total strain).

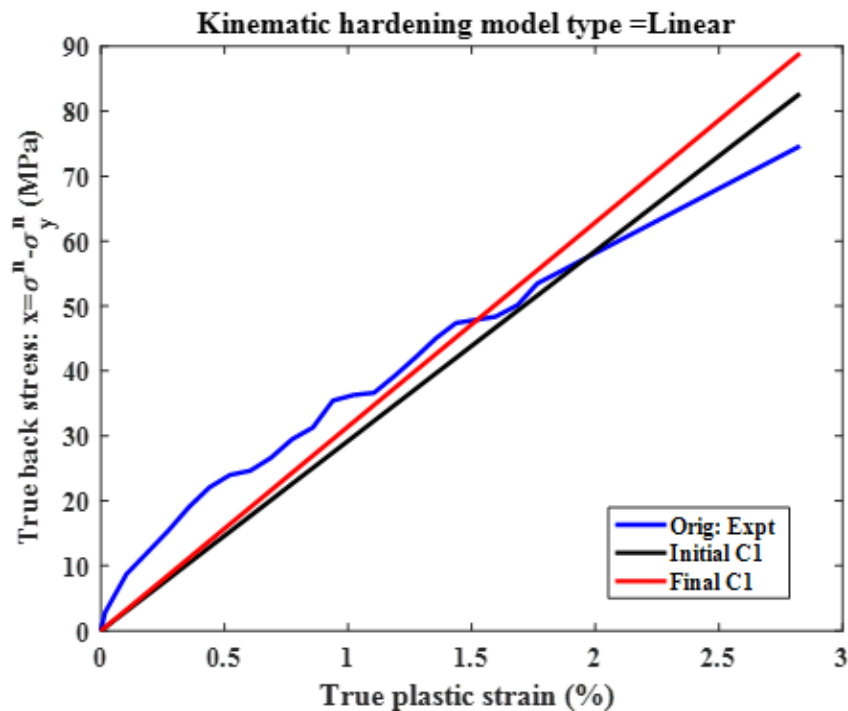


Figure 3A. 16 Comparison of predicted true back stress (using linear kinematic hardening parameter C1 and considering 0.05% offset strain as yield limit) with experimental true back stress for ET-T04 tensile test.

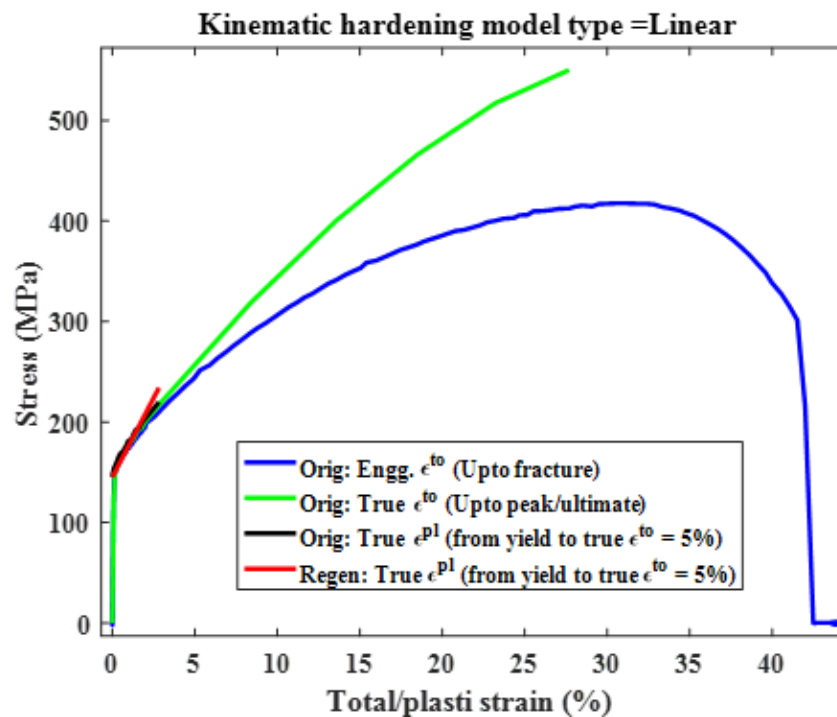


Figure 3A. 17 Comparison of predicted true total stress (using linear kinematic hardening parameter C1 and 0.05% offset strain as yield limit) with experimental true total stress for ET-T04 tensile test.

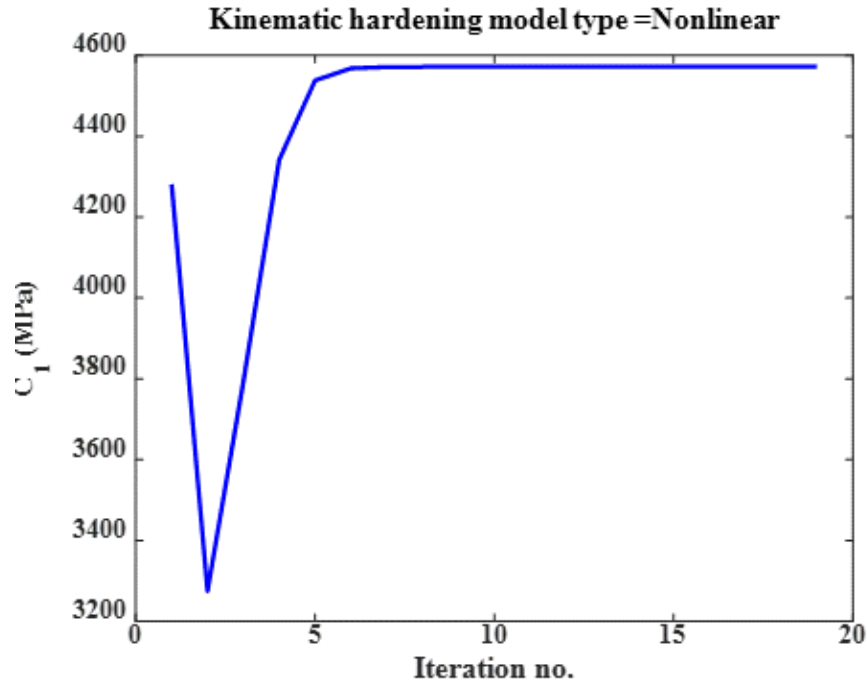


Figure 3A. 18 Nonlinear kinematic hardening constant C_1 with respect to number of iteration during parameter estimation using gradient based optimization scheme and using ET-T04 stress-strain data (from 0.05% offset yield strain limit to 2% true total strain)

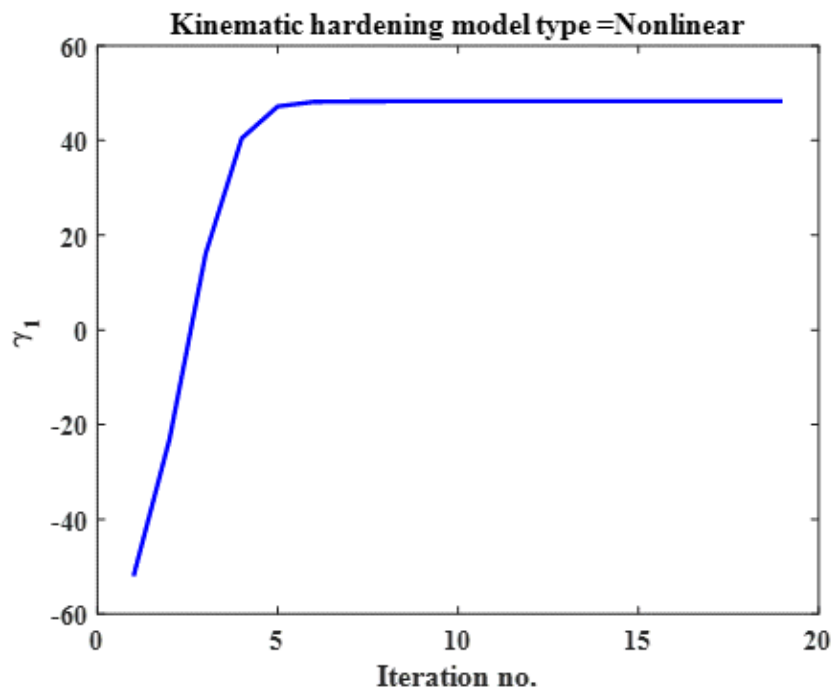


Figure 3A. 19 Nonlinear kinematic hardening constant γ_1 with respect to number of iteration during parameter estimation using gradient based optimization scheme and using ET-T04 stress-strain data (from 0.05% offset yield strain limit to 2% true total strain)

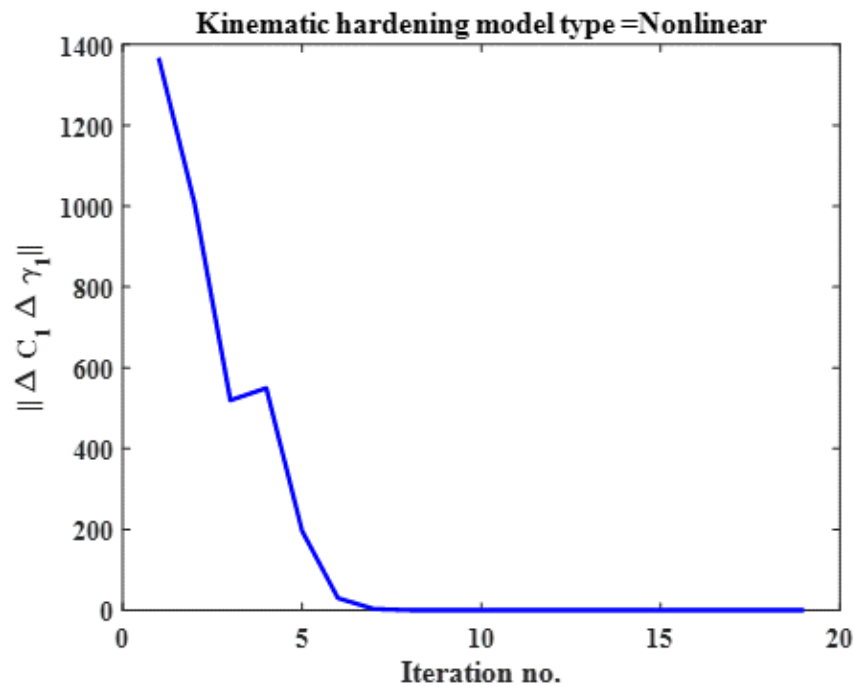


Figure 3A. 20 L2 norm (of incremental kinematic hardening constant C_1 and γ_1) with respect to number of iteration during parameter estimation using gradient based optimization scheme and using ET-T04 stress-strain data (from 0.05% offset yield strain limit to 2% true total strain).

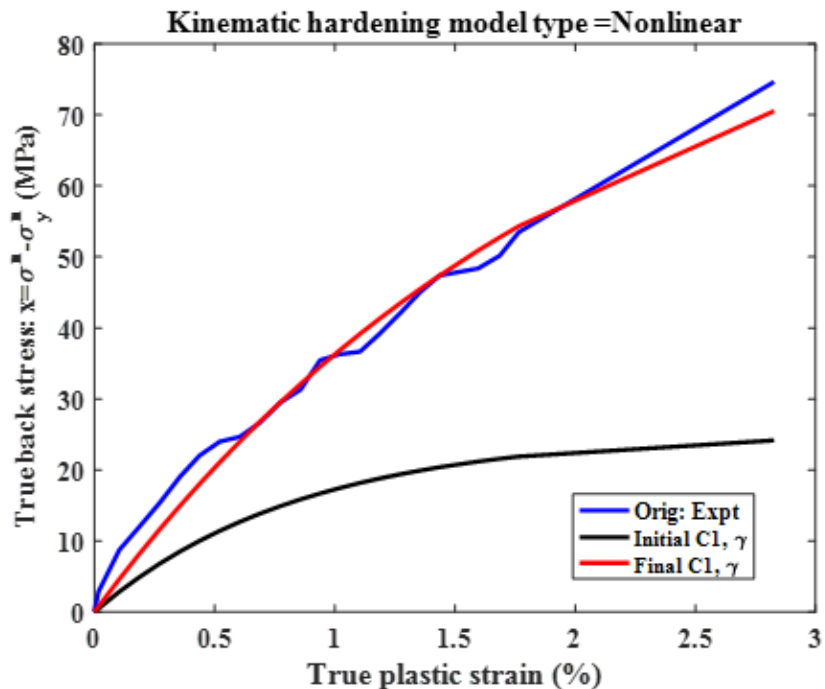


Figure 3A. 21 Comparison of predicted true back stress (using nonlinear kinematic hardening parameter C_1 and γ_1 and considering 0.05% offset yield strain as yield limit) with experimental true back stress for ET-T04 tensile test.

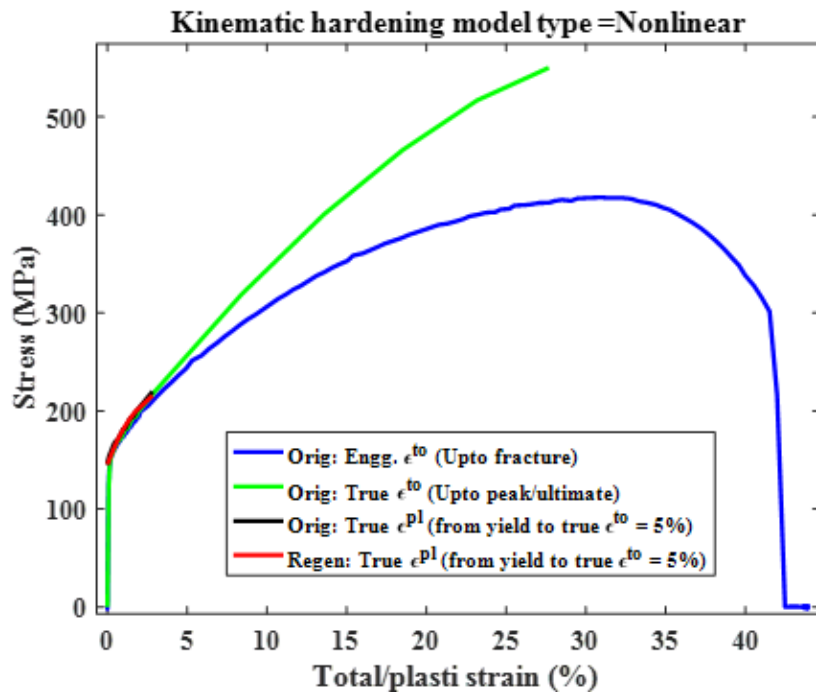


Figure 3A. 22 Comparison of predicted true total stress (using nonlinear kinematic hardening parameter C_1 and γ_1 and considering 0.05% offset yield strain as yield limit) with experimental true total stress for ET-T04 tensile test.

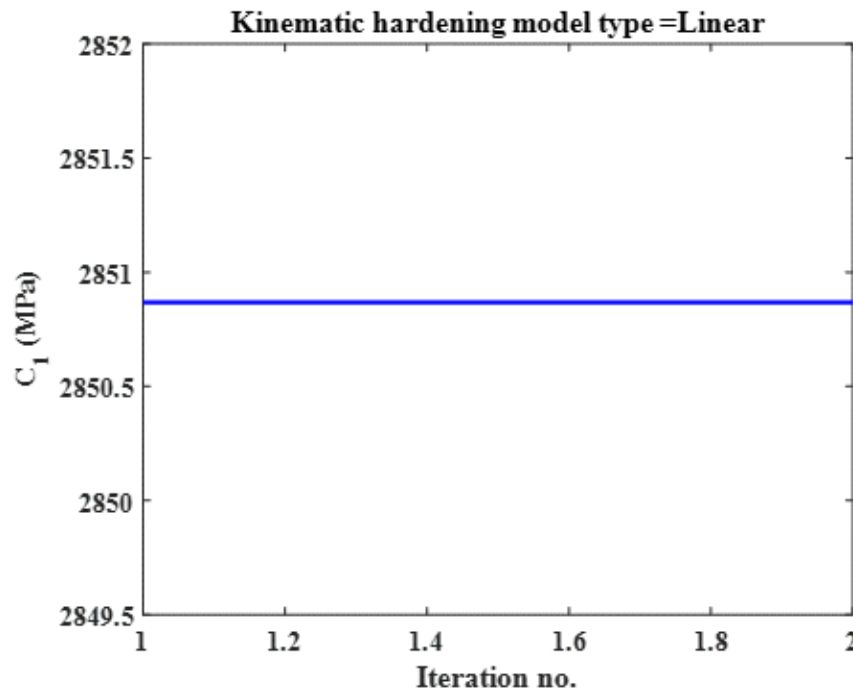


Figure 3A. 23 Linear kinematic hardening parameter C_1 with respect to number of iteration during parameter estimation using gradient based optimization scheme and using ET-T04 stress-strain data (from 0.1% offset strain yield limit to 2% true total strain).

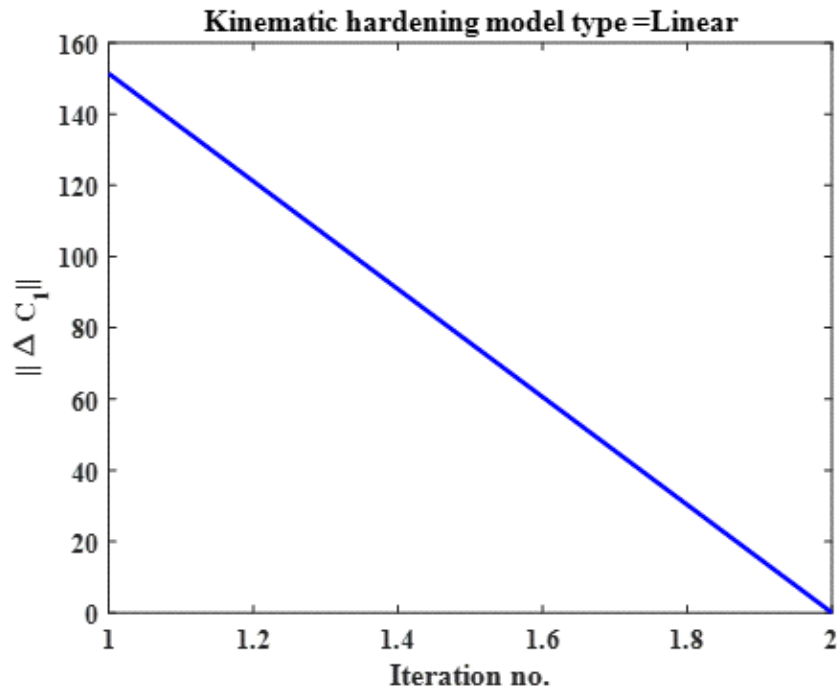


Figure 3A. 24 L2 norm (of incremental kinematic hardening constant C1) with respect to number of iteration during parameter estimation using gradient based optimization scheme and using ET-T04 stress-strain data (from 0.1% offset strain yield limit to 2% true total strain).

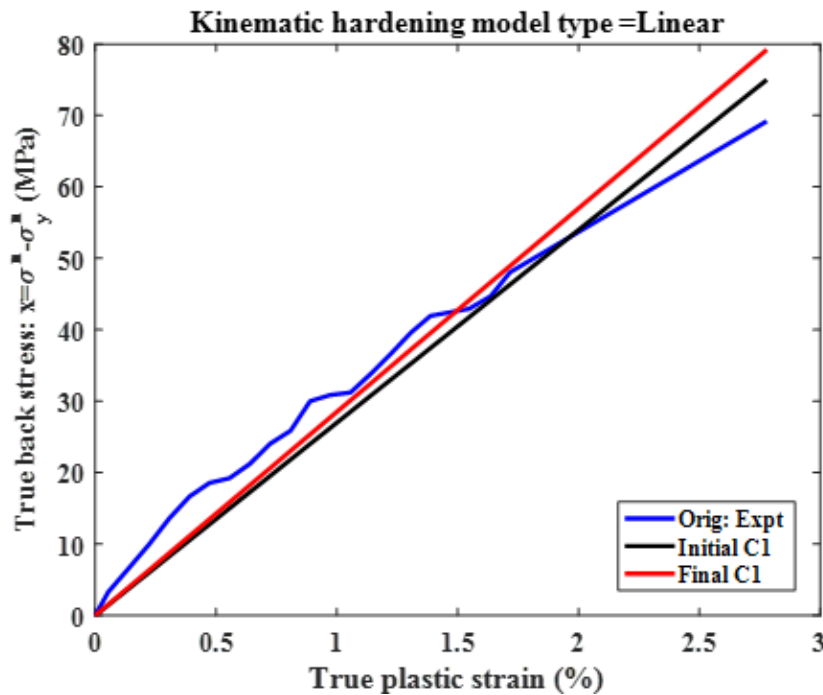


Figure 3A. 25 Comparison of predicted true back stress (using linear kinematic hardening parameter C1 and considering 0.1% offset strain as yield limit) with experimental true back stress for ET-T04 tensile test.

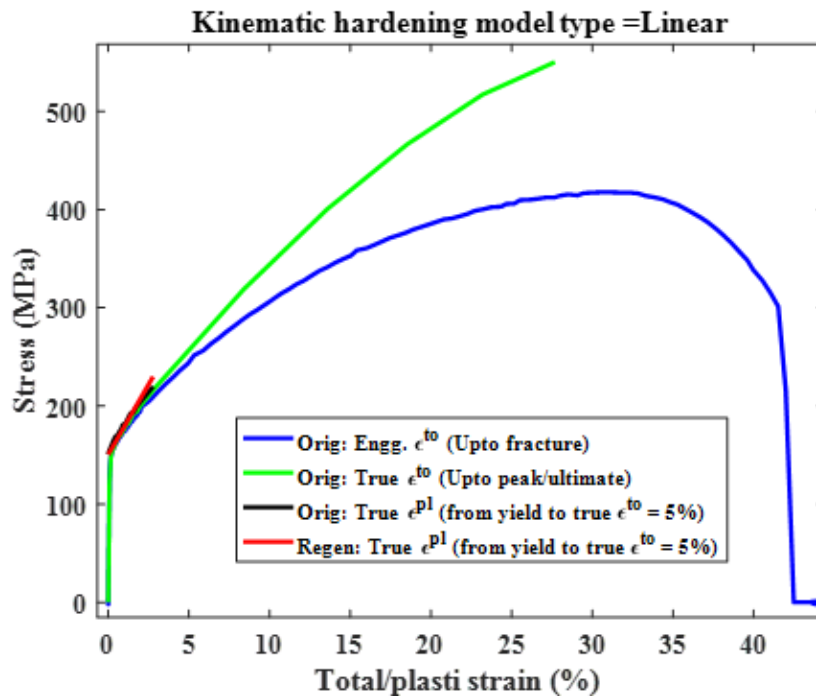


Figure 3A. 26 Comparison of predicted true total stress (using linear kinematic hardening parameter C1 and 0.1% offset strain as yield limit) with experimental true total stress for ET-T04 tensile test.

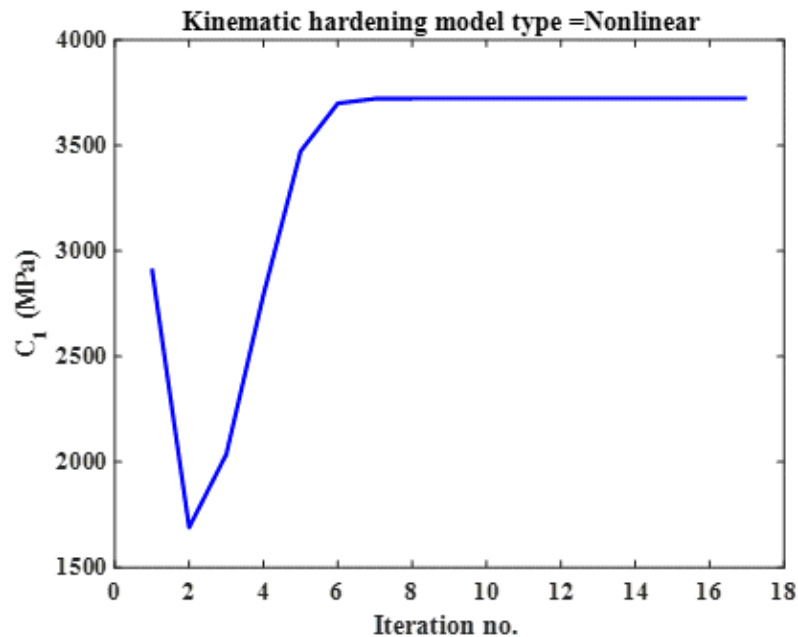


Figure 3A. 27 Nonlinear kinematic hardening constant C1 with respect to number of iteration during parameter estimation using gradient based optimization scheme and using ET-T04 stress-strain data (from 0.1% offset yield strain limit to 2% true total strain)

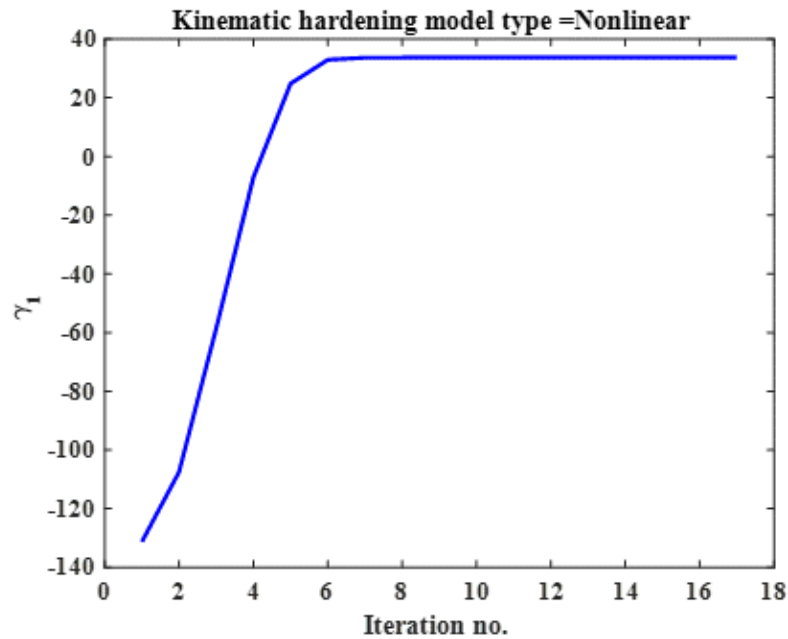


Figure 3A. 28 Nonlinear kinematic hardening constant γ_1 with respect to number of iteration during parameter estimation using gradient based optimization scheme and using ET-T04 stress-strain data (from 0.1% offset yield strain limit to 2% true total strain)

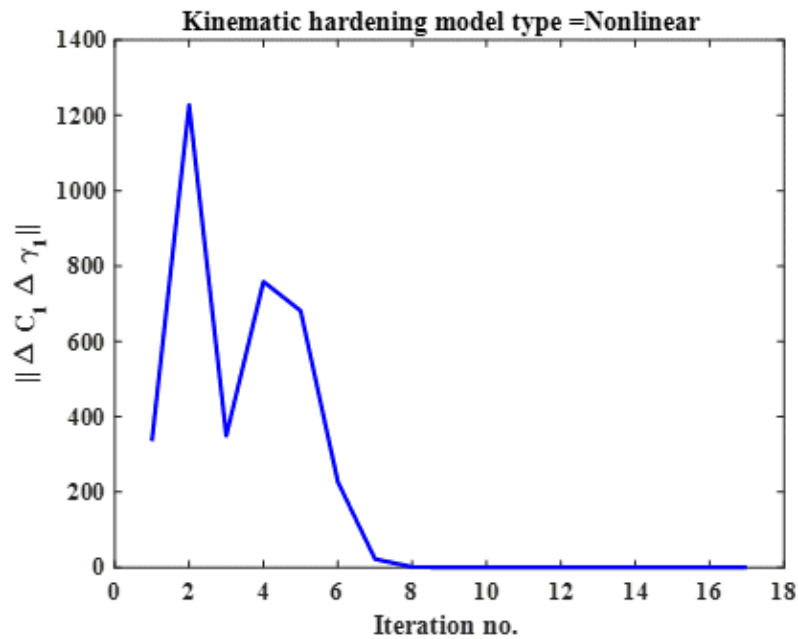


Figure 3A. 29 L2 norm (of incremental kinematic hardening constant C_1 and γ_1) with respect to number of iteration during parameter estimation using gradient based optimization scheme and using ET-T04 stress-strain data (from 0.1% offset yield strain limit to 2% true total strain).

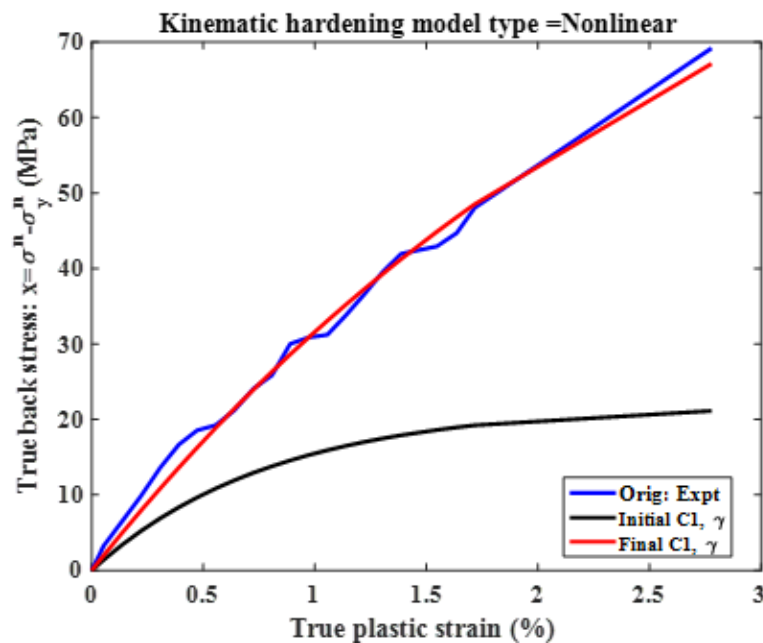


Figure 3A. 30 Comparison of predicted true back stress (using nonlinear kinematic hardening parameter C1 and γ 1 and considering 0.1% offset yield strain as yield limit) with experimental true back stress for ET-T04 tensile test.

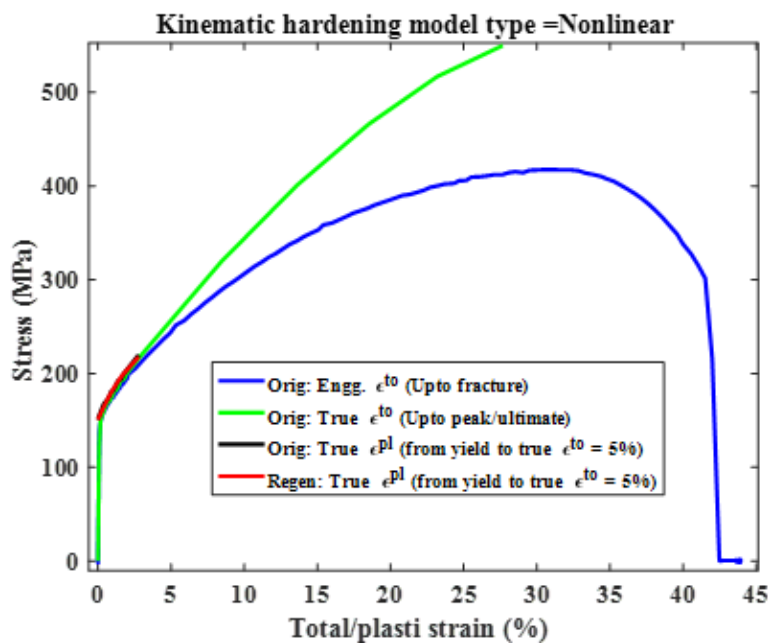


Figure 3A. 31 Comparison of predicted true total stress (using nonlinear kinematic hardening parameter C1 and γ 1 and considering 0.1% offset yield strain as yield limit) with experimental true total stress for ET-T04 tensile test.

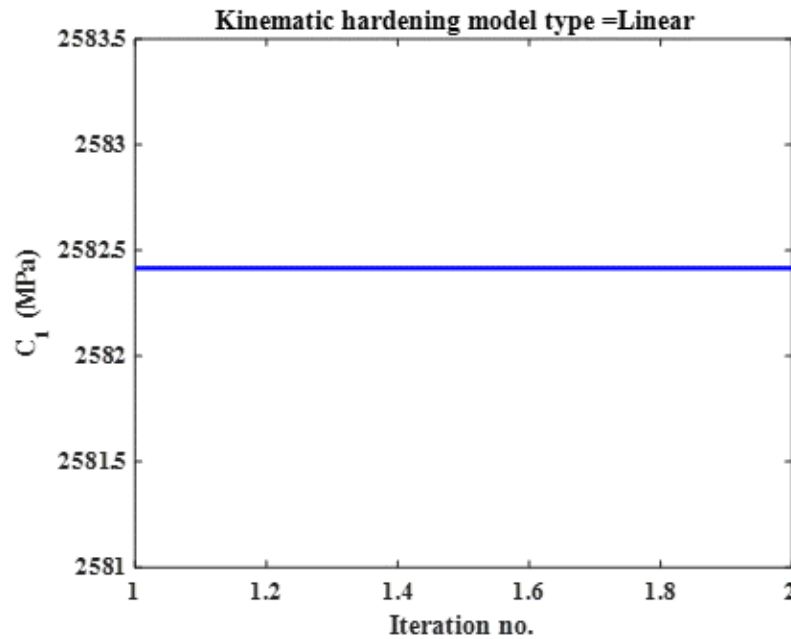


Figure 3A. 32 Linear kinematic hardening parameter C1 with respect to number of iteration during parameter estimation using gradient based optimization scheme and using ET-T04 stress-strain data (from 0.2% offset strain yield limit to 2% true total strain).

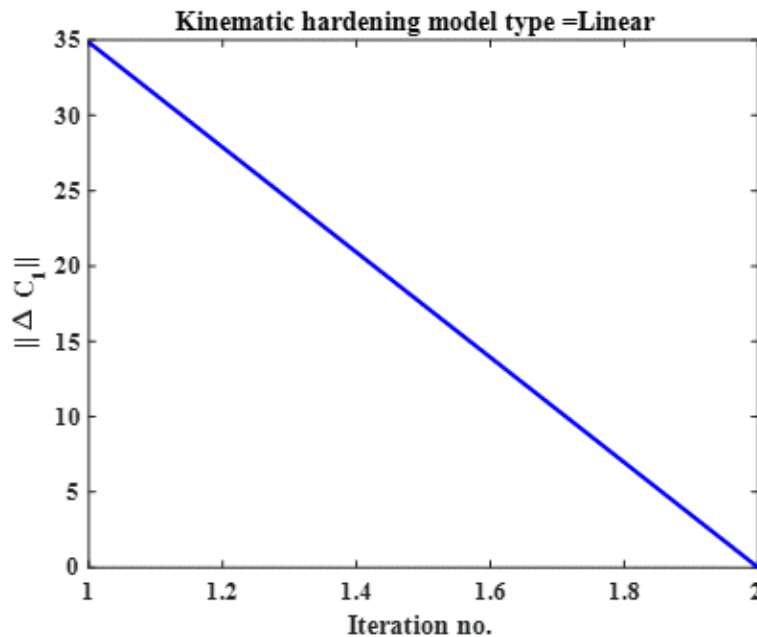


Figure 3A. 33 L2 norm (of incremental kinematic hardening constant C1) with respect to number of iteration during parameter estimation using gradient based optimization scheme and using ET-T04 stress-strain data (from 0.2% offset strain yield limit to 2% true total strain).

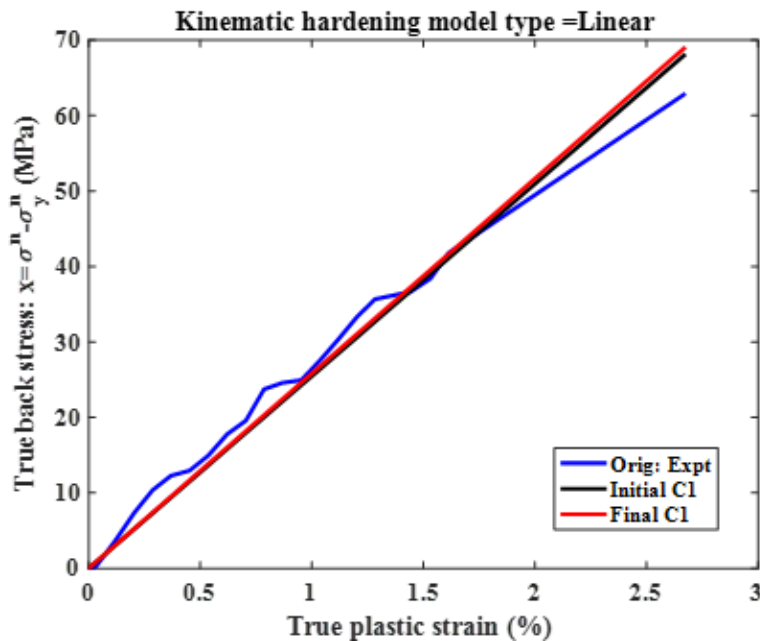


Figure 3A. 34 Comparison of predicted true back stress (using linear kinematic hardening parameter C1 and considering 0.2% offset strain as yield limit) with experimental true back stress for ET-T04 tensile test.

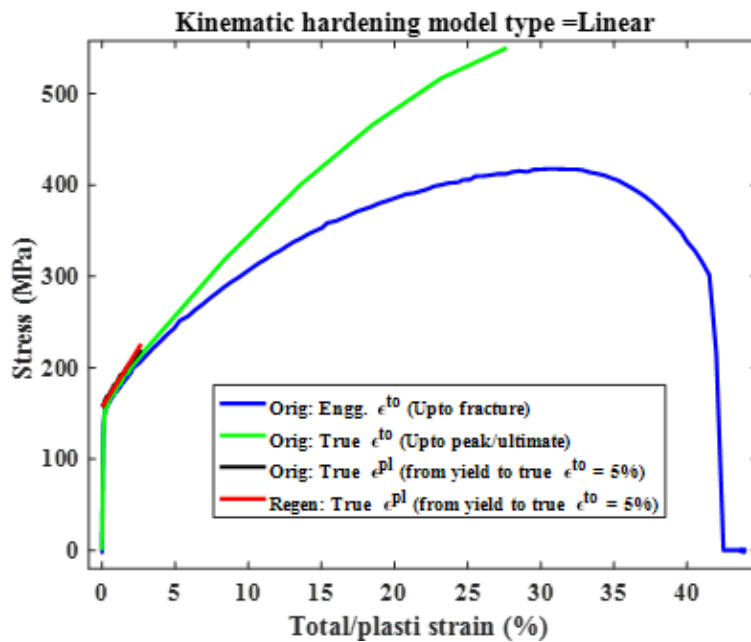


Figure 3A. 35 Comparison of predicted true total stress (using linear kinematic hardening parameter C1 and 0.2% offset strain as yield limit) with experimental true total stress for ET-T04 tensile test.

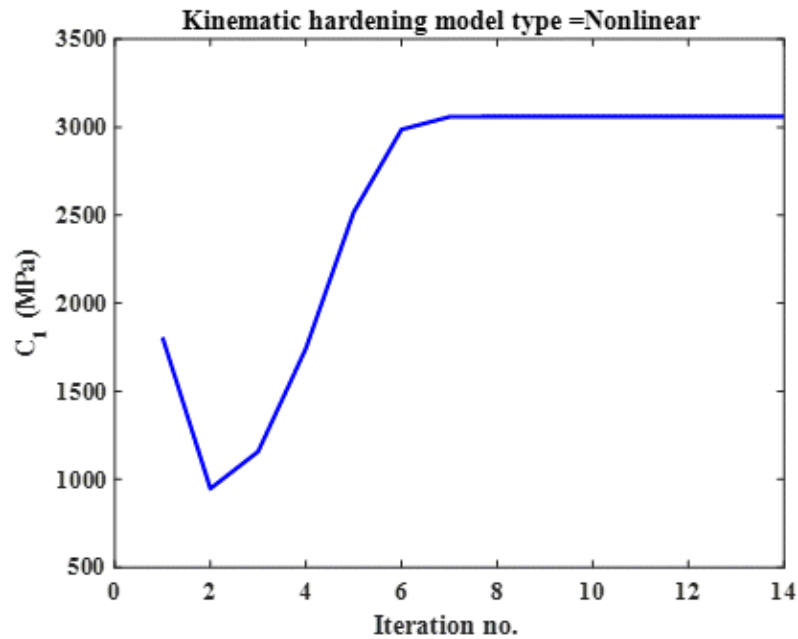


Figure 3A. 36 Nonlinear kinematic hardening constant C_1 with respect to number of iteration during parameter estimation using gradient based optimization scheme and using ET-T04 stress-strain data (from 0.2% offset yield strain limit to 2% true total strain)

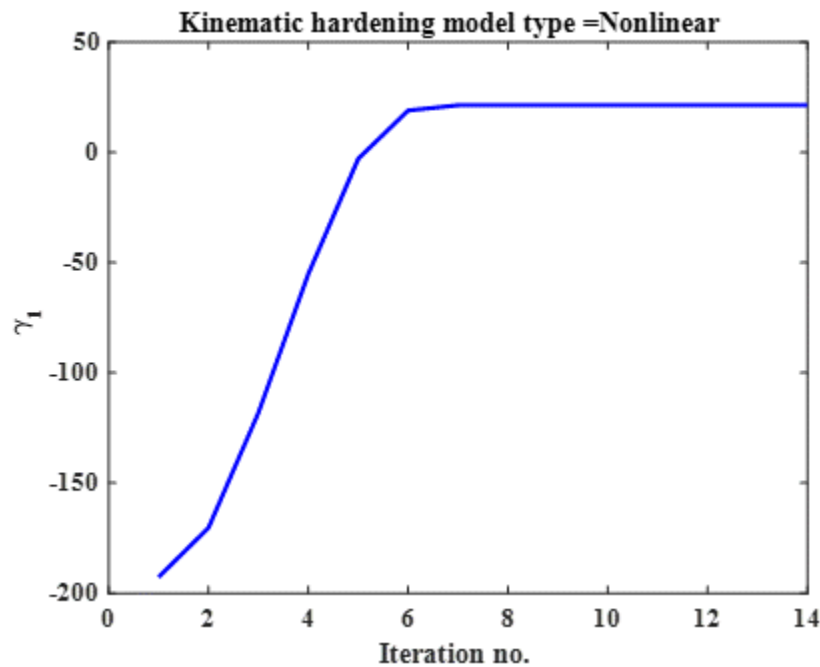


Figure 3A. 37 Nonlinear kinematic hardening constant γ_1 with respect to number of iteration during parameter estimation using gradient based optimization scheme and using ET-T04 stress-strain data (from 0.2% offset yield strain limit to 2% true total strain)

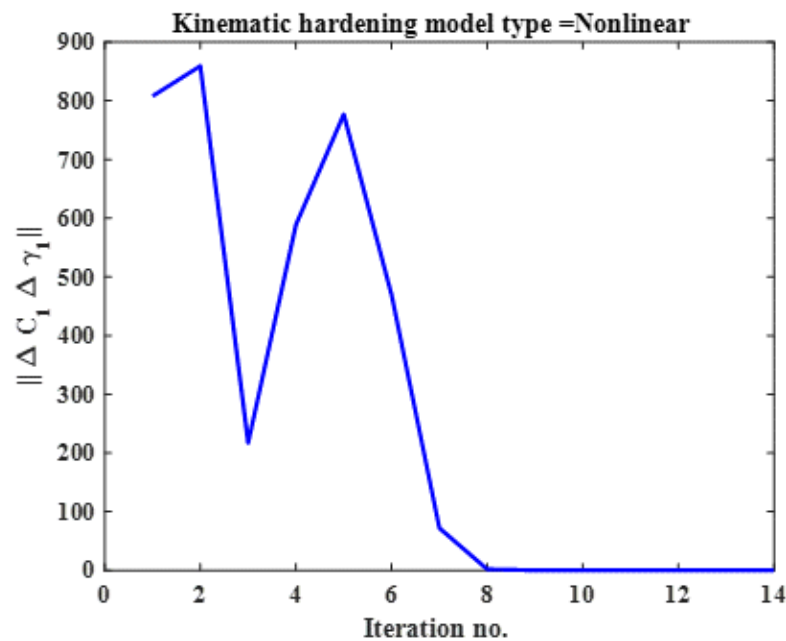


Figure 3A. 38 L2 norm (of incremental kinematic hardening constant C_1 and γ_1) with respect to number of iteration during parameter estimation using gradient based optimization scheme and using ET-T04 stress-strain data (from 0.2% offset yield strain limit to 2% true total strain).

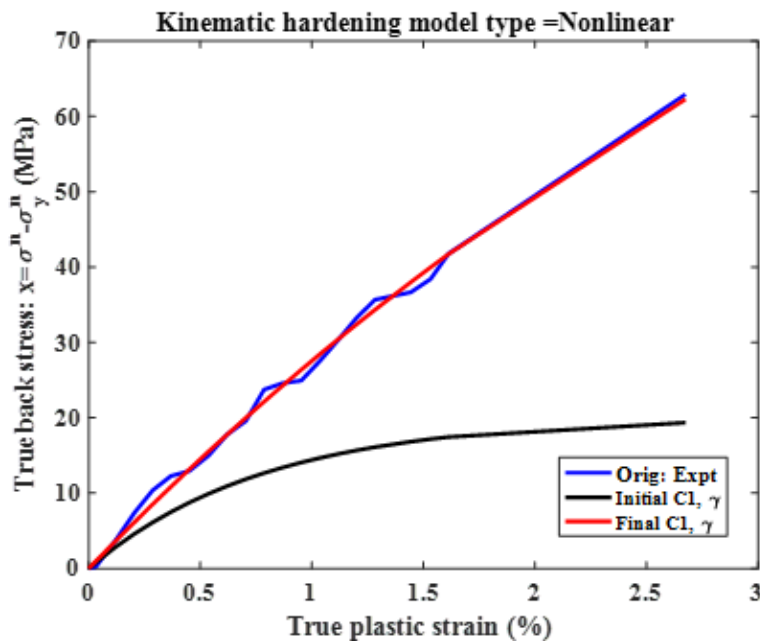


Figure 3A. 39 Comparison of predicted true back stress (using nonlinear kinematic hardening parameter C_1 and γ_1 and considering 0.2% offset yield strain as yield limit) with experimental true back stress for ET-T04 tensile test.

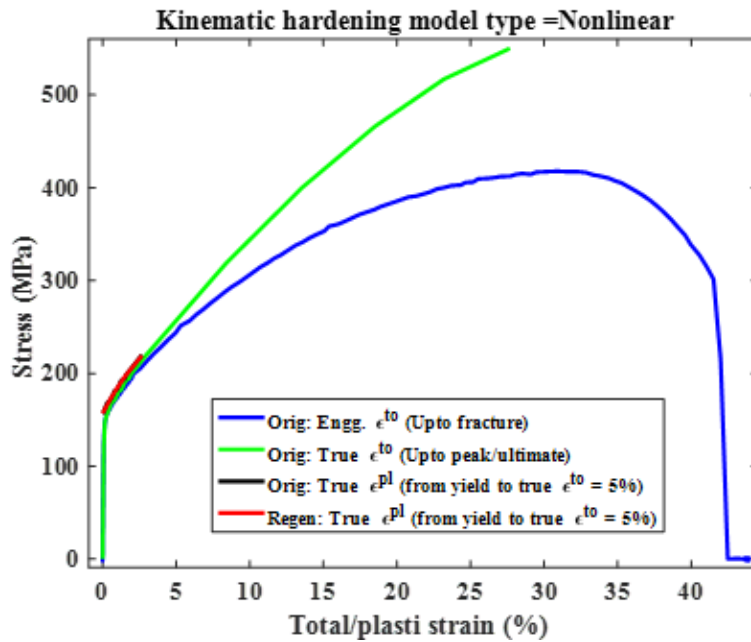


Figure 3A. 40 Comparison of predicted true total stress (using nonlinear kinematic hardening parameter C1 and γ_1 and considering 0.2% offset yield strain as yield limit) with experimental true total stress for ET-T04 tensile test.

Appendix-3B: Supplementary Results for ET-F06 Fatigue Test

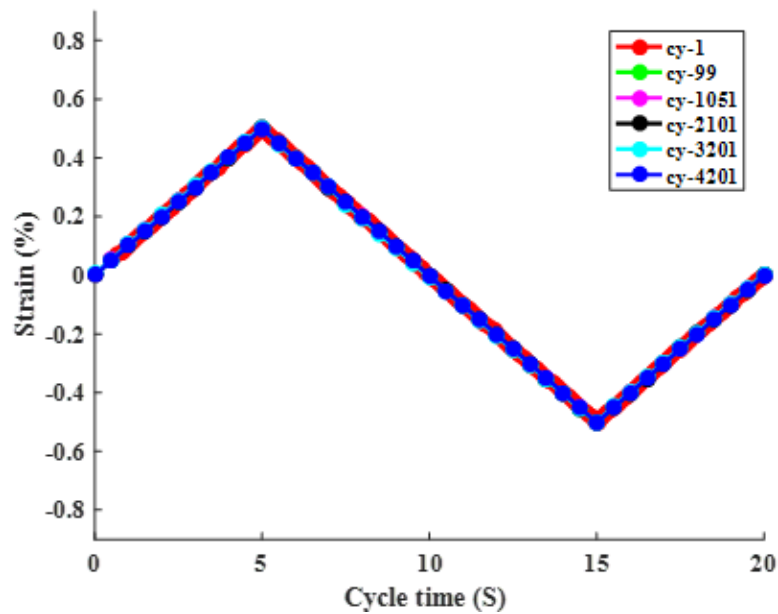


Figure 3B. 1 Intermittent cycle cyclic time versus applied strain for ET-F06 fatigue test.

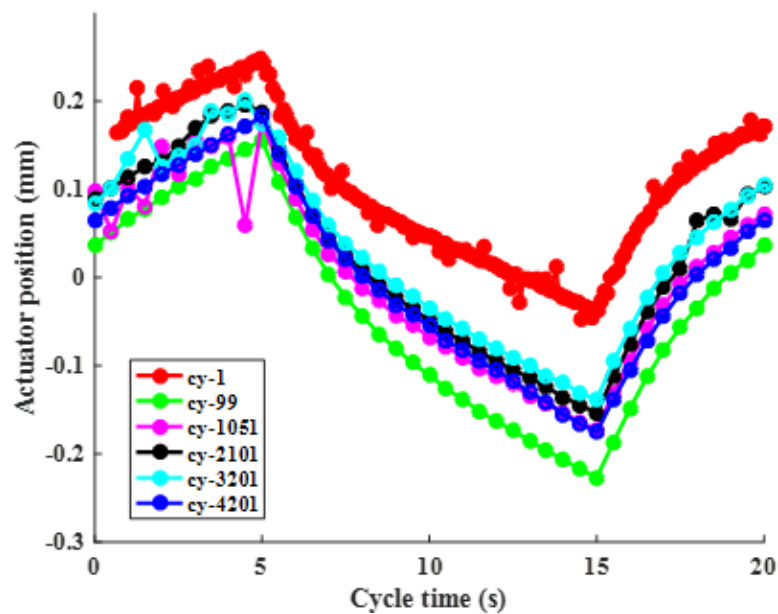


Figure 3B. 2 Intermittent cycle cyclic time versus observed frame actuator position (baseline removed) for ET-F06 fatigue test.

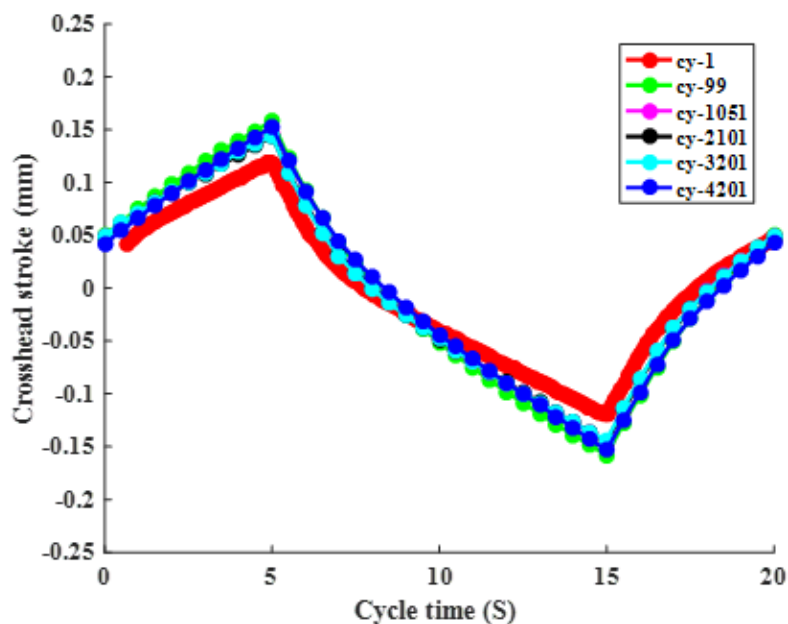


Figure 3B. 3 Intermittent cycle cyclic time versus observed stroke for ET-F06 fatigue test.

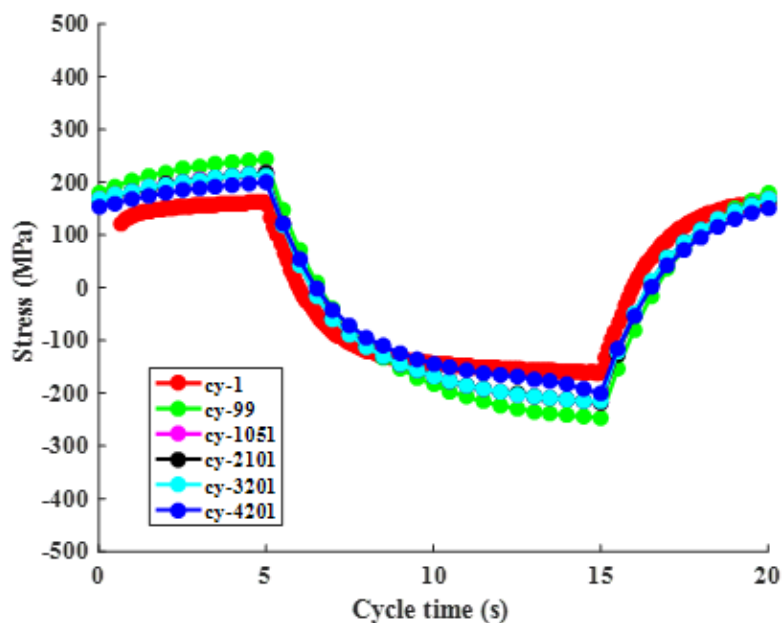


Figure 3B. 4 Intermittent cycle cyclic time versus observed stress for ET-F06 fatigue test.

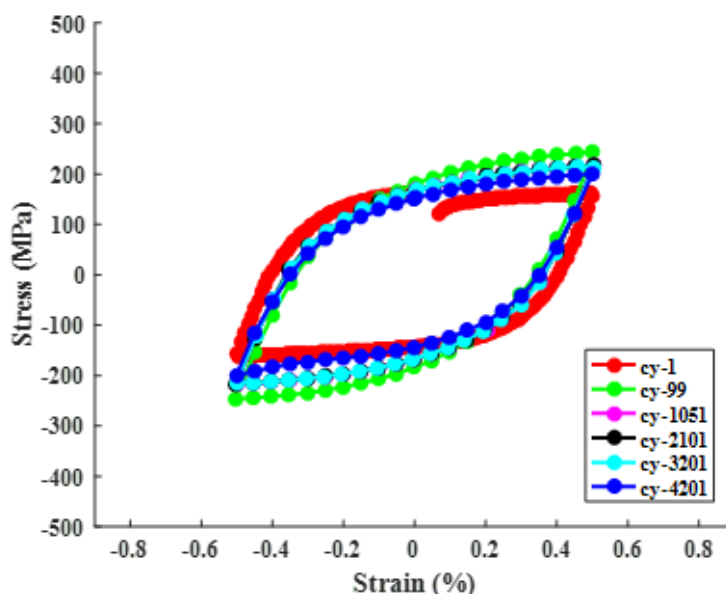


Figure 3B. 5 Intermittent cycle strain versus stress curves for ET-F06 fatigue test.

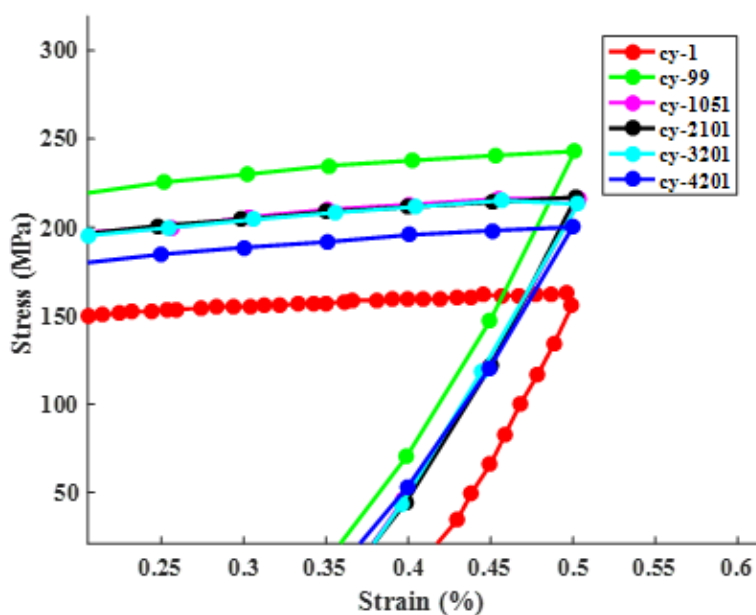


Figure 3B. 6 Magnified figure of Figure 3B. 5.

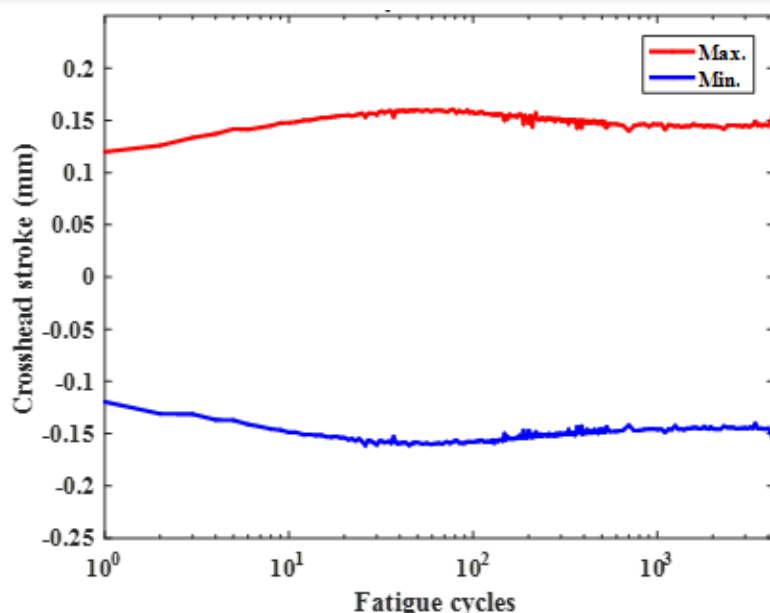


Figure 3B. 7 Maximum and minimum observed stroke during ET-F06.

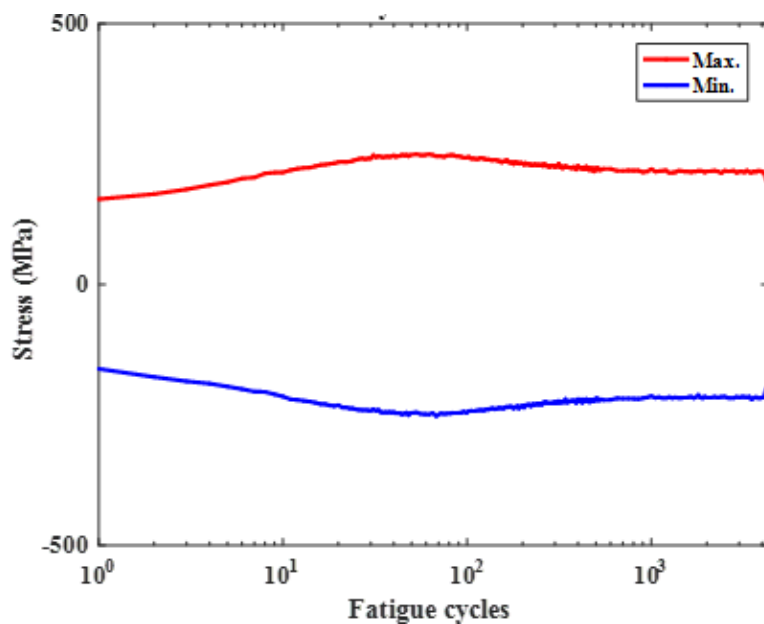


Figure 3B. 8 Maximum and minimum observed stress during ET-F06.

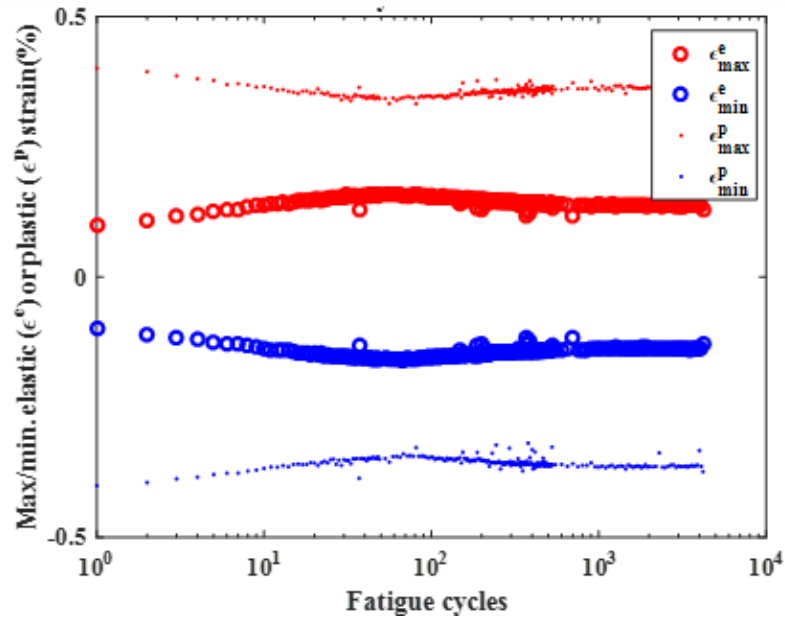


Figure 3B. 9 Maximum and minimum cycle-by-cycle elastic and plastic strain during ET-F06.

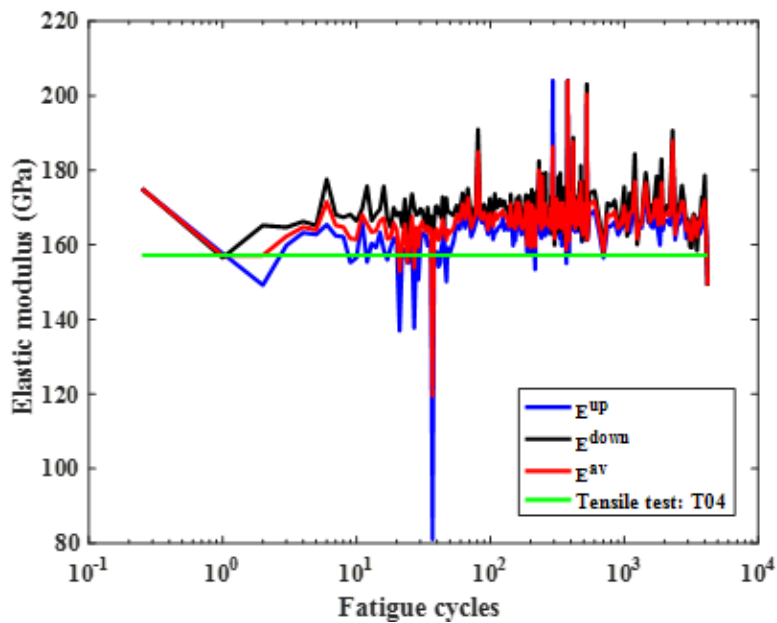


Figure 3B. 10 Fatigue cycle versus estimated elastic modulus for ET-F06 fatigue test. Also the figure shows the comparison with respect to corresponding tensile test (ET-T04) elastic modulus.

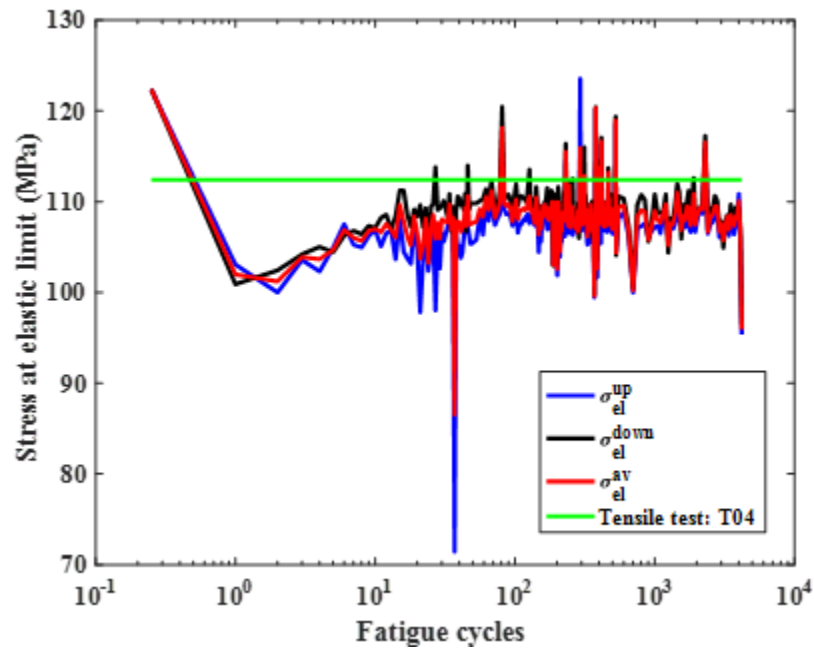


Figure 3B. 11 Fatigue cycle versus estimated stress at elastic limit for ET-F06 fatigue test. Also the figure shows the comparison with respect to corresponding tensile test (ET-T04) elastic limit stress.

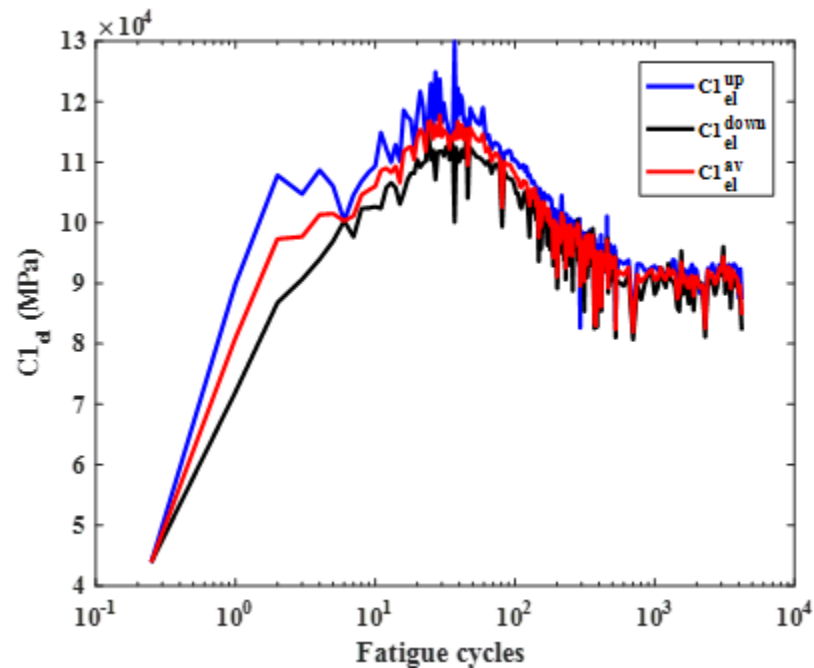


Figure 3B. 12 Fatigue cycle versus estimated nonlinear kinematic hardening or Chaboche model parameters ($C1_{el}$) for ET-F06 fatigue test, with cyclic elastic limit stress was considered to estimate the corresponding cycle back stress.

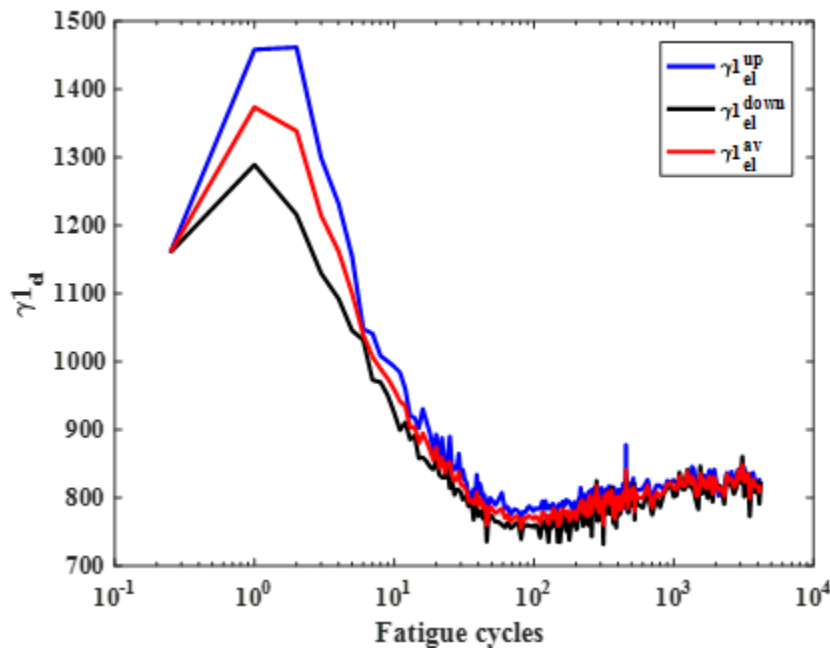


Figure 3B. 13 Fatigue cycle versus estimated nonlinear kinematic hardening or Chaboche model parameters (γ_{1d}) for ET-F06 fatigue test, with cyclic elastic limit stress was considered to estimate the corresponding cycle back stress.

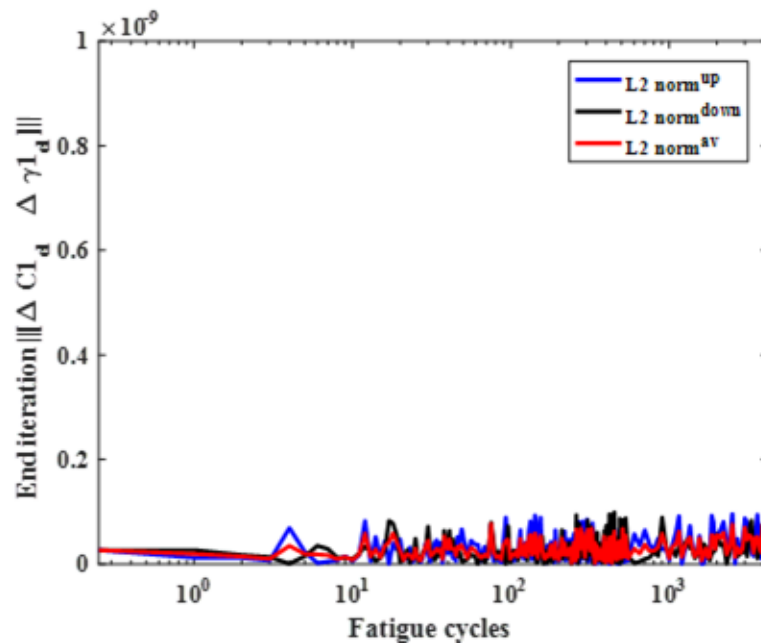


Figure 3B. 14 Fatigue cycle versus end iteration L_2 norm of the incremental nonlinear Chaboche model parameters ($C1_d$ and γ_{1d}) for ET-F06 fatigue test, with cyclic elastic limit stress was considered to estimate the corresponding cycle back stress.

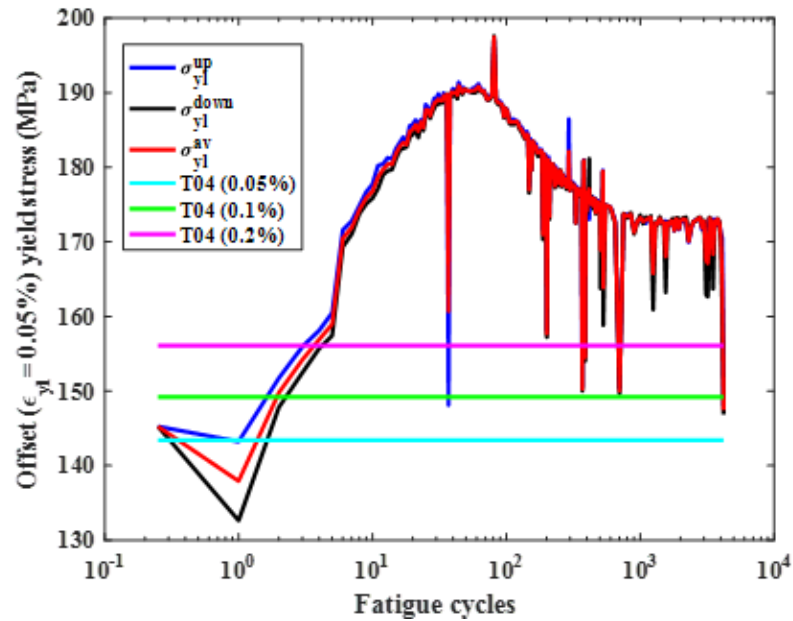


Figure 3B. 15 Fatigue cycle versus estimated stress at 0.05% offset yield limit for ET-F06 fatigue test. Also the figure shows the comparison with respect to corresponding tensile test (ET-T04) yield limit stresses.

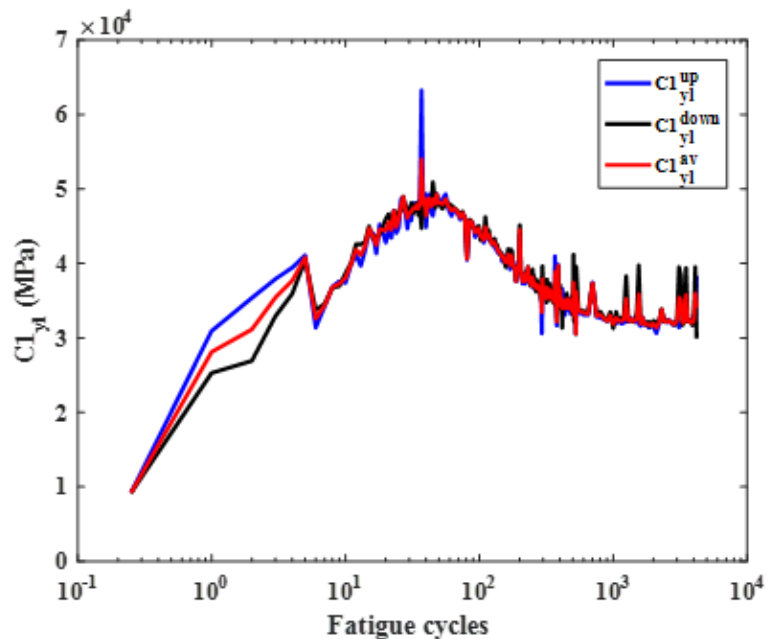


Figure 3B. 16 Fatigue cycle versus estimated nonlinear kinematic hardening or Chaboche model parameter ($C1_{yi}$) for ET-F06 fatigue test, with cyclic 0.05% offset yield limit stress was considered to estimate the corresponding cycle back stress.

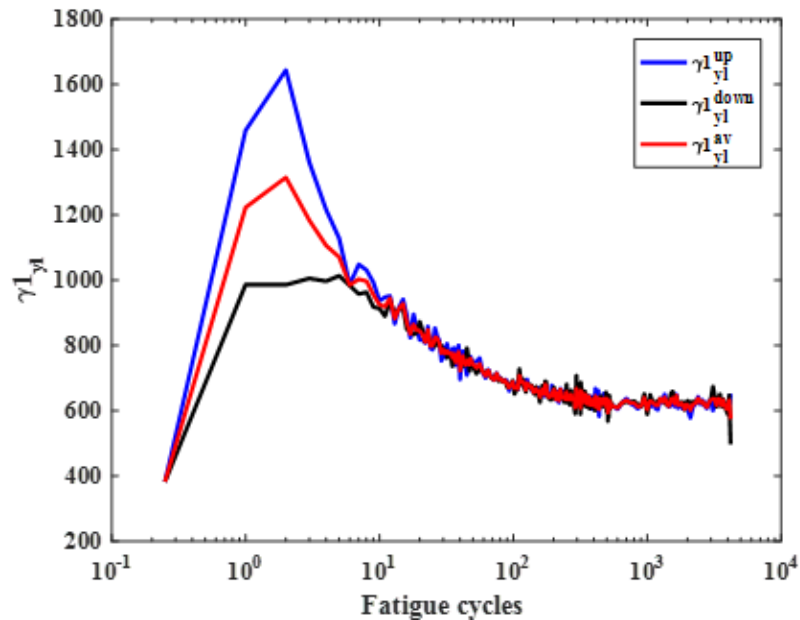


Figure 3B. 17 Fatigue cycle versus estimated nonlinear kinematic hardening or Chaboche model parameter ($\gamma_{1_{yl}}$) for ET-F06 fatigue test, with cyclic 0.05% offset yield limit stress was considered to estimate the corresponding cycle back stress.

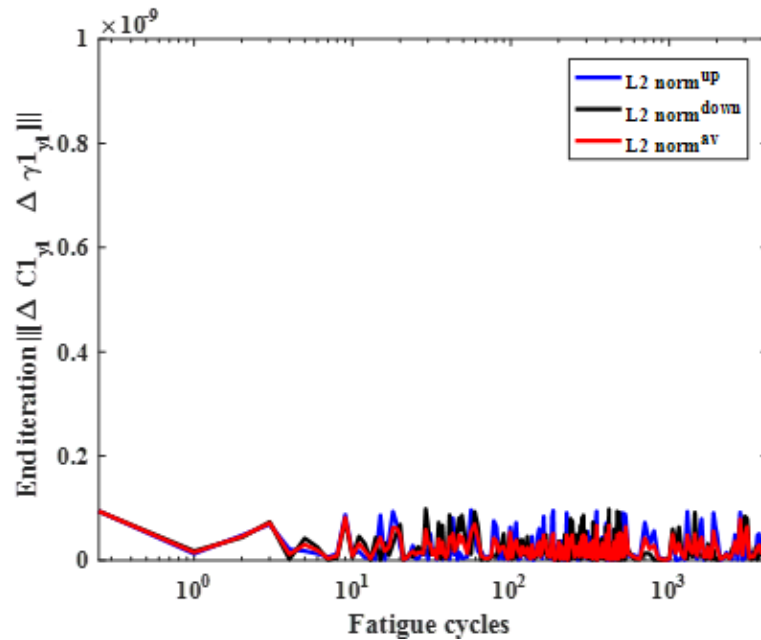


Figure 3B. 18 Fatigue cycle versus end iteration L_2 norm of the incremental nonlinear Chaboche model parameters ($C_{1_{yl}}$, $\gamma_{1_{yl}}$) for ET-F06 fatigue test, with cyclic 0.05% offset yield limit stress was considered to estimate the corresponding cycle back stress.

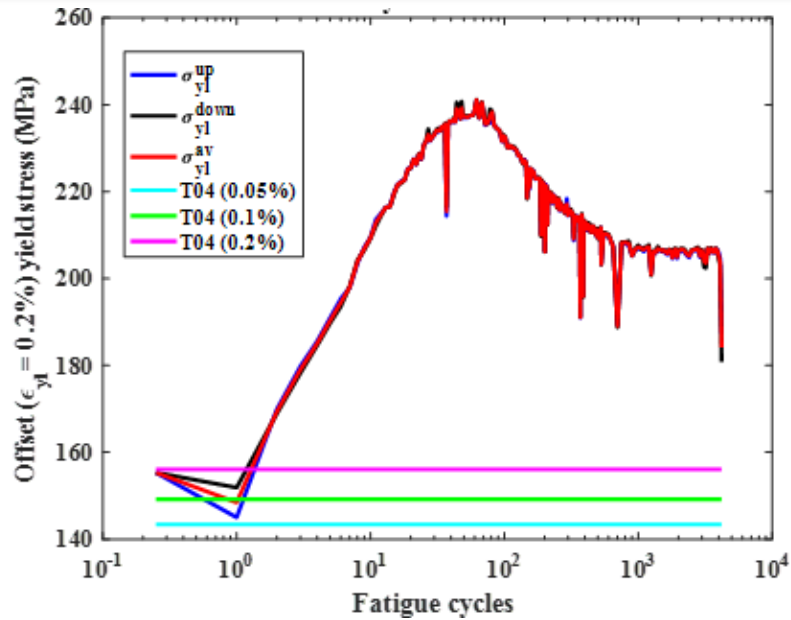


Figure 3B. 19 Fatigue cycle versus estimated stress at 0.2% offset yield limit for ET-F06 fatigue test. Also the figure shows the comparison with respect to corresponding tensile test (ET-T04) yield limit stresses.

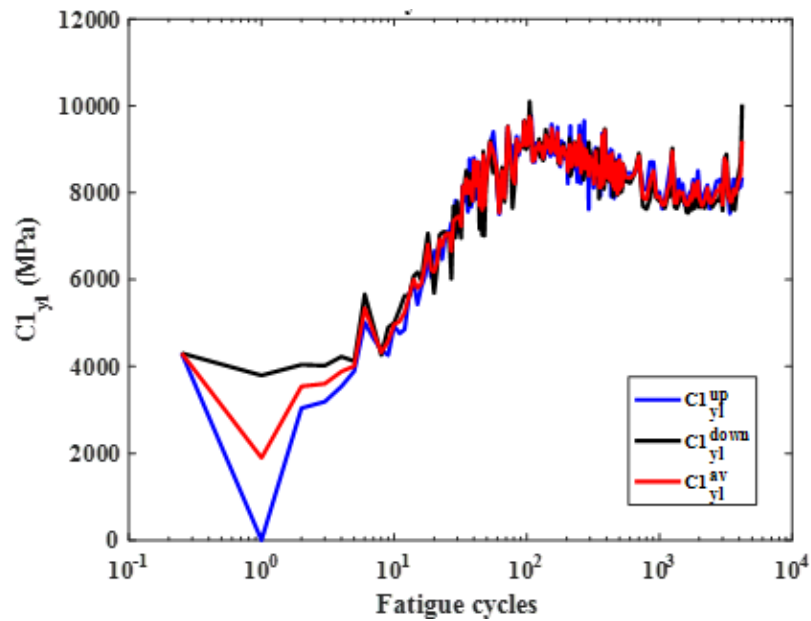


Figure 3B. 20 Fatigue cycle versus estimated linear kinematic hardening or Chaboche model parameter ($C1_{yl}$) for ET-F06 fatigue test, with cyclic 0.2% offset yield limit stress was considered to estimate the corresponding cycle back stress.

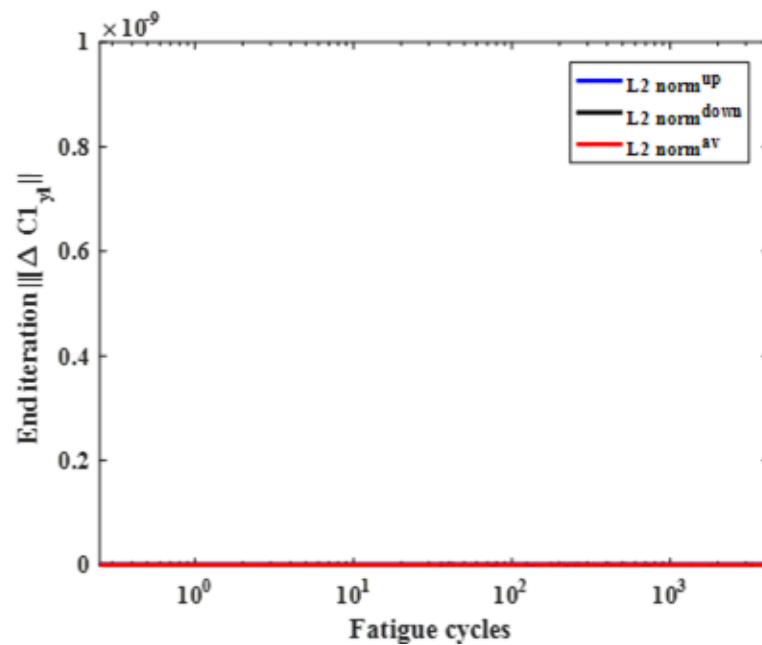


Figure 3B. 21 Fatigue cycle versus end iteration L_2 norm of the incremental linear Chaboche model parameter ($C1_{yt}$) for ET-F06 fatigue test, with cyclic 0.2% offset yield limit stress was considered to estimate the corresponding cycle back stress.

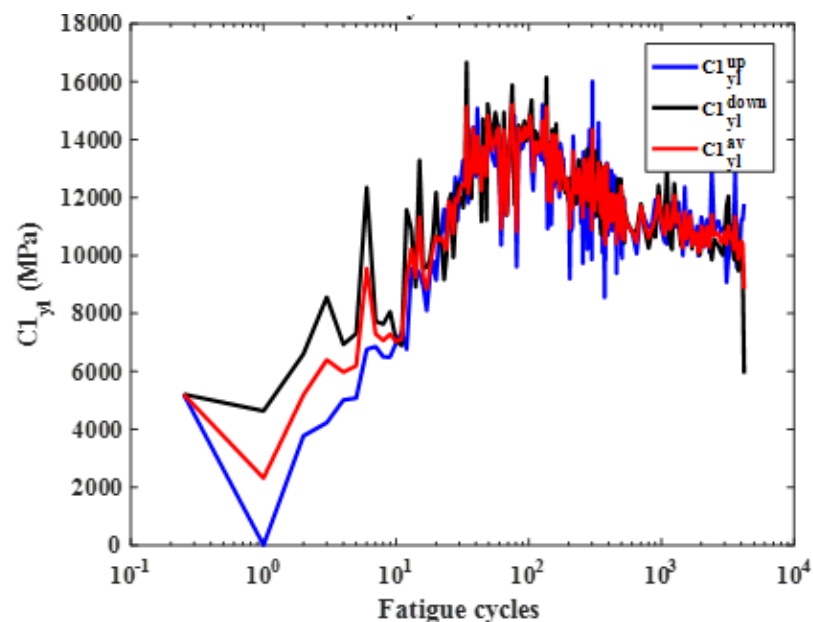


Figure 3B. 22 Fatigue cycle versus estimated nonlinear kinematic hardening or Chaboche model parameter ($C1_{yt}$) for ET-F06 fatigue test, with cyclic 0.2% offset yield limit stress was considered to estimate the corresponding cycle back stress.

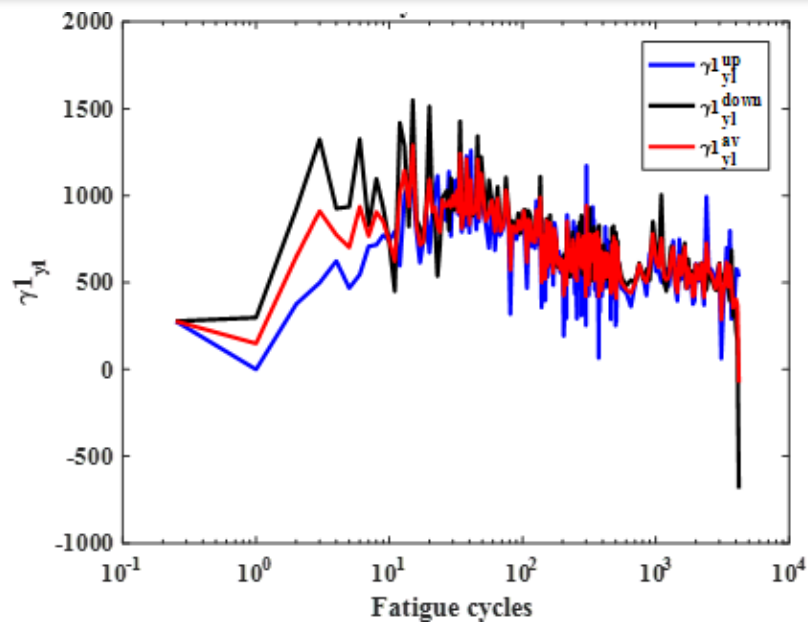


Figure 3B. 23 Fatigue cycle versus estimated nonlinear kinematic hardening or Chaboche model parameter (γ_{yl}) for ET-F06 fatigue test, with cyclic 0.2% offset yield limit stress was considered to estimate the corresponding cycle back stress.

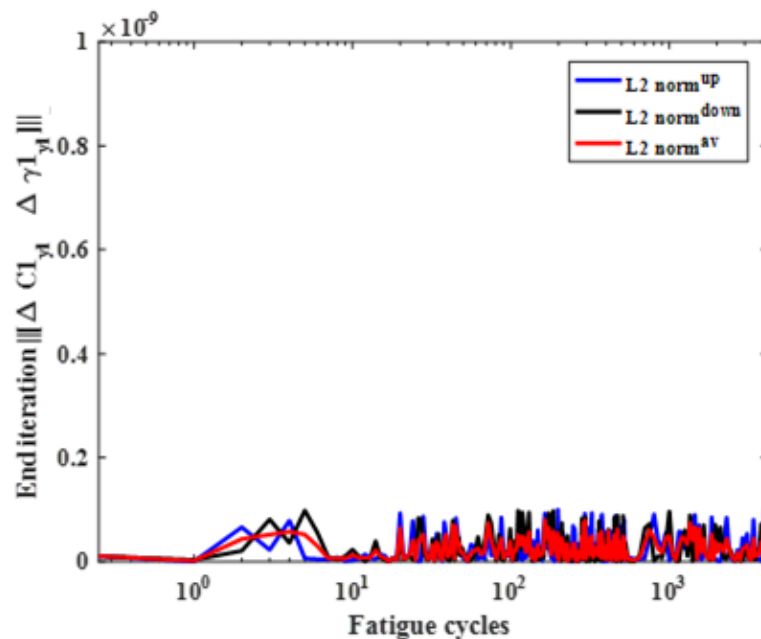


Figure 3B. 24 Fatigue cycle versus end iteration L2 norm of the incremental nonlinear Chaboche model parameters (C_{1yl} , γ_{yl}) for ET-F06 fatigue test, with cyclic 0.2% offset yield limit stress was considered to estimate the corresponding cycle back stress.

Appendix-3C: Supplementary Results for ET-F41 Fatigue Test

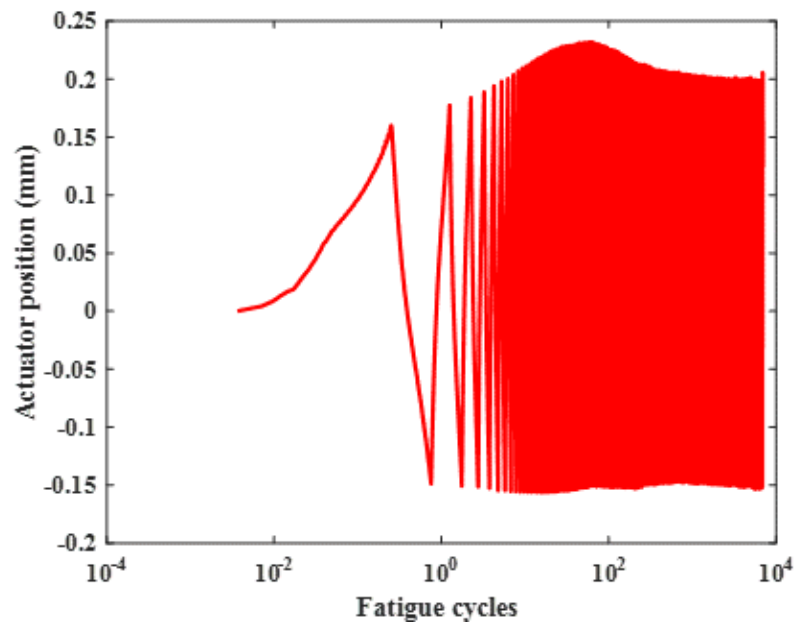


Figure 3C. 1 Observed actuator position during ET-F41.

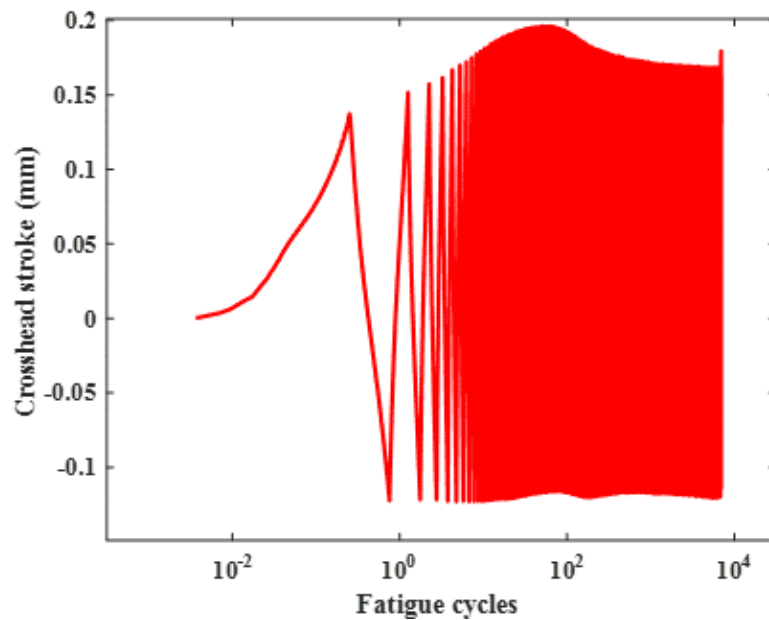


Figure 3C. 2 Observed stroke during ET-F41.

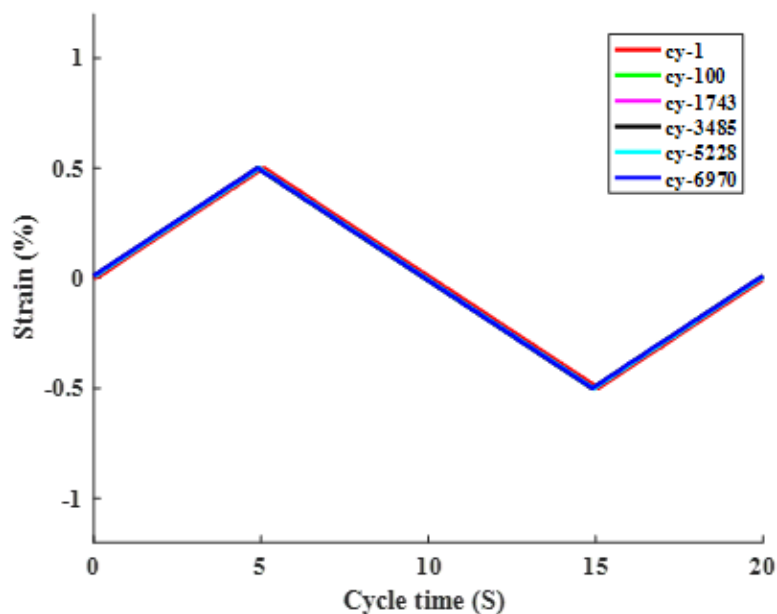


Figure 3C. 3 Intermittent cycle cyclic time versus applied strain for ET-F41 fatigue test.

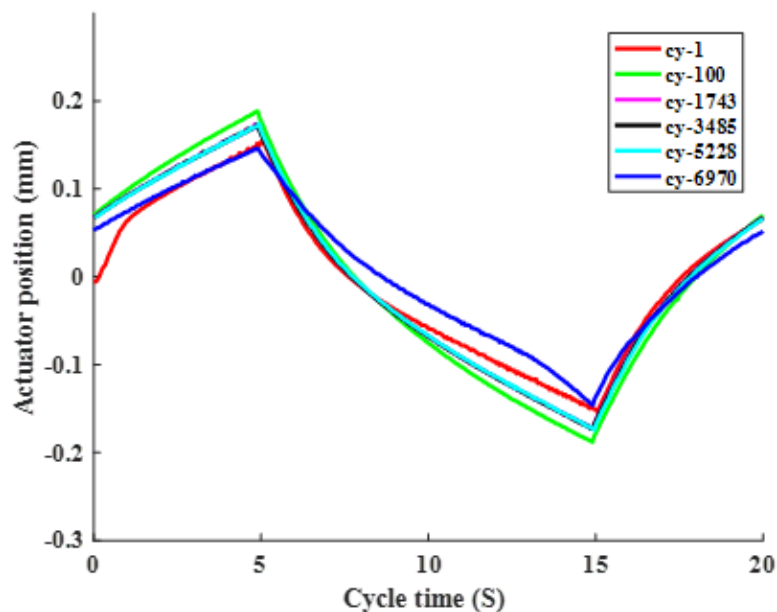


Figure 3C. 4 Intermittent cycle cyclic time versus observed frame actuator position (baseline removed) for ET-F41 fatigue test.

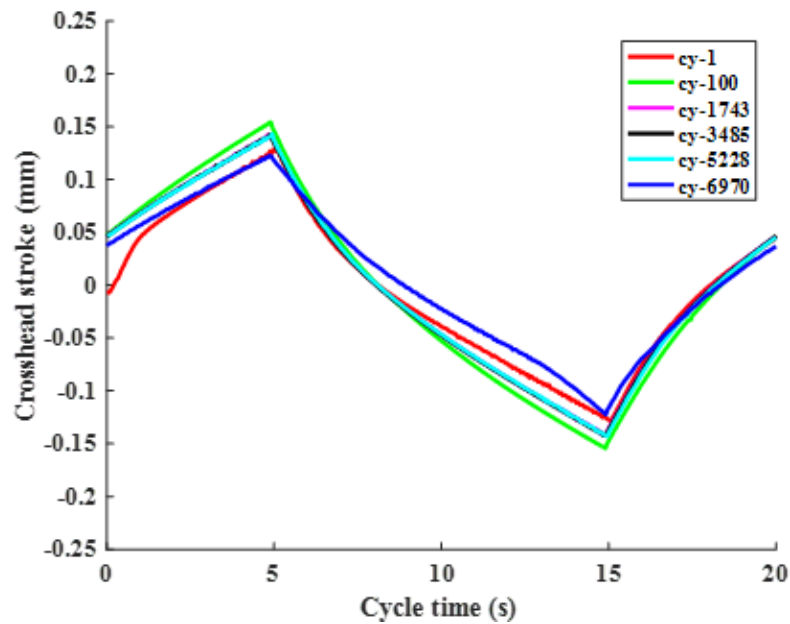


Figure 3C. 5 Intermittent cycle cyclic time versus observed stroke for ET-F41 fatigue test.

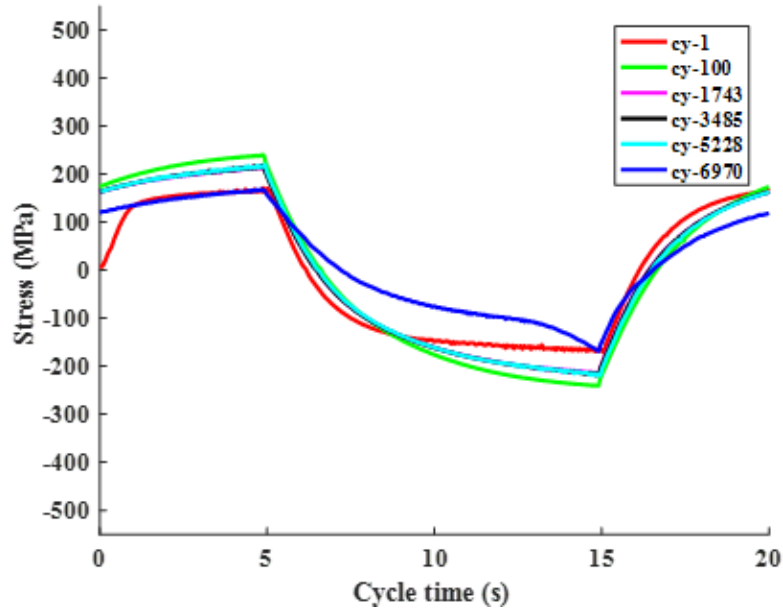


Figure 3C. 6 Intermittent cycle cyclic time versus observed stress for ET-F41 fatigue test.

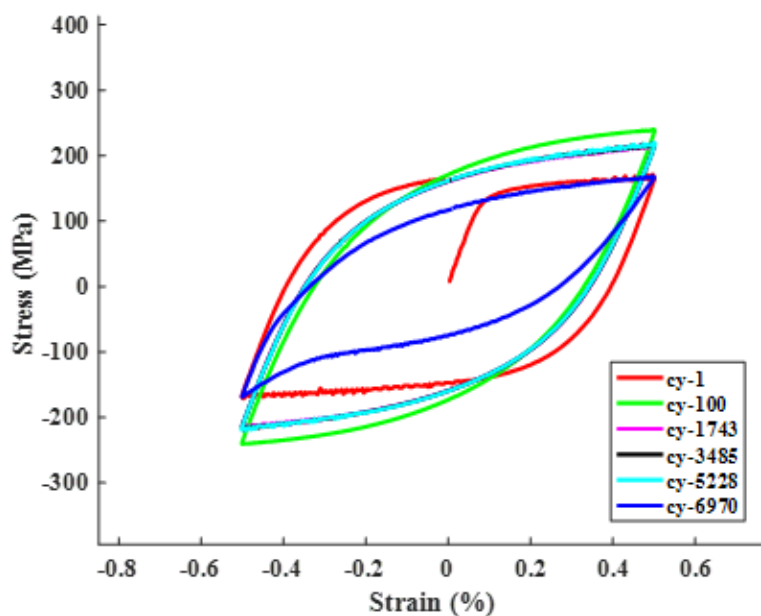


Figure 3C. 7 Intermittent cycle strain versus stress for ET-F41 fatigue test.

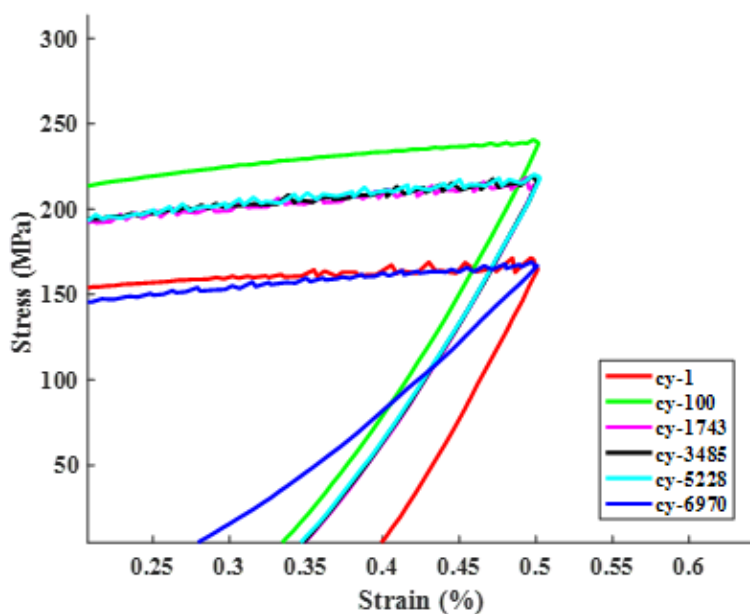


Figure 3C. 8 Magnified figure of Figure 3C. 8.

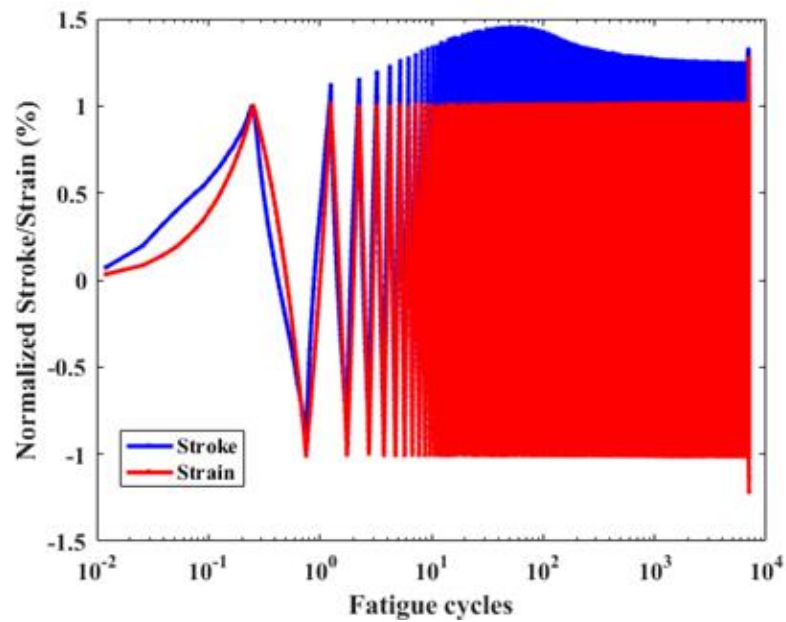


Figure 3C. 9 Time history of normalized stroke and strain measurements from ET-F41.

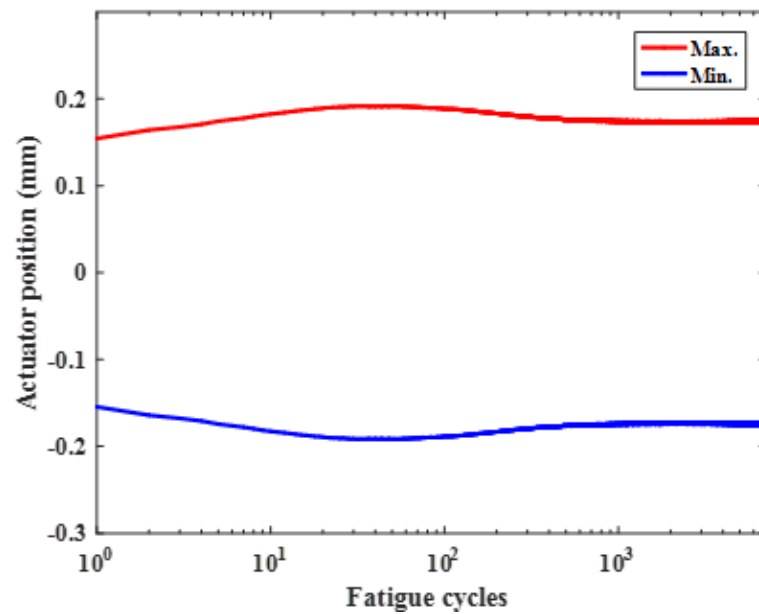


Figure 3C. 10 Maximum and minimum observed actuator position (baseline removed) during ET-F41.

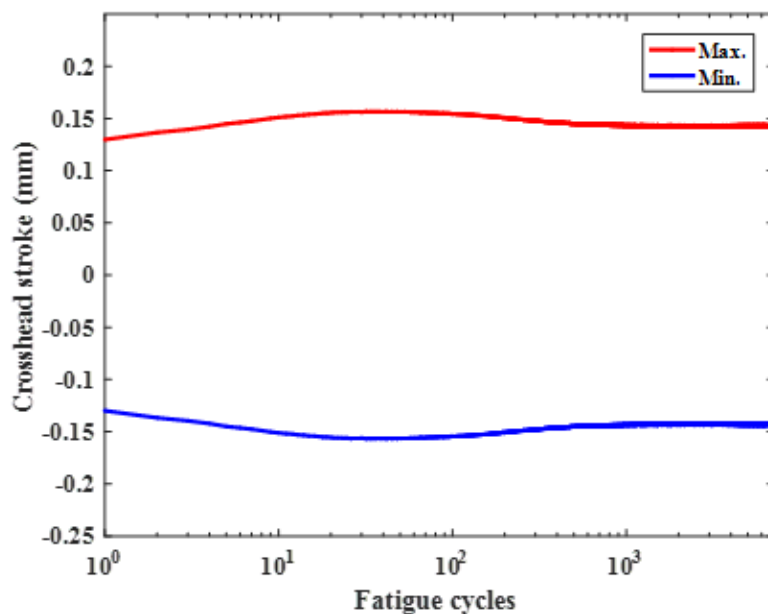


Figure 3C. 11 Maximum and minimum observed stroke (baseline removed) during ET-F41.

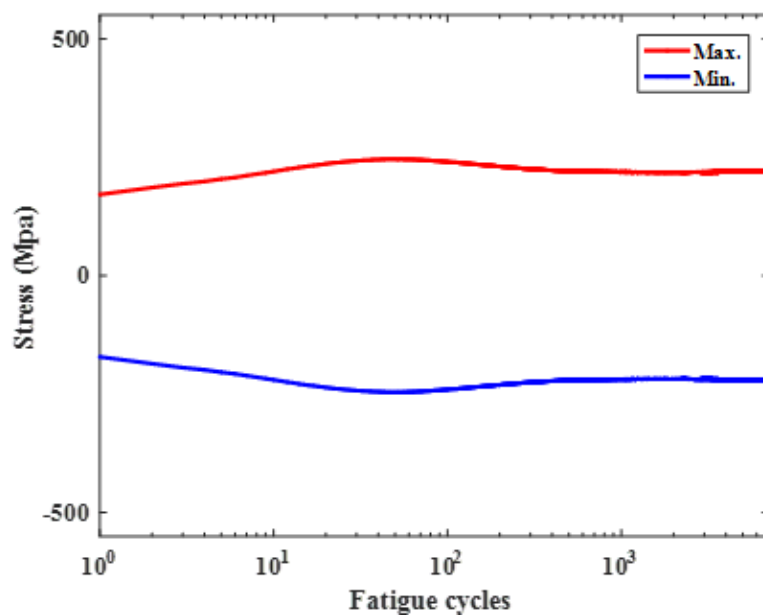


Figure 3C. 25 Maximum and minimum observed stress during ET-F41.

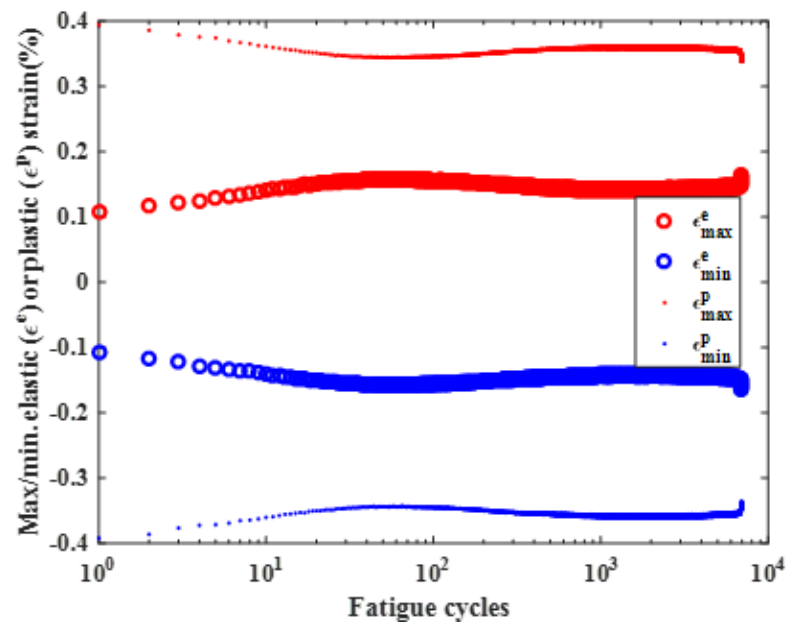


Figure 3C. 26 Maximum and minimum cycle-by-cycle elastic and plastic strain during ET-F41.

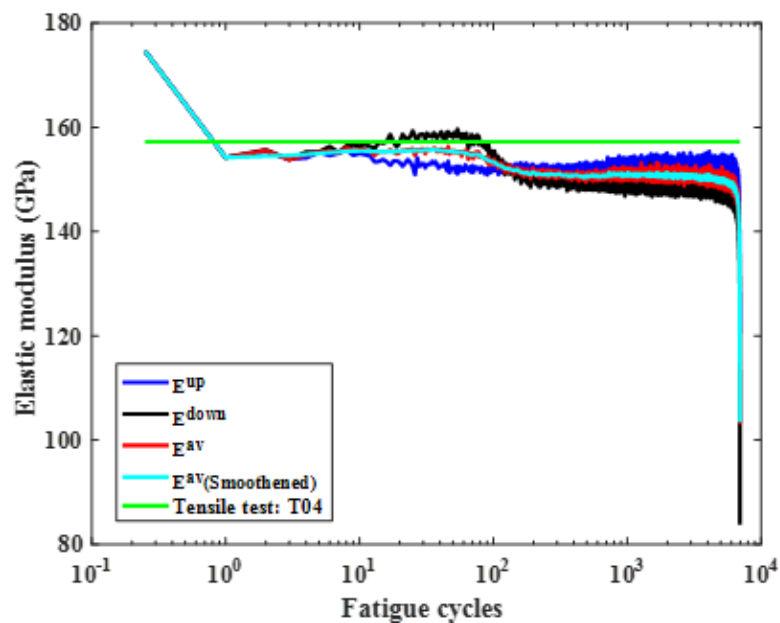


Figure 3C. 27 Fatigue cycle versus estimated elastic modulus for ET-F41 fatigue test. Also the figure shows the comparison with respect to corresponding tensile test (ET-T04) elastic modulus.

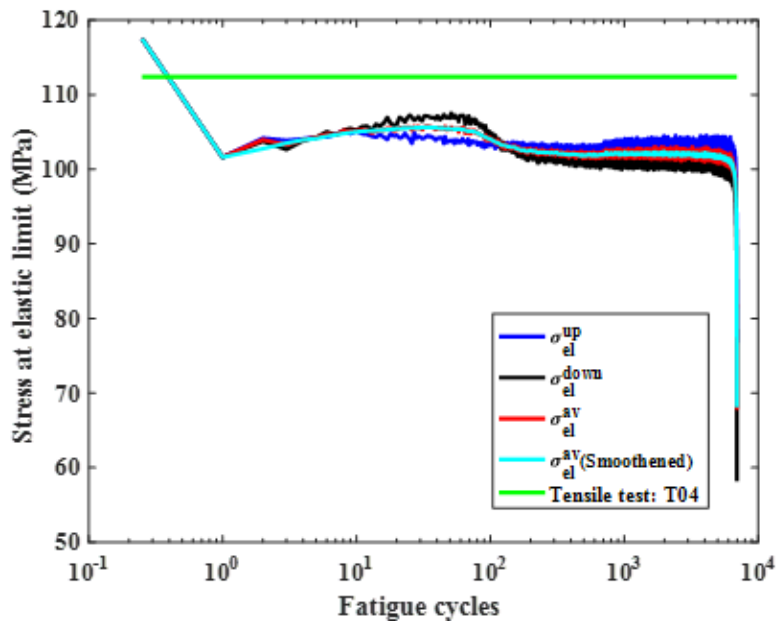


Figure 3C. 28 Fatigue cycle versus estimated stress at elastic limit for ET-F41 fatigue test. Also the figure shows the comparison with respect to corresponding tensile test (ET-T04) elastic limit stress.

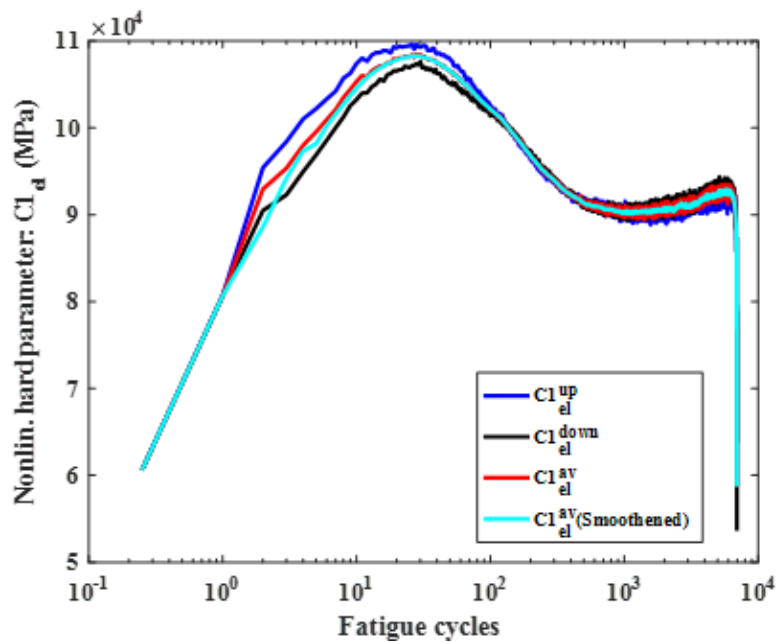


Figure 3C. 29 Fatigue cycle versus estimated nonlinear kinematic hardening or Chaboche model parameters ($C1_{el}$) for ET-F41 fatigue test, with cyclic elastic limit stress was considered to estimate the corresponding cycle back stress.

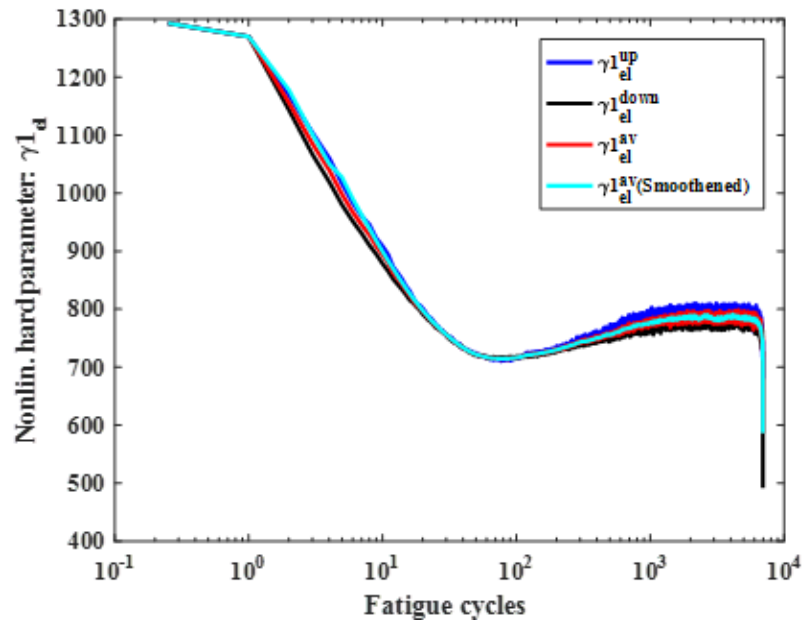


Figure 3C. 30 Fatigue cycle versus estimated nonlinear kinematic hardening or Chaboche model parameters (γ_{1d}) for ET-F41 fatigue test, with cyclic elastic limit stress was considered to estimate the corresponding cycle back stress.

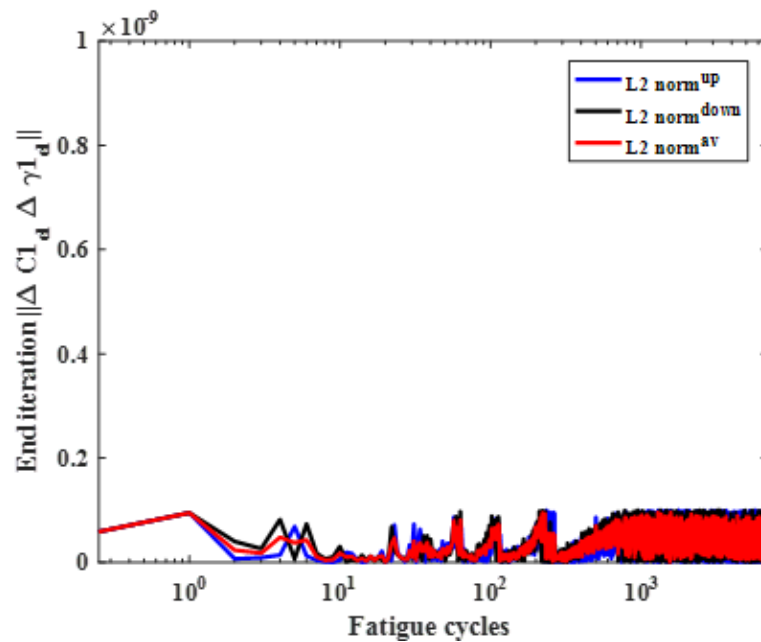


Figure 3C. 31 Fatigue cycle versus end iteration L_2 norm of the incremental nonlinear Chaboche model parameters (C_{1d} and γ_{1d}) for ET-F06 fatigue test, with cyclic elastic limit stress was considered to estimate the corresponding cycle back stress.

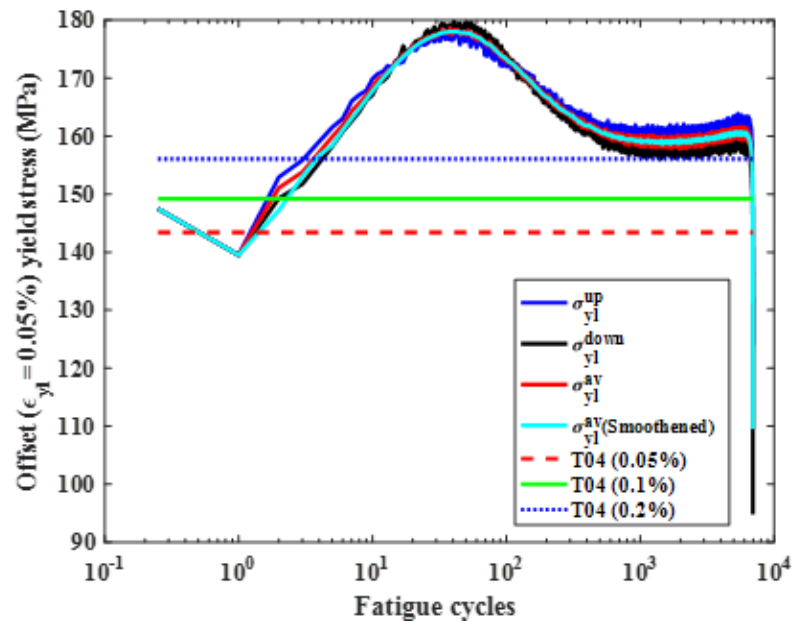


Figure 3C. 32 Fatigue cycle versus estimated stress at 0.05% offset yield limit for ET-F41 fatigue test. Also the figure shows the comparison with respect to corresponding tensile test (ET-T04) yield limit stresses.

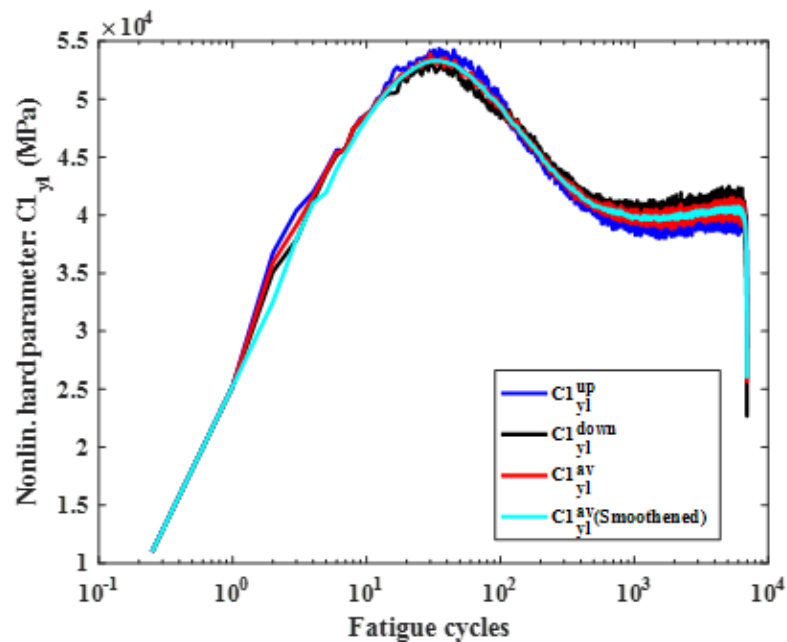


Figure 3C. 33 Fatigue cycle versus estimated nonlinear kinematic hardening or Chaboche model parameter ($C1_{yl}$) for ET-F41 fatigue test, with cyclic 0.05% offset yield limit stress was considered to estimate the corresponding cycle back stress.

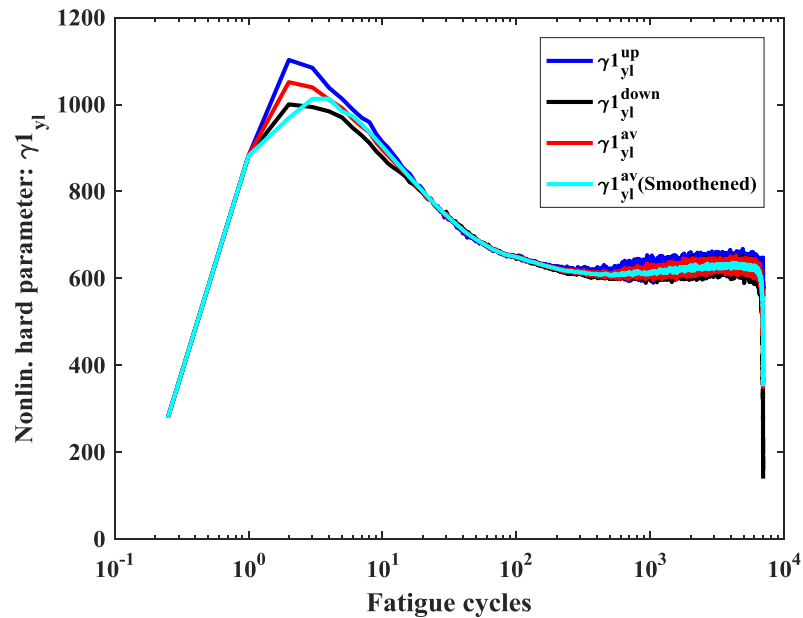


Figure 3C. 34 Fatigue cycle versus estimated nonlinear kinematic hardening or Chaboche model parameter (γ_{yl}^1) for ET-F41 fatigue test, with cyclic 0.05% offset yield limit stress was considered to estimate the corresponding cycle back stress.

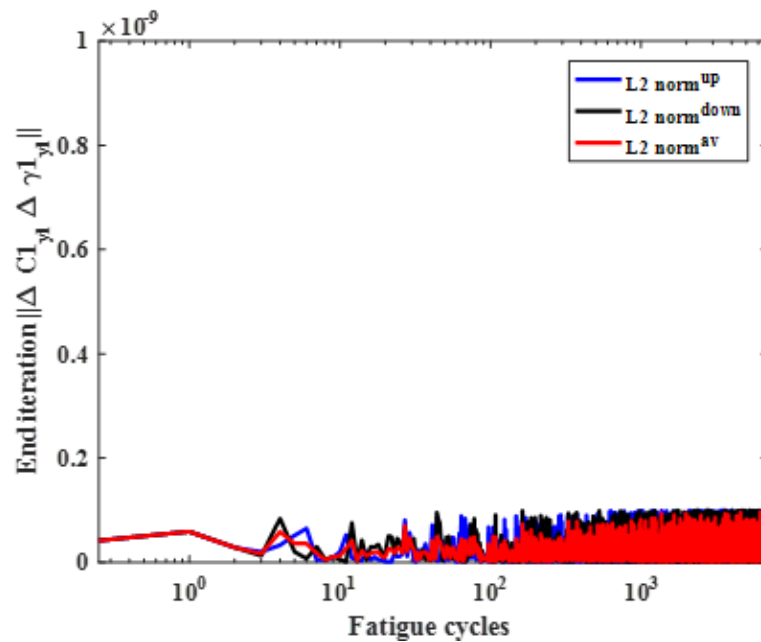


Figure 3C. 35 Fatigue cycle versus end iteration L_2 norm of the incremental nonlinear Chaboche model parameters (C_{yl}^1, γ_{yl}^1) for ET-F41 fatigue test, with cyclic 0.05% offset yield limit stress was considered to estimate the corresponding cycle back stress.

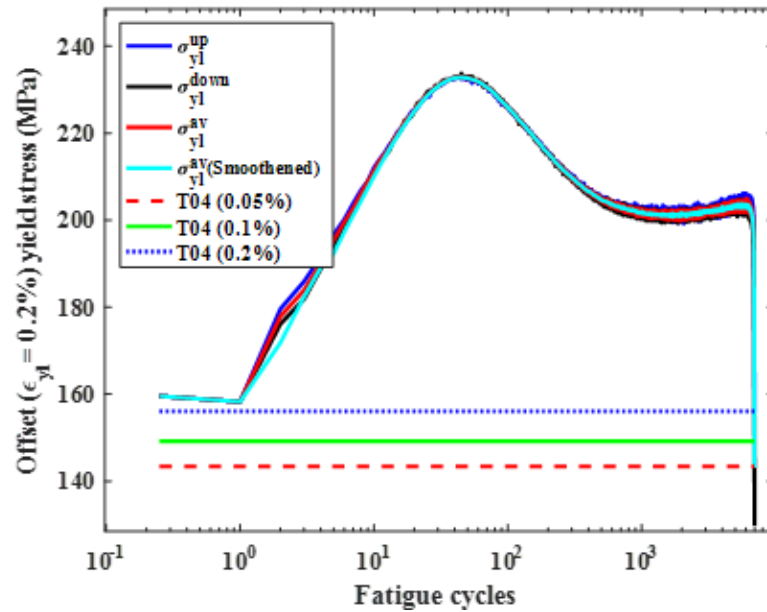


Figure 3C. 36 Fatigue cycle versus estimated stress at 0.2% offset yield limit for ET-F41 fatigue test. Also the figure shows the comparison with respect to corresponding tensile test (ET-T04) yield limit stresses.

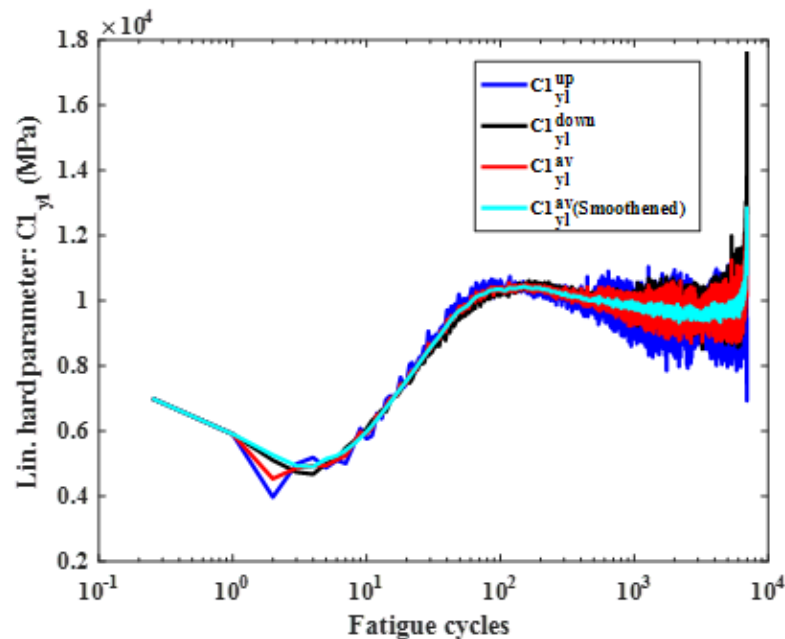


Figure 3C. 37 Fatigue cycle versus estimated linear kinematic hardening or Chaboche model parameter ($C1_{yl}$) for ET-F41 fatigue test, with cyclic 0.2% offset yield limit stress was considered to estimate the corresponding cycle back stress.

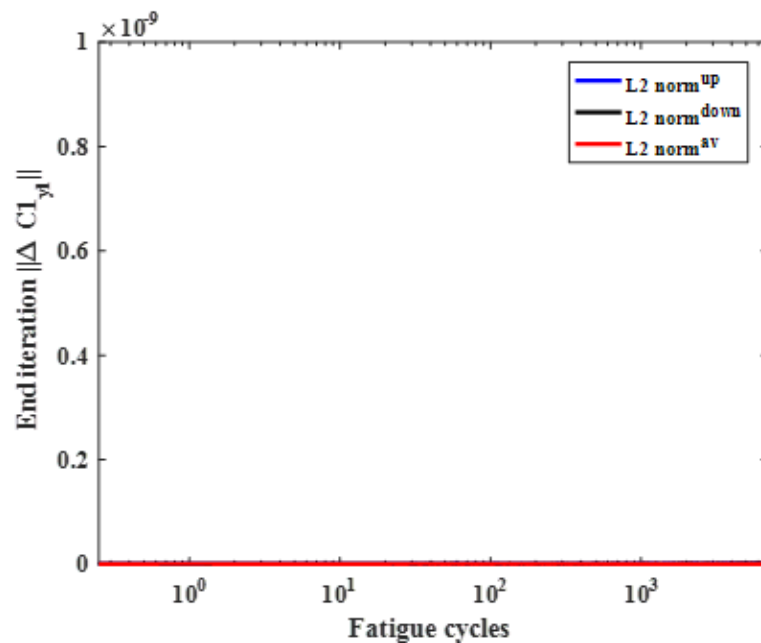


Figure 3C. 38 Fatigue cycle versus end iteration L_2 norm of the incremental linear Chaboche model parameters ($C1_{yt}$) for ET-F41 fatigue test, with cyclic 0.2% offset yield limit stress was considered to estimate the corresponding cycle back stress.

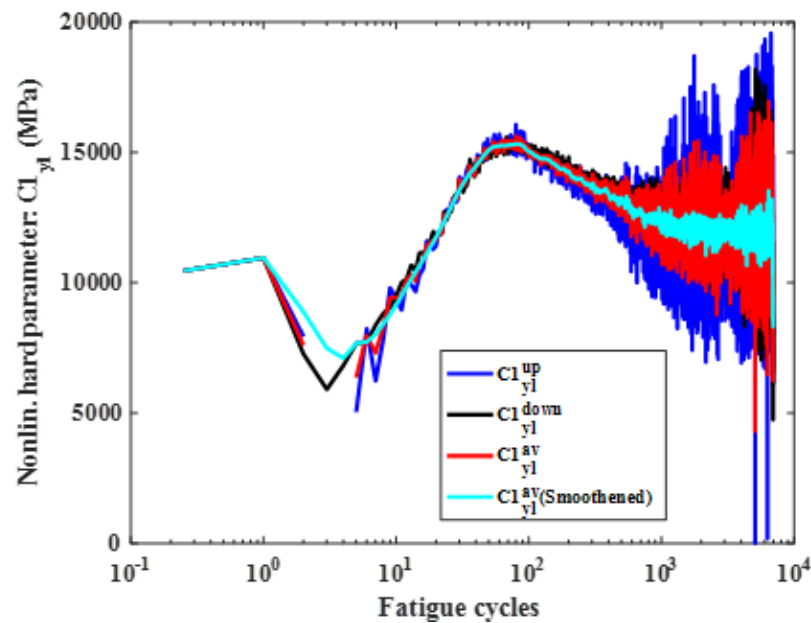


Figure 3C. 39 Fatigue cycle versus estimated nonlinear kinematic hardening or Chaboche model parameter ($C1_{yt}$) for ET-F41 fatigue test, with cyclic 0.2% offset yield limit stress was considered to estimate the corresponding cycle back stress.

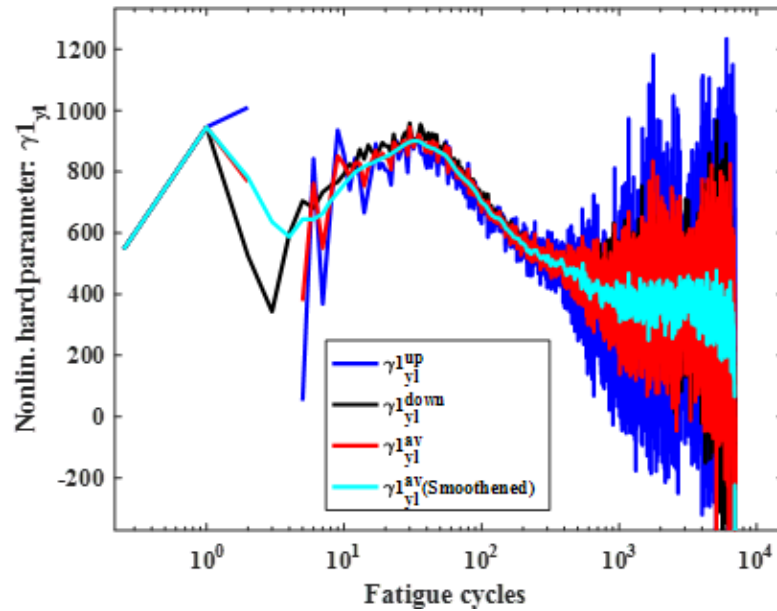


Figure 3C. 40 Fatigue cycle versus estimated nonlinear kinematic hardening or Chaboche model parameter ($\gamma_{1_{yl}}$) for ET-F41 fatigue test, with cyclic 0.2% offset yield limit stress was considered to estimate the corresponding cycle back stress.

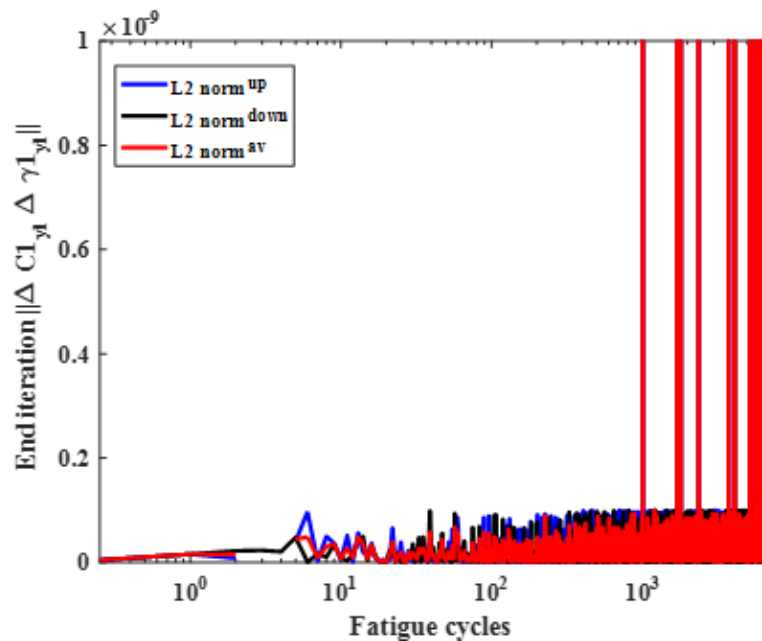


Figure 3C. 41 Fatigue cycle versus end iteration L2 norm of the incremental nonlinear Chaboche model parameters ($C_{1_{yl}}$, $\gamma_{1_{yl}}$) for ET-F41 fatigue test, with cyclic 0.2% offset yield limit stress was considered to estimate the corresponding cycle back stress. Note: high values for iteration norms and, therefore, nonlinear kinematic hardening parameters ($C_{1_{yl}}$, $\gamma_{1_{yl}}$) based on 0.2% offset yield stress should not be used for modeling fatigue behavior of 316 SS.

Appendix-3D: Supplementary Results for ET-F38 Fatigue Test

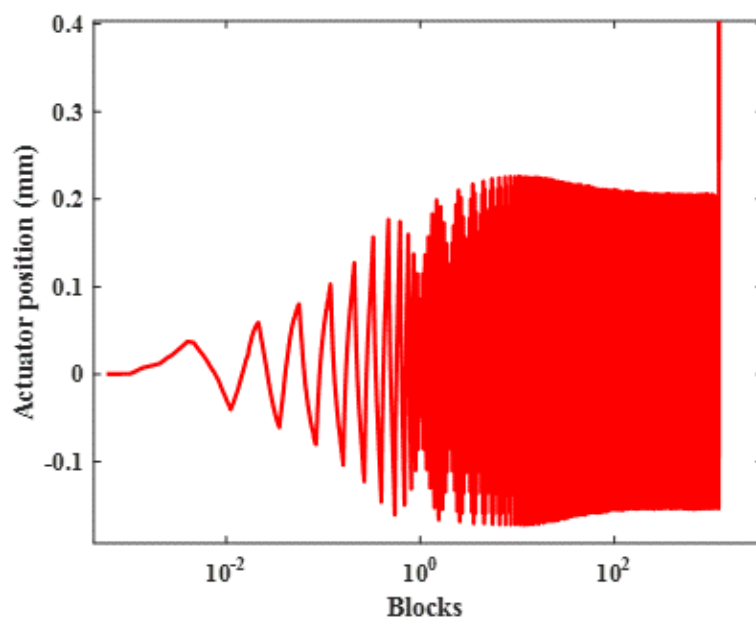


Figure 3D. 1 Observed actuator position during ET-F38.

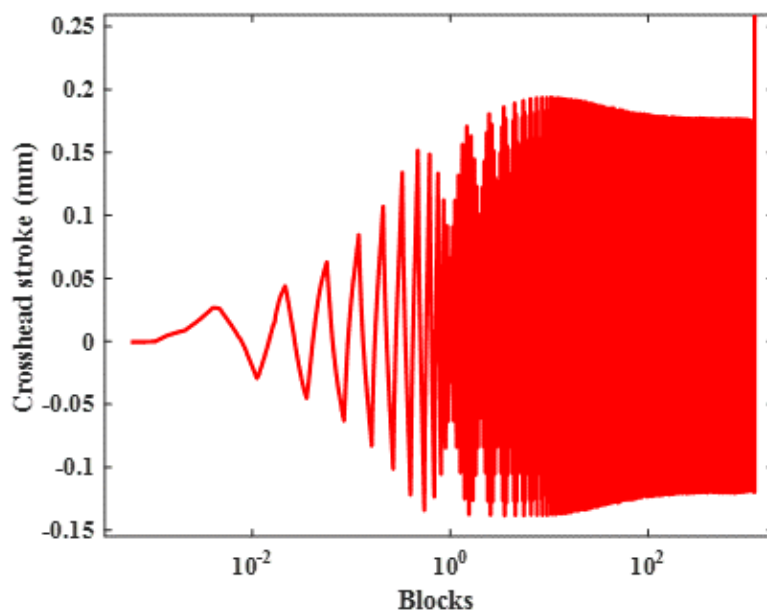


Figure 3D. 2 Observed stroke during ET-F38.

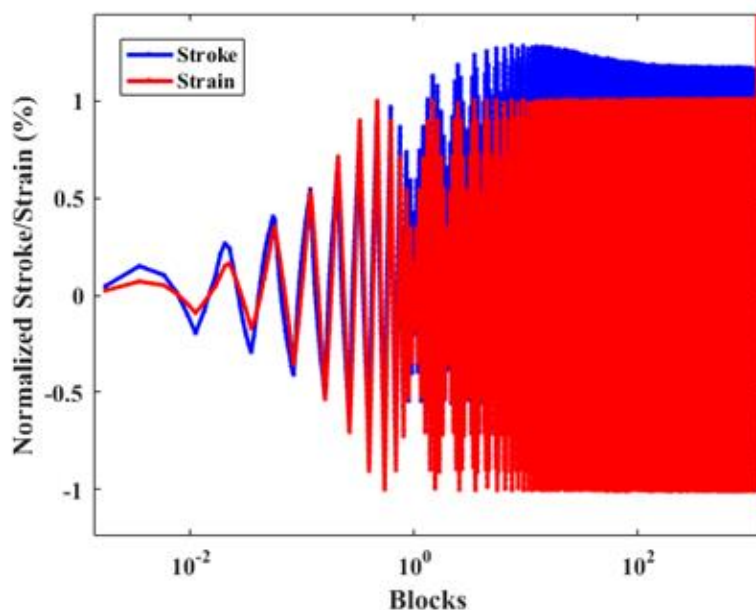


Figure 3D. 3 Time history of normalized stroke and strain measurements from ET-F38.

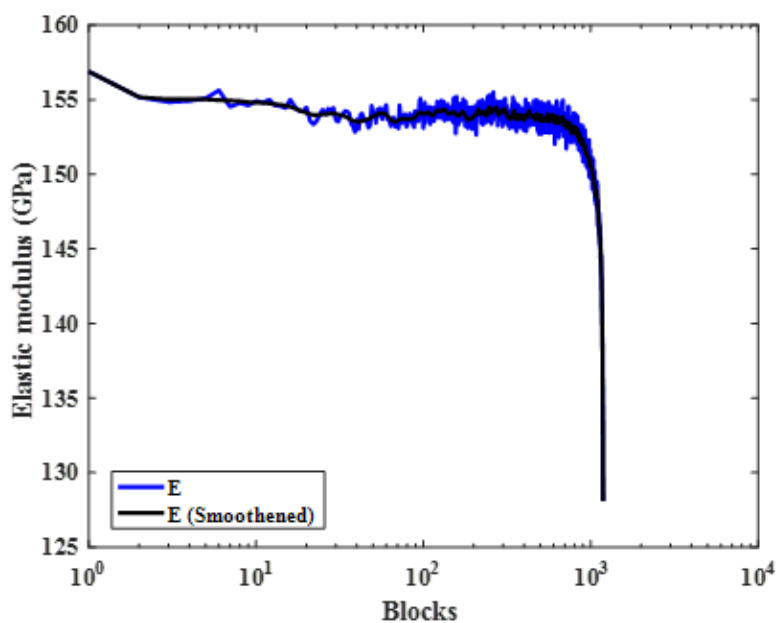


Figure 3D. 4 Block-by-block estimated elastic modulus for ET-F38 fatigue test.

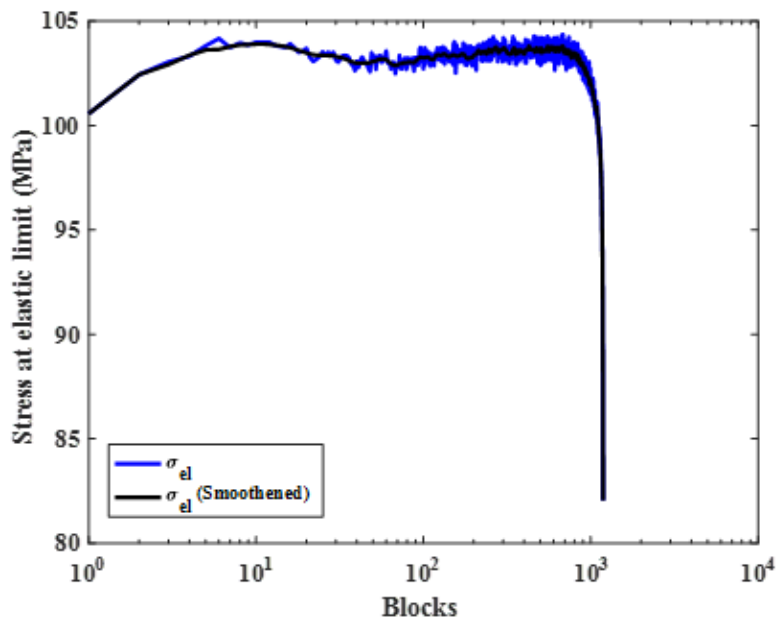


Figure 3D. 5 Block-by-block estimated stress at elastic limit for ET-F38 fatigue test.

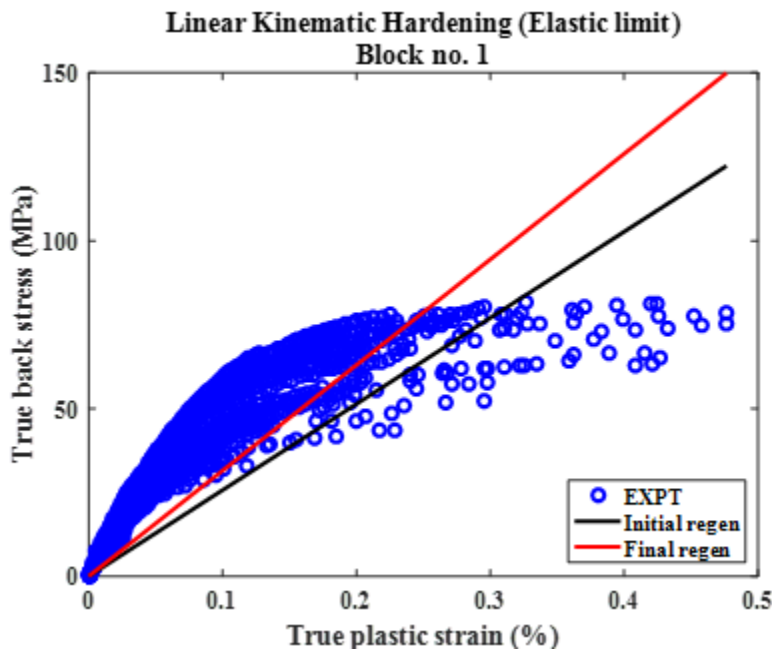


Figure 3D. 6 Comparison of experimental true back stress (as a function of true plastic strain) and predicted back stress (using linear kinematic hardening equation and estimated parameter $C1$, considering elastic limit stress as yield stress) for block-1. Solid line: prediction; Circles: experimental data from 12 fatigue cycles of block-1. Note: Bad prediction and, therefore, block-by-block linear kinematic hardening parameter $C1_{el}$ based on elastic limit stress should not be used for modeling fatigue behavior of 316 SS.

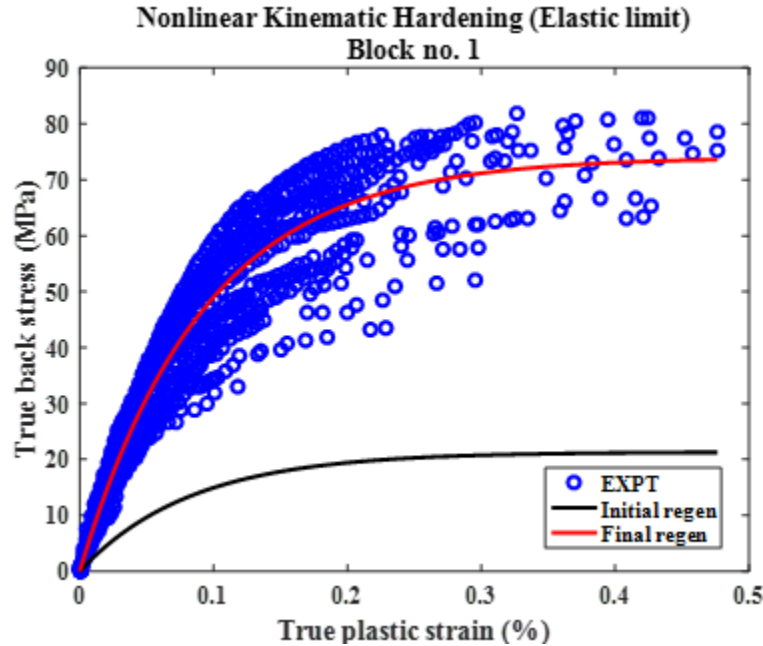


Figure 3D. 7 Comparison of experimental true back stress (as a function of true plastic strain) and predicted back stress (using nonlinear kinematic hardening equation and estimated parameters $C1_{el}$ and $\gamma1_{el}$, considering elastic limit stress as yield stress) for block-1. Solid line: prediction; Circles: experimental data from 12 fatigue cycles of block-1.

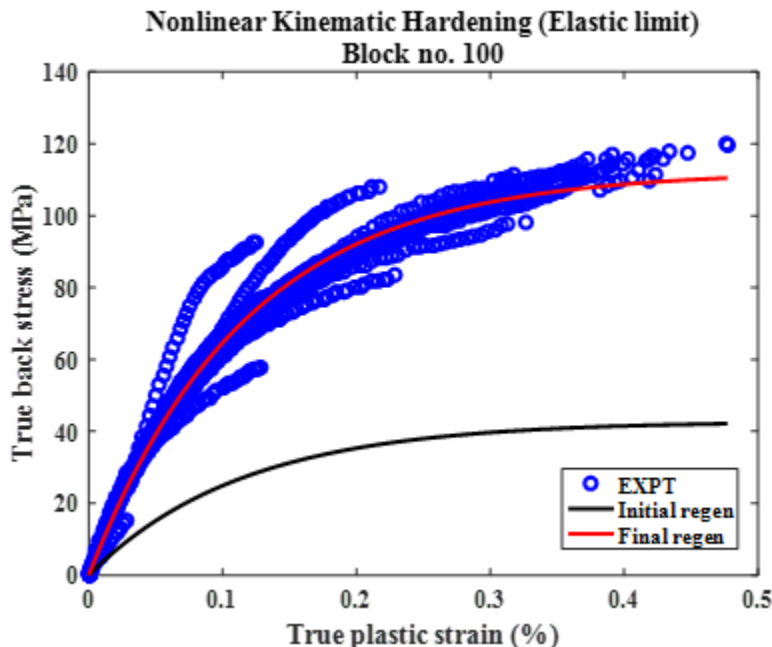


Figure 3D. 8 Comparison of experimental true back stress (as a function of true plastic strain) and predicted back stress (using nonlinear kinematic hardening equation and estimated parameters $C1_{el}$ and $\gamma1_{el}$, considering elastic limit stress as yield stress) for block-100. Solid line: prediction; Circles: experimental data from 12 fatigue cycles of block-100.

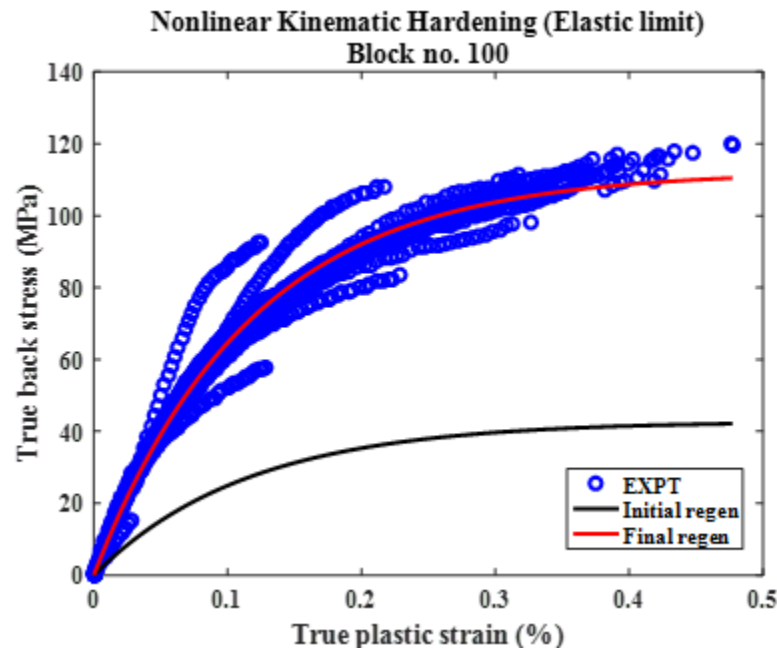


Figure 3D. 9 Comparison of experimental true back stress (as a function of true plastic strain) and predicted back stress (using nonlinear kinematic hardening equation and estimated parameters $C1_{el}$ and $\gamma1_{el}$, considering elastic limit stress as yield stress) for block-1000. Solid line: prediction; Circles: experimental data from 12 fatigue cycles of block-1000.

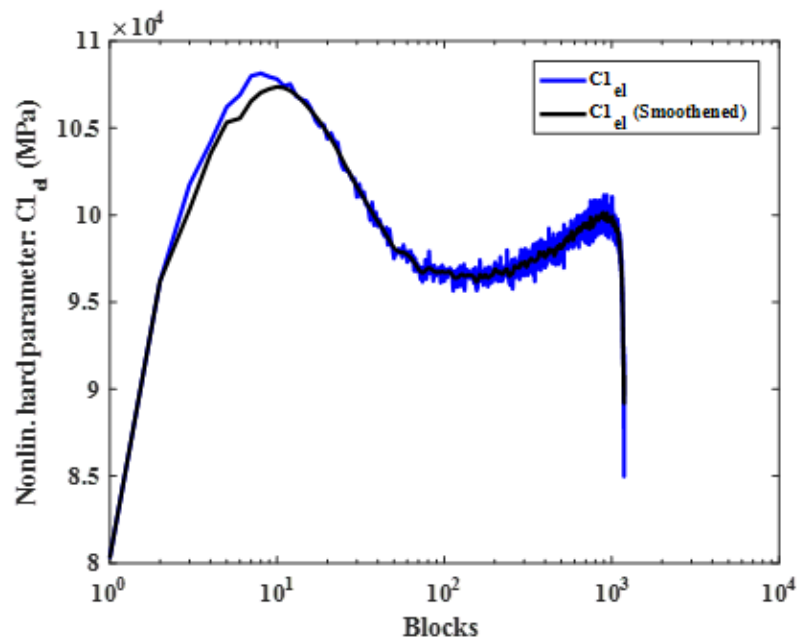


Figure 3D. 10 Block-by-block estimated nonlinear kinematic hardening or Chaboche model parameters ($C1_{el}$) for ET-F38 fatigue test, considering elastic limit stress as yield stress.

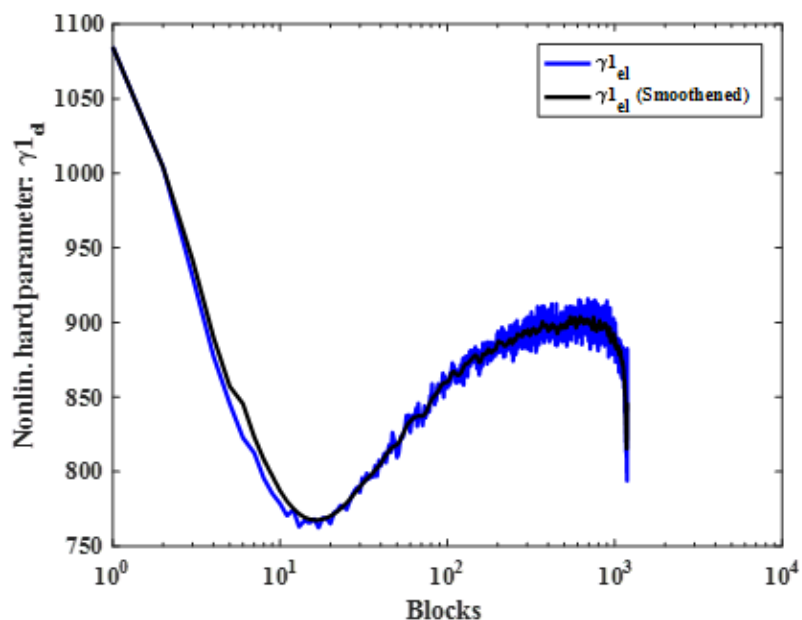


Figure 3D. 11 Block-by-block estimated nonlinear kinematic hardening or Chaboche model parameters (γ^1_{el}) for ET-F38 fatigue test, considering elastic limit stress as yield stress.

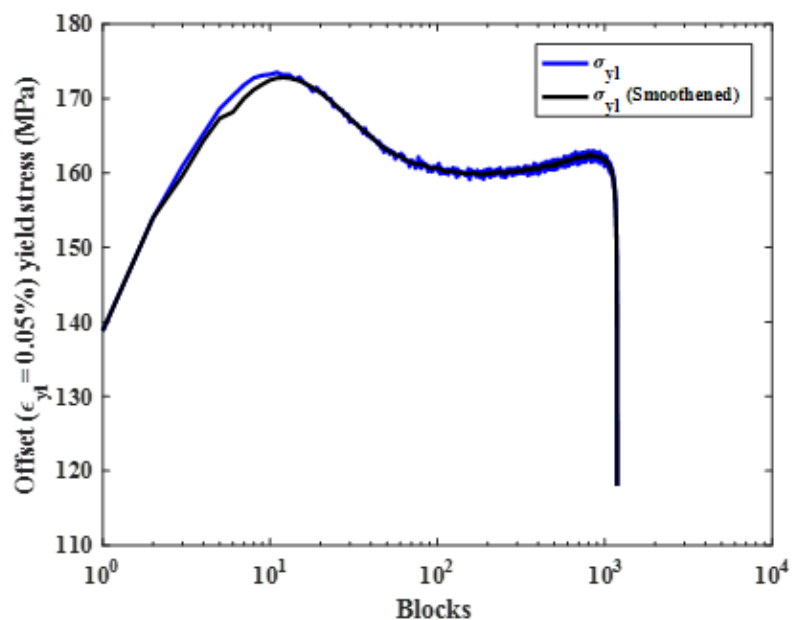


Figure 3D. 12 Block-by-block estimated stress at 0.05% offset yield limit for ET-F38 fatigue test.

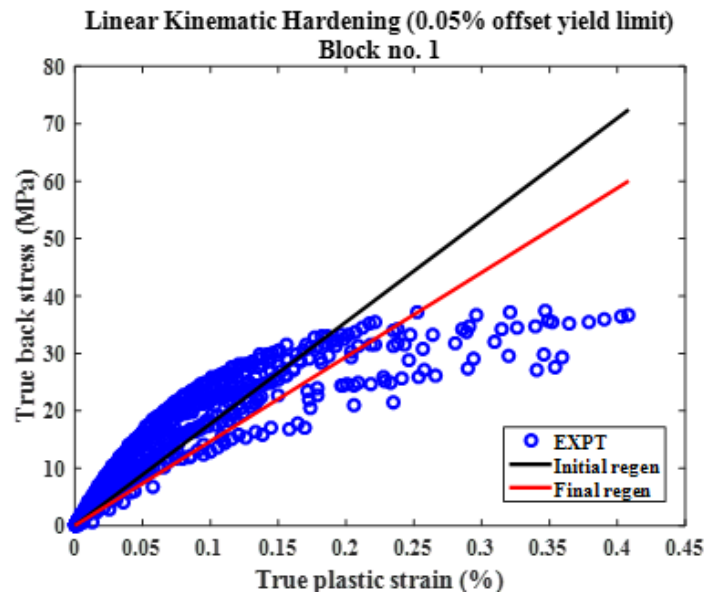


Figure 3D. 13 Comparison of experimental true back stress (as a function of true plastic strain) and predicted back stress (using linear kinematic hardening equation and estimated parameter $C1$, considering stress at 0.05% offset strain as yield stress) for block-1. Solid line: prediction; Circles: experimental data from 12 fatigue cycles of block-1. Note: Bad prediction and, therefore, linear kinematic hardening parameter $C1_{yl}$ based on 0.05% offset yield stress should not be used for modeling fatigue behavior of 316 SS.

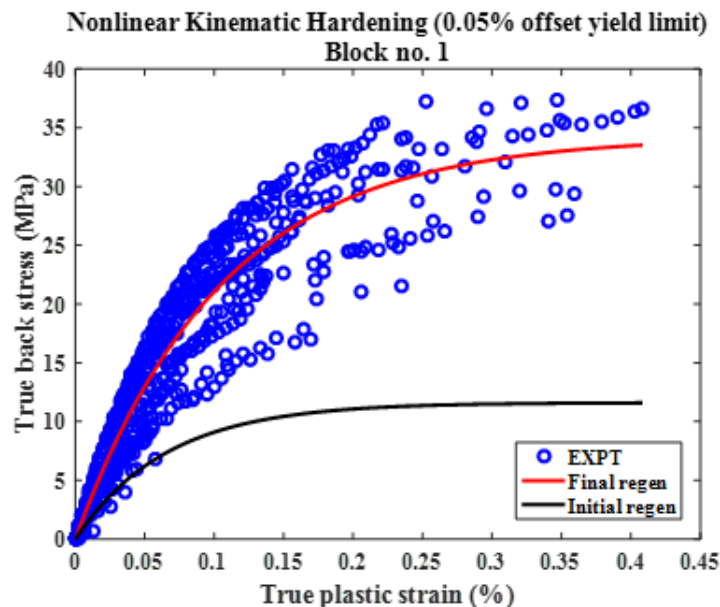


Figure 3D. 14 Comparison of experimental true back stress (as a function of true plastic strain) and predicted back stress (using nonlinear kinematic hardening equation and estimated parameters $C1_{yl}$ and $\gamma1_{yl}$, considering stress at 0.05% offset strain as yield stress) for block-1. Solid line: prediction; Circles: experimental data from 12 fatigue cycles of block-1.

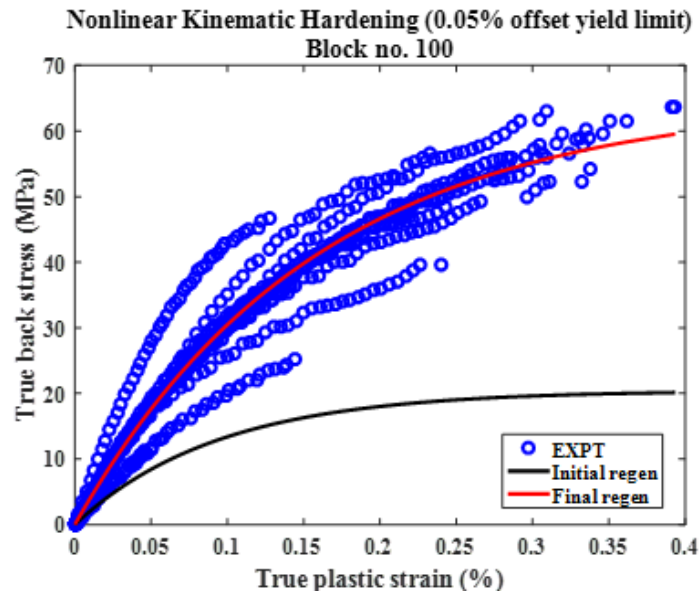


Figure 3D. 15 Comparison of experimental true back stress (as a function of true plastic strain) and predicted back stress (using nonlinear kinematic hardening equation and estimated parameters $C1_{yl}$ and $\gamma1_{yl}$, considering stress at 0.05% offset strain as yield stress) for block-100. Solid line: prediction; Circles: experimental data from 12 fatigue cycles of block-100.

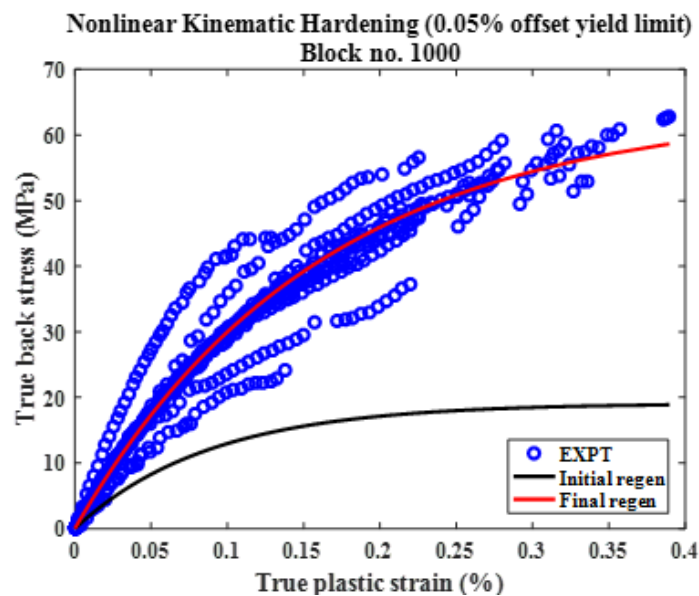


Figure 3D. 16 Comparison of experimental true back stress (as a function of true plastic strain) and predicted back stress (using nonlinear kinematic hardening equation and estimated parameters $C1_{yl}$ and $\gamma1_{yl}$, considering stress at 0.05% offset strain as yield stress) for block-1000. Solid line: prediction; Circles: experimental data from 12 fatigue cycles of block-1000.

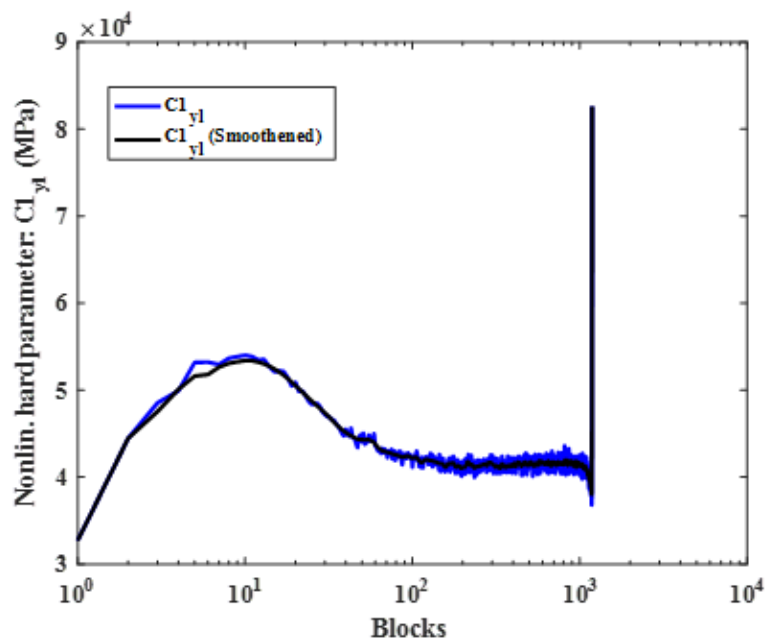


Figure 3D. 17 Block-by-block estimated nonlinear kinematic hardening or Chaboche model parameters ($C1_{y1}$) for ET-F38 fatigue test, considering stress at 0.05% offset strain as yield stress.

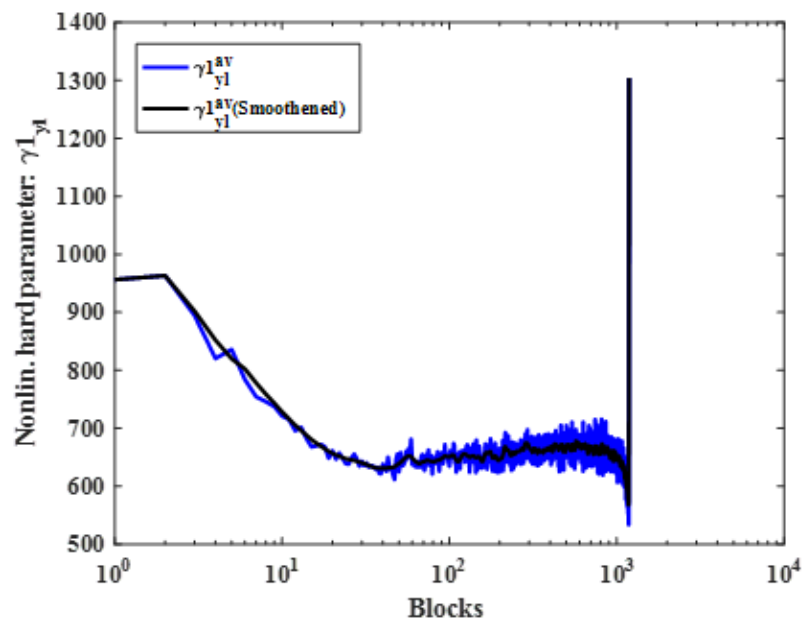


Figure 3D. 18 Block-by-block estimated nonlinear kinematic hardening or Chaboche model parameters ($\gamma1_{y1}$) for ET-F38 fatigue test, considering stress at 0.05% offset strain as yield stress.

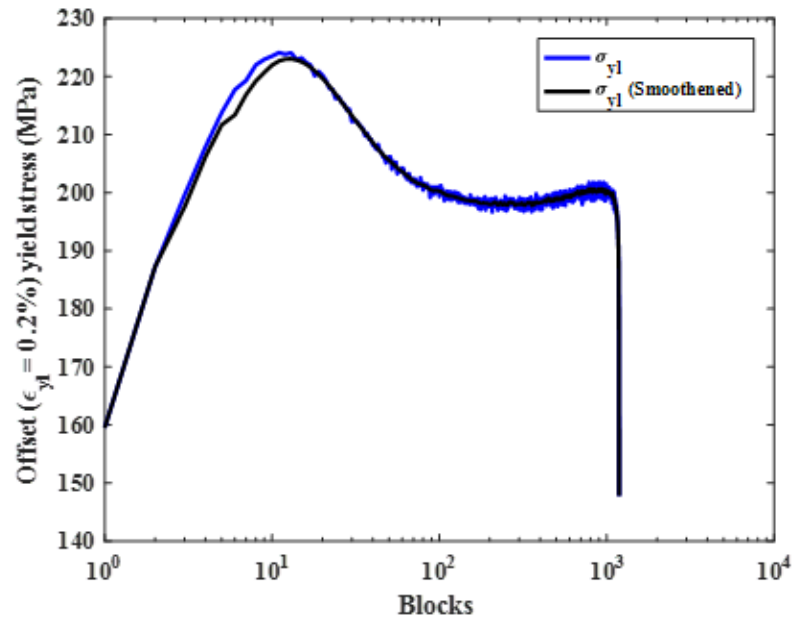


Figure 3D. 19 Block-by-block estimated stress at 0.2% offset yield limit for ET-F38 fatigue test.

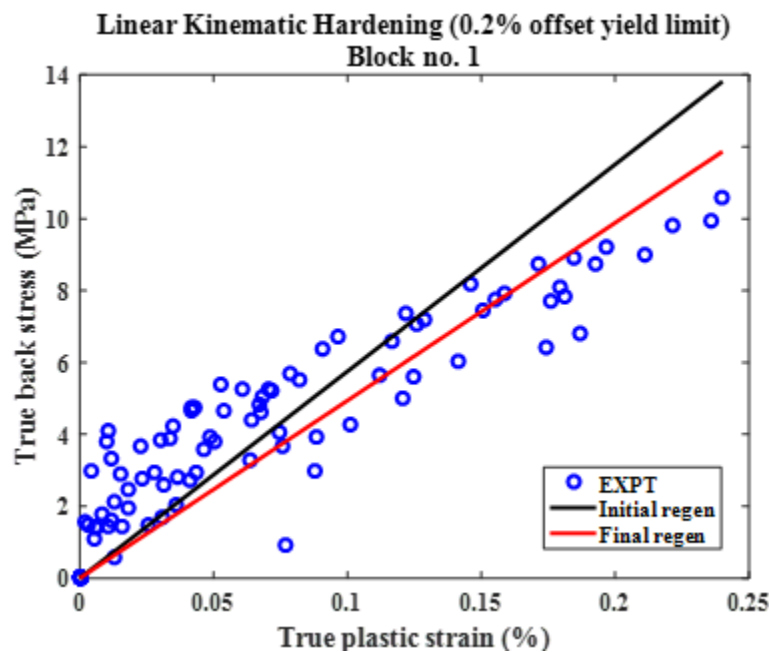


Figure 3D. 20 Comparison of experimental true back stress (as a function of true plastic strain) and predicted back stress (using linear kinematic hardening equation and estimated parameter $C1_{yl}$, considering stress at 0.2% offset strain as yield stress) for block-1. Solid line: prediction; Circles: experimental data from 12 fatigue cycles of block-1.

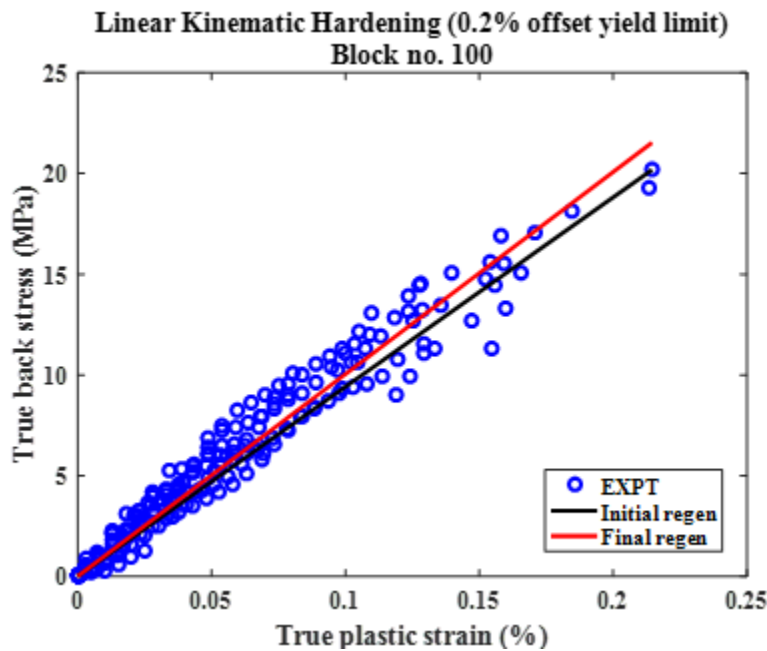


Figure 3D. 21 Comparison of experimental true back stress (as a function of true plastic strain) and predicted back stress (using linear kinematic hardening equation and estimated parameter $C1_{yl}$, considering stress at 0.2% offset strain as yield stress) for block-100. Solid line: prediction; Circles: experimental data from 12 fatigue cycles of block-100.

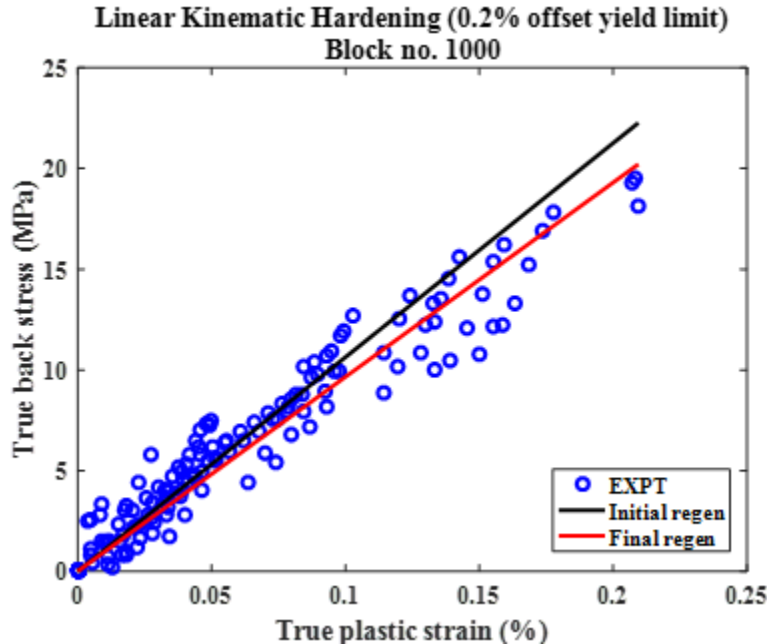


Figure 3D. 22 Comparison of experimental true back stress (as a function of true plastic strain) and predicted back stress (using linear kinematic hardening equation and estimated parameter $C1_{yl}$, considering stress at 0.2% offset strain as yield stress) for block-1000. Solid line: prediction; Circles: experimental data from 12 fatigue cycles of block-1000.

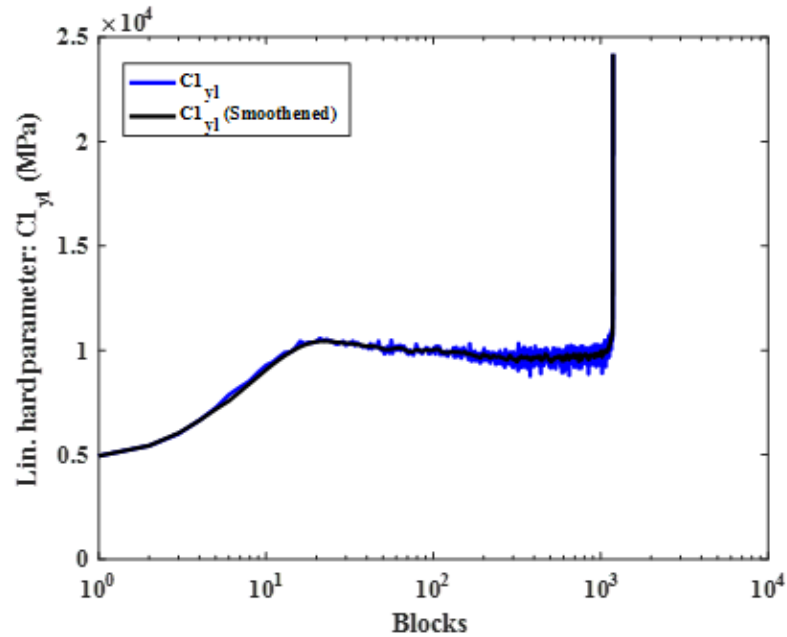


Figure 3D. 23 Block-by-block estimated linear kinematic hardening or Chaboche model parameters ($C1_{yl}$) for ET-F38 fatigue test, considering stress at 0.2% offset strain as yield stress.

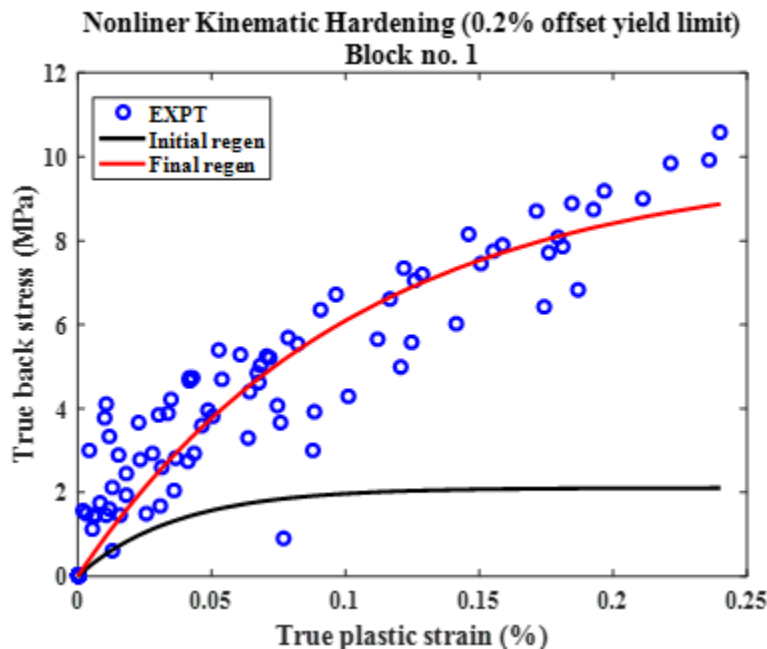


Figure 3D. 24 Comparison of experimental true back stress (as a function of true plastic strain) and predicted back stress (using nonlinear kinematic hardening equation and estimated parameters $C1_{yl}$ and $\gamma1_{yl}$, considering stress at 0.2% offset strain as yield stress) for block-1000. Solid line: prediction; Circles: experimental data from 12 fatigue cycles of block-1000.

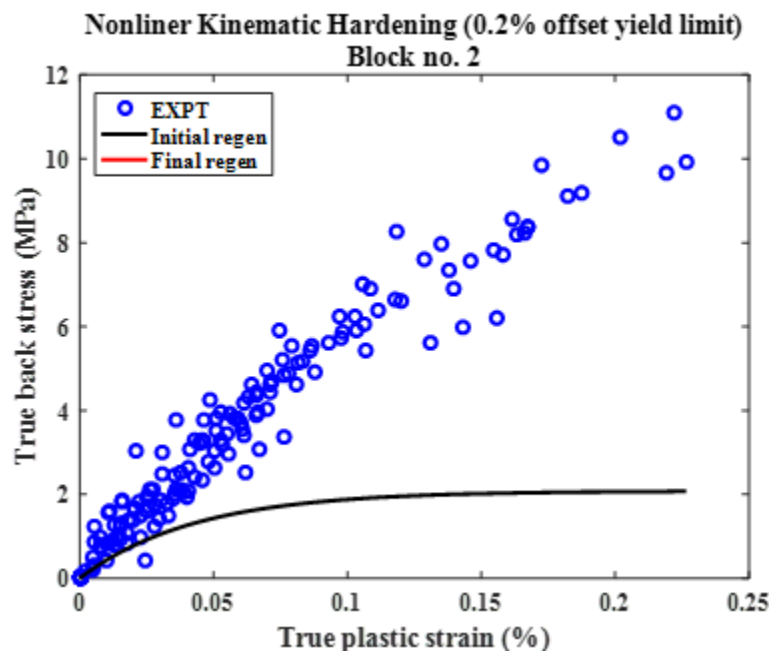


Figure 3D. 25 Comparison of experimental true back stress (as a function of true plastic strain) and predicted back stress (using nonlinear kinematic hardening equation and estimated parameters $C1_{yl}$ and $\gamma1_{yl}$, considering stress at 0.2% offset strain as yield stress) for block-2. Solid line: prediction; Circles: experimental data from 12 fatigue cycles of block-2. Note: iteration norm did not converge and, therefore, nonlinear kinematic hardening parameters ($C1_{yl}$, $\gamma1_{yl}$) based on 0.2% offset yield stress should not be used for modeling fatigue behavior of 316 SS.

Appendix-3E: Supplementary Results for ET-F40 Fatigue Test

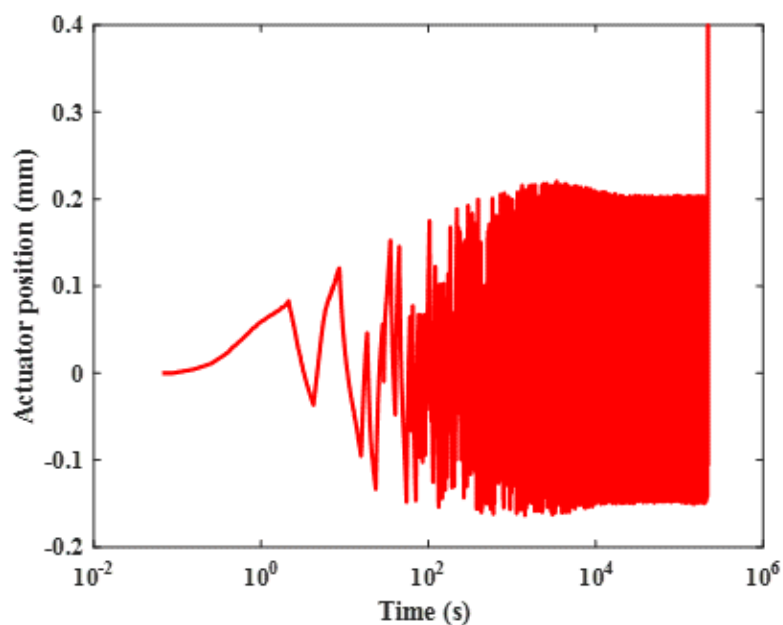


Figure 3E. 1 Observed actuator position during ET-F40. Block period = 4251 s.

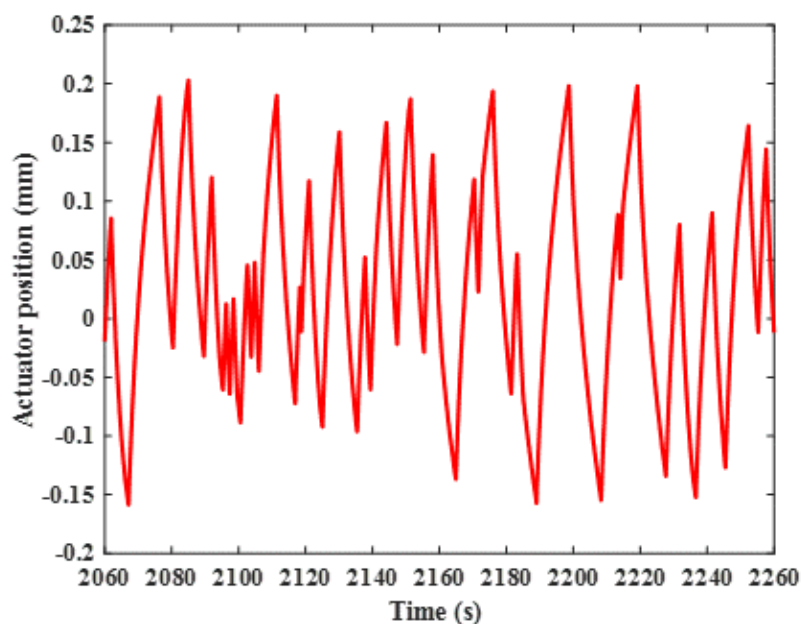


Figure 3E. 2 Magnified version of Figure 3E. 1.

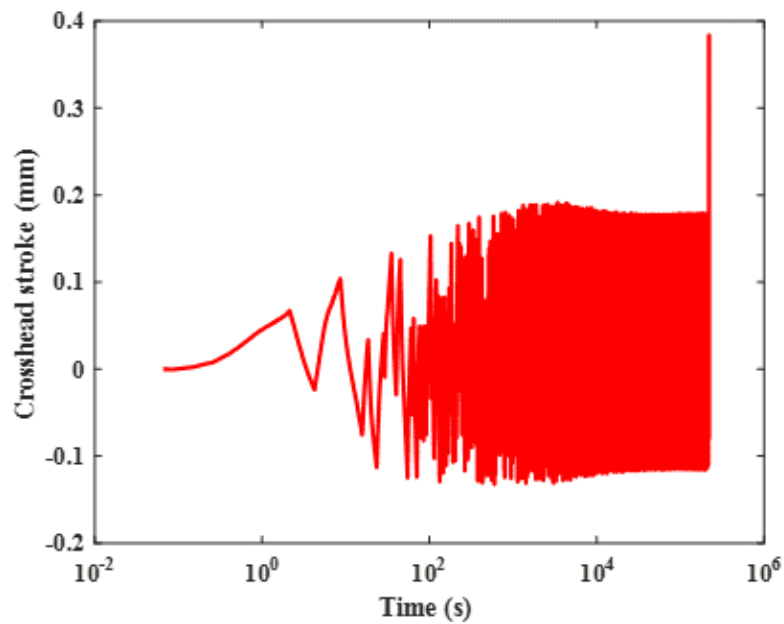


Figure 3E. 3 Observed stroke during ET-F40. Block period = 4251 s.

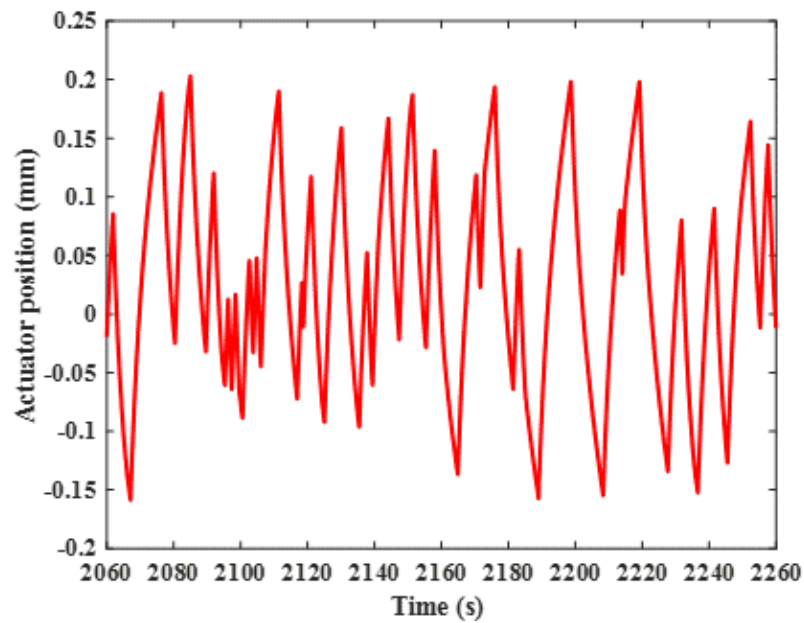


Figure 3E. 4 Magnified version of Figure 3E. 3.

This page intentionally left blank



Nuclear Engineering Division

Argonne National Laboratory
9700 South Cass Avenue, Bldg. 208
Argonne, IL 60439

www.anl.gov